8 102p.

N62-16464

Research Summary No. 36-10, Volume I

for the period June 1, 1961 to August 1, 1961

OTS PRICE

XEROX $ 9.10 ph

MICROFILM $ 3.26 mf

jpl

JET PROPULSION LABORATORY
CALIFORNIA INSTITUTE OF TECHNOLOGY
PASADENA, CALIFORNIA

September 1, 1961

N62-16464

NATIONAL AERONAUTICS AND SPACE ADMINISTRATION
CONTRACT NO. NASw-6

Research Summary No. 36-10, Volume I

for the period June 1, 1961 to August 1, 1961

JET PROPULSION LABORATORY
CALIFORNIA INSTITUTE OF TECHNOLOGY
PASADENA, CALIFORNIA

September 1, 1961

Preface

The *Research Summary* is a bimonthly report of supporting research and development conducted at the Jet Propulsion Laboratory. This periodical is issued in two volumes. Volume I is unclassified, and Volume II is classified Confidential. Text outlines are developed under JPL Division and Section titles. Reports of advanced development projects and activities having specific application to space programs sponsored by the National Aeronautics and Space Administration are published in a companion periodical, the *Space Programs Summary*.

W. H. Pickering, *Director*
Jet Propulsion Laboratory

Research Summary No. 36-10
Volume I

Copyright © 1961
Jet Propulsion Laboratory
California Institute of Technology

Contents

SPACE SCIENCES DIVISION

I. Experimental Space Science 1

Stability of Glass and the History of Meteorites,
by R. R. Marshall 1

SYSTEMS DIVISION

II. Systems Analysis 3

A. Trajectory Analysis,
by V. C. Clarke 3

B. Addition of Range in Orbit Determination of Venus Probe,
by J. D. Anderson 5

GUIDANCE AND CONTROL DIVISION

III. Guidance and Control Research 9

A. Capillary Pumping for Closed-Cycle Gas Systems,
by H. D. McGinness 9

B. Diameters of Mars and Venus,
by R. L. Wildey 13

TELECOMMUNICATIONS DIVISION

IV. Communications Systems Research 15

A. Information Processing Research,
by E. C. Posner, L. D. Baumert, R. C. Titsworth, and M. Hall 15

B. Communications Research,
by M. F. Easterling, R. P. Loomba, R. L. Choate, and A. J. Viterbi 26

V. Communications Elements Research 42

A. Low-Noise Amplifiers,
by W. H. Higa, W. H. Wells, and C. T. Stelzried 42

B. Antennas for Space Communication,
by P. D. Potter and W. V. Rusch 45

C. Thin-Film Techniques,
by W. H. Higa, R. E. Brantner, R. E. Frazer,
J. Maserjian, and H. Erpenbach 51

VI. Communication System Development 54

Communications Analysis,
by C. Gilchriest and J. C. Springett 54

Contents (Cont'd)

PHYSICAL SCIENCES DIVISION

VII. Chemistry Research 64
A. Demonstration of Long-Range Proton-Proton Spin-Spin Coupling in the NMR Spectrum of Cyclohexene,
by D. D. Elleman and S. L. Manatt 64
B. Isothermal Diffusion with a Variable Density,
by O. T. Hanna 66
C. Chemical Equilibrium in Ionized Hydrogen System,
by J. King 68
VIII. Physics Research 70
A. Fission Electric Cell Program: Capsule Calibration Experiment,
by W. F. Krieve 70
B. Electron Distribution Function of a Weakly Ionized Gas in a Magnetic Field and Time Dependent Electric Field,
by C. S. Wu and J. Zmuidzinas 71
IX. Gas Dynamics Research 74
Hypersonic Wake Studies,
by J. M. Kendall 74

ENGINEERING MECHANICS DIVISION

X. Materials Research 76
A. Solid State Research,
by P. J. Shlichta 76
B. Graphite,
by W. V. Kotlensky 78
C. Endothermal Materials,
by R. G. Nagler 79
XI. Engineering Research 81
Solar Proton Shielding,
by D. F. Spencer 81

PROPULSION DIVISION

XII. Liquid Propellant Propulsion 84
A. Combustion and Injection,
by G. I. Jaivin and A. J. Kelly 84
B. Heat Transfer and Fluid Mechanics,
by A. B. Witte and E. Y. Harper 87
XIII. Solid Propellant Propulsion 92
A. Polymer Synthesis and Characterization,
by A. J. Havlik and J. Moacanin 92
B. Polymer Degradation Mechanisms,
by J. D. Ingham and N. S. Rapp 94
References 96

SPACE SCIENCES DIVISION

I. Experimental Space Science

Stability of Glass and the History of Meteorites

R. R. Marshall

The physical constitution of meteorites reflects their violent origin. Although by no means the sole criterion, the presence of glass indicates that high temperatures followed by rapid cooling were involved in the formation of the complex agglomerations present in typical stone meteorites. The chondrites demonstrate the remarkable quasi-stability of glass over nearly 5×10^9 years. The following paragraphs summarize the physical chemistry of the transformation of glass to thermodynamically stable, crystalline assemblages and its relationship to the apparent age of stone meteorites. The complete study will appear in the *Bulletin of the Geological Society of America*.

1. Devitrification in Volcanic Glasses

Glasses are thermodynamically unstable; with time and under a variety of conditions, they become crystalline. When little water is present, devitrification may be described in much the same terms as those which apply to the crystallization of silicate melts. The writer has used simple rate theory and the available experimental data to set an approximate lower limit to the time required for thermal reconstruction of natural glasses as a function of temperature. The time required for a glass at 300°C to become a felsite is estimated to be at least a million years; at 400°C, at least a few thousand years. The secular disappearance of strain birefringence in volcanic glasses at low temperatures indicates an intermediate stage in the process of devitrification. The activation energy for thermal reconstruction is at least 50 kcal/mole and at low temperatures may be as high as 100 kcal/mole.

Along fractures in most volcanic glasses, however, devitrification is dependent upon water. In many samples, the width of the layer *hydrothermally* reconstructed is moderate to vanishingly small. The geologic ages of these glasses indicate that the rate of devitrification at low temperature (around 20°C) is no more than about 4 to 5μ in 100 million years. Hydrothermal reconstruction is very sensitive to temperature; the depth of devitrification generally varies substantially among microscopically unaltered samples from a single flow. In the least devitrified specimens, the depth of devitrification seems to be related to the age of the flow.

Presumably, the diffusion of water controls the rate of hydrothermal reconstruction. The diffusion constant at 20°C is estimated to be 10^{-23} cm^2/sec, and pressure-bomb experiments indicate an activation energy of 30 kcal/mole. Time–temperature relationships have been estimated for hydrothermal reconstruction. In contrast to thermal reconstruction, devitrification in the presence of water requires only a short time (within experimental range) at temperatures no more than about 300°C.

2. *Glass in Meteorites*

The presence of argon and the other gases in meteorites indicates that many of them have not been at elevated temperatures (except perhaps momentarily) since their formation. Measurement of the loss (through diffusion) of these gases is one of the most sensitive ways to estimate the mean temperatures to which meteorites have been exposed (Ref 1).

The argon-potassium age determinations for meteorites range up to somewhat more than 4×10^9 years (Ref 2). The ages found for the Holbrook and Richardton chondrites are 4.40×10^9 and 4.15×10^9 years, respectively. Glass has been observed in both of these meteorites (Refs 3 and 4), as well as in a number of others. Such glass is several billion years older than the oldest known terrestrial glass. Calculations indicate that if a glass remains at temperatures as high as 200°C for such long periods, thermal reconstruction will still not be complete.

Interesting conclusions have been drawn from the release of residual strain in fragments of glass from the Mighei carbonaceous chondrite (Ref 5). The age of this meteorite is probably close to that of other carbonaceous chondrites, which have been dated by the lead-lead method (R. R. Marshall, unpublished data) at about 4.6×10^9 years. If this is the case, even the rate of annealing of strain is extremely slow at low temperatures.

Most tectites, however, were formed quite recently (Ref 6). These glasses, found at widely scattered points of the Earth, seem to have been shaped in flight through the atmosphere. Because their composition is so similar to rocks at the surface of the Earth, their origin as extraterrestrial objects is questionable. In contrast to volcanic glass, the tectites possess virtually no primary microcrystalline phase. Additional research with novel approaches to the problem seem to be necessary to fully understand these strange objects.

SYSTEMS DIVISION

II. Systems Analysis

A. Trajectory Analysis

V. C. Clarke

1. Interplanetary Trajectories

As reported in two previous *Research Summaries (RS 36-8, 36-9)*, a computer study is in progress to determine the characteristics of ballistic interplanetary trajectories from Earth to Mars, to Venus, to Mercury, and to Jupiter. The results of this study will be reported in Reference 7. This report will contain the theory and analysis of three-dimensional ballistic interplanetary transfer. In addition, graphs of 18 pertinent trajectory parameters for each of six launch intervals for Venus from 1962 to 1970 and eight launch intervals to Mars from 1962 to 1977 will be illustrated. At present, all the computation and about 30% of the graphs have been completed. Publication date has been revised to November 1, 1961.

As part of the continuing effort in ballistic interplanetary trajectory analysis, a library of round-trip trajectories, both flyby and stopover, will be computed. A computer program is now being written to accomplish this phase of the analysis. A formal publication on the results of the round-trip trajectories should be ready about the end of 1961.

2. Out-of-the-Ecliptic Trajectories

In *RS 36-9*, preliminary results of a study of a special class of trajectories, called "Out-of-Ecliptic Trajectories," were given. For this class of trajectories, the primary motion is normal to the ecliptic plane, or along an Earth-centered radial direction which has a declination of about 66.5 degrees and a right ascension of about 270 degrees. An Earth-based observer would, at first, observe a space probe launched on this type of trajectory traveling outward along the radial direction with decreasing speed until it came to rest. The maximum distance of outward travel (or altitude above the ecliptic) would be proportional to the hyperbolic-excess speed (i.e., injection energy). After reaching maximum distance at zero-speed, the probe would turn around and return to Earth along the same radial, but with increasing speed. An illustration of the speed profiles for various hyperbolic-excess speeds is shown in Figure 1. The independent variable in this figure is time of flight from injection. From this figure it can be seen that the total flight time is also dependent on the hyperbolic excess speed, varying from 128 days for $V_h = 0.1$ km/sec to 182 days for $V_h = 3$ km/sec.

A Sun-based observer, who sees the Earth revolving around him once per year, would notice the probe rise from the Earth and fly directly above it with increasing

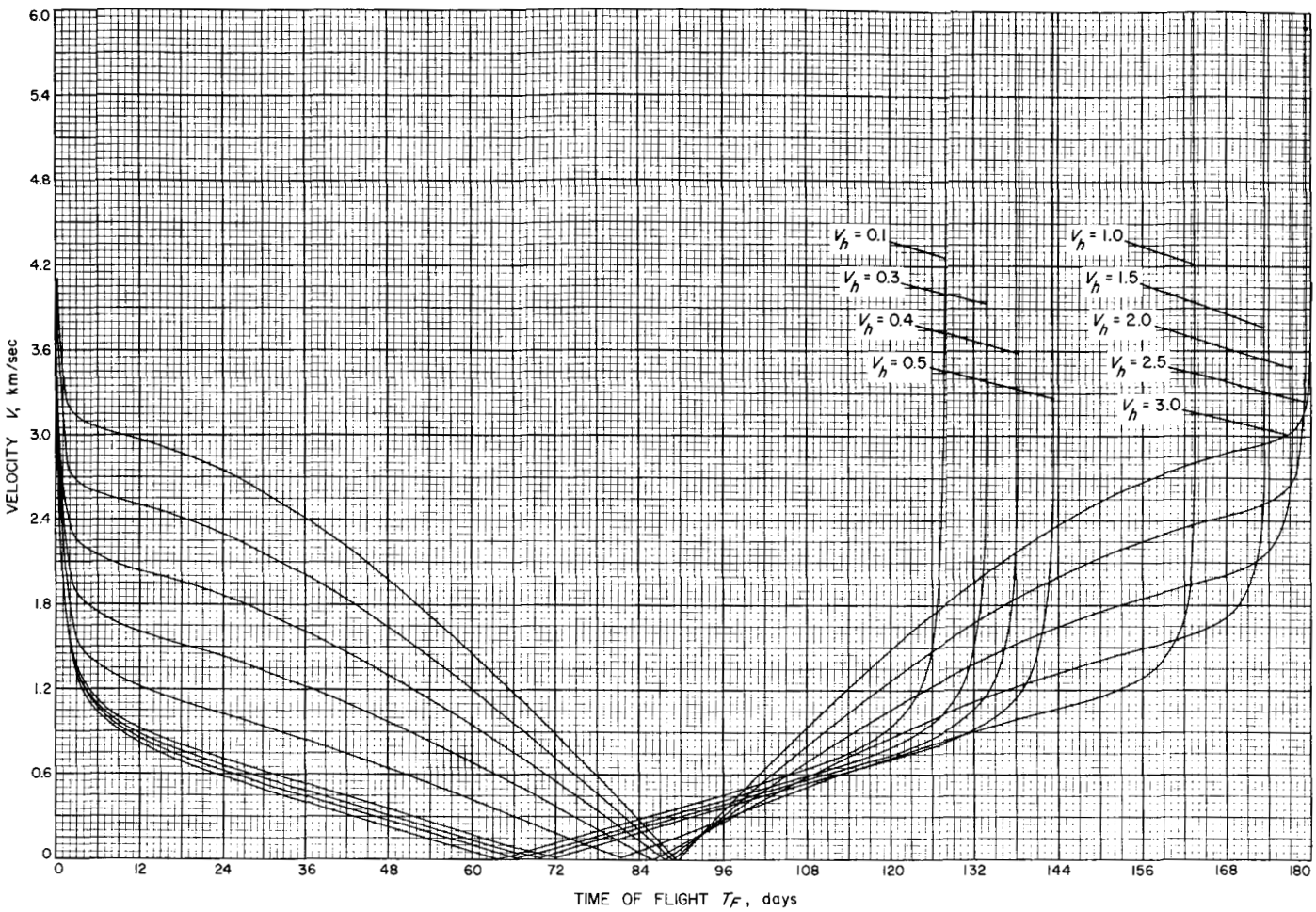

Figure 1. Velocity vs time of flight for various hyperbolic-excess speeds V_h

height until it reached a maximum point. It would then begin to descend back to Earth, and return to Earth in the same time as it took to reach maximum height from launch. The Sun-based observer would find the speed of the Earth and probe to be equal.

Either method of visualization is helpful to understand the motion of this class of trajectories. However, the former provides a simplified basis for an approximate solution to the restricted four-body problem. The Earth-based observer, using a cartesian coordinate system with the X and Y axes lying in the ecliptic plane (X being in the direction of the vernal equinox, and Z along the north ecliptic pole), sees all the motion along the Z direction and almost none along X and Y. Thus, the only equation of motion for the probe is

$$\ddot{Z} = -\frac{GM_E}{Z^2} - GM_s\left[\frac{Z}{(Z^2+R_s^2)^{3/2}}\right] - GM_m\left[\frac{Z}{(Z^2+R_m^2)^{3/2}}\right] \quad (1)$$

where G is the universal gravitational constant; M_E, M_s, M_m, are the masses of the Earth, Sun, and Moon, respectively; R_s is the mean Earth–Sun distance (149,598,500 km); and R_m is the mean Earth–Moon distance (384,400 km). In Equation (1) it is assumed that the orbit of the Earth is circular about the Sun with mean distance R_s, and the Moon's orbit is circular about the Earth with mean distance R_m. In addition, the Moon's orbit lies in the ecliptic plane. This is the restricted four-body problem. Equation (1) can be integrated to give

$$\dot{Z}^2 = \frac{2GM_E}{Z} - \frac{GM_sZ^2}{R_s^3} + \frac{2GM_m}{(Z^2+R_m^2)^{1/2}} + C \quad (2)$$

In this equation, it is assumed that the distance Z is always much less than the Earth–Sun distance R_s, so that

$$\frac{1}{(Z^2+R_s^2)^{1/2}} \simeq \frac{1}{R_s}\left[1 - \frac{1}{2}\left(\frac{Z}{R_s}\right)^2\right] \quad (3)$$

It is interesting to note that the form of Equation (2) is similar to (and can be reduced to, by eliminating the Sun and Moon) the vis viva integral of two-body theory. An important difference, however, is the presence of the negative solar term, $-2GM_s Z^2/R_s^3$. It is essentially the action of this term which causes the probe to slow to zero speed at maximum distance and return to Earth, even though its two-body energy far exceeds the two-body escape condition. Equation (2) is useful (if the lunar term is eliminated) in that if C is known, the maximum distance can be found by equating $\dot{Z}$ to zero and solving a resulting cubic in Z. Solution of the cubic provides *three* roots or values of Z where $\dot{Z} = 0$. This result is not predicted from physical reasoning and may well be a spurious one because of the approximate analysis. Further numerical evaluation is necessary to determine the significance of the three roots. Some numerical evaluation of Equation (2) has been accomplished. Values of Z and $\dot{Z}$ obtained from an exact integrating trajectory program were substituted into Equation (2) to test the "constancy" of C. Figure 2 shows a plot of C as a function of flight time. The constant was evaluated both with and without the lunar term. It is evident that the results improve if the lunar term is included. C has an average value of about 0.08 km²/sec² and a maximum variation of 15%. The cause of this variation is presumed to be due to the approximate analysis used, since circularity of Sun and Moon orbits was assumed and Earth's oblateness was neglected. In addition, it was noted that the variation reduces to as low as 4% for higher energy orbits such as $C = 2.25$ km²/sec².

Further effort is suggested on this problem because of the existence of the cubic in Z. It has been determined numerically that one of the roots coincides with the condition, $\dot{Z} = 0$. What the other two roots mean is yet to be determined.

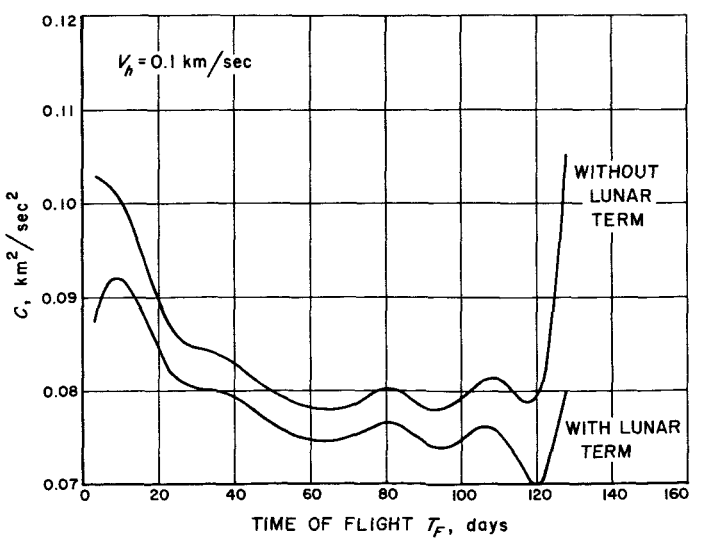

Figure 2. Test of the constancy of C

B. Addition of Range in Orbit Determination of Venus Probe

J. D. Anderson

A preliminary investigation of the use of an additional block of range data in the orbit determination of a Venus probe has been completed. This block of data could be defined by a time tag, the time of the first range point for example, and by an interval of time over which data is obtained at some prespecified rate. Then the improvement in certain orbital parameters could be specified for various blocks of data as well as for various combinations of blocks. Clearly the orbital parameters would ultimately be defined in terms of mission objectives and might take the form of miss components at Venus. Then, if an error description of these mission objective parameters had been obtained from some assumed data distribution, consisting of angular and range rate measurements, the degree of improvement in the orbit determination because of the addition of range measurements would follow. In particular, if only one block of range data defined as above is available, it would be possible to determine the optimum time point with respect to mission objectives at which the range block should be taken.

This particular problem is the one that is investigated here. The time interval of the block is assumed to be sufficiently small so that it is legitimate to treat the range data as a single measurement at a time t of observation. Further, the analysis is designed only to yield a qualitative result, the point in the trajectory where a range block is most useful in reducing the terminal miss. Also, a rigorous solution of the problem is avoided to eliminate lengthy numerical computations; for example, a numerical integration of the equations of motion for the probe. Therefore, a considerably simplified model of the orbit is employed based on the Hohmann ellipse. This orbit is a minimum-energy two-body trajectory where the probe is launched at aphelion, the probe's greatest distance from the Sun, and intercepts the orbit of Venus at perihelion, the distance of the probe's closest approach to the Sun. In effect, the motions and influence of the

Earth and Venus are totally neglected and the orbit is simply a heliocentric ellipse. In addition, the orientation of the orbit in space is assumed known precisely and the assumption that the probe is launched at aphelion is taken as a constraint on the motion. This constraint, in conjunction with the three assumed Eulerian angles which specify the orientation, removes four degrees of freedom from the general orbit. The two remaining degrees of freedom are chosen as the time of flight τ and perihelion distance q. The time of flight in the Hohmann ellipse is defined by the time it takes the probe to travel from aphelion to perihelion, or equivalently by one-half the orbital period, while the perihelion distance can be interpreted as the distance of the probe from the Sun at the terminal position. For the Venus trajectory, τ is about 146 days and q about 1.08×10^8 km. This choice of parameters is based on the fact that at perihelion an error in the time of flight represents an error tangential to the orbit plane, and an error in the perihelion distance represents a radial error. Thus, the errors in τ and q can be interpreted, respectively, as tangential and radial errors at the terminal position. The significance of τ and q in the elliptic trajectory may be more easily appreciated by expressing them in terms of the geometrical semi-major axis a and eccentricity e. By Kepler's third law, the period of a two-body orbit is proportional to the three-halves power of the semi-major axis. Therefore, because τ is one-half the orbital period

$$\tau = \frac{\pi}{Gm_0} a^{3/2} \tag{1}$$

The constants G and m_0 in the proportionality constant are, respectively, the universal gravitational constant and the mass of the Sun. The perihelion distance q is related to both a and e through the geometrical relation

$$q = a(1 - e) \tag{2}$$

With the above interpretation of the two free orbital parameters, it is clear that errors in τ and q will result in errors in the scale of the orbit through the semi-major axis and also in the shape through the eccentricity.

In the investigation of the effect of range uncertainties on the parameters τ and q, it is assumed that errors in the parameters map linearly into errors in range. The expression of this mapping is facilitated if errors in τ and q are made dimensionless by introducing the parameters a_τ and a_q such that

$$\Delta a_\tau = \frac{\Delta\tau}{\tau} \tag{3}$$

$$\Delta a_q = \frac{\Delta q}{q} \tag{4}$$

Then the error in range ρ in terms of Δa_τ and Δa_q is given by

$$\Delta\rho = \frac{\partial\rho}{\partial a_\tau}\Delta a_\tau + \frac{\partial\rho}{\partial a_q}\Delta a_q \tag{5}$$

The partial derivatives of range with respect to a_τ and a_q require an expression for the range from the observer to the probe. This is obtained geometrically by subtracting the position of the observer in heliocentric space from the position of the probe obtained by the usual Keplerian formulas that give the position of the probe as a function of time. The magnitude of the resulting vector is the range. To simplify this expression for ρ which must finally be differentiated, it is assumed that the heliocentric motion of the Earth and probe is co-planar, that the orbit of the Earth is circular, and that the observer is located at the center of the Earth. Although these assumptions can result in appreciable errors in the computation of range, it should be pointed out that the range value itself does not appear in the expression for the error mapping (5) and that the partial derivatives are the only quantities of interest.

Clearly the expression (5) for $\Delta\rho$ is not sufficient to answer the relevant question of the optimum point to take a single range measurement in the sense defined above. Instead, a covariance matrix, sometimes called a noise moment matrix, is constructed whose diagonal elements are the normal variances or mean square errors on a_τ and a_q and whose off-diagonal elements are the covariances which describe error correlations in the parameters. Of course, an expression of error in this form presupposes that the error on the range measurements obeys a normal probability distribution. Actually, this covariance matrix must describe the improvement in the parameters a_τ and a_q because of the addition of range at a time point t. Thus, it is assumed that in the absence of range the mean square error on both a_τ and a_q is unity and that the errors on these parameters is uncorrelated. This assumption implies that the a-priori covariance matrix on the parameters is the unit matrix. Certainly the choice of unity errors on these parameters is arbitrary since a_τ and a_q are dimensionless, and valid quantitative results are not expected under the many assumptions applied in this analysis.

Finally, it can be shown that the covariance matrix C which describes the range improvement in a_τ and a_q is

given in terms of the partial derivatives of range by

$$C = \left\{ \begin{pmatrix} 1 & 0 \\ 0 & 1 \end{pmatrix} + \frac{1}{\sigma^2} \begin{bmatrix} \left(\frac{\partial \rho}{\partial a_T}\right)^2 & \left(\frac{\partial \rho}{\partial a_T}\right)\left(\frac{\partial \rho}{\partial a_q}\right) \\ \left(\frac{\partial \rho}{\partial a_T}\right)\left(\frac{\partial \rho}{\partial a_q}\right) & \left(\frac{\partial \rho}{\partial a_q}\right)^2 \end{bmatrix} \right\}^{-1} \tag{6}$$

where σ^2 is the variance on the additional range measurement. For the numerical evaluation of C, σ^2 is set equal to unity in all cases and the units of range ρ are adjusted to be commensurable with σ^2; specifically, the unit of range is the range value when the probe is at perihelion, the terminal position. Now, because the partial derivatives can be evaluated as a function of time, the matrix C is a function of time also. Figures 3, 4, and 5 offer various interpretations of the resulting computations of C with time as the argument. In addition, the value of the angle θ between the position of the probe at time t and its initial position at aphelion is given as an alternate argument. In terms of the elements of the Keplerian orbit, the angle θ is 180 degrees plus the true anomaly.

Figure 3 gives an indication of the information added by a range measurement as a function of where the measurement is taken. The curve labeled $-\log |C|$ is the negative of the logarithm of the determinant of C, while the curve labeled I is more closely related to the trace of C. Explicitly

$$I = 2^{1/2} - (\text{trace } C)^{1/2} \tag{7}$$

where the trace of a matrix is defined as the sum of the diagonal elements. If the range point adds no information, the trace of C is equal to the trace of the unit matrix.

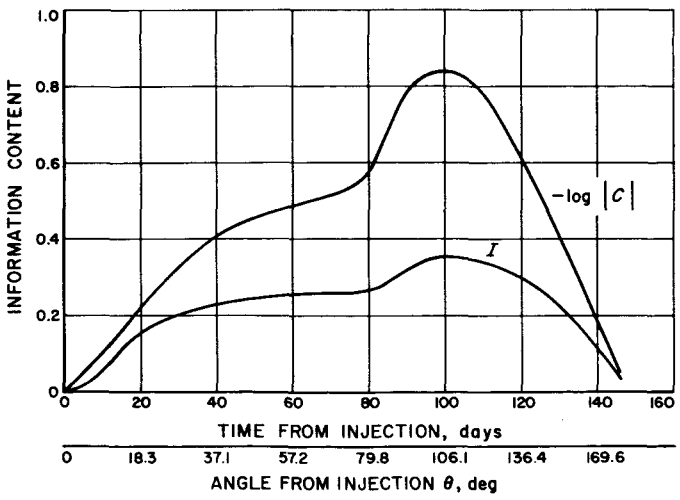

Figure 3. Information content of a single range measurement taken at time t

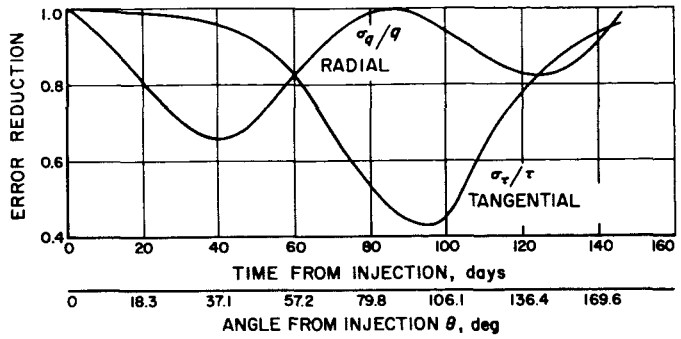

Figure 4. Error reduction in heliocentric radial and tangential components of terminal position because of addition of range at time t

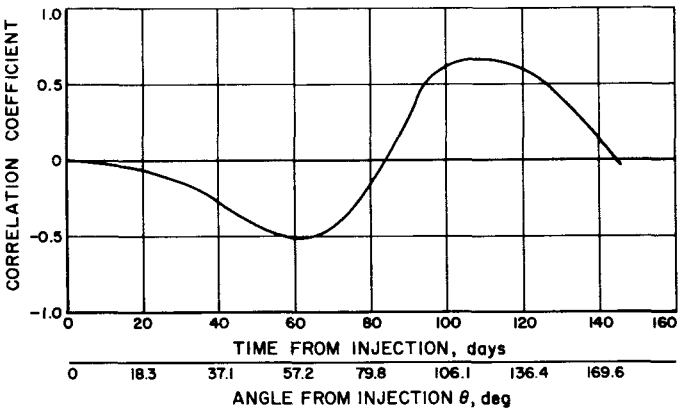

Figure 5. Correlation coefficient for terminal radial and tangential error components because of addition of range at time t

On the other hand, the determinant of the unit matrix is unity and the logarithm of its determinant is necessarily zero. Therefore, both curves in Figure 3 are referenced to zero as the point of no information.

Figure 4 is a plot of the square roots of the diagonal elements of the covariance matrix C. These quantities are interpreted as the relative errors σ_T/τ and σ_q/q in the time of flight and perihelion distance, respectively, or in the tangential and radial components of the terminal position. No improvement is reflected in unity values.

Finally, Figure 5 is a plot of the correlation coefficient $\rho_{q\tau}$ for the errors in time of flight and perihelion distance. As usual, this coefficient is defined as the quotient of the covariance over the square root of the product of the variances. That is, with the elements of C given by C_{rs}

$$\rho_{q\tau} = \frac{C_{12}}{(C_{11}\, C_{22})^{1/2}} \tag{8}$$

Because the a priori errors are assumed uncorrelated, the correlation coefficient gives some indication of how a range measurement can correlate the errors in heliocentric radial and tangential miss components.

In general, it would appear from the results given here, that if only one block of range data is possible, it should be taken at about 100 days after injection in a 146-day trajectory, although another measurement at about 40 days would help reduce the radial error. However, it is clear that a conservative attitude toward these results is in order until a rigorous quantitative error analysis is available. Such an analysis is anticipated which will be based on realistic three-dimensional trajectories of varying flight times, typical data errors and an improvement given in terms of miss components at Venus.

GUIDANCE AND CONTROL DIVISION

III. Guidance and Control Research

A. Capillary Pumping for Closed-Cycle Gas Systems

H. D. McGinness

In *Research Summaries 36-1*, *36-2*, *36-4*, and *36-7*, a closed-cycle gas supply system for gas bearing instruments was described which uses thermal power from solar or nuclear energy sources to pump a two-phase fluid from the evaporator through the gas bearing and into the condenser. A preliminary report on a feasibility study of using the capillary action of a wick for returning the condensate to the evaporator appeared in *RS 36-9*. A schematic diagram of a capillary gas-pumping system is shown in Figure 6a.

One objective in the design of a capillary pump is the attainment of the maximum mass flow at the required pressure. In order to achieve some insight into the relationship between the useful pressure created by the wick, the flow rate, and various design parameters, an analysis is presented here that is based upon a number of assumptions, some of which must be verified by experimentation.

1. Description of Capillary Gas-Pumping System

From the liquid reservoir (Fig 6a), the liquid flows through the capillaries to the menisci, across which there is a pressure increase. Evaporation occurs at the menisci, and the vapor becomes superheated as it flows toward the bearing. The vapor leaves the bearing at a reduced pressure and is condensed upon entering the liquid reservoir. The heats of vaporization and superheat are supplied by room ambient. The condenser temperature is maintained by an ice-water box. In Figure 7, the pressure–temperature cycle is shown qualitatively.

a. Pressure notation. In Figures 6 and 7, the line $P_{Li}P_{Vi}$ represents the pressure increase across the menisci; $P_{Vi}P_{VEi}$ represents the pressure drop caused by the viscous drag of the vapor flowing through the remainder of the wick, accompanied by a temperature rise; $P_{VEi}P_U$ represents the flow from the exit end of the wick to the bearing; P_UP_D is the pressure drop across the bearing; P_DP_{LBi} is the flow from the bearing to the wick entrance; $P_{LBi}P_{Li}$ represents the pressure drop of the liquid caused by the viscous drag of the liquid flow through the wick.

b. Assumptions. (1) Each wick consists of N capillary tubes in parallel, all capillaries are assumed to be identical and have the effective diameter d, and there are n stages in series. (2) Each capillary is of length L, and the meniscus stands at a distance α from the entrance end. (3) The pressure increase across each meniscus is assumed to be the same in all stages; this implies that the temperature of the liquid in the $(i + 1)$th stage is greater than that of the liquid in the ith stage. (4) The viscous flow

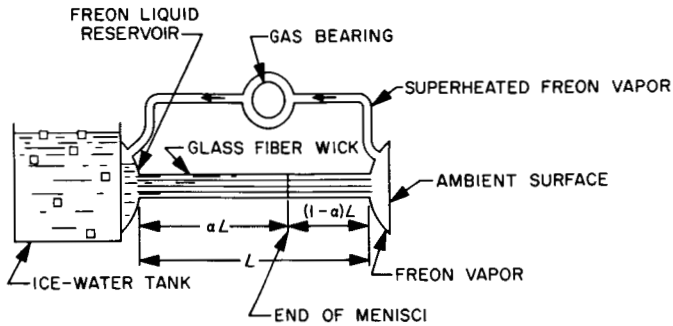

a. SINGLE-STAGE CAPILLARY PUMP

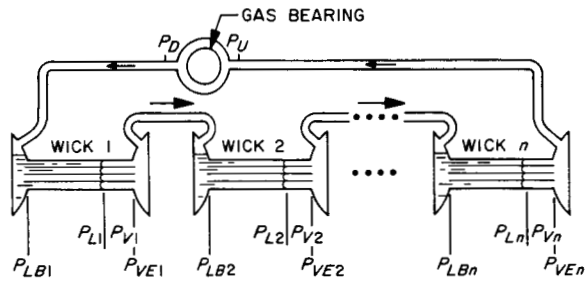

b. MULTIPLE-STAGE CAPILLARY PUMP

Figure 6. Single-stage and multiple-stage capillary pumps

theory is applicable in this system. (5) Pressure losses come from the fluid flow through the capillaries and the flow through the gas bearing; the connecting tubes are assumed to produce no pressure losses. (6) The contact angle between the menisci and the capillary walls is assumed to have the constant value θ; that is, the meniscus acts as a constant pressure pump. Admittedly this is a problematical assumption which implies that heat availability and heat transfer properties are most favorable.

2. *Analysis of Capillary Gas-Pumping System*

Using the pressure notation shown in Figure 6b, it is clear that the pressure drop across the bearing (ΔP_{BR}) is

$$P_U - P_D = \Delta P_{BR} =$$

$$\sum_{i=1}^{n} (P_{Vi} - P_{Li}) - (P_{LBi} - P_{Li}) - (P_{Vi} - P_{VEi}) \qquad (1)$$

By Assumptions (3) and (6), the first right-hand term of Equation (1) becomes

$$\sum_{i=1}^{n} (P_{Vi} - P_{Li}) = \frac{4\sigma n \cos\theta}{d} \qquad (2)$$

(*RS 36-9*) where d is the effective diameter of a capillary (the actual diameter of a circular cross section capillary), and σ is the surface tension of the liquid.

The second right-hand term is, by Assumption (4),

$$\sum_{i=1}^{n} (P_{LBi} - P_{Li}) = \frac{128 n \mu W \alpha L}{\pi N \gamma_L d^4} \qquad (3)$$

where μ_L is the absolute viscosity of the liquid, W is the weight flow, and γ_L is the weight density of the liquid.

The third right-hand term of Equation (1) is, by Assumption (4):

$$\sum_{i=1}^{n} (P_{Vi} - P_{VEi}) = \frac{128 n \mu_V W \mathrm{IIRTL}(1-\alpha)}{\pi N d^4 \left(\frac{P_{Vi} + P_{VEi}}{2}\right)} \qquad (4)$$

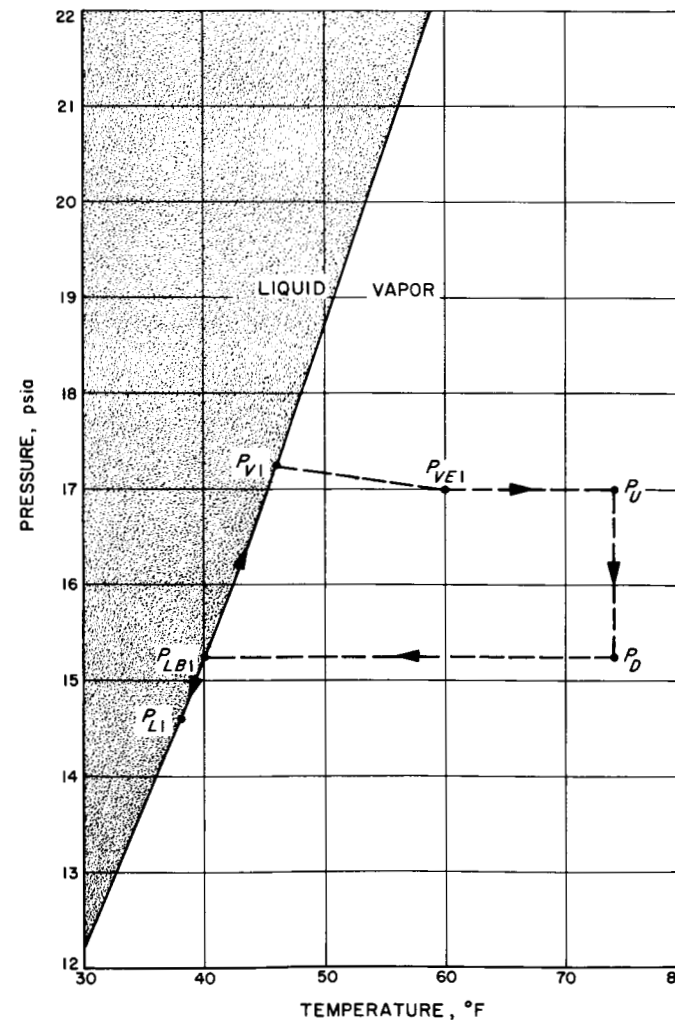

Figure 7. Pressure vs temperature for Freon 114

where μ_V is the absolute viscosity of the vapor, R is the gas constant of the vapor, and T is the absolute temperature of the vapor.

For small values of $(P_{Vi} - P_{VEi})$, the following is a convenient approximation:

$$\sum_{i=1}^{n} (P_{Vi} - P_{VEi}) \approx \frac{128 n \mu_V W L (1-\alpha)}{\pi N \gamma_V d^4} \qquad (5)$$

where γ_V is the average weight density of the vapor.

By substituting Equations (2), (3), and (5) into Equation (1), there is obtained

$$\Delta P_{BR} \approx n \left\{ \frac{4\sigma \cos\theta}{d} - \frac{128 W L}{\pi N d^4} \left[\frac{\mu_L \alpha}{\gamma_L} + \frac{\mu_V (1-\alpha)}{\gamma_V} \right] \right\} \qquad (6)$$

An examination of Equation (6) shows that it is desirable to have cos θ equal to unity in order to obtain the maximum ΔP_{BR}, the pressure difference across the bearing. Since $\mu_L/\gamma_L < \mu_V/\gamma_V$ for most fluids, it is usually desirable to have α equal to unity. With these values of α and cos θ, the weight flow W is, from Equation (6)

$$W = \frac{\pi \gamma_L N}{128 \mu_L L} \left[4\sigma d^3 - \frac{\Delta P_{BR}}{n} d^4 \right] \qquad (7)$$

Equation (7) shows that the lengths of the capillaries should be short in order to obtain the maximum flow. As L approaches zero, the assumption that the menisci act as constant pressure pumps is obviously absurd. It is thought that the best value of L is the shortest one which will permit the necessary temperature difference between the condensed liquid and the vapor. By considering the bracketed term of Equation (7), it appears that an optimum value of d, the capillary diameter, exists. By setting the derivative of the bracketed term (with respect to d) equal to zero and solving for d, the optimum value is obtained:

$$d_{opt} = \frac{3n\sigma}{\Delta P_{BR}} \qquad (8)$$

In all cases, in order to have positive flow for a given ΔP_{BR}, Equation (2) indicates that d must be less than $4n\sigma/\Delta P_{BR}$. Hence, the optimum value of d is three-fourths of the largest value that permits a positive flow. By substituting Equation (8) into Equation (7) there is obtained the maximum weight flow for the required ΔP_{BR}, when the menisci stand near the exit ends of the capillaries:

$$W_{max} = \frac{0.663 \gamma_L \sigma^4 N n^3}{\mu_L L (\Delta P_{BR})^3} \qquad (9)$$

For Freon 114, the following values pertain:

$\gamma_L = 0.052$ lb/in.^{3}

$\mu_L = 52 \cdot 10^{-9}$ lb-sec/in.^{2}

$\sigma = 7.43 \cdot 10^{-5}$ lb/in.

The substitution of these values into Equation (9) results in:

$$\left(\frac{WL}{N}\right)_{max,\ \text{Freon 114}} = 0.203 \cdot 10^{-10} \frac{n^3}{(\Delta P_{BR})^3} \qquad (10)$$

where W is in lb/sec, L in inches, and ΔP_{BR} in psi. In Figure 8, the parameter WL/N is plotted against ΔP_{BR}. The horizontal dashed lines indicate the values of the optimum capillary diameters.

3. Experimental Capillary Gas-Pumping System

The experimental test apparatus is shown schematically in Figure 9. It is a modification of that described in

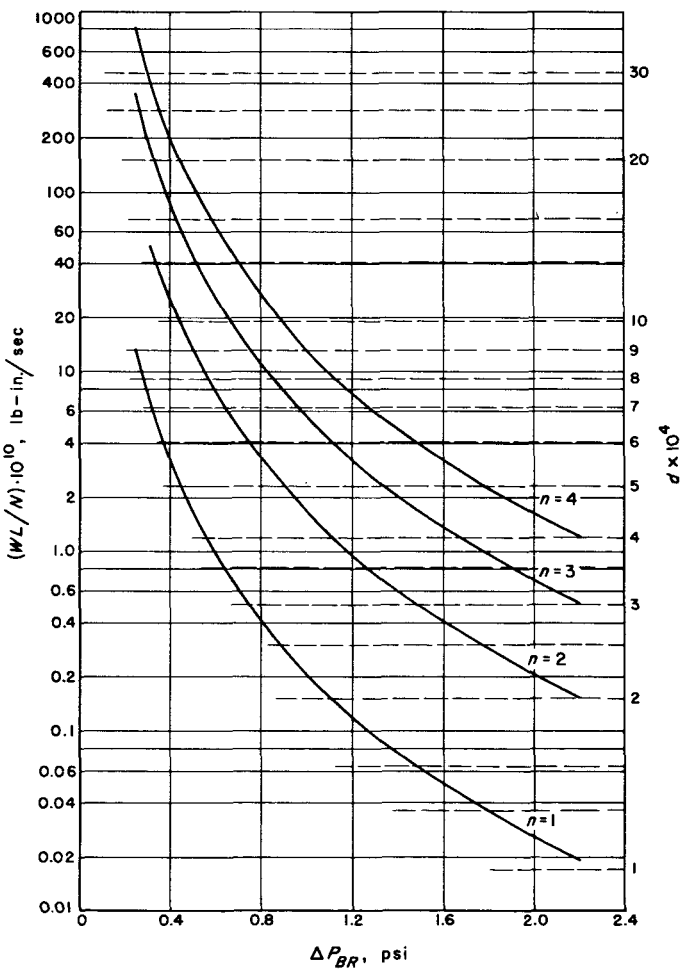

Figure 8. Weight flow vs ΔP_{BR} for optimum capillary diameter using Freon 114

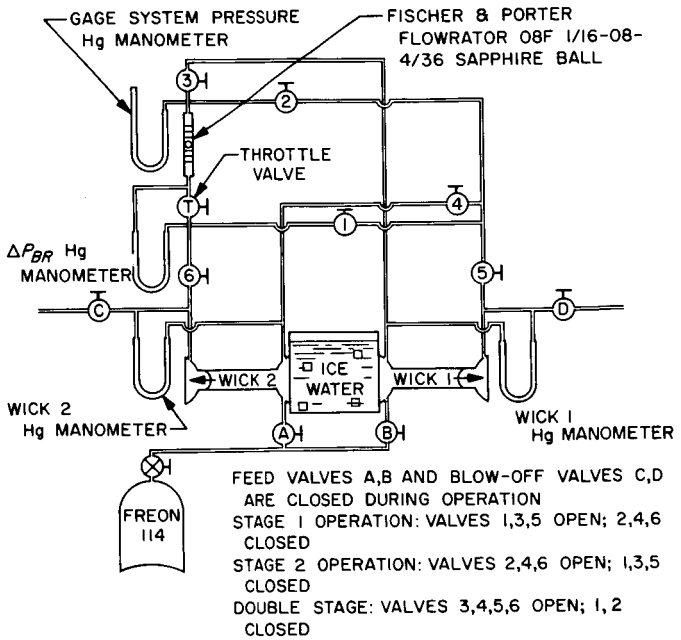

Figure 9. Capillary gas-pumping system test apparatus

Research Summary 36-9. Each wick consists of a ⅜-inch-ID × 10-inch-long glass tube compactly filled with 0.0005-inch glass fibers which flare out at each end and partially fill bell-shaped cavities. It is estimated that approximately 500,000 capillaries are formed by sets of three mutually tangent fibers. The gas bearing was simulated by a throttle valve. The Freon condenser temperature is obtained by contact with an insulated ice-water box, and the required heat comes from room ambient. By properly setting the valves, either Wick 1 or Wick 2 can be operated as a single-stage system, or the two wicks may be combined in series to operate as a double-stage system.

It was observed that immediately after a long period of no flow (i.e., with the throttle closed and with the valves set for double-stage operation), the pressure increase across Wick 1 ($\Delta P_{Wick\,1}$) was zero. Presumably this was because the temperature of the two condenser ends of the wicks were the same. By removing a part of the insulation from the ice box on the side of Wick 2 or by briefly shining a heat lamp on that side, the full pressure increase across both wicks would occur. Thus, multiple-stage operation can be achieved by maintaining the proper temperature gradient between consecutive condenser stages. A possibility of obtaining multiple-stage operation with a common condenser temperature is the introduction of a noncondensable gas between the exit end of one wick and the entrance end of the next. If such gas remains trapped between the menisci, then the required total pressure can be obtained. (The Freon vapor partial pressure will be that corresponding to the common condenser temperature.) This experiment will be performed later.

In Table 1 are listed the experimentally obtained values. Unfortunately, it is difficult to compare these values with predictions from the theory given above, primarily because the size and number of imperfectly formed capillaries is not known. Presumably, the maximum pressure difference that a wick can support continually will depend upon the size of the largest capillary, whereas the weight flow would depend upon both the sizes and number of imperfect capillaries. Obviously the experimental wicks do not satisfy Assumption (1). General performance trends, however, are qualitatively predicted by the theory.

It was observed that, for the tests listed in Table 1, condensed water covered the outside of the wick housings over approximately the first 3/10 of the wick's length. It is probable that the menisci were positioned at these points, giving an α value of 0.30. In order to test the effect of increasing α to near unity, Wick 1 was submerged in ice water over practically its entire length. The flow was held constant at $0.26 \cdot 10^{-5}$ lb-sec. The ΔP_{BR} value before the wick was chilled was 0.19 psi, whereas after chilling there was the substantially improved ΔP_{BR} value of 0.41 psi. Thus, as the theory suggests, the menisci should be made to stand near the exit end. Most probably a considerably shorter wick would produce a pressure increase,

Table 1. Measured pressures and flows at 78°F ambient

Stage	System pressure, psia	ΔP_{BR}, psi	$\Delta P_{Wick\,1}$, psi	$\Delta P_{Wick\,2}$,	Flow, lb/sec × 10^5
1	17.00	0.400	0.400	—	0
	17.97	0.285	0.285	—	0.128
	17.95	0.190	0.190	—	0.256
	17.95	0.125	0.125	—	0.360
	17.95	0.075	0.075	—	0.483
	16.80	0.025	0.025	—	0.590
2	16.80	0.425	—	0.425	0
	16.85	0.275	—	0.275	0.128
	17.00	0.175	—	0.175	0.256
	17.00	0.100	—	0.100	0.360
	17.00	0.025	—	0.025	0.466
1, 2	17.00	0.725	0.300	0.425	0
	17.00	0.475	0.225	0.250	0.131
	17.00	0.300	0.150	0.150	0.256
	17.02	0.200	0.100	0.100	0.360
	17.05	0.100	0.050	0.050	0.483

for a given flow, by a reduction of the viscous drag of the liquid flowing through the capillaries.

The last test made consisted of the substitution of a spherical gas bearing for the throttle valve. The radius of the bearing was approximately 0.75 inch and its weight was 2.68 grams. The ball was floated when operated on either or both stages. Similar tests with heavier balls will be reported later.

Proposed experiments for the future include tests with improved wick designs, experiments on a single capillary for the purpose of testing the validity of the theory presented above, and the introduction of a noncondensable gas between the wick stages.

B. Diameters of Mars and Venus

R. L. Wildey

It is desirable to know the diameters of the nearest planets in order that navigation angular measurements may be taken from them during approach by a space vehicle. Accordingly, the accuracy of the best available data for the diameters of Mars and Venus has been critically studied and is summarized here.

It should be pointed out that the term "diameter" means some stable reference isophote. Whether this is identifiable with the planet's lithosphere or is some point in the atmosphere at the limb of the planet where the light intensity has fallen off a prescribed amount is not specified. Such a definition of diameter does not necessarily introduce an error, if the navigation measurements also use a similar definition. However, the Martian phenomenon known as "blue clearing" might cause error if the diameter were being measured in blue light. The diameter, due to the thickness of the atmosphere, might possibly vary by 1% if measured during blue clearing. It has been suggested that blue clearing occurs when Mars is in opposition, but one cannot say with confidence that it occurs only at opposition because of the strong selection effect of the increased observation at this time.

Several measurements of the diameters of Mars and Venus, made before 1930 (approx), were obtained by means of a double-image device called the heliometer, which did not differ much from the modern device called the double-image micrometer. Its performance was much poorer, however. Other measurements were made using the filar eyepiece micrometer, a familiar instrument today.

In the 1920's, attempts were made to determine the diameters of planetary images on photographic plates with an ordinary precision-screw measuring engine. The average of 12 early determinations of Mars' diameter is 6788 km, but individual results varied from 6650 km to 6850 km. For Venus, the corresponding values are 12,620 km, ranging from 12,350 to 12,840 km.

It was customary to correct for systematic error by assuming that it was a constant angular amount over the entire period of observation. The true diameter under this assumption can be obtained by making measurements over a range of distances. The value of constant error thus removed was equivalent to 65 km, for the best work, to over 700 km. This method is not applicable to more modern measurements, where systematic error was estimated differently.

Three unpredictable causes of systematic error can be identified. The first, radiation, is the spread of energy from the geometrical confines of a bright image into the dark portions. It is caused by scattering of light in the retina of the eye or in the emulsion of the photographic plate as well as by some small angle scattering by the atmosphere. In all cases where the settings are made visually, error is possible because a subjective decision of where the edge of the image is must be made. This error source could be expected to vary with the observer and with the method, but it could be fairly constant for a particular series of readings.

The seeing condition, the effect of atmospheric inhomogeneity, is another difficulty always present in observations made from the Earth's surface. At Mt. Wilson and Palomar Observatories, the seeing tremor disk does not become 1 arcsec diameter or smaller more than 2 or 3% of the time. On the other hand, there are many places where the seeing gets better than this. Camichel reports that he was able to restrict his diameter measurement observations to nights when the seeing disk was less than 0".1 across at the Pic du Midi Observatory. However, a seeing disk large enough to produce a significant systematic error, and yet go undetected to the eye, could still exist.

Of all the methods which have been employed to date for the measurement of the diameters of Mars and Venus, modern double-image micrometry appears superior. The function of the double-image micrometer is well explained by Dyson (Ref 8). This instrument provides for very precise visual observation of the tangency of two images, and inherently allows for the intensity gradient

always present at the limit of the lighted area. It tends to indicate the dimension of an image to the 50% illumination level.

The double-image micrometric results obtained by Muller (Refs 9, 10) appear to be the first of significance to be reported. The instrument itself has undergone some revision by Dollfus (Ref 11) since the first one was constructed by Muller.

In the case of Venus, the double-image micrometry of Muller (Ref 12) during the superior conjunction of 1939 is available. Kuiper also gives a result, without discussion. For Mars, both Muller (Ref 10) and Dollfus (Ref 11) have determined the diameter by means of double-image micrometry.

One thing is common to all sources of systematic error mentioned. All tend to suggest that the lighted portions of images extend beyond their true boundaries in the object plane. Measurements of Mercury in transit by Dollfus, and against a dark sky by Muller (Ref 13) thus offer a way of estimating systematic error.

We find that the dark disk is 0″.03 larger than the light disk. The probable error for these determinations is about ±0″.035 apiece. If we add these probable errors in such a way as to maximize the systematic error, the dark disk becomes 0″.04 smaller than the bright disk. This figure represents the sum of two systematic errors, one for each determination. That occurring in an ordinary measurement is therefore estimated to be smaller than 0″.02. In terms of linear diameters, the unaccounted for systematic error is probably less than 15 km.

These results are given below, together with some others found in recent references, for comparison:

	Mars	Venus
Muller	6737 polar, 0.013 oblateness	12069
Dollfus	6708 polar	–
Kuiper (Ref 14)	–	12246
De Vaucouleurs (Ref 15)	6800 equatorial	12400
Rabe	–	12620

To obtain a best estimate, the Muller and Dollfus values are averaged for Mars and the Muller and Kuiper values for Venus:

Mars: polar diameter, yellow light	6722 ±22 km
oblateness	0.013 ±0.006
Venus: diameter, visual light	12157 ±43 km
oblateness	not detectable

The errors given are statistical probable errors. The Venus error is given by Muller. Mars diameter is given as 108 km larger in blue light by Dollfus (Ref 11).

These values are subject to revision as a thorough study of the question by De Vaucouleurs will soon be available (Ref 16). In particular, Muller's value for Venus may be found small.

TELECOMMUNICATIONS DIVISION

IV. Communications Systems Research

A. Information Processing Research

E. C. Posner, L. D. Baumert, R. C. Titsworth, and M. Hall

1. Search Procedures Minimizing Expected Search Time

A study has been made of search procedures for finding a satellite in a noisy sky. The part of the sky in which the satellite is known to be is assumed composed of A disjoint cells (A = about 50 in practice), each cell the size of the area of sky that the narrowest antenna beam can search. A probability space of A points will be considered, each of probability $1/A$, together with independent noise emanating from each cell. In this summary, only single-sideband transmission and white gaussian noise will be discussed; however, the results are true for wider classes. If the satellite is present in a given cell, the mean output of the search equipment is μ (a positive number); whereas, if the satellite is absent, the output is zero. The variance of the output of a single cell for observation time t is $\sigma^2/(t/t_0)$, where t_0 is a dimensioning parameter. For regions composed of cells, it is known by the independence assumption that the variance is $B\sigma^2/(t/t_0)$.

Search procedures of the following type will be considered: The probability space is cut into n equal regions, each with A/n cells, and each is searched for time t; then the regions are ranked in order of decreasing output, and each cell is sampled within the regions of size A/n, the regions of higher output being sampled first. We assume that each cell must be examined for a fixed time t_1 to finally decide whether the satellite is present in it or not. We consider the cases of sequentially sampling the n regions and simultaneously sampling them by means of n auxiliary wide-beam antennas whose characteristics are the same as the characteristics of the single large antenna with its beam widened. When $n = 1$, t should be chosen 0 in either method, and the expected time of finding the satellite is $[(A + 1)/2]t_1$. Thus, n will henceforth be assumed greater than 1 and less than or equal to A.

We observe that it would be best, if not for difficulties in moving the narrow-beam antenna, to take $n = A$ for every t. For, if we take a smaller n, we can search the regions of size A/n the time t by searching each of the A/n cells in it a time $t/(A/n)$ and then searching each of the A/n cells the time t_1 in order of decreasing output. The total time spent in the preliminary search is the same, but in the latter case we get the benefit of the extra ranking within regions. Thus, it must be still better to search all the A cells the time $t/(A/n)$ and then rank

them all. (In fact, this shows that searching all A cells first is better than any multistage process.)

We show that a saving is possible for every n with the first method (a fortiori with the second), and we compute t and the fractional saving in expected search time. The computation hinges on finding the expected number of incorrect cells examined for the time t_1 before the correct one is found. We have n independent normal variates of variance $[\sigma^2/(t/t_0)]\cdot(A/n)$, all of zero-mean except for the one of mean μ. The probability that one of the incorrect variates exceeds the one of mean μ is the probability that a normal variate of mean $-\mu$ and variance $[\sigma^2/(t/t_0)]\cdot(A/n)$ exceeds zero, for this is the density of the difference between an incorrect variate and the correct one. This density is equal to

$$pr\left[z > \mu/\sigma\left(\frac{2At_0}{nt}\right)^{1/2}\right]$$

where z has the unit normal distribution. We have $n-1$ trials; they are not independent, but we can still conclude that the expected number of incorrect cells looked at for time t_1 before the correct one is found is

$$(n-1)\,pr\left[z > \mu/\sigma\left(\frac{2At_0}{nt}\right)^{1/2}\right]$$

Thus, the expected search time in the sequential search case is

$$U_1(t) = nt + \frac{A}{n}(n-1)\,t_1 pr\left[z > \frac{\mu}{\sigma}\left(\frac{nt}{2At_0}\right)^{1/2}\right] + \frac{\frac{A}{n}+1}{2}t_1$$

and in the simultaneous search case is

$$U_2(t) = t + \frac{A}{n}(n-1)\,t_1 pr\left[z > \frac{\mu}{\sigma}\left(\frac{nt}{2At_0}\right)^{1/2}\right] + \frac{\frac{A}{n}+1}{2}t_1$$

where

$$\frac{\frac{A}{n}+1}{2}t_1$$

is the expected search time of the region of

$$A/n$$

cells containing the correct cell.

To prove that a saving is possible for every n, note that

$$U_1(0) = \frac{A+1}{2}t_1$$

and also that by computation $U_1'(t)$ is an increasing function of t in $t \geqq 0$. Thus, $U_1(t)$ is convex upward and hence has a unique critical point which must be a minimum. Since

$$U_1(0) = \frac{A+1}{2}t_1$$

the minimum, $U_{min}(t;n)$, is actually less than $[(A+1)/2]t_1$, so that a saving is possible.

The best time t to choose in the two cases can be described as follows. Define $x_1(n)$ by

$$\frac{1}{x_1(n)}\frac{1}{(2\pi)^{1/2}}e^{-[x_1(n)]^2/2} = \frac{\frac{4n}{n-1}}{\frac{t_1}{t_0}\left(\frac{\mu}{\sigma}\right)^2}$$

and $x_2(n)$ by

$$\frac{1}{x_2(n)}\frac{1}{(2\pi)^{1/2}}e^{-[x_2(n)]^2/2} = \frac{\frac{4}{n-1}}{\frac{t_1}{t_0}\left(\frac{\mu}{\sigma}\right)^2}$$

In the first case, choose

$$t = \frac{2At_0\,[x_1(n)]^2}{n\left(\frac{\mu}{\sigma}\right)^2}$$

and, in the second case,

$$t = \frac{2At_0\,[x_2(n)]^2}{n\left(\frac{\mu}{\sigma}\right)^2}$$

The accompanying graph (Fig 10) plots the fractional saving versus the number of regions n for the first method over the method of searching each cell until the satellite is found, with $A = 64$, $t_1/t_0 = 20/(\mu/\sigma)^2$. It is independent of the signal-to-noise ratio μ/σ and of t_0, and almost independent of A. With $A = 64$, $n = 8$, the saving is 0.40 by the first method, 0.75 by the second. In the first case, $(t/t_0)(\mu/\sigma)^2 = 14.6$; in the second case, $(t/t_0)(\mu/\sigma)^2 = 54.8$.

2. Sum-Free Sets

a. Introduction. A set S of integers is called sum-free if x,y in S imply $x+y$ not in S. Define $f(n)$ to be the largest integer q such that $1, 2, \cdots, q$ can be divided into sum-free sets $S_1, \cdots, S_n$. It is known that $f(1) = 1$, $f(2) = 4$, $f(3) = 13$, $f(4) \geqq 44$, $f(n) \leqq [n!\,e]$, $f(n+1) \geqq 3f(n) + 1$. We describe an exhaustive search process which was used to determine that $f(4) = 44$. Further we list several solutions for $f(4)$.

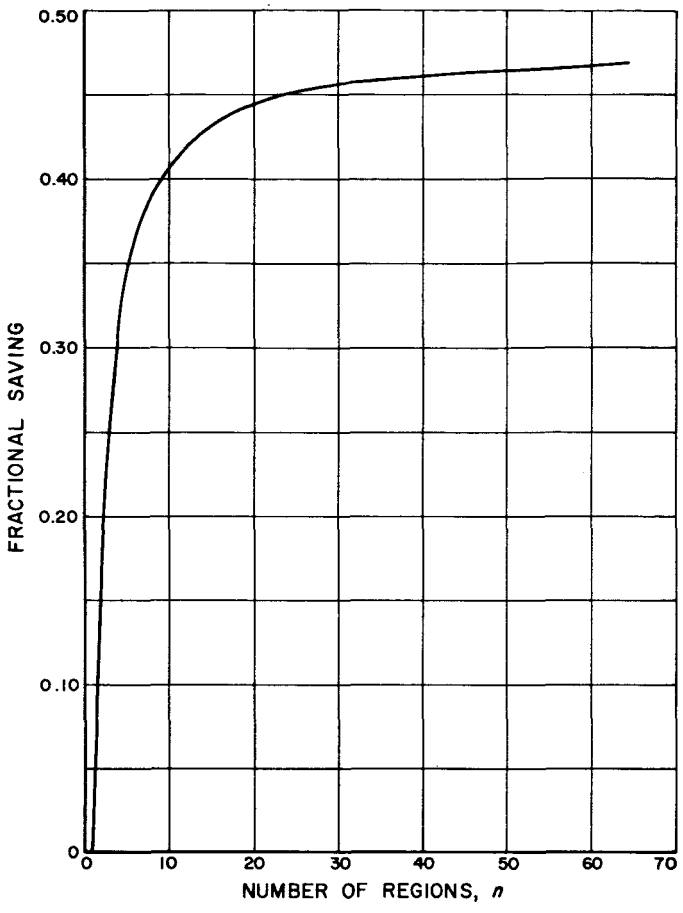

Figure 10. $\{[A+1)/2]t_1 - U_{min}(t;n)\}/[(A+1)/2]$ vs n

b. Algorithm. Relabel S_1, S_2, S_3, S_4 as A, B, C, D, respectively. Now $f(4) \geq 44$, thus let us consider distributing $1, \cdots, 45$. Suppose $1, \cdots, j-1$ have already been distributed, we then check sets A, B, C, D, in that order, to find the first one that can accept j. (At least one set can accept j, as is clear from the complete process.) Assume set B is the first such set and already contains $b_1, b_2, \cdots b_s$, then j in B precludes the admission of $b_i + j$ into $B (1 \leq i \leq s)$. Those $b_i + j \leq 45$ and not previously precluded are tagged with j. If no $b_i + j \leq 45$ is thus precluded from all 4 sets, we try placing $j+1$ as before. If some $b_i + j \leq 45$ is thus precluded from all sets we cannot get a solution for 45 with $1, \cdots, j$ so distributed. Thus we attempt to put j into C, D in that order. Failing this we try to shift $j-1$ into a lexicographically higher set than it now occupies.

If $j-1$ cannot fit, we try shifting $j-2$, etc.

If we insist that 1 belongs to set A, 2 to set B, and that $c_1 < d_1$, we have a starting point and isomorph rejection. In accordance with this then, the process terminates when 3 is moved from set C to D.

c. Solutions. If $n = 1, 2, 3$, then solutions are

$n=1$	$n=2$		$n=3$		
A	A	B	A	B	C
1	1	2	1	2	5
	4	3	4	3	6
			10	11	7
			13	12	8
					9

Of the 112 solutions which were computed, the first 18 solutions for $f(4) = 44$ are listed in Table 2. No attempt was made to find *all* solutions. Note that for $n = 1, 2, 3$, the contents of the sets in the solutions are symmetric about $\frac{1}{2}[f(n) + 1]$. If this were true for $f(4) = 44$, then 15, 30 would have to belong to the same set which contradicts the sum-free property. However, there are solutions for which this symmetry is preserved for all numbers except 15, 30 (Sol 4 in Table 2, for example).

3. Equivalence of Cyclic Sequences Under Transformers of the Affine Group

a. Introduction. Cyclic sequences which differ only in time-origin have the same autocorrelation function; some sequences, notably those with two-level autocorrelations, are insensitive to certain permutations of the sequence terms. It can be shown that if $\{\alpha_n\}$ is a cyclic sequence of length L, where L is some multiple of the actual period of $\{\alpha_n\}$, then the autocorrelation function $R^{(k)}(m)$ of $\{\alpha_{nk+t}\}$, for any integral t and k, $(k, L) = 1$, is related to the correlation $R(m)$ of $\{\alpha_n\}$ by

$$R^{(k)}(m) = R^{(1)}(km) = R(km)$$

That is, transformations of sequences in this way do not change the *values* which the correlation function assumes, but only the order in which these values appear. It is of interest then to determine the number of sequences which are *distinct* under such transformations. The set of all such permutations forms a group of operators on the domain of cyclic sequence, called an Affine Group. By applying Polya's formula, the number of equivalence classes of sequences under this group can thus be obtained.

b. Equivalence under an affine group. Let $\{\alpha_n\}$ be a cyclic sequence of length L (where L is some multiple of the actual period), each of whose elements α_n may assume one of b values. There are b^L such sequences. Define the operator g_k^t on $\{\alpha_n\}$ by

$$g_k^t \{\alpha_n\} = \{\alpha_{kn+t}\}$$

Obviously, k, t and $kn + t$ may be treated as integers modulo L because the sequences involved are cyclic.

Table 2. Solutions for $f(4) = 44$

Sol 1				Sol 2				Sol 3				Sol 4				Sol 5				Sol 6			
A	B	C	D	A	B	C	D	A	B	C	D	A	B	C	D	A	B	C	D	A	B	C	D
1	2	4	9	1	2	4	9	1	2	4	9	1	2	4	9	1	2	4	9	1	2	4	9
3	7	6	10	3	7	6	10	3	7	6	10	3	7	6	10	3	7	6	10	3	7	6	10
5	8	13	11	5	8	13	11	5	8	13	11	5	8	13	11	5	8	13	11	5	8	13	11
15	18	20	12	15	18	20	12	15	18	20	12	15	18	20	12	15	18	20	12	15	18	20	12
17	21	22	14	17	21	22	14	17	21	22	14	17	21	22	14	17	21	22	14	17	21	22	14
19	24	23	16	19	24	23	16	19	24	23	16	19	24	23	16	19	24	23	16	19	24	23	16
26	27	25	29	26	27	25	29	26	27	25	29	26	27	25	29	26	27	25	29	26	27	25	29
28	33	30	31	28	33	30	31	28	33	30	31	28	37	30	31	28	38	30	31	28	38	30	31
40	37	32	34	40	38	32	34	40	38	32	34	40	38	32	33	40	43	32	33	40	43	32	33
42	38	39	35	42	43	39	35	42	43	39	35	42	43	39	34	42	—	39	34	42	44	39	34
44	43	41	36	44	—	41	36	—	44	41	36	44	—	41	35	44	—	41	35	—	—	41	35
							37				37				36				36				36
																			37				37

Sol 7				Sol 8				Sol 9				Sol 10				Sol 11				Sol 12			
A	B	C	D	A	B	C	D	A	B	C	D	A	B	C	D	A	B	C	D	A	B	C	D
1	2	4	9	1	2	4	9	1	2	4	9	1	2	4	9	1	2	4	9	1	2	4	9
3	7	6	10	3	7	6	10	3	7	6	10	3	7	6	10	3	7	6	10	3	7	6	10
5	8	13	11	5	8	13	11	5	8	13	11	5	8	13	11	5	8	13	11	5	8	13	11
17	18	15	12	17	18	15	12	17	18	15	12	17	18	15	12	17	18	15	12	17	18	15	12
19	21	20	14	19	21	20	14	19	21	20	14	19	21	20	14	19	21	20	14	19	21	20	14
26	24	22	16	26	24	22	16	26	24	22	16	26	24	22	16	26	24	22	16	26	24	22	16
28	27	23	29	28	27	23	29	28	27	23	29	28	27	23	29	28	27	23	29	28	27	23	29
30	33	25	31	30	33	25	31	30	33	25	31	30	33	25	31	30	33	25	31	30	33	25	31
32	37	34	35	32	38	34	35	32	38	34	35	32	37	39	34	32	38	39	34	32	38	39	34
40	38	39	36	40	43	39	36	40	43	39	36	40	38	41	35	40	43	41	35	40	43	41	35
42	43	41	—	42	—	41	37	42	44	41	37	42	43	—	36	42	—	—	36	42	44	—	36
44				44								44				44			37				37

Sol 13				Sol 14				Sol 15				Sol 16				Sol 17				Sol 18			
A	B	C	D	A	B	C	D	A	B	C	D	A	B	C	D	A	B	C	D	A	B	C	D
1	2	4	9	1	2	4	9	1	2	4	9	1	2	4	9	1	2	4	9	1	2	4	9
3	7	6	10	3	7	6	10	3	7	6	10	3	7	6	10	3	7	6	10	3	7	6	10
5	8	13	11	5	8	13	11	5	8	13	11	5	8	13	11	5	8	13	11	5	8	13	11
17	18	15	12	17	18	15	12	17	18	15	12	17	18	15	12	17	18	15	12	17	18	15	12
19	21	20	14	19	21	20	14	19	21	20	14	19	21	20	14	19	21	20	14	19	21	20	14
26	24	22	16	26	24	22	16	26	24	22	16	26	24	22	16	26	24	22	16	26	24	22	16
28	27	23	29	28	27	23	29	28	27	23	29	28	27	23	29	28	27	23	29	28	27	23	29
30	37	25	31	30	38	25	31	30	38	25	31	30	37	25	31	30	38	25	31	30	38	25	31
32	38	34	33	32	43	34	33	32	43	34	33	32	38	39	33	32	43	39	33	32	43	39	33
40	43	39	35	40	—	39	35	40	44	39	35	40	43	41	34	40	—	41	34	40	44	41	34
42	—	41	36	42	—	41	36	42	—	41	36	42	—	—	35	42	—	—	35	42	—	—	35
44	—	—	—	44	—	—	37	—	—	—	37	44	—	—	36	44	—	—	36	—	—	—	36
																			37				37

Define the set G by

$$G = \{g_k^t:\ (k, L) = 1; t, k \text{ modulo } L\}$$

Lemma: G is a group (called the Affine group) of order $L\phi(L)$.

Two sequences $\{\alpha_n\}$ and $\{\beta_n\}$ are *equivalent* under G if there exists a g_r^t in G such that $g_r^t\{\beta_n\} = \{\alpha_n\}$. The number of such sequences $\{\alpha_n\}$ with the property that, given g_k^t, $g_k^t\{\alpha_n\} = \{\alpha_n\}$, is denoted

$$I(g_k^t) = \text{number of sequences invariant under } g_k^t$$

Lemma:

$$g_k^t\{\alpha_n\} = \{\alpha_n\} \text{ iff } \alpha_n = \alpha_{nk+t}$$

The constraints made upon a sequence by invariance under g_k^t are that $\alpha_m = \alpha_n$ whenever n and m are in the same *cycle* of the decomposition of the integers modulo L by the permutation

$$n \rightarrow nk + t$$

The first such cycle of g_k^t is

$$[0, t, t(k+1), \cdots, t(k^{q-1} + \cdots + 1)]$$

where q is chosen so that it is the least positive integer such that $t(k^q + k^{q-1} + \cdots + 1) = 0$. If v is the least integer modulo L not in this cycle, then we form the second cycle

$$[v, vk + t, vk^2 + t(k+1), \cdots, vk^{x-1} + t(k^{x-2} + \cdots + 1)]$$

and so on, until every integer from 0 to $L-1$ is placed in a cycle. We call such a disjoint decomposition of L the *cycles* of the permutation g_k^t, or the *equivalence classes*, or *orbits* of integers under the relation g_k^t, etc, as we choose. Denote the number of such classes by $C(k, t)$.

$C(k, t)$ = number of cycles in decomposition of integers mod L by g_k^t.

For each k relatively prime to L, there is some least positive integer q such that $k^q = 1 \pmod{L}$. This integer $E_k(L)$ is the *exponent* or *index* of k modulo L.

Lemma: $q = E_k(L)$ iff q least such that

$$1 + k + \cdots + k^{q-1} = 0 \text{ modulo } \frac{L}{(L, k-1)}$$

Proof: Assume $q = E_k, (L)$, and let $d = (L, k-1)$. Then q is the least integer such that

$$k^q - 1 = (k-1)(k^{q-1} + \cdots + 1) = mL = 0 \text{ modulo } L$$

for some m. But $[L/d, (k-1)/d] = 1$; hence, if it is true that

$$\left(\frac{k-1}{d}\right)(k^{q-1} + \cdots + 1) = 0 \text{ modulo } L/d$$

then it must also be true that

$$k^{q-1} + \cdots + 1 = 0 \text{ modulo } L/d$$

This proves the first half of the lemma.

Assume now that q is the least integer such that

$$k^{q-1} + \cdots + 1 = 0 \text{ modulo } L/d$$

Since $(k-1)/d$ is relative prime to L/d, q is also the least integer such that

$$\frac{k-1}{d}(k^{q-1} + \cdots + 1) = 0 \bmod L/d = m\,L/d$$

some m. Therefore, $k^q - 1 = mL$, some m and q is the exponent of k.

We now define a concept similar to the exponent of k. Define $N(k, L)$ to be the least integer x such that

$$1 + k + \cdots + k^x = 0 \bmod L$$

a relatively simple lemma follows:

Lemma:

$$N\left[k, \frac{L}{(L, k-1)}\right] = E_k(L)$$

Proof:

$$N\left[k, \frac{L}{(L, k-1)}\right] = q$$

means that q is the least integer such that

$$1 + k + \cdots + k^{q-1} = 0 \bmod \frac{L}{(L, k-1)}$$

Hence, that q is the exponent of k.

The main result involving $N(k, L)$ is the following:

Theorem:

$$N(k, L) = \left\{ \begin{array}{ll} L & ;\ \text{if } k = 1 \\ \dfrac{Lp}{\left(L, \dfrac{k^p - 1}{k-1}\right)} & ;\ \text{if } k \neq 1 \end{array} \right\}$$

where $p = E_k(L)$.

Proof: $1 + k + \cdots + k^{N-1} = 0(L)$ implies $k^N - 1 = 0(L)$, hence that p divides N; that is, $N = rp$, for some r, where if $N = N(k, L)$, r is the least such integer. But then

$$1 + \cdots + k^{N-1} \equiv r(1 + \cdots + k^{p-1}) = nL$$

for some n. Let $v = (L, 1 + \cdots + k^{p-1})$. If $k = 1, v = L$; and if $k \neq 1$,

$$v = \left(L, \frac{k^{p-1}}{k-1}\right)$$

Then

$$r\left(\frac{1 + k + \cdots + k^{p-1}}{v}\right) = n\frac{L}{v}$$

Since L/v and $(1 + \cdots + k^{p-1})/v$ are relatively prime, r is the least integer such that

$$r = 0 \bmod \frac{L}{v}$$

Therefore

$$r = \frac{L}{v}, \text{ and } N = \frac{L}{v}p$$

Theorem: The number of elements in the cycle of g_k^t containing the element u is

$$N\left[k, \frac{t}{(L, u(k-1)+t)}\right]$$

Proof: Let the cycle containing u have x elements. Then x is the least integer such that

$$uk^x + t(k^{x-1} + \cdots + 1) = u(L)$$

That is,

$$[u(k-1) + t](k^{x-1} + \cdots + 1) = 0(L) = nL$$

for some n. Let

$$v = (L, u(k-1) + t)$$

Then x is the least integer such that

$$k^{x-1} + \cdots + 1 = 0 \text{ modulo } \frac{L}{v}$$

Therefore $x = N(k, L/v)$.

For convenience, let us denote the number of elements in the cycle of g_k^t to which u belongs by

$$H(u; k, t) = N\left[k, \frac{1}{(L, u(k-1)+t)}\right]$$

$$= \text{number of elements in the cycle of } g_k^t \text{ to which } u \text{ belongs}$$

We readily compute the number of cycles $C(k, t)$ in the decomposition of g_k^t

Corollary:

$$C(k, t) = \sum_{u=0}^{L-1} \frac{1}{H(u; k, t)}$$

Proof: Let $U = \{u_1, u_2, \cdots, u_C\}$ be a set of representatives of the cycles of g_k^t each u_i from a different cycle. Then

$$\sum_{u=0}^{L-1} \frac{1}{H(u; k, t)} = \sum_{i=1}^{C} H(u_i; k, t)\left[\frac{1}{H(u_i; k, t)}\right] = C(k, t)$$

Theorem: The number $S(L)$ of equivalence classes of sequences under G is

$$S(L) = \frac{1}{L\phi(L)} \sum_{t=0}^{L-1} \sum_{\substack{k=1 \\ (k, L)=1}}^{L-1} b^{C(k, t)}$$

where L is the cyclic length of sequences, ϕ the Euler's Totient function, and b the number of levels of sequence

$$C(k, t) = \sum_{u=0}^{L-1} H^{-1}(u; k, t), \text{ the number of cycles of } g_k^t$$

$$H(u; k, t) = N\left(k, \frac{L}{(L, u(k-1)+t)}\right)$$

$$N(k, d) = \left\{\begin{array}{ll} d & \text{if } k = 1 \\ \dfrac{pd}{\left(d, \dfrac{k^{p-1}}{k-1}\right)} & \text{if } k \neq 1 \end{array}\right\} \text{ and } p = E_k(d)$$

$E_k(d) =$ least integer such that $k^E - 1 = 0 \bmod d$.

Proof: We apply Polya's formula

$$S(L) = \frac{1}{L\phi(L)} \sum_{g_k^t \in G} I(g_k^t)$$

To compute $I(g_k^t)$: any sequence such that $\alpha_n = \alpha_m$ whenever n and m are in the same cycle of g_k^t is left invariant by g_k^t. Hence

$$I(g_k^t) = b^{C(k, t)}$$

Therefore

$$S(L) = \frac{1}{L\phi(L)} \sum_{k, t} b^{C(k, t)}$$

Corollary: If $(L, k-1)$ divides t, then

$$C(k, t) = \sum_{d/L} \frac{\phi(d)}{E_k(d)}$$

Proof: If $(L, k-1)$ divides t, there exists a u_0 such that $u_0(k-1) + t = 0$. The mapping $v \to v + u$ of the integers modulo L onto itself is 1 to 1, and

$$(v + u_0)(k-1) + t = v(k-1)$$

Then denote $d = (L, v)$, so

$$H(v + u_0; k, t) = N\left[k, \frac{L}{(L, v(k-1))}\right] = N\left[k, \frac{L/d}{(L/d, k-1)}\right]$$
$$= E_k(L/d)$$

As v ranges over all the residues modulo L, d passes through every divisor of L, as does L/d. Hence

$$C(k, L) = \sum_{d/L} \frac{M(d)}{E_k(d)} = \sum_{d/L} \frac{M(L/d)}{E_k(L/d)}$$

where $M(q)$ is the number of residue classes v modulo L such that $L/(L,v) = q$; v must be such that $(L,v) = L/q = d$. Thus $v = rd$, where $(r, L) = 1$ and $rd = rL/q < L$, or $r < q$. Hence $M(q)$ is the number of integers less than q, relatively prime to q; that is $M(q) = \phi(q)$.

This last theorem establishes the fact that, for pure decimation (i.e., sequences under g_k^0), the number of cycles is the same as the number of "generalized" cosets, or "periods" of k modulo L, as one might expect; also, that anytime $(L, k-1)$ divides t, the number of cycles of g_k^t is the same as the number of cycles of g_k^0.

Lemma: As a function of x, $x(k-1) + t$ takes on $L/(L, k-1)$ values as $x = 0, 1, \cdots, L-1$ each $(L, k-1)$ times.

Proof: $x(k-1) + t = y(k-1) + t$ means that $x = y$ mod $L/[L, (k-1)]$. Hence $1, 2, \cdots, L/[L, (k-1)]$ are the distinct values, each assumed $[L, (k-1)]$ times.

By this lemma, the task of computing $C(k, t)$ is somewhat lessened:

$$C(k, t) = (L, k-1) \sum_{u=1}^{\frac{1}{(k-1, L)}} H^{-1}(u; kt)$$

In the special case that L is prime, $k-1$ is relatively prime to L for all k, $(k, L) = 1$, except $k = 1$. For $k = 1$,

$$N\left[1, \frac{L}{(L, t)}\right] = H(u; 1, t) = \frac{L}{(L, t)}$$

$$S(L) = \frac{1}{L(L-1)}\left\{b^L + b(L-1) + L \sum_{\substack{k=2 \\ (k, L)=1}}^{L-1} b^{\sum_{d/L} \frac{\phi(d)}{E_k(d)}}\right\}$$

The values of $S(L)$ for the first few values of L are given in Table 3.

Although the above formula presents an explicit way of expressing $S(L)$ in terms of elementary functions, it involves upward of $L^2\phi(L)$ calculations which, if done without an electronic computer, can become a long and tedious process. It seems that a simpler way to determine $S(L)$ is by

$$S(L) = \frac{1}{L\phi(L)} \sum_{t=0}^{L-1} \sum_{\substack{k=1 \\ (k, L)=1}}^{L-1} b^{C(k, t)}$$

where $C(k, t)$ is computed by looking directly at the decompositions of L by the permutation $n \to nk + t$, for each desired k, t.

Table 3. Number of inequivalent sequences of length L, $S(L)$, and of period L, $T(L)$

L	S(L)	T(L)
1	2	2
2	3	1
3	4	2
4	6	3
5	6	4
6	13	8
7	10	8
8	24	18
9	22	18
10	45	38
11	30	28
12	158	142
13	74	72
14	245	234
15	368	361
16	693	669
17	522	520
18	2,637	2,576
19	1,610	1,608
20	7,341	7,293
30	4,499,852	4,499,436
31	2,311,468	2,311,466

The number $T(L)$ of sequences with period exactly $T(L)$ can be found recursively by

$$T(L) = S(L) - S(1) \qquad \text{for prime } L$$
$$T(L) = 2S(L) - \sum_{d/L} T(d) \qquad \text{for all } L$$

where the sum is extended over all divisors d of L. This number is also given in Table 3, and plotted in the graph of Figure 11.

4. Hadamard Matrices of Order 16

It has been shown in Reference 17 that a normalized Hadamard matrix equivalent to a group matrix is itself a group matrix. This was used to prove that a second Hadamard matrix of order 16 is indeed inequivalent to

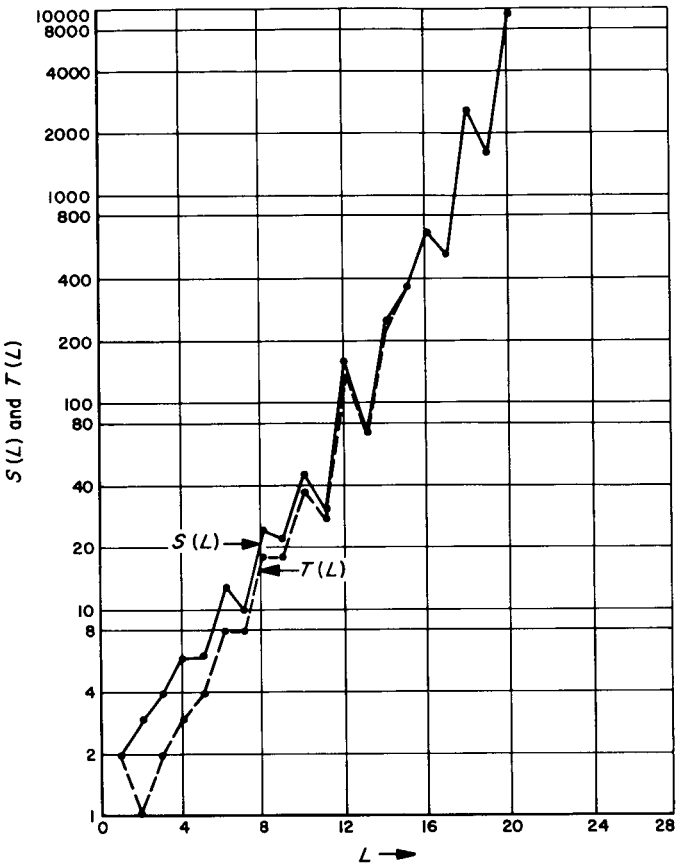

Figure 11. S(L) and T(L) versus L

the group of order 16. This report gives a list of the inequivalent Hadamard matrices of order 16. There are five different equivalence classes. Representatives are listed in Table 4 and may be described as follows:

I. The group

II. ¾ group, in which 12 rows and 12 columns agree with the group

III. ½ group, in which 8 rows and 8 columns agree with the group

IV. ⅜ group, in which 8 rows and 4 columns agree with the group

V. A second ⅜ group in which 4 rows and 8 columns agree with the group

Of these, Classes I, II, and III are equivalent to themselves under transposition of rows and columns. But transposition of rows and columns interchanges Classes IV and V.

Two Hadamard matrices are equivalent if one can be obtained from the other by permuting rows and columns and by complementing rows and columns. In the case of the matrices of orders 2, 4, 8, and 12 there is only a single class. For order 16 as we have said there are five classes, but it is worth noting that for this order equivalent matrices are equivalent under permutation of rows and columns alone, and that the complementation does not broaden the equivalence classes. This is not, in general, true for Hadamard matrices of higher order than 16, and in particular for order 20.

a. Construction of the matrices. With the matrix normalized to make the first row and column consist entirely of +1's, the positions of the +1's in the remaining 15 rows yields a 15, 7, 3 symmetric block design. If we number the columns $\infty, 0, 1, \cdots, 15$, we may use the column numbers $0, \cdots, 15$ to represent the objects of the block designs.

Two sets of the block design have three elements in common, say 0, 1, 2. Then as each pair i, j occurs together three times in the entire design, each of the pairs 0, 1; 0, 2; 1, 2 will occur together exactly once more. They may all occur together as a triple, or may occur separately. Thus, we have either the arrangement A or B below:

A	B
0, 1, 2, · · ·	0, 1, 2 · · ·
0, 1, 2, · · ·	0, 1, 2 · · ·
0, 1, 2, · · ·	0, 1 · · ·
	0, 2 · · ·
	1, 2 · · ·

The arrangement A we will refer to as a triple. This can be considered a quarter of a group since the first four lines of the group Hadamard matrix are of this type.

In our construction we can avoid duplication in two ways: First, we can list alternate arrangements in order of preference; and, second, by means of automorphisms of partial systems we can select only one of a set of equivalent designs. We shall prefer A to B above and so will retain only those completions of B which have no triples. As it turns out, no such completions of B exist, and all Hadamard matrices of order 16 contain triples.

The A type has as its first three blocks (0, 1, 2, 3, 4, 5, 6); (0, 1, 2, 7, 8, 9, 10); (0, 1, 2, 11, 12, 13, 14). If there is a further triple including 0, then by appropriate renumbering this may be taken as 0, 3, 4 with blocks (0, 3, 4, 7, 8, 11, 12); (0, 3, 4, 9, 10, 13, 14). There are two more blocks with 0, and we easily see that there are only two ways of adding them, apart from renumbering. This gives us the first two major subdivisions of A. $A1$ is (0, 5, 6, 7, 8, 13, 14); (0, 5, 6, 9, 10, 11, 12) and $A2$ is (0, 5, 6, 7, 9, 11, 13); (0, 5, 6, 8, 10,

Table 4. Representative Hadamard Matrices of Order 16

I. The Group

```
1 1 1 1  1 1 1 1  1 1 1 1  1 1 1 1
1 1 1 1  1 1 1 1  - - - -  - - - -
1 1 1 1  - - - -  1 1 1 1  - - - -
1 1 1 1  - - - -  - - - -  1 1 1 1
1 1 - -  1 1 - -  1 1 - -  1 1 - -
1 1 - -  1 1 - -  - - 1 1  - - 1 1
1 1 - -  - - 1 1  1 1 - -  - - 1 1
1 1 - -  - - 1 1  - - 1 1  1 1 - -
1 - 1 -  1 - 1 -  1 - 1 -  1 - 1 -
1 - 1 -  1 - 1 -  - 1 - 1  - 1 - 1
1 - 1 -  - 1 - 1  1 - 1 -  - 1 - 1
1 - 1 -  - 1 - 1  - 1 - 1  1 - 1 -
1 - - 1  1 - - 1  1 - - 1  1 - - 1
1 - - 1  1 - - 1  - 1 1 -  - 1 1 -
1 - - 1  - 1 1 -  1 - - 1  - 1 1 -
1 - - 1  - 1 1 -  - 1 1 -  1 - - 1
```

Triples

0, 1, 2	1, 3, 5	2, 3, 6	3, 7, 11	4, 7, 12
0, 3, 4	1, 4, 6	2, 4, 5	3, 8, 12	4, 8, 11
0, 5, 6	1, 7, 9	2, 7, 10	3, 9, 13	4, 9, 14
0, 7, 8	1, 8, 10	2, 8, 9	3, 10, 14	4, 10, 13
0, 9, 10	1, 11, 13	2, 11, 14		
0, 11, 12	1, 12, 14	2, 12, 13		
0, 13, 14				
5, 7, 13	6, 7, 14			
5, 8, 14	6, 8, 13			
5, 9, 11	6, 9, 12			
5, 10, 12	6, 10, 11			

II. ¾ Group

```
1 1 1 1  1 1 1 1  1 1 1 1  1 1 1 1
1 1 1 1  1 1 1 1  - - - -  - - - -
1 1 1 1  - - - -  1 1 1 1  - - - -
1 1 1 1  - - - -  - - - -  1 1 1 1
1 1 - -  1 1 - -  1 1 - -  1 1 - -
1 1 - -  1 1 - -  - - 1 1  - - 1 1
1 1 - -  - - 1 1  1 1 - -  - - 1 1
1 1 - -  - - 1 1  - - 1 1  1 1 - -
1 - 1 -  1 - 1 -  1 - 1 -  1 - 1 -
1 - 1 -  1 - 1 -  - 1 - 1  - 1 - 1
1 - 1 -  - 1 - 1  1 - 1 -  - 1 - 1
1 - 1 -  - 1 - 1  - 1 - 1  1 - 1 -
1 - - 1  1 - - 1  1 - - 1  1 - - 1
1 - - 1  1 - - 1  - 1 1 -  - 1 1 -
1 - - 1  - 1 1 -  1 - - 1  - 1 1 -
1 - - 1  - 1 1 -  - 1 1 -  1 - - 1
```

Triples

0, 1, 2	1, 3, 5	2, 3, 6	
0, 3, 4	1, 4, 6	2, 4, 5	
0, 5, 6	1, 7, 9	2, 7, 10	
0, 7, 8	1, 8, 10	2, 8, 9	
0, 9, 10	1, 11, 13	2, 11, 14	
0, 11, 12	1, 12, 14	2, 12, 13	
0, 13, 14			

Automorphisms

(0, 1, 2)(3, 7, 11, 5, 10, 12)(4, 9, 14, 6, 8, 13)
(0)(1, 2)(3, 9, 11)(4, 10, 12)(5, 8, 13, 6, 7, 14)
(3, 5)(7, 10)(11, 12)(4, 6)(8, 9)(13, 14)
(3, 11, 9)(4, 12, 10)(5, 13, 7)(6, 14, 8)
(7, 8)(9, 10)(11, 12)(13, 14)
(7, 9)(8, 10)(11, 13)(12, 14)
(7, 11)(8, 12)(9, 13)(10, 14)

$$\begin{pmatrix} \infty, & 0, & 1, & 2, & 3, & 4, & 5, & 6, & 7, & 8, & 9, & 10, & 11, & 12, & 13, & 14 \\ 4, & 3, & 6, & 5, & \infty, & 0, & 1, & 2, & 7, & 8, & 9, & 10, & 12, & 11, & 14, & 13 \end{pmatrix}$$ **Columns**

$$\begin{pmatrix} \infty, & 0, & -1, & -2, & 3, & 4, & -5, & -6, & 7, & 8, & -9, & -10, & 11, & 12, & -13, & -14 \\ \infty, & 0, & 2, & 1, & 3, & 4, & 6, & 5, & 9, & 10, & 8, & 7, & 13, & 14, & 12, & 11 \end{pmatrix}$$ **Rows with complementation**

III. ½ Group

```
1 1 1 1  1 1 1 1  1 1 1 1  1 1 1 1
1 1 1 1  1 1 1 1  - - - -  - - - -
1 1 1 1  - - - -  1 1 1 1  - - - -
1 1 1 1  - - - -  - - - -  1 1 1 1
1 1 - -  1 1 - -  1 1 - -  1 1 - -
1 1 - -  1 1 - -  - - 1 1  - - 1 1
1 1 - -  - - 1 1  1 1 - -  - - 1 1
1 1 - -  - - 1 1  - - 1 1  1 1 - -
1 - 1 -  1 - 1 -  1 - 1 -  1 - 1 -
1 - 1 -  1 - 1 -  - 1 - 1  - 1 - 1
1 - 1 -  - 1 - 1  1 - - 1  - 1 1 -
1 - 1 -  - 1 - 1  - 1 1 -  1 - - 1
1 - - 1  1 - - 1  1 - - 1  1 - - 1
1 - - 1  1 - - 1  - 1 1 -  - 1 1 -
1 - - 1  - 1 1 -  1 - - 1  - 1 1 -
1 - - 1  - 1 1 -  - 1 1 -  1 - - 1
```

Triples

0, 1, 2	1, 3, 5	2, 3, 6	
0, 3, 4	1, 4, 6	2, 4, 5	
0, 5, 6			
0, 7, 8			
0, 9, 10			
0, 11, 12			
0, 13, 14			

Automorphisms

(0)(1, 3, 5)(2, 4, 6)(7)(8)(9, 11, 13)(10, 12, 14)
(3, 4)(5, 6)(9, 10)(13, 14)
(7, 8)(9, 10)(11, 12)(13, 14)
(7, 9)(8, 10)(11, 13)(12, 14)
(7, 11)(8, 12)(9, 13)(10, 14)

$$\begin{pmatrix} \infty, & 0, & 1, & 2, & 3, & 4, & 5, & 6, & 7, & 8, & 9, & 10, & 11, & 12, & 13, & 14 \\ 7, & 8, & 9, & 10, & 13, & 14, & 11, & 12, & \infty, & 0, & 1, & 2, & 5, & 6, & 3, & 4 \end{pmatrix}$$ **Column permutation**

$$\begin{pmatrix} \infty, & -0, & 1, & -2, & 3, & -4, & 5, & -6, & 7, & -8, & 9, & -10, & 11, & -12, & 13, & -14 \\ \infty, & 0, & 1, & 2, & 5, & 6, & 3, & 4, & 7, & 8, & 13, & 14, & 11, & 12, & 9, & 10 \end{pmatrix}$$ **Row complementation and permutation**

Table 4. (Cont'd)

IV. 3/8 Group

```
1 1 1 1  1 1 1 1  1 1 1 1  1 1 1 1
1 1 1 1  1 1 1 1  - - - -  - - - -
1 1 1 1  - - - -  1 1 1 1  - - - -
1 1 1 1  - - - -  - - - -  1 1 1 1
-------------------------------------
1 1 - -  1 1 - -  1 1 - -  1 1 - -
1 1 - -  1 1 - -  - - 1 1  - - 1 1
1 1 - -  - - 1 1  1 1 - -  - - 1 1
1 1 - -  - - 1 1  - - 1 1  1 1 - -
-------------------------------------
1 - 1 -  1 - 1 -  1 - 1 -  1 - 1 -
1 - 1 -  1 - - 1  1 - - 1  - 1 - 1
1 - 1 -  - 1 1 -  - 1 - 1  1 - - 1
1 - 1 -  - 1 - 1  - 1 1 -  - 1 1 -
-------------------------------------
1 - - 1  1 - 1 -  - 1 - 1  - 1 1 -
1 - - 1  1 - - 1  - 1 1 -  1 - - 1
1 - - 1  - 1 1 -  1 - 1 -  - 1 - 1
1 - - 1  - 1 - 1  1 - - 1  1 - 1 -
```

Triples

0, 1, 2
0, 3, 4
0, 5, 6
0, 7, 8
0, 9, 10
0, 11, 12
0, 13, 14

Automorphisms

(0) (1, 2) (3, 4) (5, 6) (7) (8) (9, 10) (11) (12) (13) (14)
(0) (1, 3, 7) (2, 4, 8) (5, 11, 9) (6, 12, 10) (13) (14)
(0) (1) (2) (3) (4) (5, 6) (7) (8) (9, 10) (11, 12) (13, 14)
(0) (1) (2) (3, 9, 11) (4, 10, 12) (5, 7, 13) (6, 8, 14)

$$\begin{pmatrix} \infty, & 0, & 1, & 2, & 3, & 4, & 5, & 6, & 7, & 8, & 9, & 10, & 11, & 12, & 13, & 14 \\ 1, & 2, & \infty, & 0, & 5, & 6, & 3, & 4, & 11, & 12, & 13, & 14, & 7, & 8, & 9, & 10 \end{pmatrix}$$ Column permutation

$$\begin{pmatrix} \infty, & 0, & 1, & 2, & -3, & -4, & -5, & -6, & 7, & 8, & 9, & 10, & -11, & -12, & -13, & -14 \\ \infty, & 0, & 2, & 1, & 4, & 3, & 5, & 6, & 7, & 9, & 8, & 10, & 14, & 12, & 13, & 11 \end{pmatrix}$$ Row complementation and permutation

V. 3/8 Group

```
1 1 1 1  1 1 1 1  1 1 1 1  1 1 1 1
1 1 1 1  1 1 1 1  - - - -  - - - -
1 1 1 1  - - - -  1 1 1 1  - - - -
1 1 1 1  - - - -  - - - -  1 1 1 1
-------------------------------------
1 1 - -  1 1 - -  1 1 - -  1 1 - -
1 1 - -  1 1 - -  - - 1 1  - - 1 1
1 1 - -  - - 1 1  1 - 1 -  1 - 1 -
1 1 - -  - - 1 1  - 1 - 1  - 1 - 1
-------------------------------------
1 - 1 -  1 - 1 -  1 1 - -  - - 1 1
1 - 1 -  1 - 1 -  - - 1 1  1 1 - -
1 - 1 -  - 1 - 1  1 - - 1  - 1 1 -
1 - 1 -  - 1 - 1  - 1 1 -  1 - - 1
-------------------------------------
1 - - 1  1 - - 1  1 - 1 -  - 1 - 1
1 - - 1  1 - - 1  - 1 - 1  1 - 1 -
1 - - 1  - 1 1 -  1 - - 1  1 - - 1
1 - - 1  - 1 1 -  - 1 1 -  - 1 1 -
```

Triples

0, 1, 2 1, 3, 5 2, 3, 6
0, 3, 4 1, 4, 6 2, 4, 5
0, 5, 6

Automorphisms

(0, 1, 2) (3, 4, 6) (5) (7) (8, 10, 9) (11, 13, 14) (12)
(0, 1, 3) (2, 5, 4) (6) (7) (8) (9, 13, 12) (10, 14, 11)
(7, 8) (9, 10) (11, 12) (13, 14)
(7, 9) (8, 10) (11, 13) (12, 14)
(7, 11) (8, 12) (9, 13) (10, 14)

$$\begin{pmatrix} \infty, & 0, & 1, & 2, & 3, & 4, & 5, & 6, & 7, & 8, & 9, & 10, & 11, & 12, & 13, & 14 \\ 9, & 7, & 10, & 8, & 13, & 11, & 14, & 12, & \infty, & 0, & 2, & 1, & 6, & 5, & 3, & 4 \end{pmatrix}$$ Column permutation

$$\begin{pmatrix} \infty, & -0, & 1, & -2, & 3, & -4, & 5, & -6, & 7, & -8, & 9, & -10, & 11, & -12, & 13, & -14 \\ \infty, & 0, & 1, & 2, & 5, & 6, & 11, & 12, & 4, & 3, & 8, & 7, & 14, & 13, & 10, & 9 \end{pmatrix}$$ Row complementation and permutation

12, 14). We shall prefer $A1$ to $A2$. Here $A1$ is a half-group, since its 8 rows in matrix form are half the group Hadamard matrix. We note that whenever we have two triples with a letter in common they may be remembered as 0, 1, 2 and 0, 3, 4 giving us either $A1$ or $A2$, and this will be preferred to other classifications. The type $A3$ will consist of those categories in which there is not a further triple including 0. A fourth block including 0 may be taken as (0, 3, 4, 7, 8, 11, 12). If 0, 3, 4 is not a triple, the other three lines are of the form (0, 3, 5); (0, 4, 6); (0, 5, 6) or (0, 3, 6); (0, 4, 5); (0, 5, 6) and by interchanging 5 and 6 these are the same. Similarly, since there is not a triple 0, 7, 8 or 0, 11, 12, we may take the remaining three lines with 0 to include pairs

3, 5	7, 9	11, 13
4, 6	8, 10	12, 14
5, 6	9, 10	13, 14

in some combination. There are in fact exactly 8 permissible combinations, as listed in Table 5. These are, however, all equivalent. For the renumbering (3, 4) (5, 6) interchanges ① and ⑤; ② and ⑦; ③ and ⑥; and ④ and ⑧. The renumbering (7, 8) (9, 10) (11, 12) (13, 14) interchanges ① and ④; ② and ③; ⑤ and ⑧; and ⑥

and ⑦. Also the renumbering (11, 12) (13, 14) interchanges ① and ②. From this we see that all are equivalent to ① and this we take as the representative for *A*3.

We shall prefer *A*1 and *A*2 to *A*3. Proceeding under these rules and using automorphisms of partial designs whenever possible we find that

*A*1 has 4 inequivalent completions; I, II, III, IV.

*A*2 has a completion inequivalent to those of *A*1; it is V.

*A*3 has no completions inequivalent to I, II, III, IV, V.

b. Equivalence classes of the matrices. In the preceding section we constructed five representative Hadamard matrices which from the method of our construction are such that every Hadamard matrix of order 16 is equivalent to one of these under the operations of complementing rows and columns and permuting rows and columns. We shall now show that these five matrices are inequivalent.

Our method of construction was in fact such that every normalized Hadamard matrix is equivalent to one of the five under permutation of rows or columns. The positions of the 1's in a normalized matrix (excluding the top row and left column) when taken by rows give us a 15, 7, 3 block design. Permutation of the rows of the matrix permutes the blocks of the design. Permutation of the columns of the matrix is equivalent to a substitution on the elements of the design. These operations clearly take a triple into a triple, and so the number of triples is an invariant under row and column permutations of the non-normalized rows and columns of any normalized matrix. The number of triples is as follows:

I. 35

II. 19

III. 11

IV. 7

V. 7

But in IV all triples contain the number 0, while in V the 7 triples do not have any number common to all of them. Thus, the five representatives are inequivalent under row and column permutation. The operation of transposing rows and columns was not included in our definition of equivalence, but it is worth noting that matrices I and II are their own transposes, while IV and V are transposes of each other. III is not symmetric but is equivalent to its transpose if after transposition we make the following interchange of columns: (3, 5) (4, 6) (11, 13) (12, 14) and an appropriate row permutation which happens also to be (3, 5) (4, 6) (11, 13) (12, 14).

Table 5. Permissible combinations

①	0, 3, 4, 7, 8, 11, 12 0, 3, 5, 7, 9, 13, 14 0, 4, 6, 9, 10, 11, 13 0, 5, 6, 8, 10, 12, 14	⑤	0, 3, 4, 7, 8, 11, 12 0, 3, 5, 9, 10, 11, 13 0, 4, 6, 7, 9, 13, 14 0, 5, 6, 8, 10, 12, 14
②	0, 3, 4, 7, 8, 11, 12 0, 3, 5, 7, 9, 13, 14 0, 4, 6, 9, 10, 12, 14 0, 5, 6, 8, 10, 11, 13	⑥	0, 3, 4, 7, 8, 11, 12 0, 3, 5, 9, 10, 11, 13 0, 4, 6, 8, 10, 13, 14 0, 5, 6, 7, 9, 12, 14
③	0, 3, 4, 7, 8, 11, 12 0, 3, 5, 8, 10, 13, 14 0, 4, 6, 9, 10, 11, 13 0, 5, 6, 7, 9, 12, 14	⑦	0, 3, 4, 7, 8, 11, 12 0, 3, 5, 9, 10, 12, 14 0, 4, 6, 7, 9, 13, 14 0, 5, 6, 8, 10, 11, 13
④	0, 3, 4, 7, 8, 11, 12 0, 3, 5, 8, 10, 13, 14 0, 4, 6, 9, 10, 12, 14 0, 5, 6, 7, 9, 11, 13	⑧	0, 3, 4, 7, 8, 11, 12 0, 3, 5, 9, 10, 12, 14 0, 4, 6, 8, 10, 13, 14 0, 5, 6, 7, 9, 11, 13

The effect of complementation remains to be considered. Any succession of complementation and permutation of columns may be achieved by multiplication of the Hadamard matrix H on the right by a monomial permutation, the monomial factor being -1 for a complementation. A monomial permutation on the left complements and permutes rows. The full group of equivalences is given by the mappings $H \rightarrow AHB$, where A and B are arbitrary monomial permutations with monomial factors ± 1. For any H we always have $IHI = H$ and $(-I)\,H\,(-I) = H$. If H_1 and H_2 are both normalized and $H_2 = AH_1B$ we can write $A = P_1C_1$ and $B = C_2P_2$, where C_1 and C_2 are complementations and P_1 and P_2 are permutations. Then in $C_1H_1C_2 = P_1^{-1}H_2P_2^{-1}$ we will have exactly one row consisting entirely of 1's and exactly one column consisting entirely of 1's. If $C_1H_1C_2$ is normalized then we easily see that either $C_1 = C_2 = I$ or $C_1 = C_2 = -I$, and in either event $C_1H_1C_2 = H_1$.

We shall show that for each of our five representative matrices H_1, H_2, H_3, H_4, H_5, the automorphisms (A, B) with $H_i = AH_iB$ are transitive on the rows and the columns independently. This will show that the five classes are distinct. For suppose that we have $H_i = AH_jB$, $i \neq j$ with some monomial A and B. Then there is an appropriate automorph $H_j = DH_jE$ such that in $H_i = (AD)H_j(EB)$ AD fixes the first row and EB fixes the first column. But then we see that either $AD = P_1$, $EB = P_2$ or $AD = -P_1$, $EB = -P_2$, where P_1 and P_2 are permutations and $H_i = P_1H_jP_2$ with the first row and column fixed. But we have already noted from consideration of the triples that this is impossible with $i \neq j$.

We shall show that for each of H_1, H_2, H_3, H_4, H_5 the automorphisms fixing the first row are transitive on

all the columns, whence from our observation that the transposes are again the same classes, there will also be automorphisms fixing the first column and transitive on all the rows.

For H_1, the group matrix, if we multiply all rows by the kth row then the kth row becomes all 1's, the rows are merely permuted and the first column is left unchanged. This proves our assertion for the group matrix, confirming in this instance the result in *RS 36-9* (Vol I, p 28). For Case II an automorphism which moves the first column (numbered ∞) is given by the following operation on the rows

$$\begin{pmatrix} \infty,0,-1,-2,3,4,-5,-6,7, & 8,-9,-10,11,12,-13,-14 \\ \infty,0, & 2, & 1,3,4, & 6, & 5,9,10, & 8, & 7,13,14, & 12, & 11 \end{pmatrix}$$

Here the notation $\binom{-1}{2}$ means that row number 1 is complemented and moved to position number 2. The columns are merely permuted and not complemented, according to the following permutation

$$\begin{pmatrix} \infty, 0, 1, 2, & 3, 4, 5, 6, 7, 8, 9, 10, 11, 12, 13, 14 \\ 4, 3, 6, 5, & \infty, 0, 1, 2, 7, 8, 9, 10, 12, 11, 14, 13 \end{pmatrix}$$

The automorphisms listed with H_2 in the table are given entirely in terms of substitutions on the block design and so are effectively automorphisms fixing both row ∞ and column ∞ permuting the columns as the permutation describes and then followed by an appropriate, but unlisted, permutation of rows. For Case II we see that the column permutation just given together with the permutations of the automorphism give a group of automorphisms of H_2 fixing row ∞ and transitive on all the columns.

Similarly in the list, for each of the matrices H_3, H_4, H_5, of Cases III, IV, V, we give automorphisms and include one fixing the first row and moving the first column so that there is a group of automorphisms fixing the first row and transitive on all the columns. As $H_2^T = H_2$, H_3^T is equivalent to H_3 and $H_4^T = H_5$ these matrices also have a group of automorphisms fixing the first column and transitive on all the rows. As was remarked previously this shows that if there is any equivalence between the matrices H_1, H_2, H_3, H_4, H_5 then there is an equivalence fixing the normalized row and column. But such an equivalence is a row and column permutation equivalence, and consideration of the triples excludes this. Thus, we have five distinct classes of Hadamard matrices of order 16 whose representatives are given in the listing of Table 4.

The new Hadamard matrix of order 16 (*RS 36-9*) is equivalent to H_3 in our list, if its columns are renumbered by the permutation

$$\begin{pmatrix} \infty, 0, 1, 2, 3, & 4, & 5, 6, 7, 8, & 9, 10, 11, 12, 13, 14 \\ \infty, 7, 9, 2, 5, 14, 12, 4, 1, 8, 10, & 0, 13, & 3, 11, & 6 \end{pmatrix}$$

The 16-6-2 designs were enumerated in Reference 18. Such a design yields a Hadamard matrix of order 16, but not in normalized form, if we associate each of the 16 blocks with a row and place $+1$'s in the columns corresponding to the six numbers of the block and -1's in the rest. Husain (Ref 18) found three classes of designs; when put into normalized form we find that Husain's Number 1 is I in our list, Number 2 is V in our list and Number 3 is IV in our list. It is curious that III and IV in our list cannot be put into the 16-6-2 form by appropriate complementation of rows and columns.

B. Communications Research

M. F. Easterling, R. P. Loomba, R. L. Choate, and A. J. Viterbi

1. The Evolution of Ranging Codes

As the technique of ranging has developed through research, analysis, and experiment, there has been a continuous evolution of the ranging codes employed. It is the purpose of this report to summarize briefly this evolution and to present a new type of ranging code that meets the requirements of a transponder ranging system capable of operating over interplanetary distances.

The original investigation of acquirable ranging codes was concerned with demonstrating correlation properties and showing how these properties permitted the easy acquisition of the codes even in the presence of noise. At this time, the first work on acquisition procedures was done when it was realized that acquisition was easier when correlating a code with one of its components than when correlating a code with itself (*RS 36-1*, Vol I, pp 42–46). Immediately, the problem of finding a good ranging code was broadened: instead of requiring just a code with good autocorrelation properties, it was now necessary to find a code with good correlation properties between the code and various functions of its components, together with a procedure that specified the function to be used while acquiring each of the several code components.

The second stage in the evolution came when a clock was incorporated in the code so that the ranging receiver could track the code (*RS 36-2*, Vol I, pp 31–32). The original idea was to multiply the transmitted code by the clock so that the result of the correlation operation in the receiver would be a clock signal for a phase-locked loop to track instead of just a dc signal to indicate correlation. The first step in the acquisition procedure was to acquire one component by sweeping and lock the phase-locked loop when the component came into phase. The loop would then track the received clock, holding the first component in phase and providing synchronized timing for the other components so that they could be acquired by stepping rather than by sweeping. Since a high-performance system was desired, the bandwidth of the phase-locked loop was to be made very narrow, which imposed a severe limitation on the sweep rate at which the loop would lock. It was clear that, if somehow a clock signal could be sent along with the code, the phase-locked loop could be locked up independently of any component of the code.

The third stage in the evolution then was a code which had a clock component, that is a code which was correlated with a clock. Because the clock is not a pseudo-random code, it could not be treated as the other components of the code. The first embodiment of this idea was in a code designed for radar tracking Earth satellites and was based on the idea of switching back and forth between the code and the clock (*RS 36-5*, Vol I, pp 46–47). Thus, even before any of the code components were acquired, the phase-locked loop would be presented with a clock signal part of the time. Because the switching frequency was very much above the bandwidth of the phase-locked loop, the loop tracked through the intervals of no clock signal and treated the intermittent signal as though it were a continuous signal of reduced level. In setting up the acquisition procedure for this system, a conscious effort was made (1) to optimize the acquisition procedure so that the correlation was high throughout the procedure to hold the loop in lock and (2) to assure that the changes in correlation as each component was acquired were also high.

Before the satellite tracking experiments of November and December 1960 (*RS 36-8*, pp 52–57), the design of codes was done somewhat independently of the design of the ranging receiver. During the experiments, it was realized that the form of a ranging receiver placed additional restraints on the ranging code. This is largely because, to combat noise, the multiplication representing the correlation process is done while the codes are carried as modulation products on the RF carrier. As a result of the experience gained from the satellite experiments, two lines of work were pursued. One was concerned with improving the ranging receiver and has led to a balance-modulated ranging receiver (*RS 36-7*, Vol I, pp 62–65). The other has been concerned with the development of a form of ranging code that specifically meets the requirements for a transponder ranging system to operate over interplanetary distances.

A study of the overall ranging system indicated that the following requirements should be met: (1) The form of a transmitted code should not change from step to step of the acquisition procedure except where such a change is used for signaling; this speeds the acquisition process by eliminating the need to wait for the signal to propagate to the spacecraft and back between steps. (2) The transmitted code should be balanced; i.e., it should have equally many ones and zeros so that the unmodulated portion of the carrier does not have its phase shifted by the modulating code. (3) The transmitted code should have a clock component that can be acquired independently of any of the pseudo-random components of the code, and the resulting control S-curve should be clean and well-defined. (4) The form of the code should permit the selection of almost any desired number of components. (5) The form of the code should permit optimization in the sense of obtaining large changes in the correlation as each component is acquired.

A code form which meets all of the above requirements is:

$$\text{Transmitted code} = FCl + \bar{F}\,[G \oplus Cl]$$

where F is an acquirable code with one or more components, Cl is the clock, and G is an acquirable code with one or more components, all different from the components in F. An example of such a code together with its acquisition procedure is given in Table 6 where

$F = X =$ a single-component code

$G =$ a three-component code

$= AB + BC + AC$

In Table 6, a given component of the receiver code is designated by a capital letter if it is in phase with the corresponding component of the received code, and by a lower-case letter if it is not.

2. General-Purpose Sequence Generator

A sequence generator capable of generating all binary sequences of length up to 64 has been implemented. This sequence generator is capable of generating a total of $2^{65}-2$ different sequences. In order to generate any one

Table 6. Transmitted code = $X\,CI + \bar{X}[(AB + BC + AC) \oplus CI]$

Step No.	Purpose	Condition	Receiver code	Correlation
1	Acquire clock	Clock not acquired	Zero	0
		Clock acquired	Zero	50%
2	Acquire X	X not acquired	$\bar{x}$	25%
		X acquired	X	50%
3	Acquire A	A not acquired	$\bar{X}a$	50%
		A acquired	$\bar{X}A$	75%
4	Acquire B	B not acquired	$\bar{X}b$	50%
		B acquired	$\bar{X}B$	75%
5	Acquire C	C not acquired	$\bar{X}c$	50%
		C acquired	$\bar{X}C$	75%
6	Tracking code	Tracking	$\bar{X}[AB + BC + AC]$	100%

of the available sequences, a minimum of 6 and a maximum of 22 external connections are needed.

The sequence generator can be looked at as made up of two parts. The first part generates one sequence of every length up to a maximum length of 64. That is to say the first part is capable of generating 64 different sequences, each one of different length. The second part contains logic with the help of which it is possible to obtain all possible sequences of all lengths up to 64.

a. Theoretical background. The theory on which the first part of the sequence generator is based, is well known (Refs 19, 20). Such a device can be thought of as an n-stage shift register with standard feedback logic and a word detector. The number of stages required is determined from the fact that an n-stage shift register can generate a sequence of maximum length $2^n - 1$. The theory behind the second part is the main theme of this work. In order to generate all sequences of length up to 2^n it is necessary to make provisions for obtaining all the functions of n binary variables. This is exactly what the logic in the second part does. This makes it possible to obtain all possible functions of n variables in a very compact fashion. Let $f(x_1, x_2, x_3, \cdots, x_n)$ be a function of n binary variables. Then $f(x_1, x_2, x_3, \cdots, x_n)$, written as f_n for the sake of brevity, can be expressed in terms of two functions of $n-1$ variables. That is

$$f_n = \bar{x}_1 f^a_{n-1} + \bar{x}_1 f^b_{n-1}$$

where

$$f^a_{n-1} = f(1, x_2 x_3, \cdots, x_n)$$

and

$$f^b_{n-1} = f(0, x_2, x_3, \cdots, x_n)$$

Similarly f^a_{n-1} and f^b_{n-1} can each be written in terms of two functions of $n-2$ variables. This means that f_n can be expressed in terms of four functions of $n-2$ variables. That is

$$f_n = x_1 x_2 f^c_{n-2} + x_1 \bar{x}_2 f^d_{n-2} + \bar{x}_1 x_2 f^g_{n-2} + \bar{x}_1 \bar{x}_2 f^h_{n-2}$$

where

$$f^c_{n-2} = f(1, 1, x_5, \cdots, x_n)$$
$$f^d_{n-2} = f(1, 0, x_3, \cdots, x_n)$$
$$f^g_{n-2} = f(0, 1, x_3, \cdots, x_n)$$
$$f^h_{n-2} = f(0, 0, x_3, \cdots, x_n)$$

Proceeding in the same fashion, f_n can be written in terms of eight functions of $(n-3)$ variables, 16 functions of $(n-4)$ variables, and so on. In general, any function of n binary variables can be reduced to 2^k functions of $n-k$ variables. The reduction tree for $k = 3$ is shown in Figure 12.

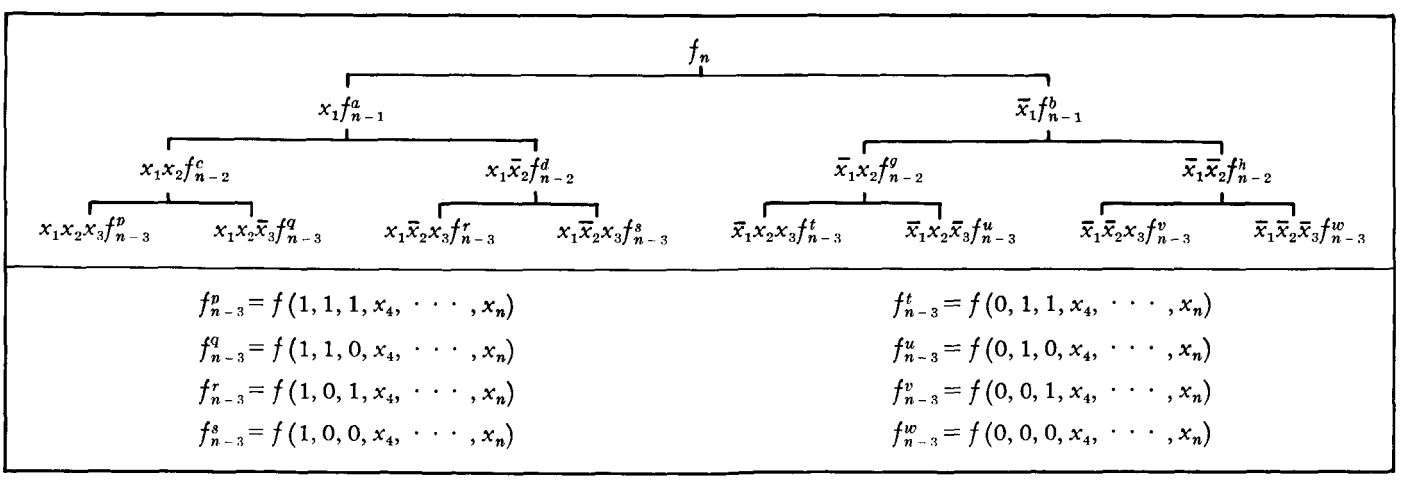

Figure 12. Reduction tree showing eight functions of $n - 3$ variables

If this reduction is carried down, the resulting tree will have 2^{n-3} functions of 3 variables, or 2^{n-2} functions of two variables, or 2^{n-1} functions of one variable. But there are only four distinct functions of one variable, 16 distinct functions of two variables, and 256 distinct functions of 3 variables. Therefore, the optimum way of implementing the logic is to carry the reduction tree to a point such that the 2^k functions of $n-k$ variables equal the total number of distinct functions of $(n-k)$ variables. Hence, the optimum reduction tree is that for which $2^k = 2^{2^{n-k}}$. The above relation is not satisfied for all values of n and k, and as a result the optimum reduction tree cannot be constructed for all numbers of variables. Table 7 gives the different values of n for which $2^k = 2^{2^{n-k}}$, and the optimum reduction tree is possible for these values of n and k.

The sequence generator will need three different components: a shift register with standard feedback and a word detector for generating one sequence of every length, an optimum reduction tree for reducing a single function of n variables into 2^k functions of $n-k$ variables, and a function generator capable of generating all distinct functions of $(n-k)$ variables.

The shift register with its feedback logic can be wired permanently, and n switches can be connected to control the input to the word detector. The 2^n different combinations of these n switches, taken n at a time, will give 2^n different lengths of the available sequences.

For obtaining any prescribed sequence, two groups of connections will have to be made. The word detector connections giving the desired length, and a maximum of 2^k connections between the reduction tree and the functions of $(n-k)$ variables giving the desired sequence. Hence, a minimum of n, and a maximum of $n + 2^k$ connections will be required for the generation of the prescribed sequence. The total number of sequences available in this manner is $2^{2^n+1} - 2$.

b. Shift register design. The complete design of this sequence generator requires three different subdesigns. The subdesign of a shift register and word detector combination is rather standard. For a maximum sequence length of 64, a six-stage shift register with standard feedback and a word detector will be all that would be required. Without the word detector, the shift register with feedback alone is capable of generating only one period. The rest of the 63 periods are obtained with the help of the word detector. Depending upon the feedback logic, the word detector connections for different periods can be determined once and for all. These connections can be written down in the form of a table, and for any particular period the connections can be looked up from the table. The block diagram of a typical six-stage shift register with standard feedback and word detector is shown in Figure 13.

Table 7. Values of *n*

n	k	$2^k = 2^{2^{n-k}}$
1	1	2
3	2	4
6	4	16
11	8	256
20	16	65,536
37	32	4,294,967,296

c. Reduction tree design. The next subdesign is that of the optimum reduction tree. From Table 7, for n equal to 6, the optimum reduction tree is possible for k equal to 4. That is, the reduction of the function of six variables is to be carried to the point so as to obtain $2^4 = 16$ functions of $6 - 4 = 2$ variables. These sixteen functions of two variables can be written as shown in Table 8. The tree reducing the given function of six variables into sixteen functions of two variables is shown in Figure 14. In an abbreviated notation the sixteen functions of two variables can be written as shown also in Table 8. In the abbreviated expression, the different i's starting from i_0 to i_{15} are sixteen functions of two variables.

d. Function generator design. The third and last subdesign is that of a function generator capable of generating all sixteen functions of two variables. For the sake of brevity these functions are denoted by different g's, starting from g_0 up to g_{15}. Table 8 shows the sixteen functions of two variables. From Table 8 it can be observed that the function g_0 is always zero, whereas function g_{15} is always unity. Similarly the remaining

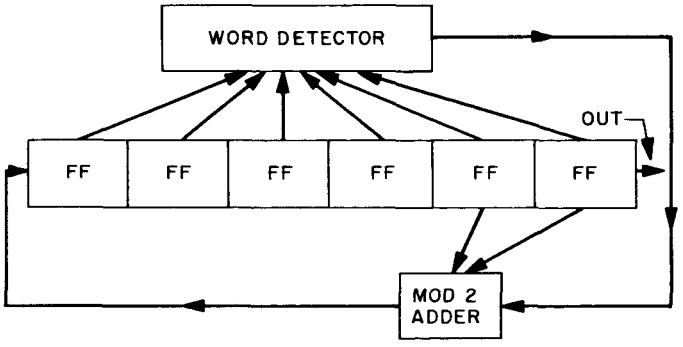

Figure 13. Six-stage shift register with standard feedback word detector

Table 8. Sixteen functions of two variables

Sixteen functions of two variables

$$f(x_1, x_2, x_3, x_4, x_5, x_6) = \bar{x}_1\bar{x}_2\bar{x}_3\bar{x}_4 f(0,0,0,0,x_5,x_6) + \bar{x}_1\bar{x}_2\bar{x}_3x_4 f(0,0,0,1,x_5,x_6) + \bar{x}_1\bar{x}_2x_3\bar{x}_4 f(0,0,1,0,x_5,x_6) + \bar{x}_1\bar{x}_2x_3x_4 f(0,0,1,1,x_5,x_6) + \bar{x}_1x_2\bar{x}_3\bar{x}_4 f(0,1,0,0,x_5,x_6) + \bar{x}_1x_2\bar{x}_3x_4 f(0,1,0,1,x_5,x_6) + \bar{x}_1x_2x_3\bar{x}_4 f(0,1,1,0,x_5,x_6) + \bar{x}_1x_2x_3x_4 f(0,1,1,1,x_5,x_6) + x_1\bar{x}_2\bar{x}_3\bar{x}_4 f(1,0,0,0,x_5,x_6) + x_1\bar{x}_2\bar{x}_3x_4 f(1,0,0,1,x_5,x_6) + x_1\bar{x}_2x_3\bar{x}_4 f(1,0,1,0,x_5,x_6) + x_1\bar{x}_2x_3x_4 f(1,0,1,1,x_5,x_6) + x_1x_2\bar{x}_3\bar{x}_4 f(1,1,0,0,x_5,x_6) + x_1x_2\bar{x}_3x_4 f(1,1,0,1,x_5,x_6) + x_1x_2x_3\bar{x}_4 f(1,1,1,0,x_5,x_6) + x_1x_2x_3x_4 f(1,1,1,1,x_5,x_6)$$

Abbreviated notation of sixteen functions of two variables[a]

$$f(x_1, x_2, x_3, x_4, x_5, x_6) = \bar{x}_1\bar{x}_2\bar{x}_3\bar{x}_4\, i_0 + \bar{x}_1\bar{x}_2\bar{x}_3x_4\, i_1 + \bar{x}_1\bar{x}_2x_3\bar{x}_4\, i_2 + \bar{x}_1\bar{x}_2x_3x_4\, i_3 + \bar{x}_1x_2\bar{x}_3\bar{x}_4\, i_4 + \bar{x}_1x_2\bar{x}_3x_4\, i_5 + \bar{x}_1x_2x_3\bar{x}_4\, i_6 + \bar{x}_1x_2x_3x_4\, i_7 + x_1\bar{x}_2\bar{x}_3\bar{x}_4\, i_8 + x_1\bar{x}_2\bar{x}_3x_4\, i_9 + x_1\bar{x}_2x_3\bar{x}_4\, i_{10} + x_1\bar{x}_2x_3x_4\, i_{11} + x_1x_2\bar{x}_3\bar{x}_4\, i_{12} + x_1x_2\bar{x}_3x_4\, i_{13} + x_1x_2x_3\bar{x}_4\, i_{14} + x_1x_2x_3x_4\, i_{15}$$

x_5	x_6	g_0	g_1	g_2	g_3	g_4	g_5	g_6	g_7	g_8	g_9	g_{10}	g_{11}	g_{12}	g_{13}	g_{14}	g_{15}
0	0	0	1	0	1	0	1	0	1	0	1	0	1	0	1	0	1
0	1	0	0	1	1	0	0	1	1	0	0	1	1	0	0	1	1
1	0	0	0	0	0	1	1	1	1	0	0	0	0	1	1	1	1
1	1	0	0	0	0	0	0	0	0	1	1	1	1	1	1	1	1

[a]The different i's starting from i_0 to i_{15} are sixteen functions of two variables.

fourteen functions form seven pairs of complementary functions. The functions g_{12} and g_3 are the variable x_5 and its complement. Similarly functions g_{10} and g_5 are the variable x_6 and its complement, respectively. The remaining ten functions can be classified into five pairs: g_1 and g_{14}; g_2 and g_{13}; g_4 and g_{11}; g_6 and g_9; and g_7 and g_8. Figure 14 shows a function generator.

A machine embodying these ideas has been constructed and operated in the laboratory from 1-mc commercial digital building blocks. The six connections which select the word to be detected by the word detector are made by six toggle switches. The sixteen connections by which the proper function of two variables is connected to each input of the reduction tree are made by patch cords on a patch board. The sequence, which repeats continuously, is on an oscilloscope. In all, only 21 digital modules are required for the entire machine.

3. Analysis of Angle Modulation Communications Systems

a. Introduction. The investigation of angle modulation communications systems utilizing phase-locked demodulators has continued. This investigation has two major purposes to accomplish. The first purpose is to compare the performance of phase modulation (PM) and frequency modulation (FM) communications systems under the constraint that the receiving system utilize only phase-locked demodulators. The second purpose is to provide a sound analytical basis for the design of analog telemetry systems (Ref 21). The consideration of the FM phase-locked demodulator is of interest because of recent work (Refs 22 to 26) on FM discriminators with negative feedback.

The analysis (Ref 27) of a PM system with single-tone modulation has shown that a "PM improvement factor" can be obtained by transmitting at high modulation indices and demodulating by means of a properly designed phase-locked demodulator. When the RF power levels are significantly above the receiver threshold, it was shown that a margin of safety exists which may be traded for additional signal-to-noise ratio (SNR) at the demodulated output of the receiver. It was also demonstrated that optimum values of receiver bandwidth and transmitter modulation index exists for providing the maximum output SNR at the demodulated output for a specified input SNR.

This report presents a summary of the results obtained in the continuation of the investigation. The performance of the PM system has been determined for a noise-like modulating signal since this is probably more representative of a practical application than is the sine wave modulation. The comparison of PM and FM reveals the superiority of the PM system under the constraint that the receivers utilize only phase-locked demodulators. However, when transmitting zero-frequency signals (dc), it is necessary to pre-emphasize the low frequencies in order to eliminate the infinite error produced by oscillator instability in the pure PM system. The performance of the PM system with pre-emphasis is shown to be in agreement with that of the pure PM system for both single-tone and noise-like modulation.

b. Results. The simplified block diagrams of Figures 15 to 17 represent the communications systems considered in this report. The PM system of Figure 15 was analyzed in a previous paper (Ref 27) for single-tone modulation. The equations which represent the performance of the systems considered here are summarized in Figures 15 to 17. The simplified forms of these equations are based upon the following assumptions:

(1) A linearized representation of the phase-locked-loop.

(2) High values of input SNR.

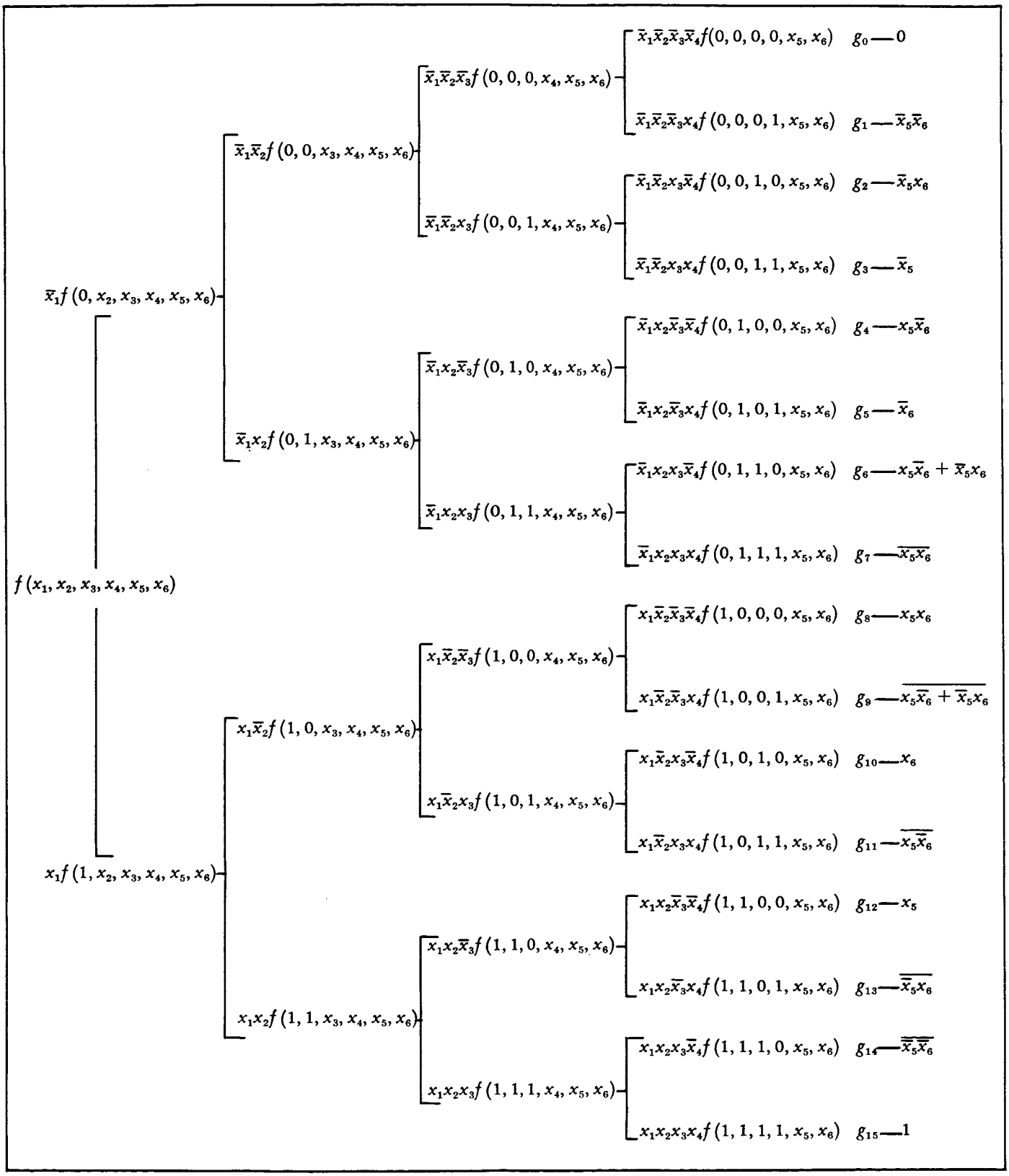

Figure 14. Optimum reduction tree and function generator

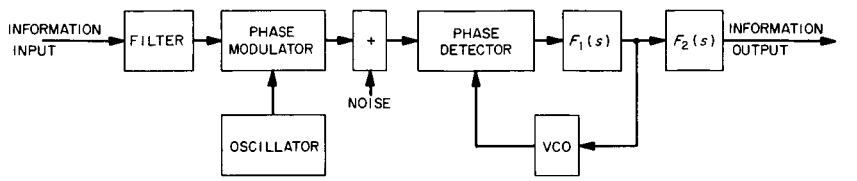

PM COMMUNICATIONS SYSTEM

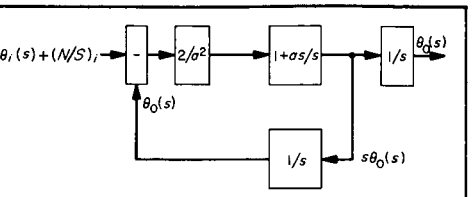

LINEARIZED EQUIVALENT SYSTEM FOR PM RECEIVER

Summary of analysis

$$H_p(s) = \frac{\theta_o}{\theta_i}(s) = \frac{1 + as}{1 + as + \frac{a^2 s^2}{2}}; \qquad 2B_L \equiv \frac{1}{2\pi j}\int_{-j\infty}^{j\infty} |H_p(s)|^2\, ds = \frac{3}{2a}, \text{ cps}$$

$$\Phi_N(s) = \left(\frac{N^2}{S^2}\right)_i \frac{1}{2B_N} \text{ radians}^2/\text{cps}; \qquad \sigma_{np}^2 = \frac{1}{2\pi j}\int_{-j\infty}^{j\infty} \Phi_N(s)\,|H_p(s)|^2\, ds = 2B_L\Phi_N(0), \text{ radians}^2$$

$$\sigma_{sp}^2 = \frac{1}{2\pi j}\int_{-j\infty}^{j\infty} \Phi_{sp}(s)\,|1 - H_p(s)|^2\, ds; \quad \sigma_{sp}^2 + \sigma_{np}^2 \leq 1 \text{ radian}^2, \text{ for phase-lock}$$

Single-tone modulation

$$\Phi_{sp}(\omega) = 2\pi m_p^2\left[\tfrac{1}{2}\delta(\omega - \omega_m) + \tfrac{1}{2}\delta(\omega + \omega_m)\right]$$

$$\sigma_{sp}^2 = \frac{81\pi^4}{64}\frac{f_m^4}{B_L^2}\left[\frac{1}{1 + \frac{81\pi^4}{64}\frac{f_m^4}{B_L^4}}\right]m_p^2$$

$$S_0^2 = \frac{1}{2\pi j}\int_{-j\infty}^{j\infty} \Phi_{sp}(s)\,|H_p(s)|^2\, ds = \left[\frac{1 + \frac{9\pi^2}{4}\frac{f_m^2}{B_L^2}}{1 + \frac{81\pi^4}{64}\frac{f_m^4}{B_L^4}}\right]m_p^2$$

$$\left(\frac{S_0^2}{\sigma_{np}^2}\right)_{for\ max\ m_p} = \frac{64}{81\pi^4}\frac{B_L^4}{f_m^4}\left[1 + \frac{9\pi^2}{4}\frac{f_m^2}{B_L^2}\right]\left[\left(\frac{S^2}{N^2}\right)_i \frac{2B_N}{2B_L} - 1\right]$$

Noise-like modulation

$$\Phi_{sp}(\omega) = \frac{m_p^2}{2f_{max}}, \text{ radians}^2/\text{cps}$$

$$\sigma_{sp}^2 = \frac{81\pi^4}{320}\frac{f_{max}^4}{B_L^4}m_p^2, \text{ radians}^2$$

$$S_0^2 = \frac{1}{2\pi j}\int_{-j\infty}^{j\infty} \Phi_{sp}(s)\,|H_p(s)|^2\, ds = \left[1 + \frac{3\pi^2}{4}\frac{f_{max}^2}{B_L^2}\right]m_p^2, \text{ radians}^2$$

$$\left(\frac{S_0^2}{\sigma_{np}^2}\right)_{for\ max\ m_p} = \frac{320}{81\pi^4}\frac{B_L^4}{f_{max}^4}\left[1 + \frac{3\pi^2}{4}\frac{f_{max}^2}{B_L^2}\right]\left[\left(\frac{S^2}{N^2}\right)_i \frac{2B_N}{2B_L} - 1\right]$$

Figure 15. PM communications system

(3) Threshold condition of the phase-locked-loop when the total mean square phase error is 1 radian² (Ref 22).

(4) An output SNR which is defined as the ratio of mean-square signal power to the mean-square noise error.

(5) A maximum modulating frequency which is much less than the equivalent noise bandwidth, $f_m << B_L$.

(6) A pre-emphasis filter time constant, $\tau >> 3/4B_L$.

It should be noted that the definition of output SNR as used in this analysis is for convenience in comparing the different systems. In actual practice the output SNR does not tend to infinity, but it approaches a constant value determined by the distortion initially designed into the system. In designing a system it is necessary to define the output SNR as the ratio of mean-square signal

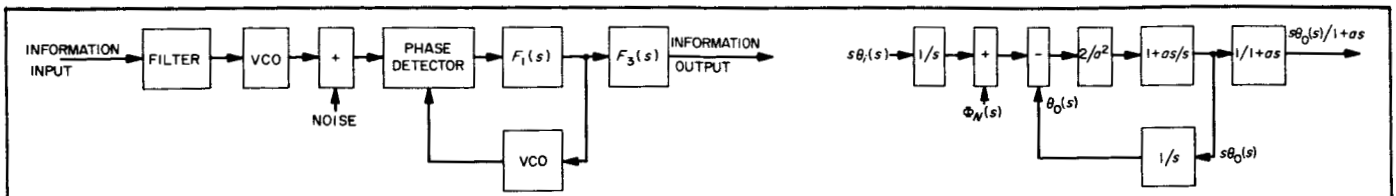

FM COMMUNICATIONS SYSTEM

LINEARIZED EQUIVALENT OF FM COMMUNICATIONS SYSTEM

Summary of analysis

$$H_p(s) = \frac{1 + as}{1 + as + \frac{a^2 s^2}{2}}; \quad 2B_L \equiv \frac{1}{2\pi j}\int_{-j\infty}^{j\infty} |H_p(s)|^2\, ds = \frac{3}{2a}; \quad H_f(s) = \frac{1}{2\pi}\left[\frac{s}{1 + as + \frac{a^2 s^2}{2}}\right], \text{ cps/rad}$$

$$\Phi_N(s) = \left(\frac{N^2}{S^2}\right)_i \frac{1}{2B_N}, \text{ rad}^2/\text{cps}; \qquad \sigma_{np}^2 = \frac{1}{2\pi j}\int_{-j\infty}^{j\infty} \Phi_N(s)\,|H_p(s)|^2\, ds = 2B_L\Phi_N(0), \text{ rad}^2$$

Information spectral density $= \Phi_{sf}(f)$, cps²/cps; Integrated spectral density $= \frac{1}{f^2}\Phi_{sf}(f)$, rad²/cps

$$\sigma_{sp}^2 = \int_{-\infty}^{\infty} \frac{\Phi_{sf}(f)}{f^2}|1 - H_p(f)|^2\, df, \text{ rad}^2; \qquad \sigma_{nf}^2 = \int_{-\infty}^{\infty} \Phi_N(f)\,|H_f(f)|^2\, df, \text{ cps}^2$$

$$S_0^2 = \int_{-\infty}^{\infty} \frac{\Phi_{sf}(f)}{f^2}|H_f(f)|^2\, df, \text{ cps}^2 \qquad \sigma_{sf}^2 = \int_{-\infty}^{\infty} \frac{\Phi_{sf}(f)}{f^2}\left|\frac{1}{2\pi}\left[j2\pi f - \frac{j2\pi f}{1 + j2\pi af - 2\pi^2 a^2 f^2}\right]\right|^2 df$$

Sine-wave modulation

$$\Phi_{sf}(f) = f_m^2 m_f^2\,[\tfrac{1}{2}\delta(f - f_m) + \tfrac{1}{2}\delta(f + f_m)]$$

$$\sigma_{np}^2 = 2B_L\Phi_N(0)$$

$$\sigma_{sp}^2 = \left[\frac{\frac{81\pi^4}{64}\frac{f_m^4}{B_L^4}}{1 + \frac{81\pi^4}{64}\frac{f_m^4}{B_L^4}}\right] m_f^2$$

$$\sigma_{nf}^2 = \frac{16B_L^3\,\Phi_N(0)}{27\pi^2}$$

$$\sigma_{sf}^2 = \frac{9\pi^2}{4}\frac{f_m^4}{B_L^2}\left[\frac{1 + \frac{9\pi^2}{16}\frac{f_m^2}{B_L^2}}{1 + \frac{81\pi^4}{64}\frac{f_m^4}{B_L^4}}\right] m_f^2$$

$$\left(\frac{S_0^2}{\sigma_{nf}^2}\right)_{for\ max\ m_f} = \frac{8}{3\pi^2}\left[\frac{B_L^2}{f_m^2}\right]\left[\left(\frac{S^2}{N^2}\right)_i \frac{2B_N}{2B_L} - 1\right]$$

Noise-like modulation

$$\Phi_{sf}(f) = \tfrac{1}{2}m_f^2 f_{max}, \text{ cps}^2/\text{cps}$$

$$\sigma_{np}^2 = 2B_L\Phi_N(0), \text{ rad}^2$$

$$\sigma_{sp}^2 = \frac{27\pi^4}{64}\frac{f_{max}^4}{B_L^4} m_f^2, \text{ rad}^2$$

$$\sigma_{nf}^2 = \frac{16B_L^3\,\Phi_N(0)}{27\pi^2}, \text{ cps}^2$$

$$\sigma_{sf}^2 = \frac{3\pi^2}{4}\frac{f_{max}^4}{B_L^2}\left[\frac{1 + \frac{9\pi^2}{16}\frac{f_{max}^2}{B_L^2}}{1 + \frac{81\pi^4}{64}\frac{f_{max}^4}{B_L^4}}\right] m_f^2, \text{ cps}^2$$

$$\left(\frac{S_0^2}{\sigma_{nf}^2}\right)_{for\ max\ m_f} = \frac{8}{\pi^2}\frac{B_L^2}{f_{max}^2}\left[\left(\frac{S^2}{N^2}\right)_i \frac{2B_N}{2B_L} - 1\right]$$

Figure 16. FM communications system

power to the total mean-square error at the demodulator output (Ref 21).

The performance of the systems is described graphically in Figures 18 to 25. The output SNR has been maximized for an input noise spectral density corresponding to an input SNR of 12 db in a 6-kc bandwidth,[a] under the constraint that the total mean-square phase error does

[a]This value of input SNR is approximately the "breaking point" or threshold of a high deviation ratio FM system employing a limiter.

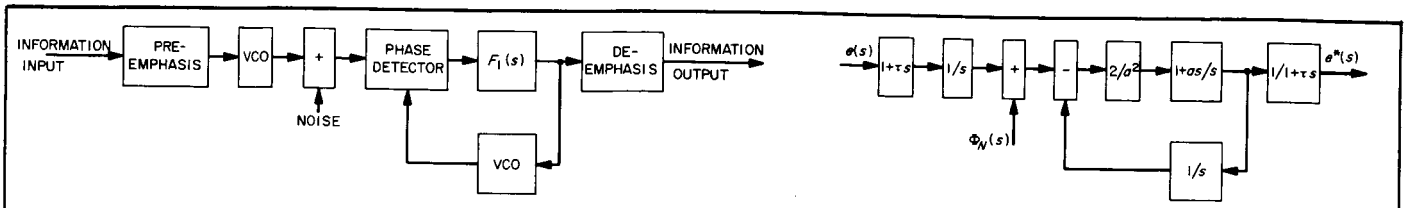

PM WITH PRE-EMPHASIS COMMUNICATIONS SYSTEM

LINEARIZED EQUIVALENT OF PM WITH PRE-EMPHASIS COMMUNICATION SYSTEM

Summary of analysis

$$\frac{e^*(s)}{e(s)} = \frac{1+as}{1+as+\frac{a^2s^2}{2}}; \quad H_R(s) = \frac{s(1+as)}{2\pi(1+\tau s)\left(1+as+\frac{a^2s^2}{2}\right)}, \text{ cps/rad}; \quad H_p(s) = \frac{1+as}{1+as+\frac{a^2s^2}{2}}; \quad 2B_L = \frac{3}{2a}, \text{ cps}$$

Information spectral density $= \Phi_{sf}(f)$, cps²/cps; Integrated spectral density $= \frac{\Phi_{sf}(f)}{f^2}$, rad²/cps;

$$\Phi_N(s) = \left(\frac{N^2}{S^2}\right)_i \frac{1}{2B_N}, \text{ rad}^2/\text{cps} \quad \sigma_{np}^2 = 2B_L\Phi_N(0); \quad \sigma_{nf}^2 = \frac{1}{2\pi}\int_{-\infty}^{\infty}\Phi_N(\omega)\,|H_R(\omega)|^2\,d\omega, \text{ cps}^2$$

$$\sigma_{sp}^2 = \frac{1}{2\pi}\int_{-\infty}^{\infty}\frac{\Phi_{sf}(\omega)}{\left(\frac{\omega}{2\pi}\right)^2}(1+\tau^2\omega^2)\,|1-H_p(\omega)|^2\,d\omega, \text{ rad}^2/\text{cps}$$

$$\sigma_{sf}^2 = \frac{1}{2\pi}\int_{-\infty}^{\infty}\frac{\Phi_{sf}(\omega)}{\left(\frac{\omega}{2\pi}\right)^2}\left|1-\frac{e^*(\omega)}{e(\omega)}\right|^2 d\omega, \text{ cps}^2; \quad S_0^2 = \frac{1}{2\pi}\int_{-\infty}^{\infty}\frac{\Phi_{sf}(\omega)}{\left(\frac{\omega}{2\pi}\right)^2}(1+\tau^2\omega^2)\,|H_R(\omega)|^2\,d\omega, \text{ cps}^2$$

Sine-wave modulation

$$\Phi_{sf}(\omega) = 2\pi f_m^2 m_f^2\left[\tfrac{1}{2}\delta(\omega-\omega_m)+\tfrac{1}{2}\delta(\omega+\omega_m)\right], \text{ cps}^2/\text{cps}$$

$$\sigma_{np}^2 = 2B_L\Phi_N(0), \text{ rad}^2$$

$$\sigma_{sp}^2 = \frac{81\pi^4 f_m^4}{64B_L^4}\left[\frac{1+4\pi^2 f_m^2\tau^2}{1+\frac{81\pi^4}{64}\frac{f_m^4}{B_L^4}}\right]m_f^2, \text{ rad}^2$$

$$\sigma_{nf}^2 = \frac{\Phi_N(0)}{4\pi^2}\left[\frac{a+\frac{3\tau}{2}}{\frac{a^3\tau}{2}+a^2\tau^2+a\tau^3}\right], \text{ cps}^2$$

$$\sigma_{sf}^2 = \left[\frac{\frac{81\pi^4 f_m^4}{64B_L^4}}{1+\frac{81\pi^4 f_m^4}{64B_L^4}}\right]m_f^2, \text{ cps}^2$$

$$S_0^2 = \left[\frac{1+\frac{9\pi^2}{4}\frac{f_m^2}{B_L^2}}{1+\frac{81\pi^4}{64}\frac{f_m^4}{B_L^4}}\right]m_f^2 f_m^2, \text{ cps}^2$$

$$\left(\frac{S_0^2}{\sigma_{np}^2}\right)_{for\ max\ m_p} = \frac{64}{81\pi^4}\frac{B_L^4}{f_m^4}\left[1+\frac{9\pi^2}{4}\frac{f_m^2}{B_L^2}\right]\left[\left(\frac{S^2}{N^2}\right)_i\frac{2B_N}{2B_L}-1\right]$$

Noise-like modulation

$$\Phi_{sf}(\omega) = \tfrac{1}{2}m_f^2 f_{max}, \text{ cps}^2/\text{cps}$$

$$\sigma_{np}^2 = 2B_L\Phi_N(0), \text{ rad}^2$$

$$\sigma_{sp}^2 = \frac{81\tau^2\pi^6}{80}\frac{f_{max}^6}{B_L^4}m_f^2, \text{ rad}^2$$

$$\sigma_{nf}^2 = \frac{\Phi_N(0)}{4\pi^2}\left[\frac{a+\frac{3\tau}{2}}{\frac{a^3\tau}{2}+a^2\tau^2+a\tau^3}\right], \text{ cps}^2$$

$$\sigma_{sf}^2 = \left[\frac{81\pi^4}{320}\frac{f_{max}^6}{B_L^4}\right]m_f^2, \text{ cps}^2$$

$$S_0^2 = \left[1+\frac{3\pi^2}{4}\frac{f_{max}}{B_L^2}\right]m_f^2 f_{max}^2, \text{ cps}^2$$

$$\left(\frac{S_0^2}{\sigma_{np}^2}\right)_{for\ max\ m_p} = \frac{320}{81\pi^4}\frac{B_L^4}{f_{max}^4}\left[1+\frac{3\pi^2}{4}\frac{f_{max}^2}{B_L^2}\right]\left[\left(\frac{S^2}{N^2}\right)_i\frac{2B_N}{2B_L}-1\right]$$

Figure 17. PM with pre-emphasis communications system

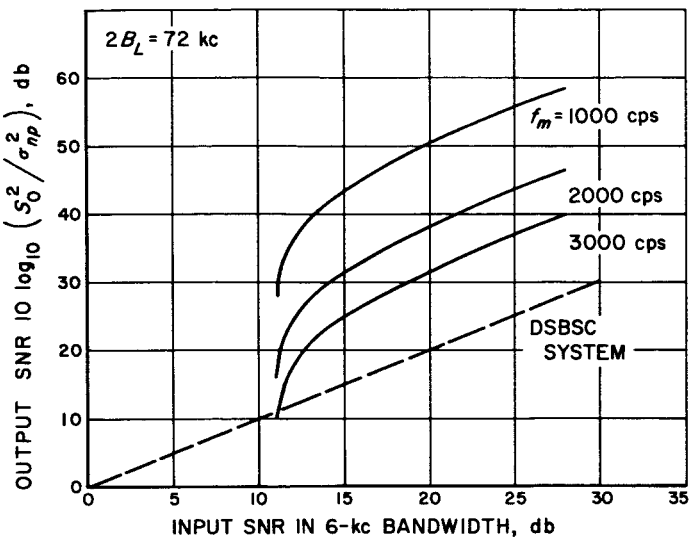

Figure 18. Output SNR vs input SNR for a PM system with sine wave modulation

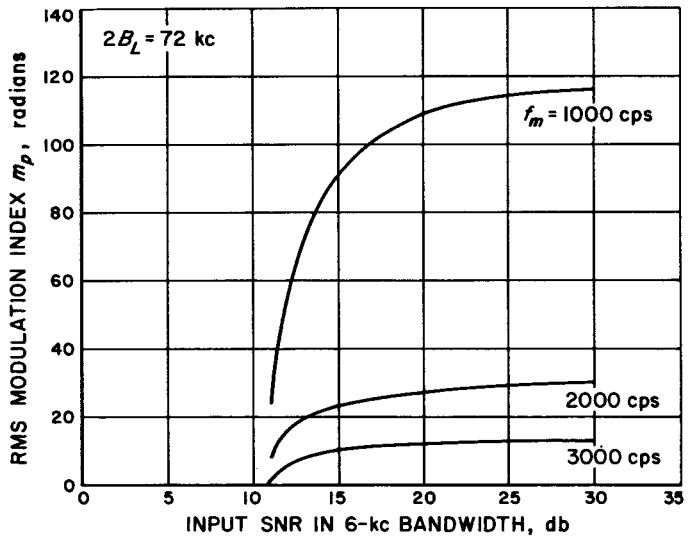

Figure 19. Modulation index vs input SNR for a PM system with sine wave modulation

not exceed the value of 1 radian² (Ref 22). The equivalent noise bandwidths of the receivers which provide the optimum output SNR are $2B_L = 72$ kc for the PM system and $2B_L = 48$ kc for the FM system. For each curve of output SNR, the transmitter modulation index has been increased to the maximum allowable value for which the total mean-square phase error is 1 radian² (Ref 22). The curves of Figures 19, 21, 23, and 25 show the maximum allowable values of rms modulation index for each case. The SNR performance of a dual-sideband suppressed carrier (DSBSC) system is included for comparison.

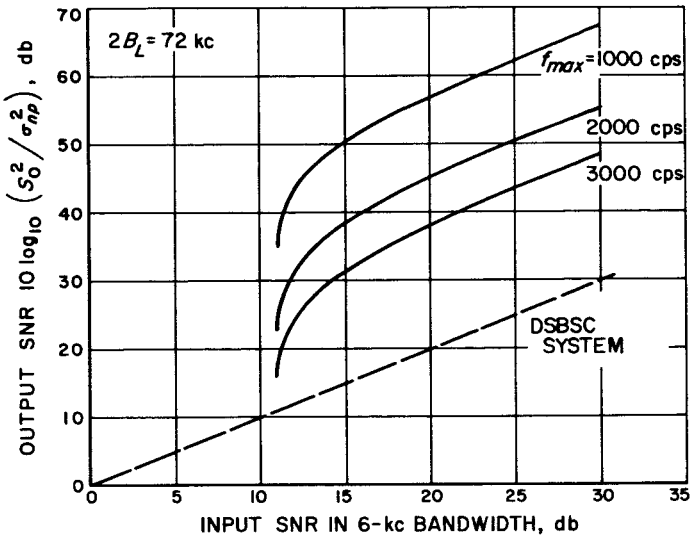

Figure 20. Output SNR vs input SNR for a PM system with noise-like modulation

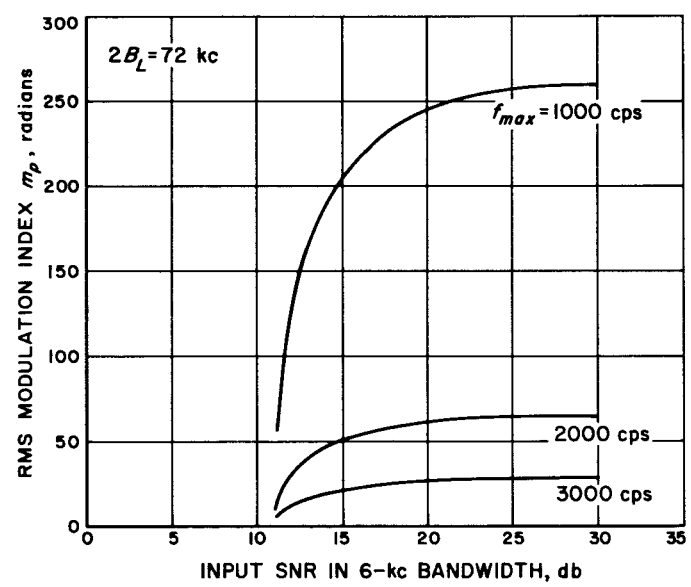

Figure 21. Modulation index vs input SNR for a PM system with noise-like modulation

The performance curves of Figures 18 and 22 indicate that the PM system is greatly superior (roughly 6 to 15 db) to the FM system when the receivers are constrained to employing phase-locked demodulators. The curves of Figures 18 and 20 show that the output SNR of the PM system assuming a noise-like modulating signal is 6.5 to 7 db higher than when a single-tone modulating signal is assumed. The output SNR of the PM system with pre-emphasis of the low frequencies as described by the equations of Figure 17 is in agreement with the output SNR of the pure PM system given in Figure 15.

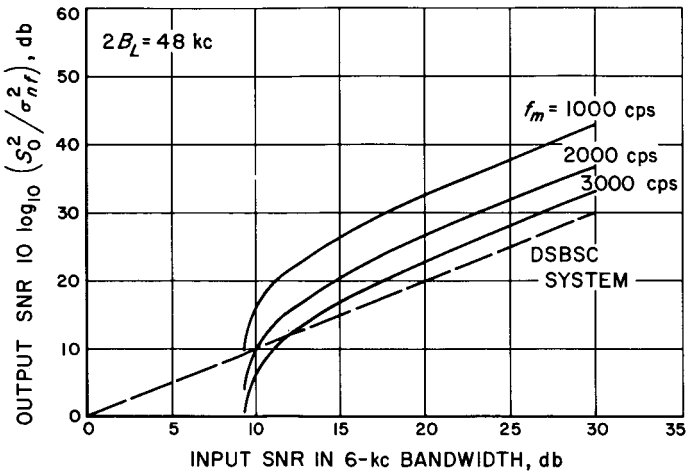

Figure 22. Output SNR vs input SNR for a FM system with sine wave modulation

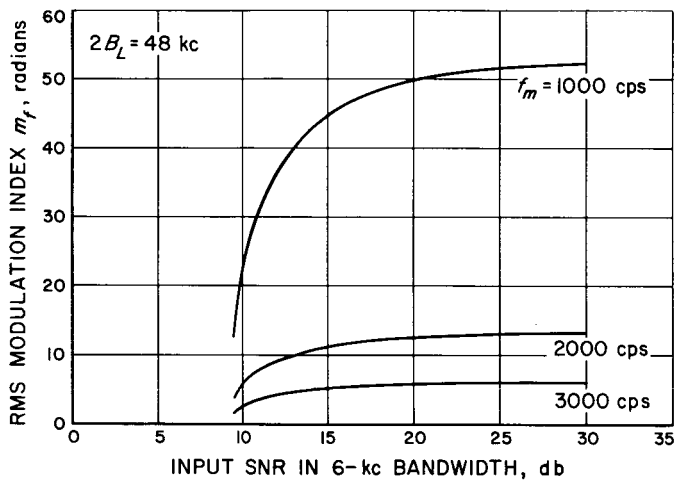

Figure 23. Modulation index vs input SNR for a FM system with sine wave modulation

c. Conclusions. The results of this analysis show that the PM system is greatly superior to the FM system under the constraint of utilizing phase-locked demodulators. However, it is surmised that an optimum FM demodulator would provide roughly equivalent performance to the PM system.

It is shown that a properly designed PM system with pre-emphasis of the low modulation frequencies is capable of performance equivalent to the pure PM system (compare Figs 15 and 17). This is a significant result when it is desired to transmit zero frequency (dc) signals because of the detrimental effect of oscillator instability on the pure PM system.

The equations which describe the performance of the systems can be used as the basis for designing low-power

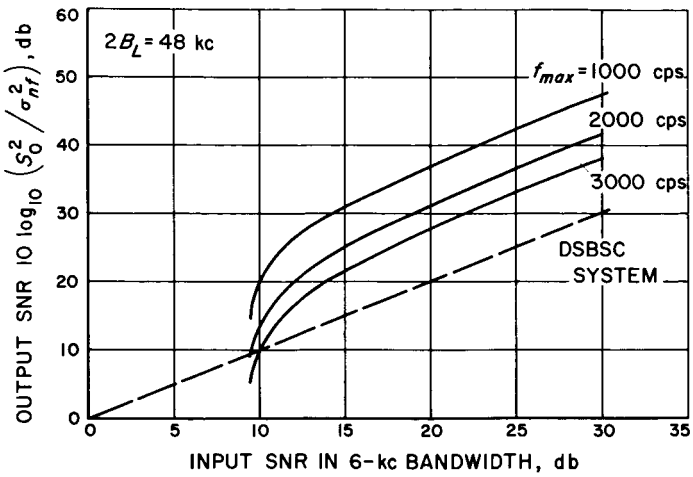

Figure 24. Output SNR vs input SNR for a FM system with noise-like modulation

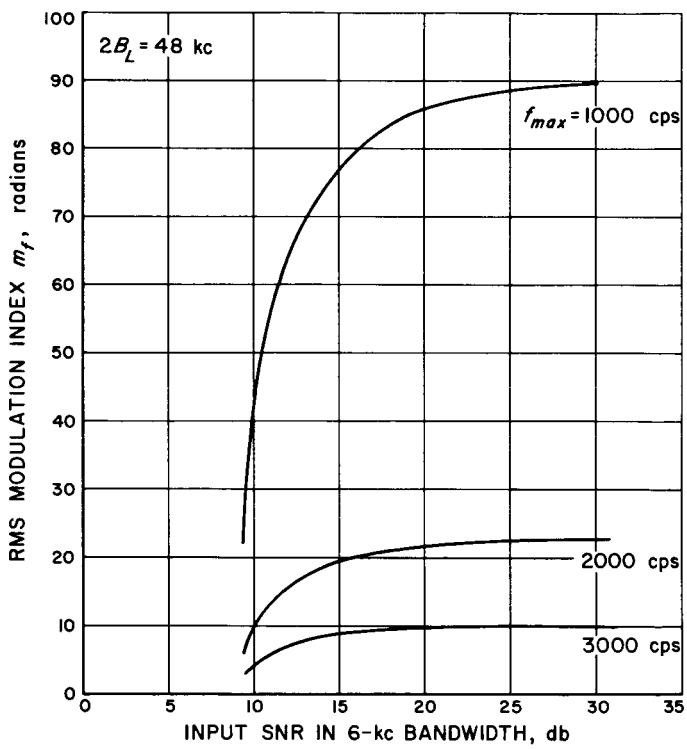

Figure 25. Modulation index vs input SNR for a FM system with noise-like modulation

analog telemetry systems. The procedure for designing telemetry systems from these equations is illustrated in Reference 21.

4. Design of a Digital Coded Telemetry System

a. Introduction. This report will describe techniques for designing a coded telemetry system, using word cor-

relation of the type described in Reference 28, with standard digital equipment (i.e., digital logic, flip-flops, and delay lines). Thus, the task of implementing the system is reduced from one of constructing specific hardware components to one of logical design using digital building blocks. In other words, a telemetry system is treated as a special-purpose digital computer.

The system block diagram is shown in Figure 26. A binary input in blocks of 5 bits is assumed with a teletype data rate of 22 millisec/bit, or approximately 45 bits/sec.[a] The channel subcarrier is chosen to be 4 kc (250 μsec/cyc).

b. Modulator design. The binary data is presented in blocks of 5, and a 16-symbol bi-orthogonal code is used. In Reference 28, it is shown that such a code is generated by placing four of the data bits into a maximum-length linear shift register and allowing this to run for 15 symbol periods. The fifth data bit is sent uncoded as the first symbol. The fifteen symbols generated in this way by the shift register are then sent unaltered if the fifth data bit was a "0," or they are complemented if it was a "1." Since the data bit synchronization period is 22 millisec, the word synchronization pulse W must occur every 110 millisec and the symbol synchronization pulse S every 6875 μsec. It is assumed that a 1-mc clock is available; thus, all the synchronization pulses may be derived by multiplying the basic 1-μsec period digitally by means of counters. The coder described above is shown in Figure 26a as the front end of the modulator. The first four data bits are introduced into the shift register at the word synchronization time W, and the register is shifted at the symbol synchronization times S. The fifth data bit is inserted into a flip-flop whose output is fed continually to an output logic package. A one-symbol period delay must be inserted between the shift register output and the output logic package. This logic is an "exclusive-OR" gate or modulo-2 adder. In this way, the fifth bit is sent as the first symbol unaltered. Then the fifteen symbols generated by the shift register are sent unaltered or complemented, depending on the state of the flip-flop.

The modulation of the subcarrier by the code can also be performed digitally. The 4-kc subcarrier can be generated as a square wave of 250 μsec by counting the 1-μsec clock. Bi-phase modulation of the subcarrier by the code is equivalent to multiplication by +1 or −1 corresponding to a "1" or "0" respectively. This in turn is equivalent to the complement of an "exclusive-OR" operation or modulo 2 addition, as will now be shown. The multiplication table of the code by the subcarrier is:

	Subcarrier	
Code	−1	+1
−1	+1	−1
+1	−1	+1

The truth table for modulo 2 addition of two binary variables is:

	0	1
0	0	1
1	1	0

and its complement is:

	0	1
0	1	0
1	0	1

Thus, associating a +1 with a "1" and a −1 with a "0" yields the following logical expression for multiplication:

$$\text{Multiplier output} = \overline{\text{code}} \cdot \overline{\text{subcarrier}} + \text{code} \cdot \text{subcarrier}$$

The output of this multiplier logic package is then a square wave amplitude-modulated by the code. The dc value is unimportant since it can be eliminated in modulating the main carrier.

The spectrum of a square wave coherently modulated by a binary code is derived in Reference 29. However, the exact expression for the spectrum is not required in the analysis. As will be shown in the last section, the effect of a filter in the channel on the performance of the system can be determined without regard to the form of the spectrum.

c. Analog channel. After the digital coding and modulation process, the telemetry signal is used to modulate the main carrier and transmitted. In this process a certain amount of linear filtering may be necessary because of bandwidth or equipment limitations. The channel is assumed to be perturbed by the additive white gaussian noise. The receiver will demodulate the carrier coherently and translate the noisy telemetry signal to its original frequency (4 kc). A certain amount of linear filtering is also inherent in the RF portion of the receiver. Since the process of modulating the carrier is simply a frequency translation, the overall block diagram of the channel and carrier modulation and demodulation may be simplified, shown to only the linear filtering and noise

[a]The system is designed to be compatible with the binary data source and digital telemetry test unit described in JPL *Research Summary* 36-7, Vol I, pp 67–69.

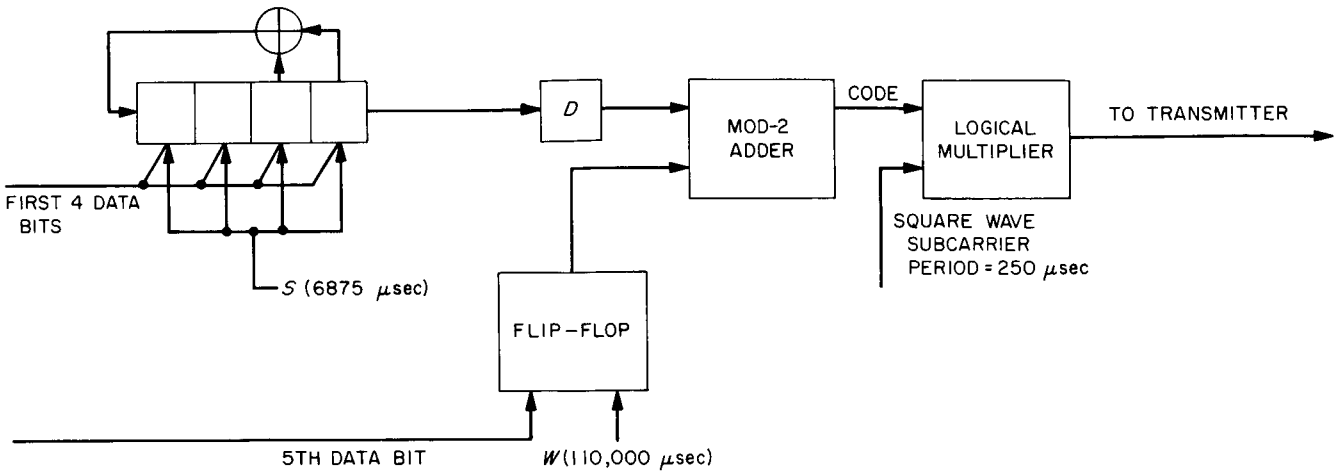

a. DIGITAL CODER-MODULATOR

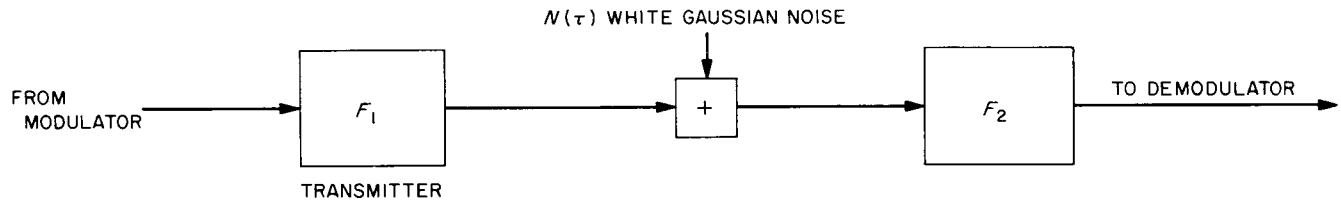

b. ANALOG CHANNEL

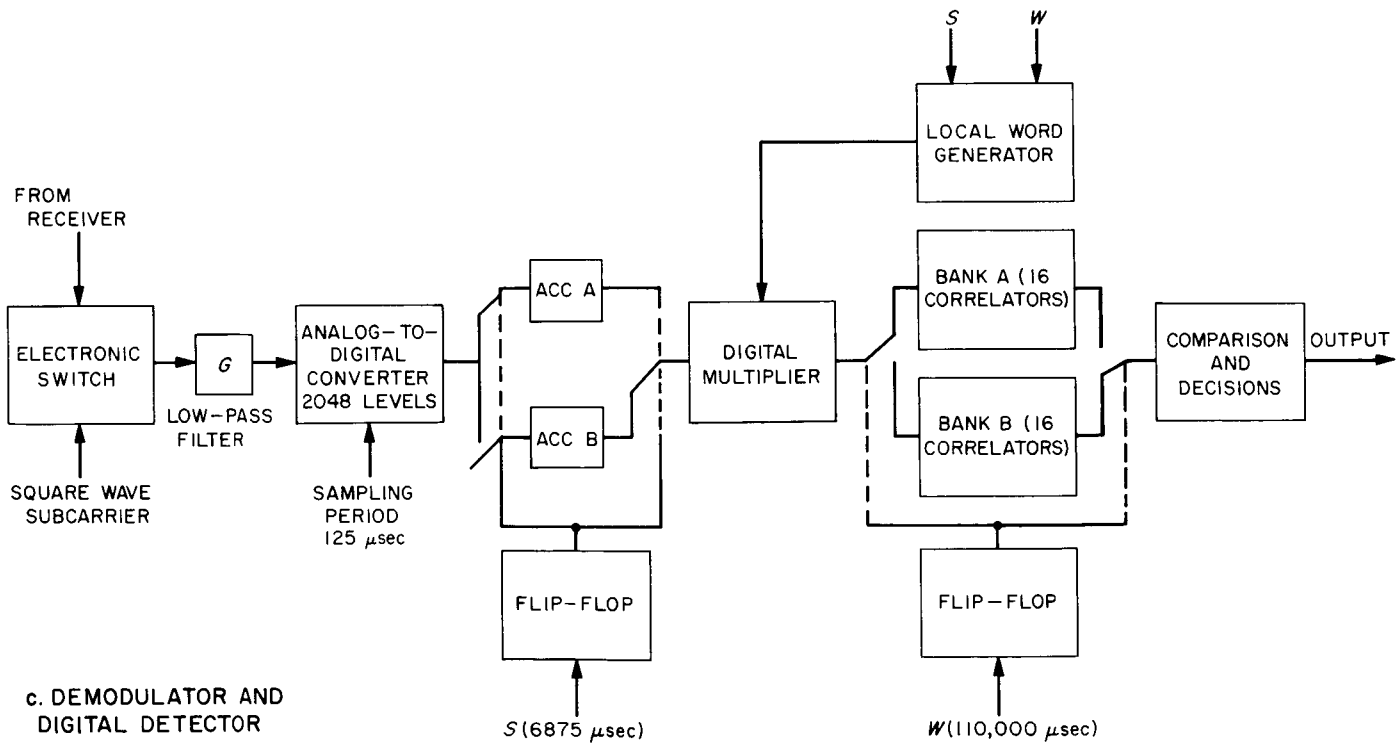

c. DEMODULATOR AND DIGITAL DETECTOR

Figure 26. Digital coder-modulator, analog channel, demodulator, and digital detector

source (Fig 26b). The subcarrier must also be detected coherently and fed to the digital demodulator. This is rendered possible by transmission of a small amount of unmodulated subcarrier. Symbol and word synchronization are also assumed available. Symbol synchronization may be attained by correlation detection and also word synchronization if a comma-free code word set is used. However, these matters will not be discussed in this report.

d. Digital demodulator and decoder design. The detection process in the analog case (Ref 28) requires multiplication of the incoming code word by all possible code words, integration over the word period, and a decision at the end of the word period which determines which word was most probably sent.

The equivalent digital operations and their mechanization will now be described in detail. Theoretical performance of the digital detector will be treated in the next section and compared with its analog counterpart. For the moment, it will suffice to note that the digital equivalent of integration is summation. Also, multiplication of the received binary code word by a locally generated word followed by integration over the word period can be performed equivalently by integration over the symbol period followed by addition or subtraction of the integrated received symbol to the word accumulator depending on whether the locally generated symbol is a "1" or a "0."

The demodulation of the square wave subcarrier can be performed by means of an electronic switch which is triggered by a locally generated subcarrier such that it passes the signal unaltered during the positive square wave peaks and inverts it during the negative peaks. The demodulated telemetry signal is then filtered by a linear low-pass filter G in preparation for the digital detection process. The transfer function of this filter is critical to the performance of the system as will be shown in the next section. An analog-to-digital converter then samples the demodulated telemetry signal at intervals of 125 μsec (4 kc) and quantizes it into 2048 levels (10 binary bits plus a sign digit). These quantized samples are summed over one symbol period (6875 μsec) in an accumulator. At the end of the sample period, the first accumulator will have summed 55 samples of at most 10 binary bits plus a sign digit. Therefore, its capacity must be 16 bits plus a sign digit. The output of this first accumulator at the end of the symbol period is fed to 16 different accumulators.

In each of these accumulators this binary number is added or subtracted according to whether the code word corresponding to the given accumulator is a "1" or a "0" during the given symbol period. Since each word contains 16 symbols, each of these accumulators must be capable of containing 20 bits plus a sign digit. At the end of each word, the 16 accumulators are compared and the one containing the largest binary number in absolute value is selected. This together with the sign of the number determines which word was most probably sent.

The mechanization of these operations is shown in Figure 26c. Two accumulators must be used to perform the task of accumulating over the symbol period. While ACC A sums the samples over one symbol period, ACC B reads the total over the previous symbol period into the bank of 16 accumulators. During the next symbol period the roles of ACC A and ACC B are reversed. The switching of operations of the two accumulators is controlled by a set–reset flip-flop which is triggered by the symbol synchronization pulse. As was described above, the accumulation process in these BANKS is controlled by code word generators. The 16 code words are generated by means of a shift register identical to that described under the modulator design section. Since the 16 code words are cyclic, each is a time shift of another and hence all 16 can be generated by a single shift register in which delays are introduced to produce the various different words simultaneously. In fact, if serial logic is used the two accumulator BANKS can be long delay lines (at least 336 μsec each, since they must contain 16 words with 21 binary bits each). The code word generator can be synchronized with the accumulator BANK such that the proper symbol appears from the code word generator to determine whether the output of ACC A or ACC B for a given symbol period should be added or subtracted into a given accumulator of the proper BANK.

e. Theoretical performance of digital telemetry system. The modulated telemetry signal was shown to be a square wave ampltitude-modulated by a binary code. The simplified channel (as described in Sec c) consists of a low-pass filter, F_1, followed by a noise-adding junction, followed by another low-pass filter, F_2. All that is required of these filters is that they be sufficiently wideband that they will pass a 4-kc square wave without attenuating the peaks significantly. Let us consider the worst case, where F_1 and F_2 are both one-stage RC low-pass filters of transfer function

$$F_1(s) = F_2(s) = \frac{a}{s+a} \tag{1}$$

The problem is to find the 3-db radian frequency a, such that the filters will not significantly attenuate the square

wave at the end of each half-cycle. Assuming a square wave of amplitude 1, the Laplace transform of the filtered square wave during the half-cycle of duration t_0 is

$$\frac{1}{s}\left(\frac{a}{s+a}\right)^2$$

which has the inverse transform $u(t) - e^{-at}(1 + at)$. Therefore, at the end of the half-cycle the filtered square wave will be of amplitude $1 - e^{-at_0}(1 + at_0)$. Letting $a = 10/t_0$ makes this amplitude 0.9995, which represents a negligible loss. In the system design, the half-period $t_0 = 125$ μsec, which would require that $a = 8 \times 10^4$ rad/sec = 12.8 kc. Thus, if the analog-to-digital converter samples the demodulated signal at times corresponding to the end of the square wave half-period, virtually no attenuation will occur due to F_1 and F_2, provided their 3-db bandwidths are made at least 3.2 times the fundamental frequency of the telemetry subcarrier (4 kc).

After the demodulation process, the signal passes through another low-pass filter G prior to sampling. This will also be taken to be a one-stage RC filter of transfer function

$$G(s) = \frac{b}{s+b} \tag{2}$$

In the absence of noise and neglecting the effect of the filter F_1 and F_2, the output of $G(s)$ during the first symbol period is

$$0(s) = S^{1/2}\frac{b}{s(s+b)} \tag{3}$$

where S is the received signal power. This signal is sampled periodically at intervals $t_0 = 125$ μsec. Using standard sampled-data notation, the z-transform of the sampler output is

$$0(z) = S^{1/2}\left[\frac{b}{s(s+b)}\right]^* = S^{1/2}\left[\frac{z}{z-1} - \frac{z}{z-e^{-bt_0}}\right] \tag{4}$$

The output at the nth sampling interval is found by taking the inverse z transform

$$0(nt_0) = \int_\Gamma 0(z)\, z^{n-1}\, dz$$

where the contour Γ is the unit circle. To get around the difficulty that $0(z)$ has a pole on the unit circle at $z = 1$, this pole is shifted to $1 - \varepsilon$, the contour integration is performed, and then the limit of the integral is found as $\varepsilon \to 0$. This yields

$$\begin{aligned} 0(nt_0) &= S^{1/2} \lim_{\varepsilon \to 0} \int_\Gamma \frac{z^n(1 - \varepsilon - e^{-bt_0})}{(z - 1 + \varepsilon)(z - e^{-bt_0})}\, dz \\ &= S^{1/2}(1 - e^{-nbt_0}) \end{aligned} \tag{5}$$

The average of the M samples over one period is given by

$$\begin{aligned} m_S &= \frac{1}{M}\sum_{n=1}^{M} 0(nt_0) = S^{1/2}\left[1 - \frac{1}{N}\sum_{n=1}^{N} e^{-nbt_0}\right] \\ &= S^{1/2}\left[1 - \frac{e^{-bt_0}(1 - e^{-Mbt_0})}{M(1 - e^{-bt_0})}\right] \end{aligned} \tag{6}$$

where the number of samples/symbol $M = 55$, as was stated in Section d. This makes the sample mean over one symbol quite close to $S^{1/2}$ provided t_0 is not too small. If bt_0 is made sufficiently large for this purpose, Mbt_0 will be quite large so that the final sample of the symbol $0(Mt_0)$ as given by Equation 5 will be quite close to $S^{1/2}$, and thus there will be no significant attenuation due to filtering in case the next symbol is of the opposite binary state. Therefore, the sample mean over one word period will be essentially the same as over one symbol.

The remaining problem is to determine the effect of the additive noise on the correlator output. This is measured by the variance on the sample mean over one word period. The variance of the sample mean for a process of mean zero, variance σ^2, and autocorrelation function $R(\tau)$ is given in Reference 30 as

$$\sigma_m^2 = \frac{1}{N}\left[\sigma^2 + 2\sum_{k=1}^{N-1}\left(1 - \frac{k}{N}\right)R(kt_0)\right] \tag{7}$$

where t_0 is the sampling period and N is the number of samples. The process in this case is filtered gaussian noise. The filter is $G(s) = b/(s + b)$ since the effect of $F_2(s)$ on the noise is negligible (its bandwidth being many times that of G as will be shown presently). The variance of white noise of one-sided spectral density N_0 filtered by $G(s)$ is

$$\sigma^2 = \frac{1}{2\pi}\int_{-\infty}^{\infty}\frac{N_0}{2}\frac{b^2}{\omega^2 + b^2}\, d\omega = \frac{N_0 b}{4} \tag{8}$$

and its correlation function is

$$R(\tau) = \sigma^2 e^{-b|\tau|} \tag{9}$$

Then the variance of the sample mean using Equations 7, 8, and 9 is

$$\begin{aligned} \sigma_s^2 &= \frac{\sigma^2}{N}\left[1 + 2\sum_{k=1}^{N-1}\left(1 - \frac{k}{N}\right)e^{-bt_0}\right] \\ &= \frac{N_0 b}{4N}\left\{1 + 2\left[\frac{e^{-bt_0} - e^{-Nbt_0}}{1 - e^{-bt_0}}\right]\left[1 - \frac{1}{N(1 - e^{-bt_0})}\right]\right\} \end{aligned} \tag{10}$$

Since the sample mean is to be taken over one word time, N is the number of samples per word. Let $T = Nt_0$ be the word time. Then N is equal to the number of symbols/word times the number of samples/symbol,

which is in this case, $16 \times 55 = 880$. Since N is very large, e^{-Nbt_0} is entirely negligible and Equation 10 is approximately

$$\sigma_s^2 \approx \left(\frac{N_0}{2T}\right)\left(\frac{bt_0}{2}\right)\left(\frac{1+e^{-bt_0}}{1-e^{-bt_0}}\right) \tag{11}$$

The parameter which determines the performance of the detector is the ratio of the mean output of the correlator corresponding to the word sent to the square root of the variance. For the analog case this is (Ref 28):

$$\frac{m}{\sigma} = \left(\frac{2ST}{N_0}\right)^{1/2}$$

For the digital system discussed, this parameter is found from Equations 6 and 11 to be

$$\frac{m_s}{\sigma_s} = \left\{\left(\frac{2ST}{N_0}\right)\frac{\left[1-\frac{e^{-bt_0}(1-e^{-Mbt_0})}{M(1-e^{-bt_0})}\right]^2}{\left(\frac{bt_0}{2}\right)\left(\frac{1+e^{-bt_0}}{1-e^{-bt_0}}\right)}\right\}^{1/2} \quad \text{where } M = 55 \tag{12}$$

The term multiplying $2ST/N_0$ may properly be called the degradation factor of the digital system. It is found that this degradation factor reaches a peak when $bt_0 = 0.5$. This peak is 0.935, which represents a loss relative to the ideal correlation detector of 0.3 db.

Since $t_0 = 125$ μsec, b must be made equal to 4×10^3 rad/sec or 635 cps. This justifies neglecting the effect of filter F_2 on the noise since its 3-db bandwidth is 20 times that of G.

Actually the degradation could be reduced by using a more elaborate transfer function for $G(s)$. In fact, it can be shown that if G were an ideal square-cutoff low-pass filter the degradation could be entirely eliminated. Investigation is in progress on physically realizable filters which will improve the performance of the system.

The degradation which might be caused by the quantization in converting from analog to digital form can be shown to be entirely negligible because of the large number (2048) of quantum levels employed.

V. Communications Elements Research

A. Low-Noise Amplifiers

W. H. Higa, W. H. Wells, and C. T. Stelzried

1. Heterodyne Properties of Quantum Mechanical Systems

The previous issue of this *Summary* (*RS 36-9*) reported that a theoretical analysis was in progress to determine the heterodyne properties of a three-level quantum mechanical system. Such systems are located, for example, at the active sites in maser materials, e.g., ruby. The analysis has been completed, and the mixing action confirmed. Line shapes, bandwidths, and noise properties are similar to those for other maser-like devices. Detailed mathematical expressions for the spectra contain so many parameters that it is impractical to provide equations and graphs here.

When a signal at one of the three resonant frequencies is applied to the system along with radiation from a local oscillator (pump), the system radiates at the third frequency in a manner dependent on the phase at the two applied frequencies. Thus, a noisy pump produces a noisy output as in the case of an ordinary classical mixer.

A difficulty arises when the wavelengths are short compared to the overall dimensions of the active material. The active sites must be located only at points where they will radiate in a manner that interferes constructively. This requires that the active material be 'sliced' into very accurate pieces. The width of the pieces must be the order of magnitude of the longest wavelength of the three frequencies. Thus, one could not mix three optical frequencies, because no technique is available for making layers of active material with optical spacings. However, mixing two optical frequencies that differ by a microwave frequency is apparently feasible because the phase difference between the two light waves accumulates a significant amount (say π radians) only over distances the order of a microwavelength. An experiment to verify the theoretical predictions is being considered.

2. Instrumentation for Noise Temperature Measurements

The precise measurement of absolute noise temperature has been investigated at JPL in parallel with the work on low-noise antennas and amplifiers. At present, refined instrumentation for use in future experiments on the Goldstone 85-foot antennas is being studied. The previous JPL studies in this field are reported in *RS 36-1* to *36-9* and *SPS 37-9*.

A 2388-mc radiometer has been assembled in the laboratory, and its sensitivity and stability are being evaluated. Switching for gain stabilization is not used at the input of the receiver, so it is a "total-power" radiometer. This type of design requires great care in the power supplies and local oscillator to achieve sufficient gain stability to provide a satisfactory sensitivity ($<1°K$).

The receiver shown in the block diagram (Fig 27) consists of a 2388-mc mixer (1N21F diode), a 10-mc IF amplifier utilizing a cascode circuit and two grounded cathode stages, and a diode detector. The purpose in using a 10-mc IF is to obtain a useful input at both signal and image frequencies and to realize a lower receiver noise temperature. The number of stages is minimized to reduce the effect of external influences on the receiver. The gain of the receiver from 2388-mc input to dc output is approximately 51 db, the 3-db bandwidth of the 10-mc amplifier is 3.5 mc, and the equivalent dual channel receiver noise temperature is about 200°K. With a liquid nitrogen cooled termination as an input source, and with a 1-second integration time, the rms thermal noise referred to the input is approximately

$$\Delta T \approx \frac{T_s}{(B\tau)^{1/2}} = \frac{200 + 78}{(3.5 \times 10^6)^{1/2}} = 0.15°\text{K}$$

For measurement of noise temperatures in the range 10 to 100°K, the system sensitivity is of that order (0.15°K). A gain fluctuation of 0.05% during an observation-calibration will appear the same at the receiver output as an input signal change of 0.15°K (0.05% of 278°K). The objective gain stability for the radiometer system is 0.02% (0.001 db). A receiver gain stability of 0.02% requires a B+ and filament voltage stability of approximately 0.005% and 0.002%, respectively. A John Fluke Model 301E power supply for the B+ has a rated stability of 0.005% per hour. Stability tests under laboratory environments show a short-term stability (minutes) of about 0.005%. A completely suitable filament supply has not yet been found. A Sorenson QR36-4A with a storage battery has been used in a temporary arrangement to supply the filament voltage (Fig 28). The filament voltage stability with and without the battery is shown in Figure 29. The short-term stability (minutes) is about 0.0003% with the battery and about 0.01% without the battery.

Evaluation of the low-noise, high-stability, 30-mc IF amplifier described in *RS 36-9* has continued. Three 30-mc matching networks (Fig 30) for the cascode input

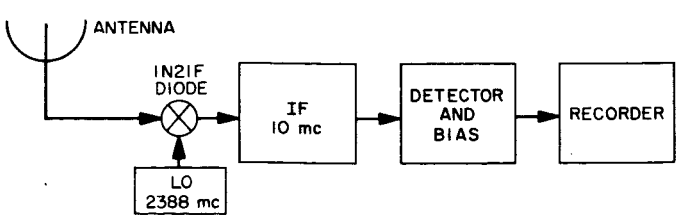

Figure 27. Noise temperature measuring 2388-mc total-power radiometer

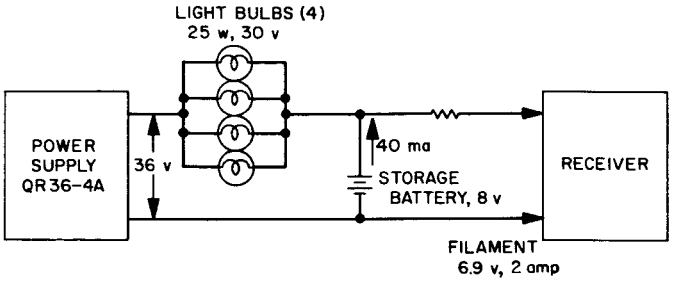

Figure 28. Storage battery regulated filament supply circuit

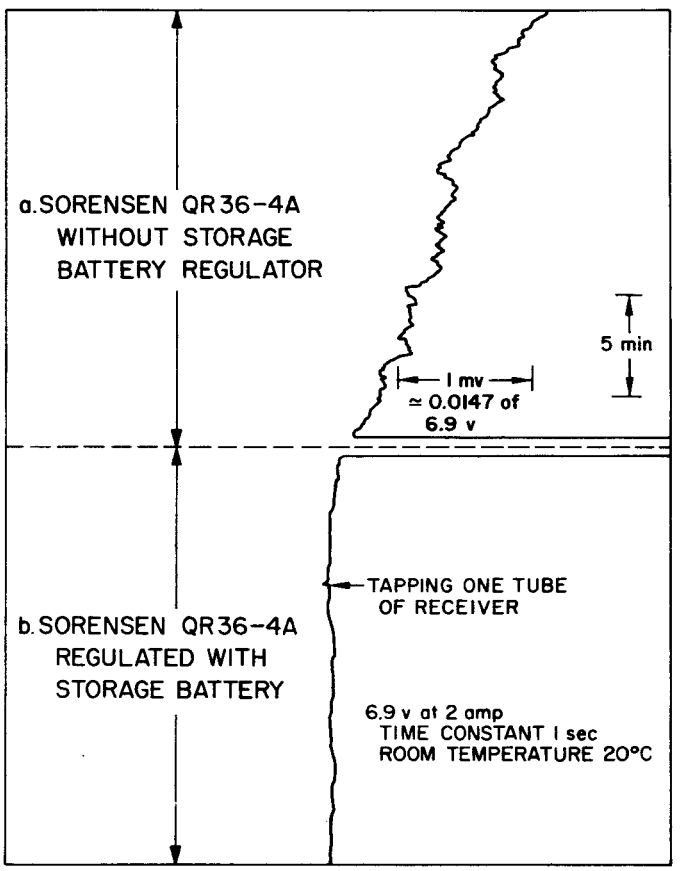

Figure 29. Filament voltage stability in the laboratory

circuit have been experimentally evaluated, matching from 50, 100, 200, and 400-ohm source impedances. The optimized values for the components for a 400-ohm source impedance are shown in Figure 30. A photograph of the T-network[a] is shown in Figure 31. The optimum

[a]The original design for the T-section was obtained from Gordon Stanley of the Radio Astronomy Dept of the California Institute of Technology.

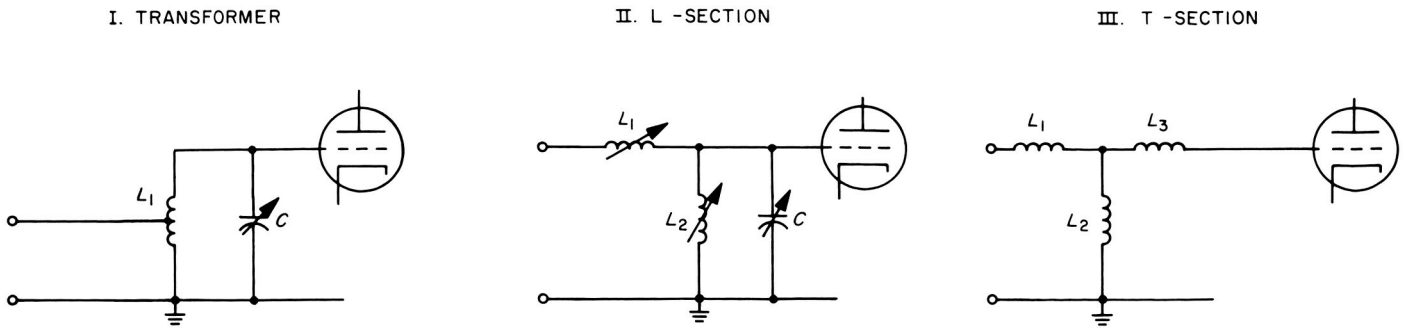

L_1 = 11.5 TURNS No. 16 TIN-PLATED WIRE, TAPPED 4.5 TURNS FROM TOP, 5/8-in. ID, 1-in. LONG
Q = 460
C_1 = 3-25 $\mu\mu$f AIR VARIABLE,
NF AT 400 Ω = 0.5-0.6 db

L_1 = 18 TURNS No. 20 TIN-PLATED WIRE, SLUG TUNED, 1-in. LONG, 0.5-in. ID, Q=240, 2.8 μh, SELF-RESONANT AT 110 mc
L_2 = 22 TURNS No. 26 ENAMEL WIRE, SLUG TUNED, 5/8-in. LONG, 3/8-in. ID, Q=245, 2.8 μh, SELF-RESONANT AT 140 mc
C_1 = VC-5
NF AT 400 Ω = 0.5 db

L_1 = 8.5 TURNS No. 14 TIN-PLATED WIRE, 15/16-in. LONG, WOUND ON 5/8-in. D POLYSTYRENE FORM, 9 TURNS PER in.
L_2=L_3 = 10 TURNS No. 14 TIN-PLATED WIRE, 1/16-in. LONG, WOUND ON 5/8-in. D POLYSTYRENE FORM, 9 TURNS PER in., Q = 420, 0.9 μh
NF AT 400 Ω = 0.5-0.6 db

Figure 30. Three types of 30-mc matching networks

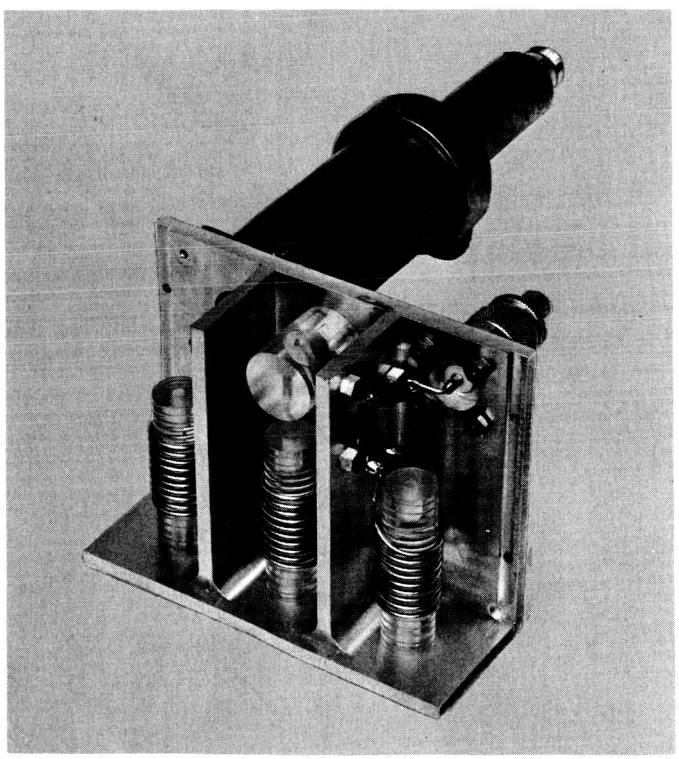

Figure 31. Experimental 30-mc T-matching network

noise figure of the 30-mc IF was typically 0.5 to 0.6 db for all networks for any source impedance.

The neutralizing network consisted of a series coil (34 turns of No. 26 enamel wire on a toroid core) and capacitor (500 μf dc blocking) between the grid and plate of the first stage. Removal of the neutralizing network increased the noise figure of the 30-mc amplifier by about 0.3 db.

The input networks for the 10- and 30-mc IF's were also optimized to a diode mixer at 960 mc. The mixer network consisted of a ¼-wavelength matching section, diode holder, LO probe, LO filter, and double-stub tuner. The best noise figures (dual channel) obtained were 2.3 db with the 10-mc amplifier and 2.5 db for the 30-mc amplifier. Similar tests with a high-quality commercial mixer and 30-mc amplifier gave a noise figure of 3.8 db. The mixer and 30-mc IF amplifier were evaluated with an AIL 30-mc precision attenuator and liquid nitrogen and ambient temperature terminations to give an absolute noise figure. An HP 340B noise figure meter was used for comparison measurements.

A parametric amplifier may be suitable for use in low-temperature instrumentation equipment. A series resonant lumped element degenerate parametric amplifier (Ref 31) has been constructed to operate at 960 mc with a Hughes Type 2810 germanium varactor. Because the varactor diode inductance is in series with the circuit inductance (Fig 32), it does not deteriorate performance as in a parallel configuration. Figure 33 shows a photograph of the amplifier. The diode is matched to the circulator for proper gain with the ¼-wavelength section at the bottom of the photograph. The pump is applied through the probe shown to the right. The bias is applied

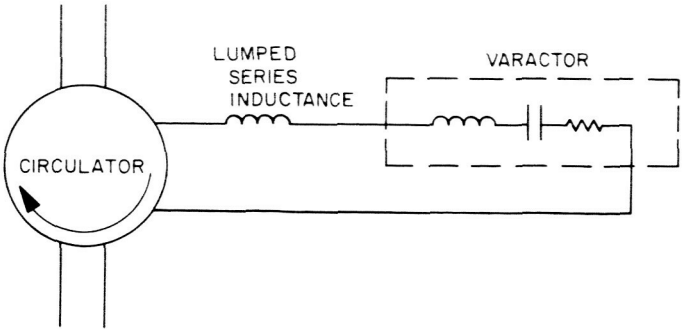

Figure 32. Series resonant degenerate parametric amplifier

at the top to an RF shorted block. The required series inductance is obtained by movement of the block. At 10-db gain, the bandwidth is 130 mc. With 15 db of paramp gain, the system temperature measured using a 1000°K followup mixer was 63°K. The contribution of the paramp to the system noise temperature was less than 20°K.

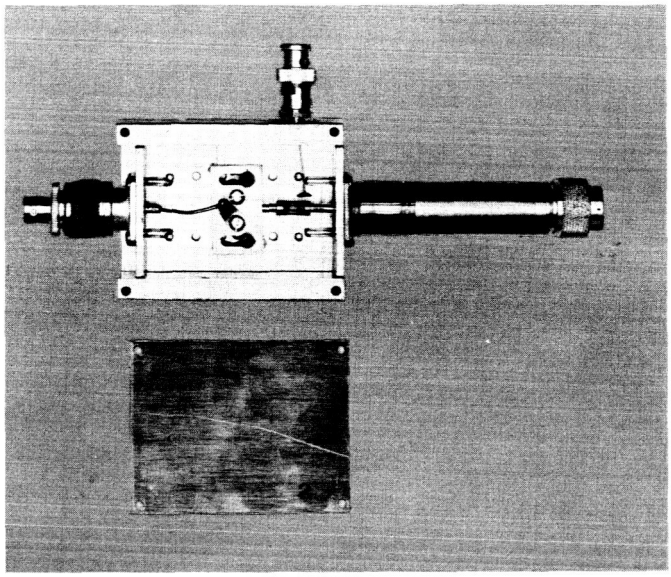

Figure 33. Series resonant 960-mc degenerate parametric amplifier

B. Antennas for Space Communication

P. D. Potter and W. V. Rusch

1. Antenna Feed Research

a. Introduction. Large paraboloidal reflector ground antennas are used widely in space communications and radio/radar astronomy. The need to obtain maximum performance from the expensive instruments lends new importance to the problem of optimum feed system design. For receiving applications where the critical system criterion is signal-to-noise ratio, a figure of merit for the antenna system, defined as the ratio of the antenna effective area to the receiving system noise temperature is a useful concept. Since a significant contribution to system noise may be introduced by the antenna, an optimum feed system would not only result in very high aperture efficiency but would also result in very low effective antenna noise temperature.

At the Jet Propulsion Laboratory, a program exists to develop practical feed systems which realize a close approximation to the optimum. Also, work is being carried out on an 85-foot paraboloid at the Goldstone Tracking Station to develop improved techniques for measurement of both aperture efficiency (i.e., gain) and effective antenna noise temperature.

b. Cassegrain feed system studies. It appears that a Cassegrain feed system may be designed to produce a relatively low effective antenna noise temperature, while at the same time providing a relatively high aperture efficiency.

The basic properties of the Cassegrain system were described in *RS* 36-9. The major problem in Cassegrain design is that of efficiently illuminating the hyperboloidal subreflector. A compromise must be made between the interrelated problems of uniform subreflector illumination and spillover around the subreflector. Not only is the aperture efficiency affected by this compromise, but also the antenna system forward side-lobe level is drastically affected by the subreflector spillover.

An experimental program is in progress at JPL to derive suitable feeds for Cassegrain systems with the object of producing more uniform subreflector illumination and lower spillover than is normally achieved with a conventional circular or rectangular horn. Modified horn and shaped reflector type antennas are being considered.

As a preliminary experiment in the use of shaped reflectors, a reflector of revolution with a diameter of 20 wavelengths was designed using optical synthesis techniques to produce a sector beam 27.6 degrees wide. An illumination taper of 10 db was used to illuminate the shaped reflector. Measured E- and H-plane patterns of this antenna are shown in Figure 34. It can be seen from

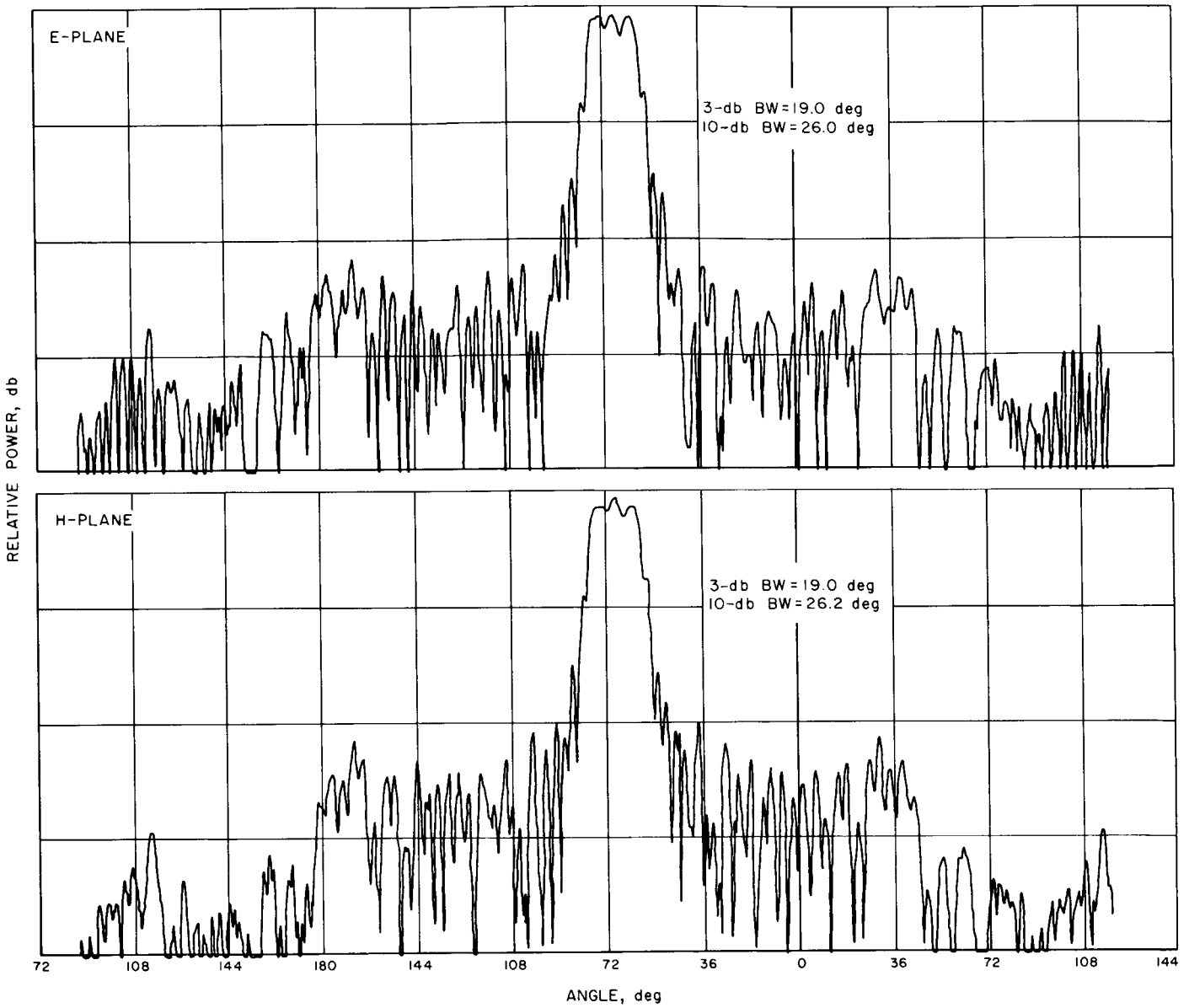

Figure 34. Shaped reflector rectangular E- and H-plane patterns

these patterns that the measured 10-db beamwidth of 26.0 degrees is very close to the design value of 27.6 degrees. Although the wide-angle sidelobe structure is below the isotropic level (the pattern directivity is approximately 22 db) it is believed that considerable improvement can be achieved. As an experiment, the shaped reflector was replaced with microwave absorber. Patterns taken of this configuration indicate that most of the high wide-angle sidelobe level is produced by spurious radiation from the illuminating horn. Improved feed horn designs are now being investigated.

The sectorial nature of the shaped-reflector antenna is clearly shown by the E- and H-plane polar patterns in Figure 35. The measured phase deviation associated with the amplitude ripples was found to be negligible. The measured phase center of the antenna was very near the point predicted by the optical synthesis procedure used in the design.

To estimate the performance of the shaped reflector in a Cassegrain system, geometrical optics were used to calculate a subreflector radiation pattern for the subreflector

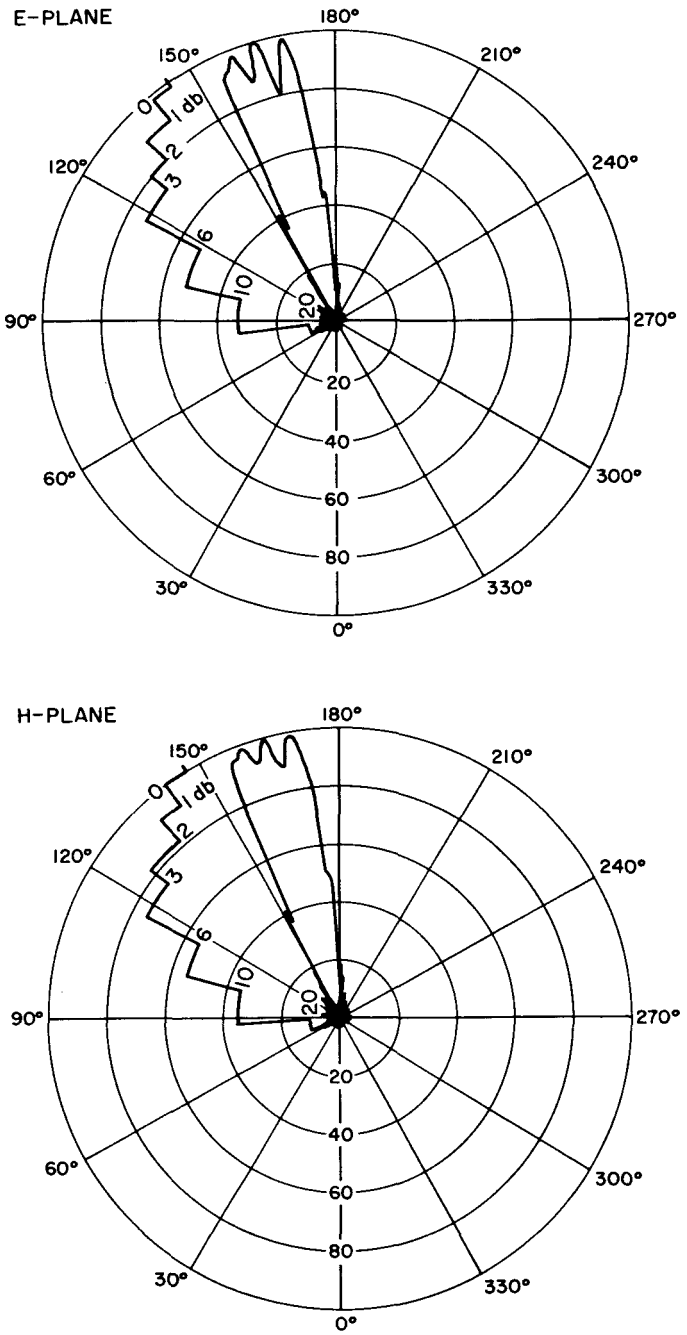

Figure 35. Shaped reflector polar E- and H-plane patterns

illuminated by the patterns shown in Figures 34 and 35. A dish half-aperture angle of 61 degrees and a magnification factor of 5 were assumed. The calculated subreflector pattern is shown in Figure 36. Graphical integration of this pattern indicates an overall antenna efficiency of 85%. Further experimental work with this type of antenna is in progress.

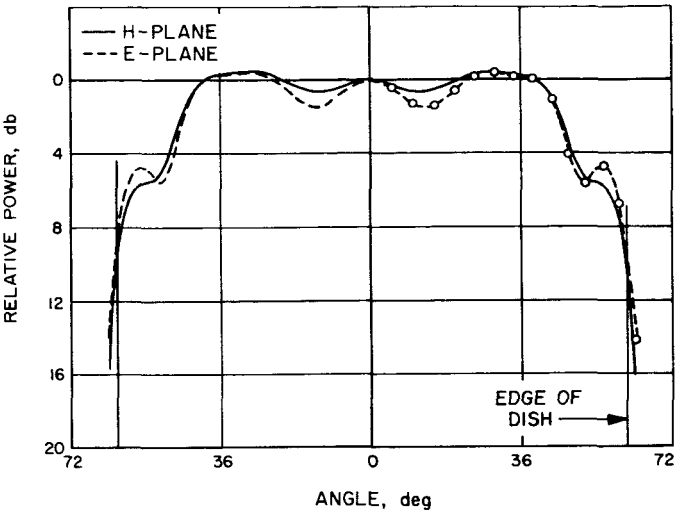

Figure 36. Predicted dish illumination patterns

The geometrical parameters of the Cassegrain system are shown in Figure 37. The hyperbola is characterized by the two focal points F and F', which are in turn determined by the parameters a and c. The point F is normally made to coincide with the focal point of the paraboloid, and the point F' is made to coincide with the feed phase center. In a practical system, however, it is not always possible to axially locate the feed phase center at F'. This problem may arise due to physical constraints, operational frequency changes, or feed modifications. In this case, however, it is possible to relocate the hyperboloid along its axis to partially compensate the feed defocusing error. It is useful to have analytical relations which predict approximately the necessary hyperboloid relocation to compensate the feed defocusing, as well as an indication of the degree of compensation possible. Using the coordinates and parameters defined in Figure 37, the equation of the hyperbola is given by:

$$\frac{x^2}{a^2} - \frac{y^2}{c^2 - a^2} = 1 \qquad (1)$$

From Equation (1), the physical shape of the curve is given by

$$x - a = a\left[\left(\frac{y^2}{c^2 - a^2} + 1\right)^{1/2} - 1\right] \qquad (2)$$

If the system is defocused, i.e., x, a, and c are changed to new values x_1, a_1, and c_1; and the curve shape, $x - a$, is held constant, it is clear that Equation (2) will not be

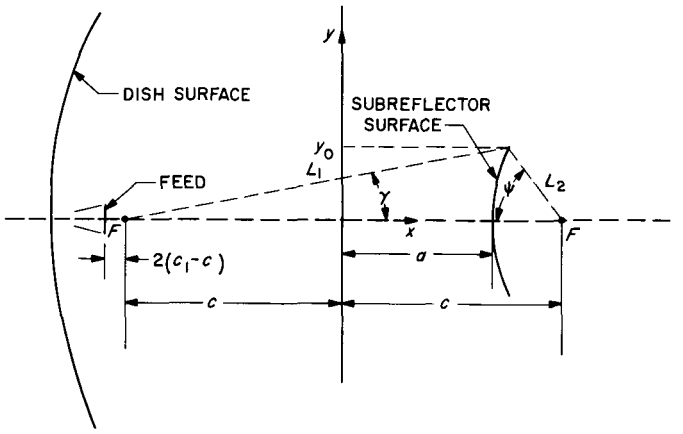

Figure 37. Cassegrain geometry

satisfied for all values of y. Therefore, perfect compensation is not possible. It is interesting, however, to investigate the geometrical path length deviation as a function of y with the system perfectly compensated at $y = 0$ and $y = y_0$. To do this, the following equation must be solved for a, as a function of a, c, c_1, and y_0:

$$a_1\left[\left(\frac{y_0^2}{c_1^2 - a_1^2} + 1\right)^{1/2} - 1\right] = a\left[\left(\frac{y_0^2}{c^2 - a^2} + 1\right)^{1/2} - 1\right] \qquad (3)$$

Although Equation (3) can be expressed as a cubic equation and solved exactly, it is generally more expeditious to use an approximate solution followed by numerical iteration. An approximate solution to Equation (3) which is generally accurate within 1% is given by:

$$a_1 = \frac{-\frac{c^2 - a^2}{a} + \left[\left(\frac{c^2 - a^2}{a}\right)^2 + 4c_1^2\right]^{1/2}}{2} \qquad (4)$$

A typical specific example was evaluated numerically. The assumed parameters and results are given in Table 9. With reference to Figure 37, it can be seen that a net path length error, given by $(L_2 - L_1) - 2a$, will result in the defocused system. A plot of this error for the numerical example in Table 9 is shown in Figure 38. Phase front data taken on a scale model of the system in the numerical example above has qualitatively confirmed the negligible effect predicted by Figure 38. More refined phase front measurements are in progress.

Table 9. Numerical example

Parameter	Original value	Defocused value
Focal length— $2c \cdot 2c_1$	228.000 in. = 19.000 ft	324.000 in. = 27.000 ft
Horn defocusing, $2(c_1 - c)$	0	96.000 in. = 8.000 ft
Hyperboloid curve	Same	Same
a	75.267 in.	—
a_1	—	Approx solution: 120.462 in. Exact solution: 119.565 in. Approx error: 0.897 in.
φ (Fig 37)	60.000 deg	56.798 deg
γ (Fig 37)	13.476 deg	9.316 deg
Hyperboloid defocusing	0	3.702 in.
Ratio of horn to hyperboloid defocusing	—	25.932

2. *Analysis of Paraboloidal Reflector with Axial Dipole Feed*

a. Introduction. The current-distribution method of vector diffraction theory (Ref 32) is being employed in the analysis of low-noise reflector-type antennas. (Refer to *RS 36-8*, Vol I, pp 35–39, for a report of previous work.) This method is being used because it includes the longitudinal components of current which contribute to wide-angle radiation. However, due to computational problems it is only feasible to obtain numerical results for antenna gain and equivalent noise temperature from the current-distribution method when the entire antenna geometry is assumed to be a figure of revolution. Although the reflectors themselves are usually surfaces of revolution, the directivity pattern of the primary feed is seldom axially symmetric. Furthermore, even if that condition is

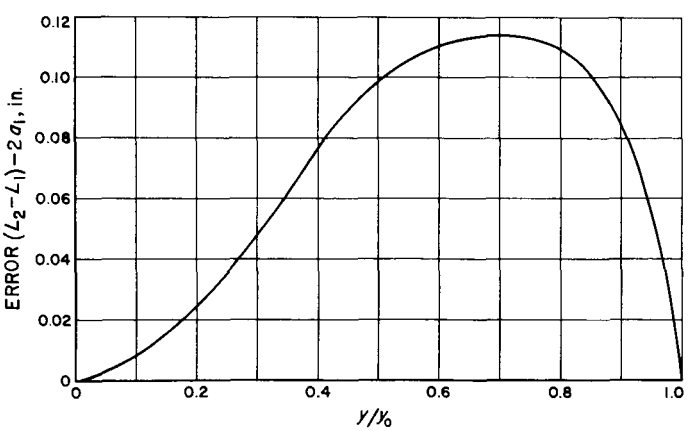

Figure 38. Path length error

realized, cross-polarization effects lead to an asymmetric secondary pattern.

To provide a configuration which is amenable both to analysis with the surface-current integral and verification by experiment, a paraboloidal reflector with axial-dipole feed has been selected. This geometry is impractical for the requirements of deep space communication since it produces an axial null; however, it appears to be well suited for the purpose of the present investigation, which is to provide more knowledge of the various diffraction and interference effects in reflector-type antennas.

b. Derivation of scattered field. A linear dipole is placed at the focus of a paraboloid of revolution and oriented along the axis (Fig 39). The primary radiation field of this linear source is

$$\overline{E_d} = AP(\theta)\frac{e^{ikR}}{R}\bar{a}_\theta \tag{1}$$

where $\overline{a_\theta}$ is a unit vector in the θ-direction. For very thin, resonant dipoles the primary directivity pattern is

$$P(\theta) = \frac{\cos\left(\frac{M\pi}{2}\cos\theta\right)}{\sin\theta} \qquad M = 1, 3, 5, \cdots \tag{2}$$

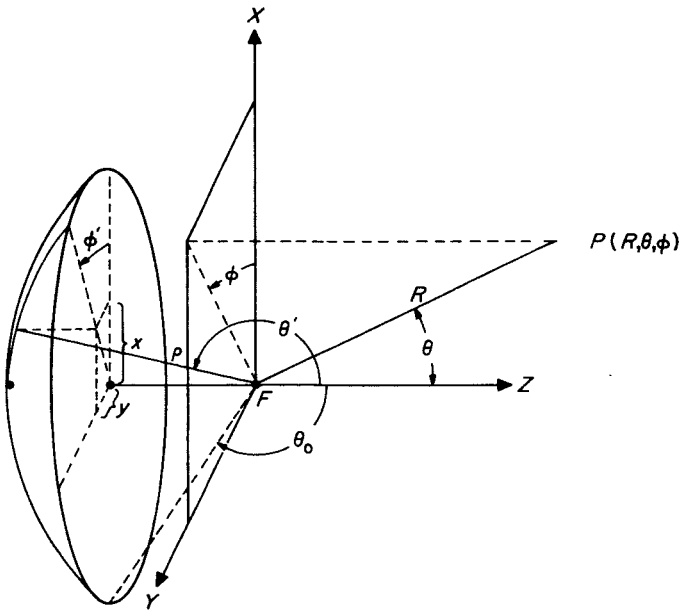

Figure 39. Geometry of antenna

Using the surface-current integral, it is possible to show that the azimuthal-component of the scattered field ($E_{\phi s}$) is identically zero, and the 0-component of the scattered field is

$$E_{\theta s} = i\alpha\beta A\frac{e^{ikR}}{R}e^{i\alpha\beta\cos^2(\theta/2)} \times \int_{\theta_0}^{\pi} e^{i\alpha\beta\sin^2(\theta/2)\cot^2(\theta'/2)}F(\theta,\theta')\,d\theta' \tag{3}$$

where

$$\alpha = \pi\left(\frac{D}{\lambda}\right), \tag{3a}$$

$$\beta = 4\left(\frac{f}{D}\right) \tag{3b}$$

and

$$F(\theta,\theta') = P(\theta')\cot\left(\frac{\theta}{2}\right)\left\{\sin\theta\cot\left(\frac{\theta'}{2}\right)J_0\left[\alpha\beta\sin\theta\cot\left(\frac{\theta'}{2}\right)\right] + i\cos\theta\,J_1\left[\alpha\beta\sin\theta\cot\left(\frac{\theta'}{2}\right)\right]\right\} \tag{3c}$$

The total radiation field is then obtained by superposition of the fields from Equations (1) and (8); for $R >> \lambda$,

$$\overline{E} = \left[AP(\theta)\frac{e^{ikR}}{R} + E_{\theta s}\right]\overline{A_\theta} \tag{4}$$

c. Calculation of scattered field. Numerical results of the absolute gain function for a $\lambda/2$-resonant dipole primary feed are plotted in Figure 40. The integrals have been evaluated for a relatively shallow dish ($\theta_0 \simeq 120$ deg). Figure 40b results from $(\alpha\beta) = 140.5\pi$, which corresponds to a Goldstone Station 85-foot antenna operating at 960 mc. Because of the perfect axial symmetry, the radiation pattern is a figure of revolution, and the main beam is "hollow." In the region between a few degrees and 120 degrees, the primary pattern is easily recognizable. Because the reflector is shallow, there is considerable spill-over and the primary radiation clearly dominates the reflected radiation at wide angles. Between 120 degrees and 180 degrees (the shadow region), diffraction effects produce a highly oscillatory but relatively small field.

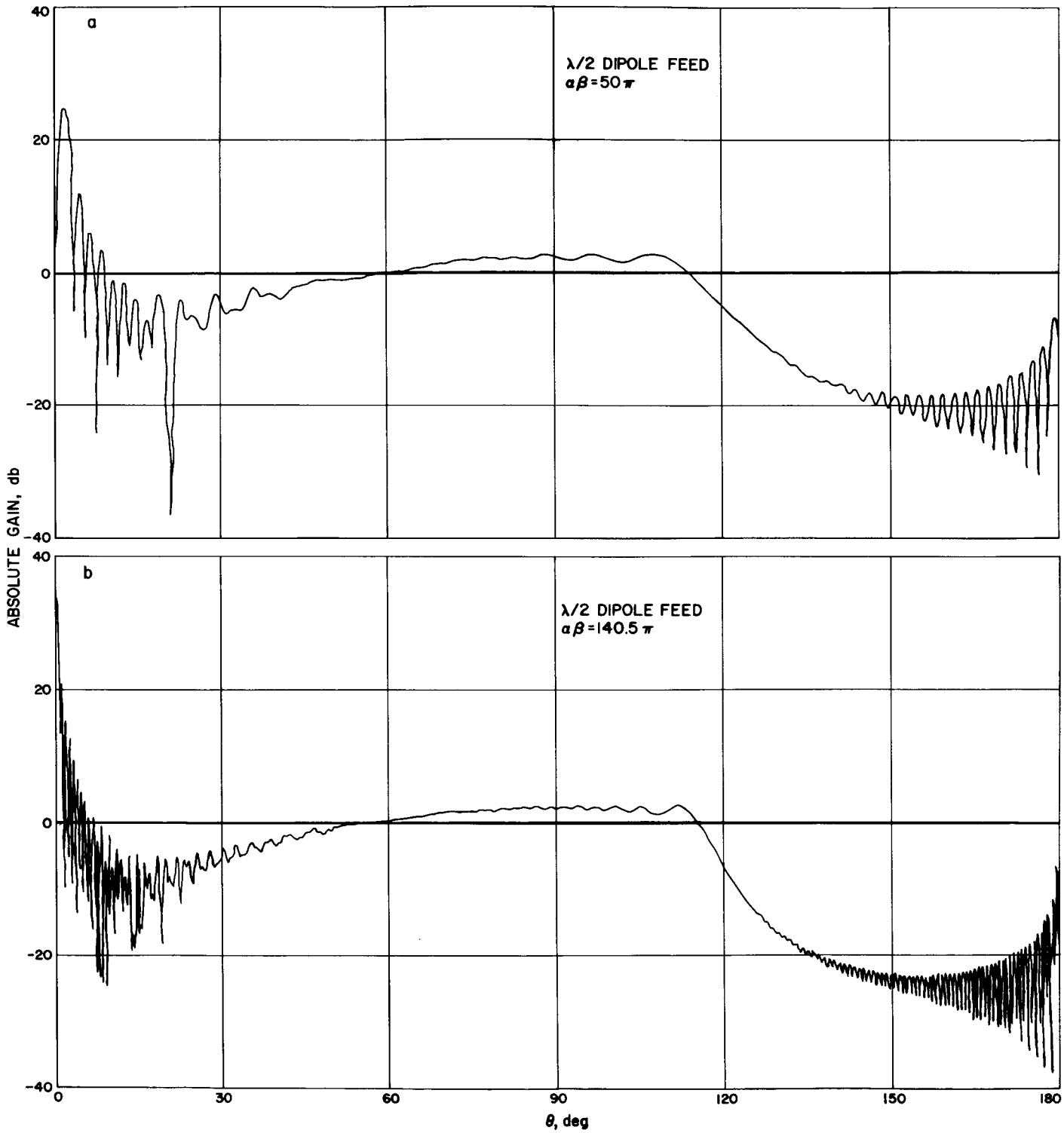

Figure 40. Absolute gain vs angle for axial λ/2 dipole feed, $\alpha\beta = 50\pi$ and 140.5π

C. Thin-Film Techniques

W. H. Higa, R. E. Brantner, R. E. Frazer, J. Maserjian, and H. Erpenbach

1. Superconductive Mixers

In modern microwave receiving systems, the conventional mixers because of their noisiness are preceded by rather complex maser and/or parametric amplifiers. It has been suggested that accomplishing the mixing operation at cryogenic temperatures could drastically reduce the noise contribution of a mixer. To investigate this possibility, experiments are being conducted in mixing action by utilization of superconducting phenomena. Three effects are being studied: The first is the Meissner effect, the property that a superconductor excludes all magnetic flux from its bulk. The second effect is the destruction of superconductivity by an electric current of sufficient magnitude flowing through the material. The third effect is allied with the second; it is the destruction of superconductivity by an external magnetic field of sufficient strength.

In a set of preliminary tests using the Meissner effect, thin sheets (0.005 to 0.010 in.) of tantalum, vanadium, and niobium were inserted singly between a pair of coils, and the assembly was immersed in liquid helium. A low-level signal applied to the input coil was coupled weakly to the output coil in the absence of a magnetic field of critical strength; when a magnetic field of critical strength was applied, close coupling was obtained. In the absence of an external magnetic field, large input signal power produced close coupling. An unexpected result of the latter test was the generation of strong harmonics of the input frequency, with the amplitude of the fundamental decreasing radically under certain conditions of signal power and frequency. Further tests of this effect are being performed.

To produce high-frequency mixers, two types of elements are being tested. Their operation is based on the second and third superconductive effects mentioned above. One type is made of tantalum wire with diameters from 1 to 5 mils. Several of these wire elements have been constructed, and some have exhibited superconductive properties. It was found that the tantalum wire used in these elements must be out-gassed by heating to incandescence in a vacuum in order to assure superconductive properties. None of the wire elements have been successfully operated as mixers. The other type of element consists of a thin film of tantalum, ranging from 400 to 20,000 angstrom units thick, deposited on a sapphire substrate. None of the thin film units produced thus far have exhibited superconductive properties.

2. Advanced Digital Techniques

The JPL research activity in coding and space communications includes a study of thin film techniques as applied to advanced digital communication concepts. The objective of the present effort is to design a switching matrix to implement boolean algebraic processes. The basic element of such networks is a single-pole double-throw "switch" capable of operation in excess of 1 mc. To perform the desired range of operations, a branching array terminating in up to 2^{10} (1024) such switch elements is required.

Switching using light (photon) energy as a coupling agent between signalling device and switched element is particularly interesting for two reasons: (1) The source and receptor can be physically separated by the use of imaging optics or an array or bundle of fibre optics. (2) Cross coupling from interelement capacitance is eliminated even at high pulse rates. The difficult problem is producing rapid pulses of sufficient energy to activate a detector after transmission through the optical system.

One photon source capable of the necessary pulse operation is the back-biased junction in a silicon diode. In the typical configuration the light generated during avalanche breakdown is reabsorbed before it can escape from the bulk of the material normal to the junction. However, where the junction intersects a surface, as in a planar transistor structure, the emission appears as a ring of light in the plane of the surface. Such junctions have been driven at rates up to 1 mc, and the emission monitored with an electron multiplier phototube. The phototube output faithfully tracks the driving signal up to about 100 kc; the limits imposed by the inductance of the silicon slice and the contacting probe distort the response at higher frequencies. When driven with a mercury relay pulser yielding very sharp pulses at a 1-kmc rate, the present configuration yields an initial pulse of about 5 nanosec followed by a damped ringing lasting about 10 nanosec.

Investigation of possible switching elements will be continued. A new wafer support and probe are being built to minimize inductive effects and include the junction as part of a coaxial cavity.

3. Single-Crystal Films

The investigation of microzone growing of single-crystal films has continued (*RS 36-4* to *36-9*, Ref 33). Since the last report period, the microzone-melting exper-

iments have used controlled scanning of the electron beam. For this purpose a deflection coil was introduced into the electron beam apparatus, which is now functioning properly. Some preliminary results have been obtained from these experiments with germanium films.

The electron beam has been scanned several mils in a sinusoidal manner at frequencies ranging from 0.1 to 1200 cps. Simultaneously, the specimen is moved in a transverse direction so that the oscillating path overlaps and a continuous microzone-melted region occurs. Figure 41a shows a region of a 15-micron germanium film scanned at 0.5 cps with 12.5 mils peak-to-peak deflection. This corresponds to a zone velocity of 25 mils/sec compared to the traversed rate of 0.6 mil/sec. A striking difference in the texture is obvious between the scanned region (at the right) and the path occurring with the scanning turned off (at the left). It has been determined that this is a consequence of the difference in zone velocities and not the seeding effect of the adjacent film.

Similar appearances occur at higher scanning frequencies except for the closer spacing of the overlapping zone edges which are barely observable under the oblique illumination used. Figure 41b shows a film grown with a scanning rate of 120 cps. A slight mounding of the scanned region is believed due to the elongation of the zone with increased velocity. This becomes severe at still higher frequencies and appears to affect the growth process as evidenced by a fine mosaic structure at the surface. Figure 41c shows this structure on a region scanned at 960 cps.

Since the above samples were made with a germanium film 15 microns thick, the zone diameter of 25 microns (1 mil) is reasonable. In fact, because of thermal conduction laterally along the film, a lower practical limit in zone size is of the order of the film thickness. The underlying sapphire substrate was polished with 3 μ diamond grit which gave a sufficiently rough surface to affect the smoothness of the germanium film.

Another sample was prepared with a 4-micron thick germanium film which had been evaporated on a No. 320 ground sapphire finish, resulting in a very rough surface. The results, however, were very consistent with those above, indicating that the surface uniformity has no obvious effect on the growth process. An interesting additional result was achieved when the zone size was increased to over 2 mils. The growth in the scanned region shows serrated bands looking very much like 111 oriented dendrites (Fig 42a). The serrations are probably grain boundaries separating the dendrites and appear to follow definite planes perpendicular to the surface.

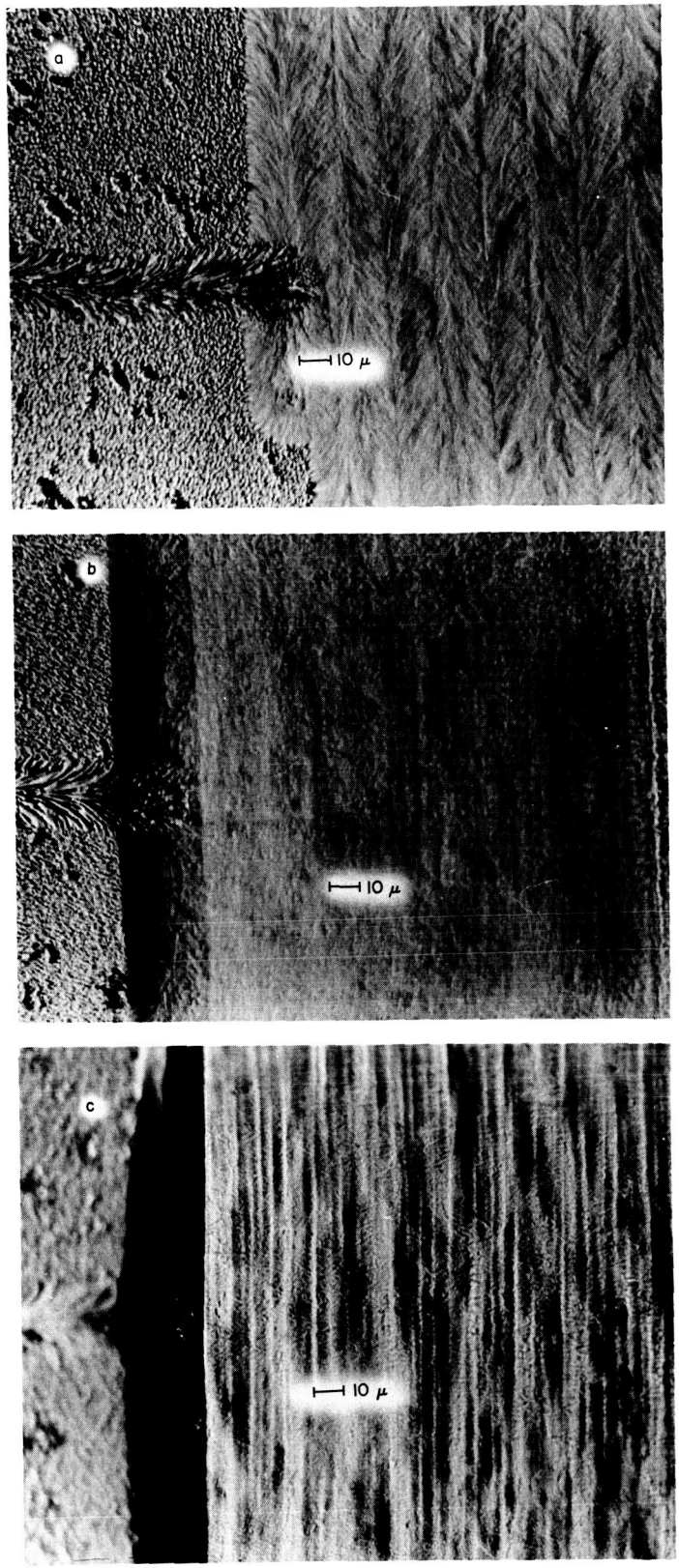

Figure 41. Microzone-melted Ge film scanned with 1-mil zone at various rates

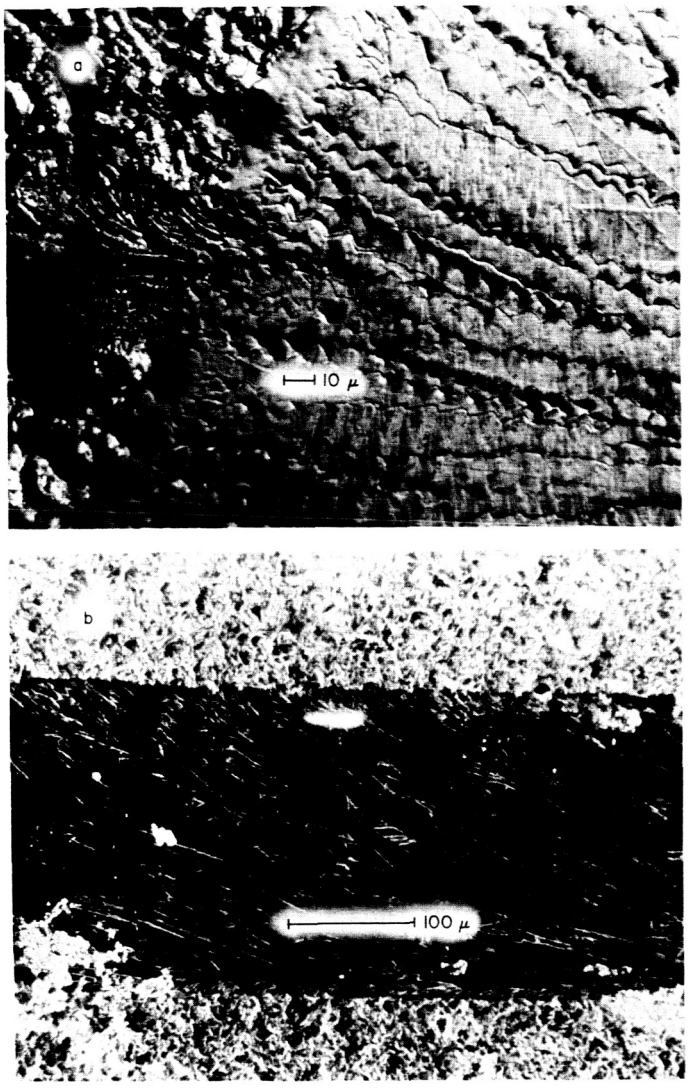

Figure 42. Microzone-melted Ge film scanned with large zone (>2 mils), also shown in dark field after etch

Etching studies of this sample reveal all the scanned regions including the dendrites to be 111 oriented along the surface. Figure 42b shows an etched (WAg) region under dark field. This region had been scanned at 10 cps with a 1-mil zone and clearly reveals the 111 planes with steps separating different levels. The rough-textured areas on the scanned region are deposits left by the etching process. Similar results are obtained with other scanned regions except that the slower scans give less flatness, revealed by a larger number of steps.

The results obtained thus far continue to be encouraging. Future work will involve more etching studies of regions scanned under different conditions. Samples will again be prepared on fire-polished sapphire substrates since the orienting influence of the underlying substrate seems less important with the use of scanning, and a smooth flat surface is highly desirable. Future plans involve electrical tests of the films which, however, await further work on the etching technique.

4. Superconducting Thin Films

Work is continuing on the techniques for producing superconducting thin films. (See *RS 36-7* to *36-9* for past work.) Attempts have been made to deposit thin films of tantalum by sublimation onto sapphire substrates. Two tantalum film samples have been produced, but tests for superconductivity were negative.

The high vapor pressure of tantalum at 10^{-6} mm Hg vacuum makes it extremely difficult to obtain the rate of evaporation necessary for pure deposits by sublimation. The vapor pressure and evaporation rates of tantalum (Ref 34) are given in Table 10. Figure 43 shows the partial pressure curve of tantalum, with those of tungsten, niobium (Ref 35), and molybdenum for comparison.

Electron beam evaporation will be used in the next attempt to deposit superconducting tantalum thin films; this method has been successfully used at JPL to produce superconducting niobium thin films.

Table 10. Vapor pressure and evaporation rates of tantalum

Vapor pressure, mm Hg	1×10^{-5}	1×10^{-4}	1×10^{-3}
Temperature, °C	2407	2599	2820
Rate of evaporation, gm/cm²/sec	1.55×10^{-7}	1.48×10^{-6}	1.41×10^{-5}
Vapor pressure at melting point, 5×10^{-3} mm Hg; vapor pressure at 1737°C, 9.5×10^{-11} mm Hg.			

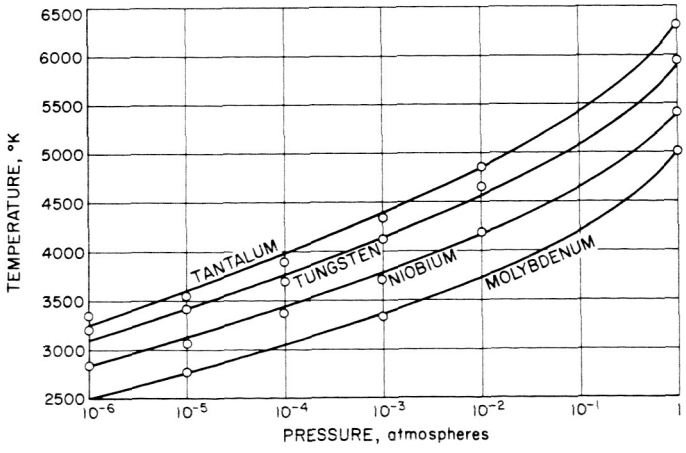

Figure 43. Partial pressures of tantalum, tungsten, niobium, and molybdenum

VI. Communication System Development

Communications Analysis

C. Gilchriest and J. C. Springett

1. Pseudonoise System Lock-In

An analog-computer simulation program to determine the lock-in characteristics of pseudonoise (PN) systems was described in *RS 36-9* (pp 51–54). That discussion indicated an additional area which should be studied before complete knowledge was obtained on PN system synchronization. That area was the operation of the pseudonoise system lock-in near unstable points.

Figure 44 shows a block diagram of the essential elements of the system being considered. In determining the lock-in characteristics, the error function of the loop (output of the second multiplier of the receiver section) must be known. Its characteristics are a function of the specific mechanization and will be discussed with greater detail in Section 2, entitled Pseudonoise System Cross Correlation Functions.

In *RS 36-9*, two mechanizations were considered: the second multiplier signal channel inputs were designated as Case I, for sine wave inputs (possibly a limiter followed by a band-pass filter), and Case II, for square wave inputs (possibly a limiter only). These two cases assume that code switching (*RS 36-6*, Vol 1, and Sec 3) is used. Although code switching is necessary in the practical case, as will be shown, the analog-computer simulation program was continued in order to put arguments pro and con on a sound footing. The areas investigated were the unstable (sometimes referred to as quasi-stable)

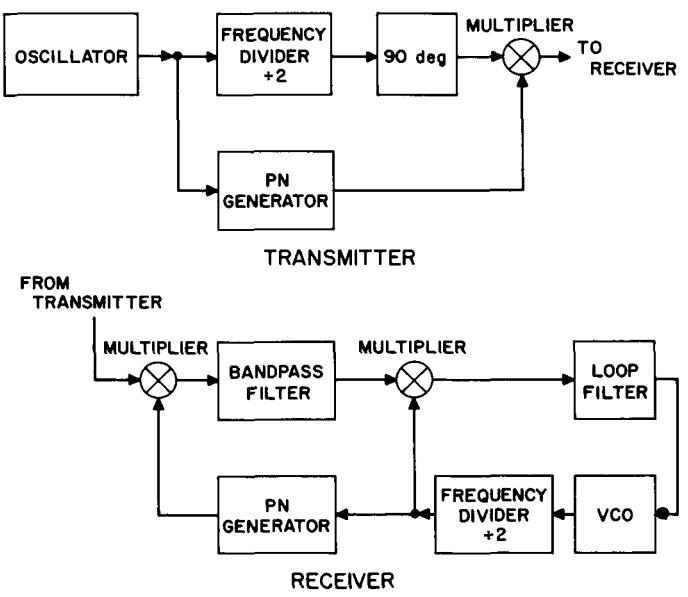

Figure 44. Basic PN synchronization system

points. These are here referred to as Cases III and IV. Case III considers sine wave inputs (possibly a limiter followed by a band-pass filter) near the unstable points, and Case IV considers square wave inputs (possibly a limiter only) near the unstable points. The error functions for these mechanizations are shown in Figures 45 and 46. Figure 45 illustrates the facts that (1) in between the S-curves the gain is essentially zero and (2) the polarities of the S-curves alternate sequentially. The S-curves whose central part has a positive slope are referred to as stable points, and those whose central part has a negative slope are referred to as unstable points. Code switching yields a system which has only stable points.

The equivalent system simulated is shown in Figure 47. To investigate stable points, the sign of $N(\varepsilon)$ will be positive; and to investigate unstable points, the sign of $N(\varepsilon)$ will be negative. It should be noted that the variables to be plotted are θ_0 and $\dot{\theta}_0$, which are the familiar phase plane plots (Ref 36). Phase plane plots are much more useful than time plots since the lock-in time is determined largely by the probability of being at any particular θ_0, when lock-in is initiated, and by $\dot{\theta}_0$. The values of K were chosen as indicated because a system would normally be designed so that the bandwidth and transfer function were specified near threshold where the suppression factor α, due to a bandpass limiter, would be less than 1 (K is taken as 1 at this value of α). At high S/N, the gain K would then be larger and the system should be studied under these circumstances. On the other hand, the small-gain S-curves between the wanted lock-in points should also be studied; hence, the small values of K. K is taken only between 0.1 and 10 since the simulation problem becomes more difficult for a wider range of values, and yet the values are sufficient to determine an empirical law for estimations.

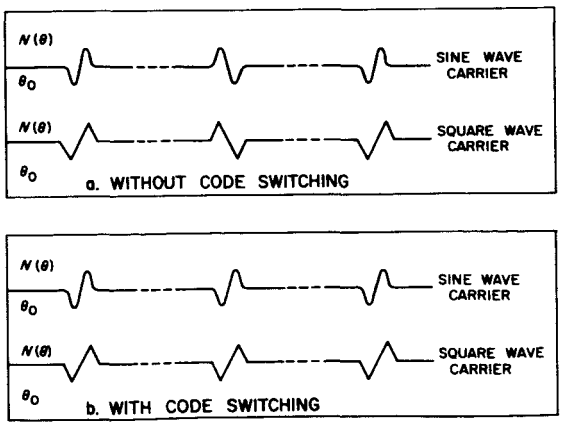

Figure 45. Pseudonoise system error functions without and with code switching

Figure 48 shows the phase plane plot (Ref 36) for Case III for $K = 1$ (about an unstable point). For a particular large value of $|\dot{\theta}_i(0)/B_0|$ it should be noticed that the plane is traversed from one side to the other and that the value upon reaching the other side is $< |\dot{\theta}_i(0)/B_0|$. If on the other hand, the value of $|\dot{\theta}_i(0)/B_0|$ is less than some critical value, the trajectory curves around and is finally rejected out the same side with a velocity of the opposite sign of that which it entered. Note that in Cases I and III the critical value of $\dot{\theta}_0/B_0$ near the stable points is slightly larger than the

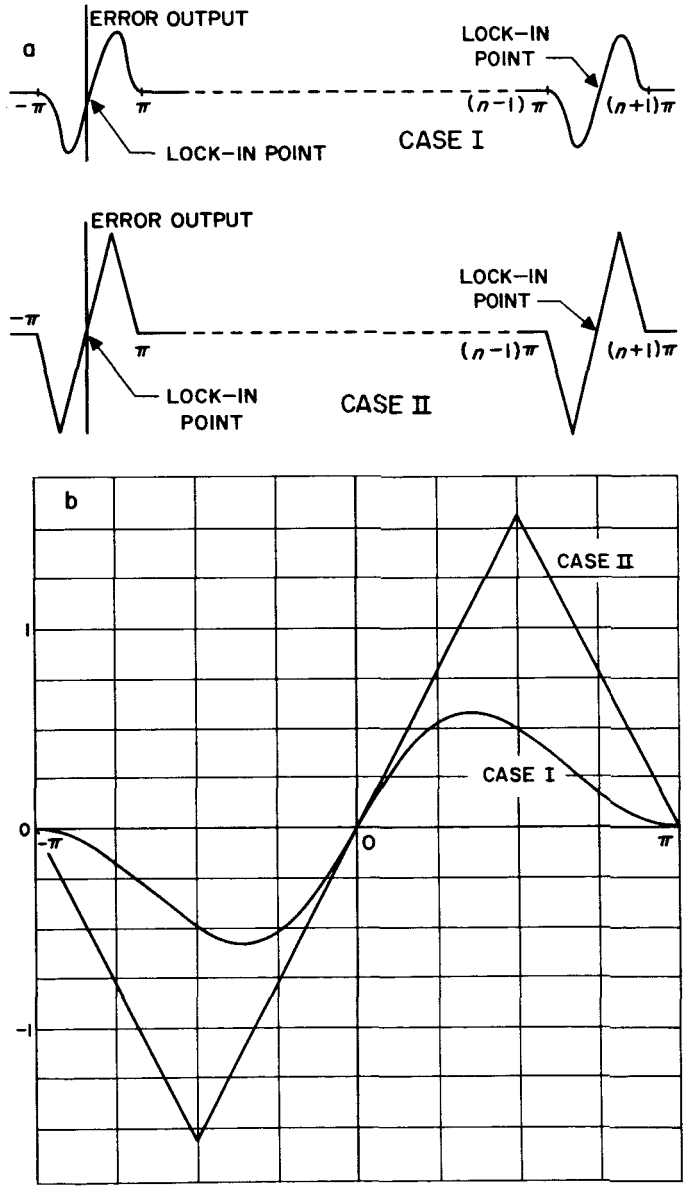

Figure 46. Pseudonoise system error functions near stable points

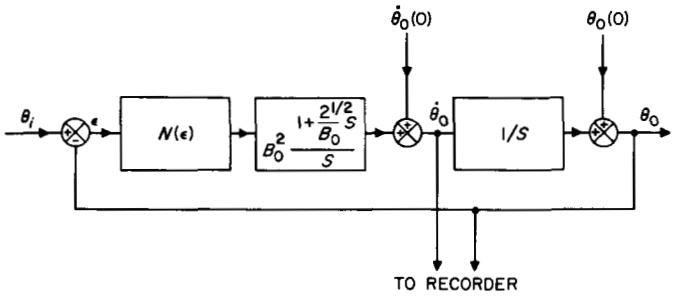

CASE I

$N(\epsilon)=K0,\ \epsilon<-\pi$

$=\frac{K}{\pi}(\epsilon+\pi)\sin\epsilon,\ -\pi\le\epsilon\le0$

$=-\frac{K}{\pi}(\epsilon-\pi)\sin\epsilon,\ 0\le\epsilon\le\pi$

$=K0,\ \pi<\epsilon$

CASE II

$N(\epsilon)=K0,\ \epsilon<-\pi$

$=-K(\epsilon+\pi),\ -\pi\le\epsilon\le-\frac{\pi}{2}$

$=K\epsilon,\ -\frac{\pi}{2}\le\epsilon\le\frac{\pi}{2}$

$=-K(\epsilon-\pi),\ \frac{\pi}{2}\le\epsilon\le\pi$

$=K0,\ \epsilon>\pi$

WHERE $K=10,\ (10)^{2/3},\ (10)^{1/3},\ 1,\ (1/10)^{2/3},\ (1/10)^{1/3},\ 1/10$ A GAIN FACTOR

$\theta_0(0)=-\pi$ WHEN $\dot\theta_0>0$

$\theta_0(0)=\pi$ WHEN $\dot\theta_0<0$

$\theta_i=0$

Figure 47. Pseudonoise system simulation

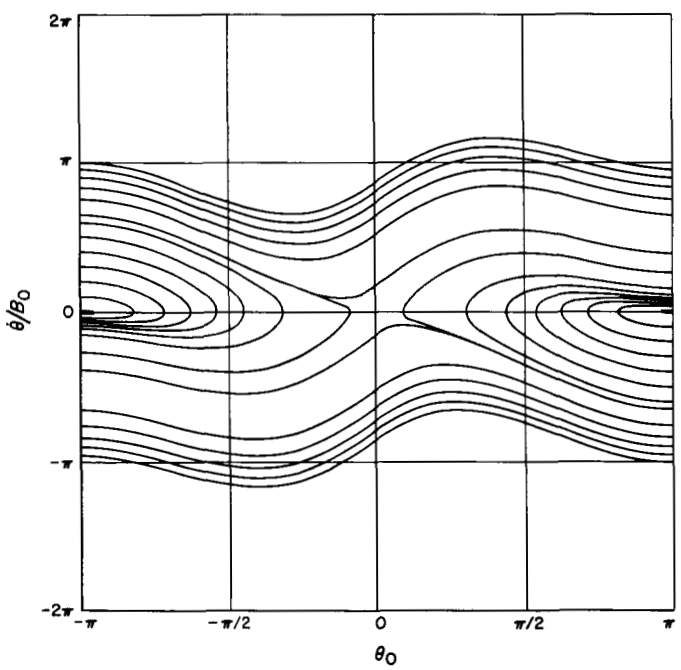

Figure 48. Phase plane plot, unity gain, Case III

critical value $\dot\theta_0/B_0$ near the unstable points, thus leaving a small range of values of $\dot\theta_0/B_0$ for which the system would lock up on first passage of a stable point without having reversed direction. It is important not to reverse direction, even though the system would lock up on the passage of the next stable point, because the velocity on being rejected from near an unstable point is so much smaller that the time to traverse between the unstable and the stable points would be large.

Figure 49 shows only the critical values (obtained by changing the sign of integrators of the computer and running backward from $\dot\theta_0/B_0 = 0 + \delta$ (δ = a small value > 0) for various gains (Case III). This emphasizes the fact that even though a small range of values between the critical values of the stable and unstable points exist a slight change in gain K (or equivalent suppression factor) can alter this situation. Similar remarks can be made on Case IV, whose results are shown in Figures 50 and 51. Typical lock-in operation is shown in Figure 52 and a summary of the information from Figures 48 through 51 is given in Figure 53.

In summary, it can be said that systems which have only stable points will lock in much faster and are much more predictable with varying signal-to-noise ratios than are systems containing both stable and unstable points.

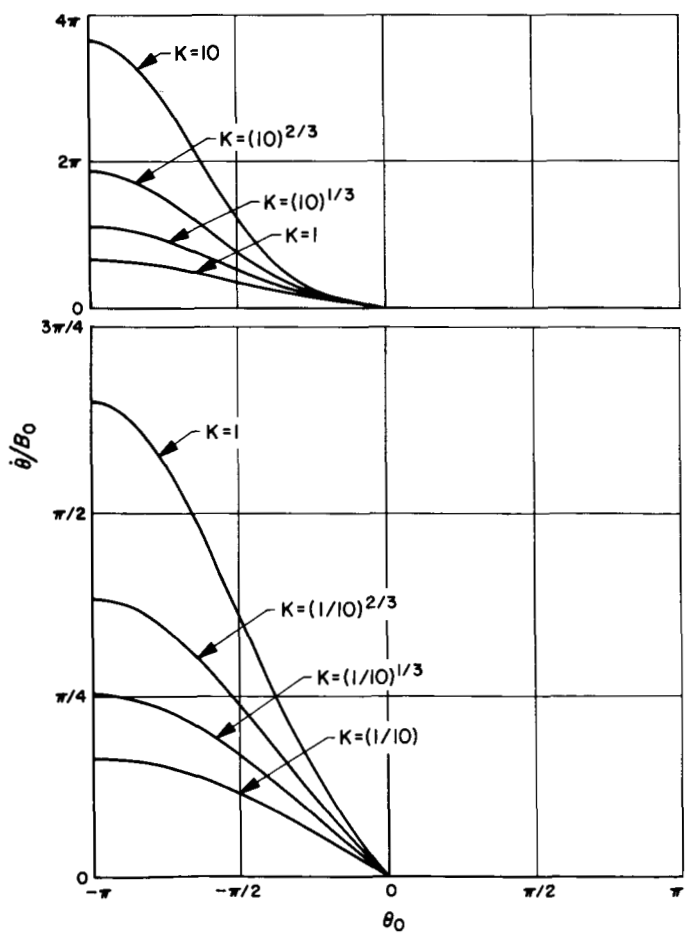

Figure 49. Phase plane plot, critical $\dot\theta/B_0$ for various gains, Case III

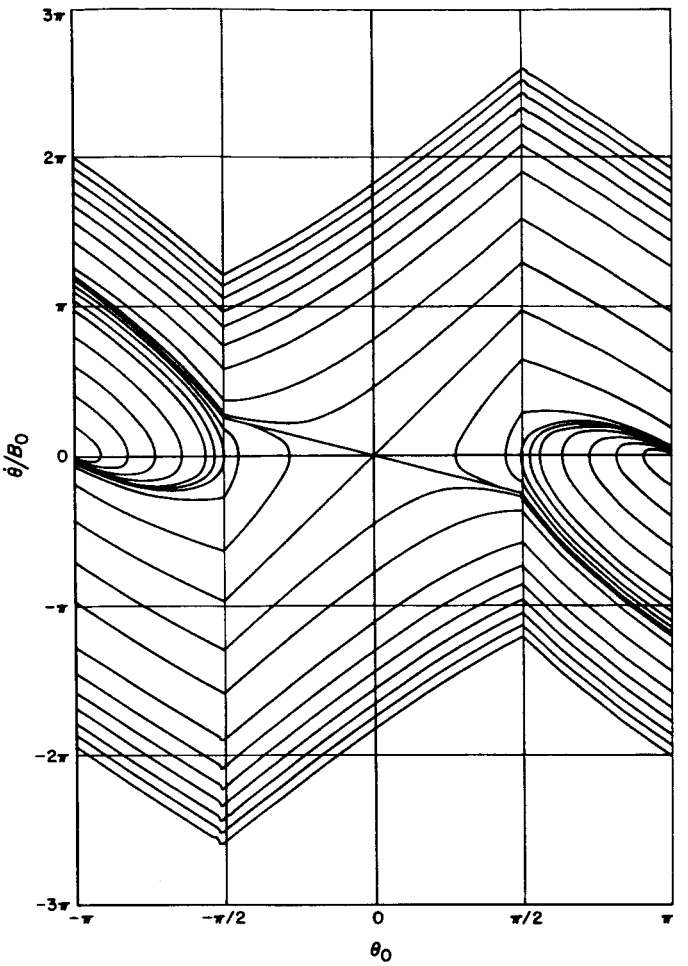

Figure 50. Phase plane plot, unity gain, Case IV

2. Pseudonoise System Correlation Function, or Loop Error Function

In the preceding section and in *RS 36-9*, considerable attention was given to the lock-in characteristics of the pseudonoise system with different loop error functions without any justification for choosing these particular functions. It is the purpose of this section to show how these are derived and how various system parameters affect the error function.

The system and parameters being considered are shown in Figure 54. In this figure, three parameters are used (θ, β, ξ). These were introduced for the following reasons: First, it will be noticed that a basic phase shift of $\pi/2$ was used at the transmission end; this was chosen to control the spectrum as indicated in *RS 36-5* and Reference 37; a parameter ϕ was introduced at both ends to show the effect of the carrier angle on the correlation function, or loop error function. Second, a parameter ξ was chosen to show the effect of misadjustment of the carrier angle at the transmission end; this might be caused by a bandpass filter or some poorly controlled adjustment. Third, a parameter β was chosen to show the effect of the misadjustment of the bandpass filter in the receiving end. The phase characteristic of a filter can be shown to cause a delay equivalent to $\tau = d\theta/df$, which does not affect this analysis, and a phase change in the carrier equivalent to the offset phase of the filter at the carrier frequency. This last parameter does affect the system.

The method of obtaining the cross correlation function is relatively simple. One needs only to take a basic period of the code and multiply it by the particular carrier at each terminal, as shown in Figure 55. These are then displaced from one another, and the product is averaged over the basic period. Notice that the code outside the basic interval is equally probable to be ± 1 and will therefore contribute nothing to the average when not matched exactly (Fig 56). The results of these evaluations are shown in Figures 57 to 62.

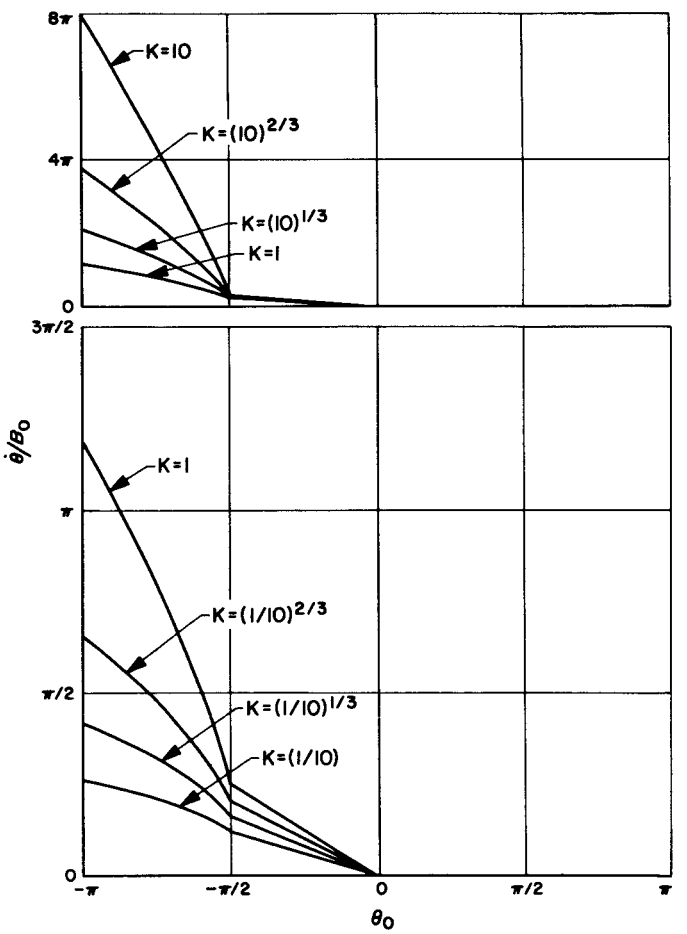

Figure 51. Phase plane plot, critical θ/B_0 for various gains, Case IV

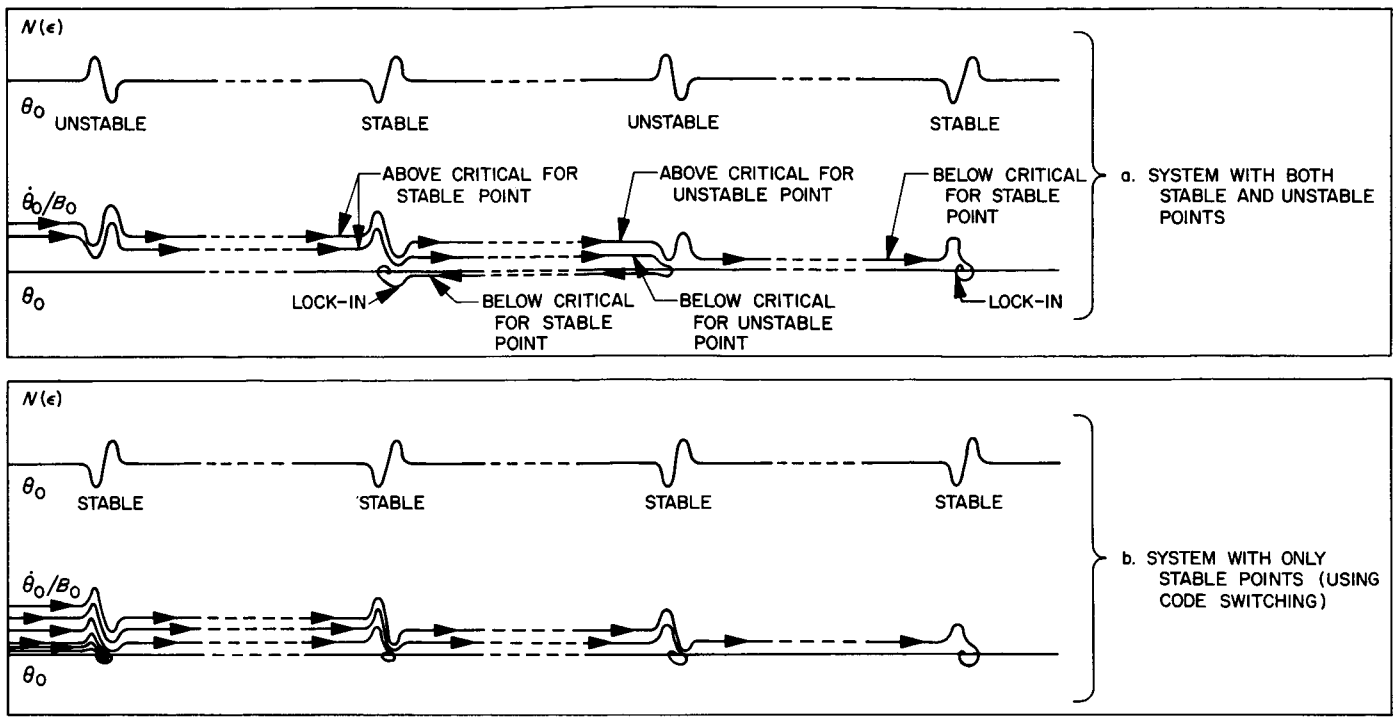

Figure 52. Qualitative pseudonoise system lock-in

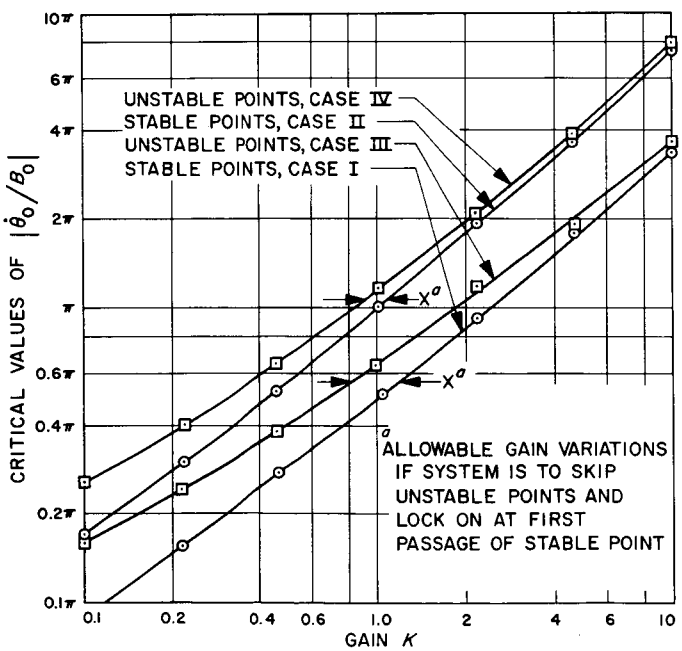

Figure 53. Critical values of $|\dot{\theta}_i(0)/B_0|$ for various gains, pseudonoise systems

It can be concluded from these graphs that in any change from the ideal situation (that is $\theta = 0$, $\beta = 0$, and $\xi = 0$), the error functions are asymmetrical and in some cases ($\theta \neq 0$ and $\beta \neq 0$) the error functions have unstable points which the preceding section has shown to be undesirable. It seems reasonable to assume (from the results of the preceding section) that the peaks of the unstable points should not be more than 10% of the peaks of the stable points and the asymmetry should not be more than 10%. If these criteria are used, then the cumulative effect of the phase errors should not exceed 5 degrees for the sine wave carrier (on the basis of asymmetry) and 5 degrees for the square wave carrier (on the basis of peak unstable points). Another fact that can be concluded is that only the ideal situation ($\theta = 0$, $\beta = 0$, and $\xi = 0$) for the sine wave carrier yields an error function which is the product of the autocorrelation functions of the carrier and of the code.

The ideal correlation functions (the most symmetrical) are the ones chosen for analysis in the preceding section.

3. New Properties and Methods of Code Switching

Code switching was devised as a means of correcting the quasi-stable lock points that occur in a PN synchronization system where correlation techniques are used to lock without ambiguity a local PN code generator to a received signal consisting of a PN code and a subcarrier f_s. The code switching technique has been previously described in *RS 36-6*. Adaptations of code switching to

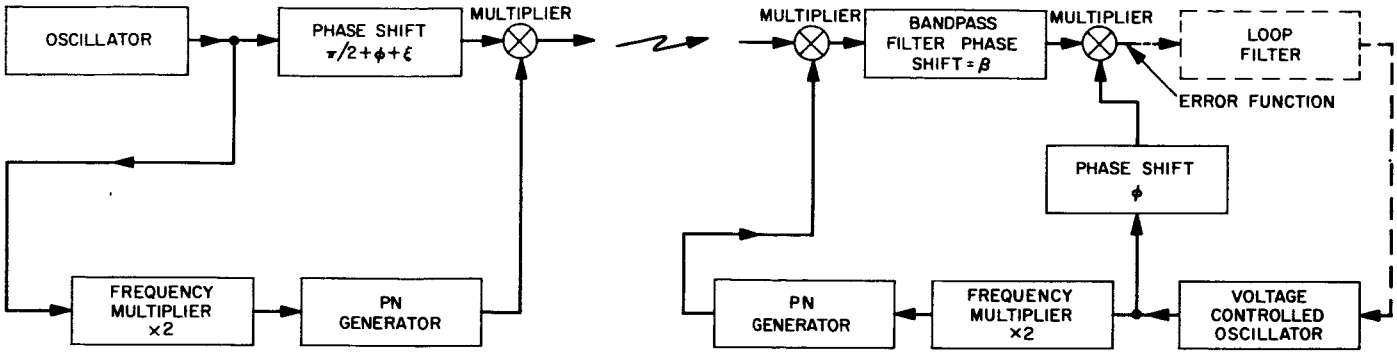

a. ACTUAL SYSTEM BLOCK DIAGRAM

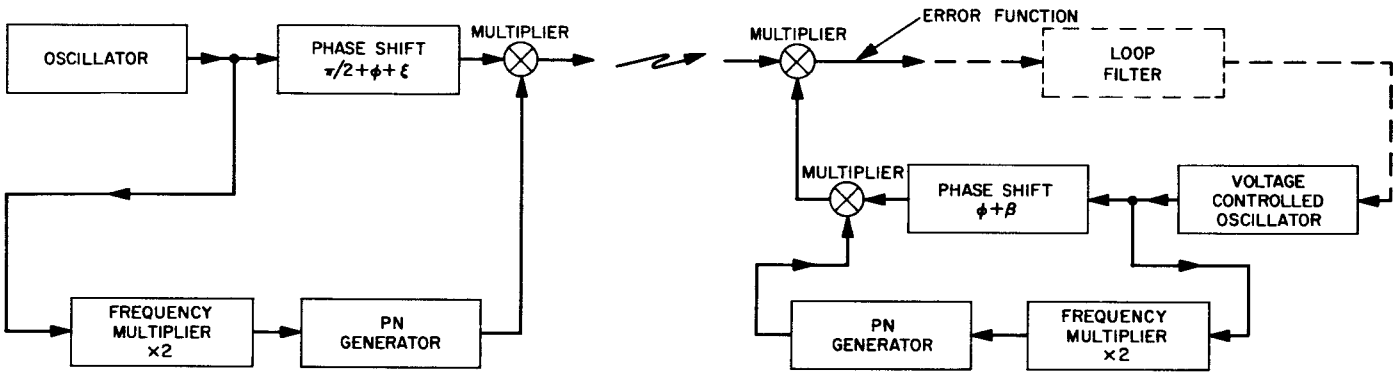

b. EQUIVALENT SYSTEM

Figure 54. Pseudonoise system block diagram

communication systems were implemented in the manner outlined in *RS 36-6* and had been considered satisfactory until recent measurements indicated that the double loop error function contained significantly large ambiguous lock points. Further measurements made on the autocorrelation function of the switched codes showed that significant distortion of the normal or expected autocorrelation had resulted; in particular a wide deviation from the $1/(2^n - 1)$ nature of the function between the points of maximum correlation. These results have prompted a re-evaluation of the code-switching technique and the properties of cyclically complemented codes.

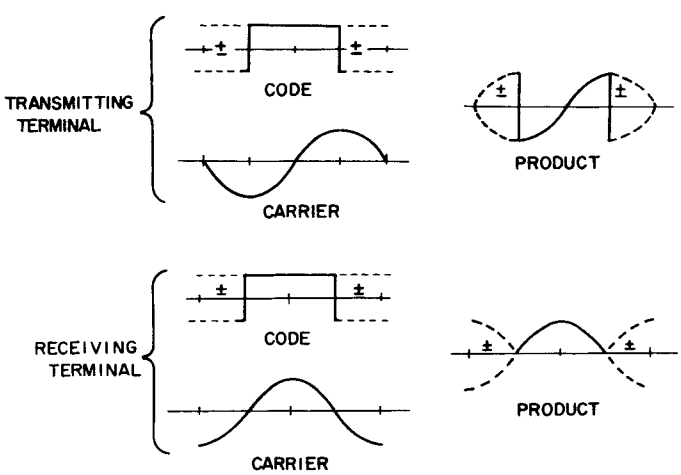

Figure 55. Wave forms of pseudonoise system, sine wave carrier

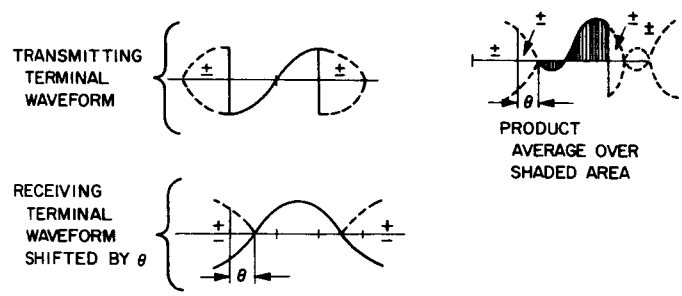

Figure 56. Process for calculating cross correlation function for pseudonoise system, sine wave carrier

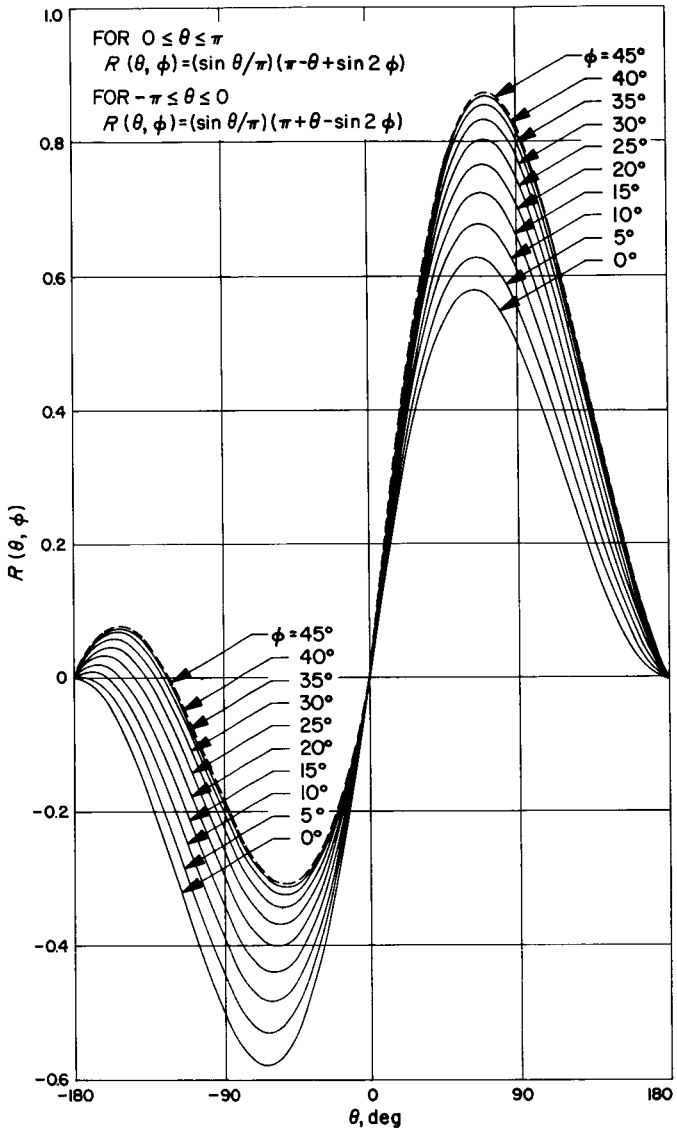

Figure 57. PN system correlation function $R(\theta, \phi)$ for sine wave carrier and various carrier phase angles ϕ

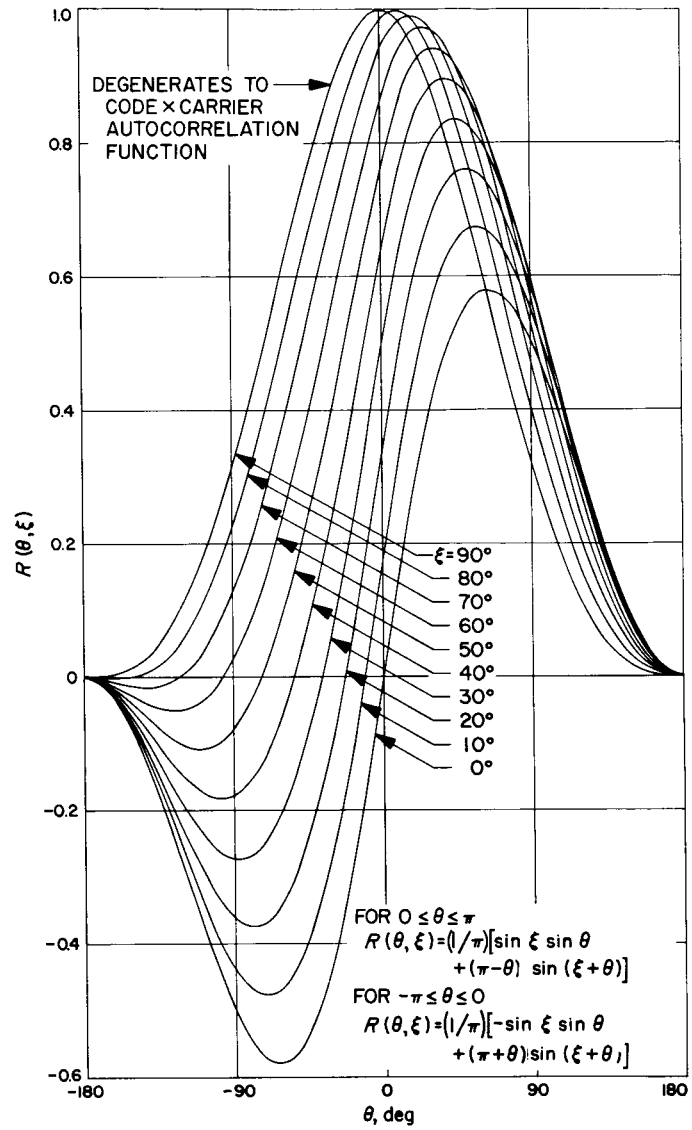

Figure 58. PN system correlation function $R(\theta, \xi)$ for sine wave carrier and various phase errors ξ in 90-degree channel

Further code switching properties. The original means of inverting the undesired portion of the synchronizing systems double loop error function is outlined in *RS 36-6* using the 7-bit PN code, 1110010, as an illustration. The results of that analysis have not been substantiated by the measurements made on systems using longer than length-7 PN codes in the synchronizing loop; however, verification of the switched properties of the length-7 PN code has been obtained. As a result, further investigation of the properties of the 7-bit code provides a starting point for determining the necessary requirements for switching the longer length PN codes.

First, it is significant to note that when the 7-bit code is cyclically complemented at the beginning of the three "1's," and then mod-2 added with f_s, the result is the original unswitched code run backwards, i.e.,

PN	$\overline{\text{PN}}$	
1110010	:0001101	switched PN
1010101	:0101010	f_s
0100111	:0100111	unswitched PN

If one now examines the 7-bit code mod-2 f_s for other switching combinations, the result obtained is not the

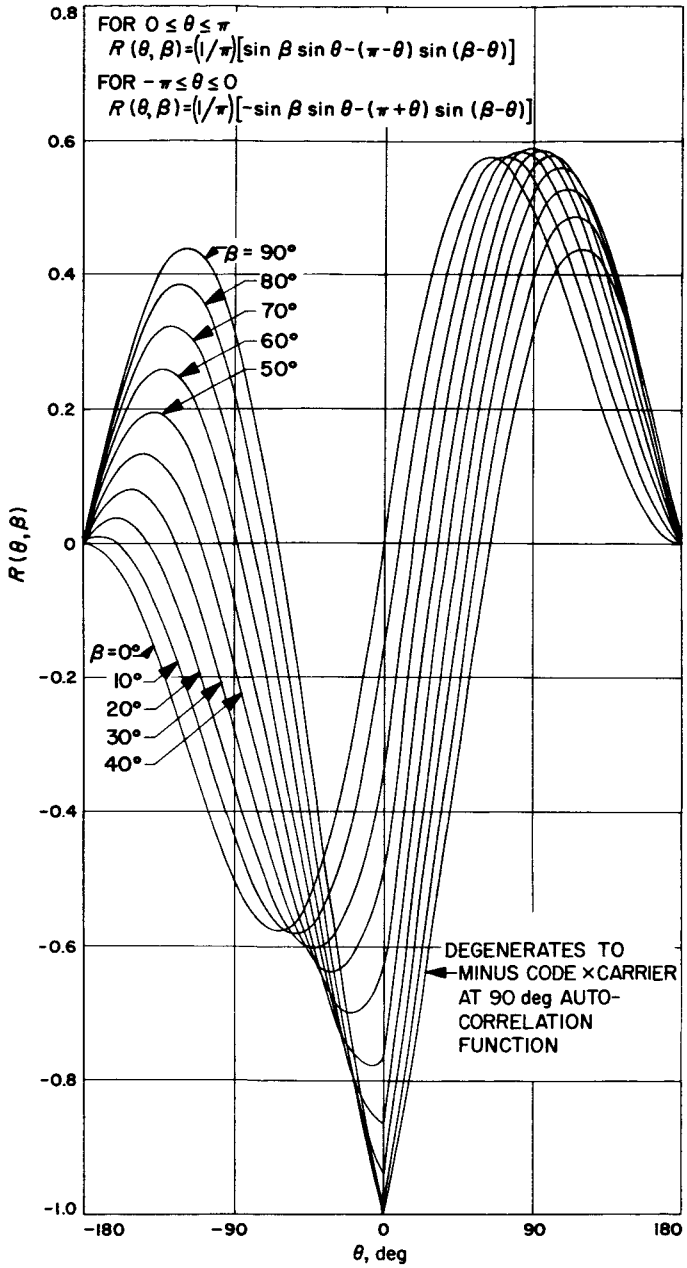

Figure 59. PN system correlation function $R(\theta, \beta)$ for sine wave carrier and various phase errors β in 0-degree channel

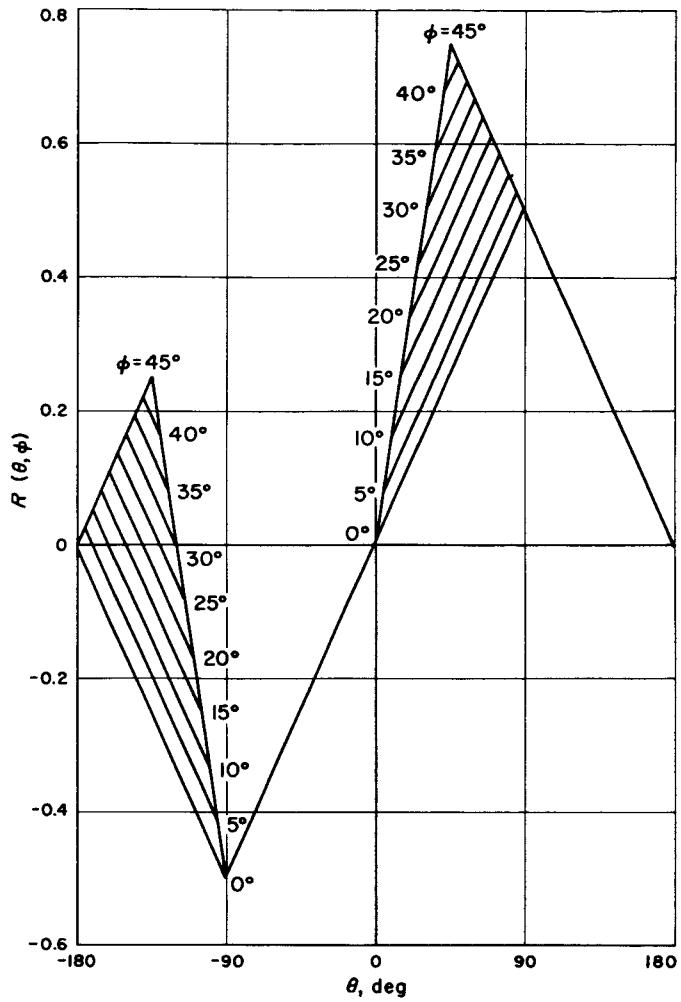

Figure 60. PN system correlation function $R(\theta, \phi)$ for square wave carrier and various carrier phase angles ϕ

unswitched PN code, in example,

PN	$\overline{\text{PN}}$	PN	
111:	1101000:	0010	switched PN
101:	0101010:	1010	f_s
010:	1000010:	1000	

Note also that the "1" and "0" balance is also destroyed, and, in fact, the loop error function obtained using this switched code contains ambiguities. As a result, it can be conjectured that the proper point to switch the code is the position where the switched code mod-2 f_s results in the original code or possibly another PN code of the same length possessing the necessary cycle and add properties.

The autocorrelation properties of the 7-bit switched code, 11100100001101, are also important as the nature of this function appears to be necessary for a switched code to result in the proper loop error function. As shown in Figure 63a, it is seen that the maximum correlation points are $+1$ and -1, and all others alternate between $+1/7$ and $-1/7$ in a periodic manner. It has been found that the 7-bit PN code can be switched at only one point in order to effect an unambiguous error function.

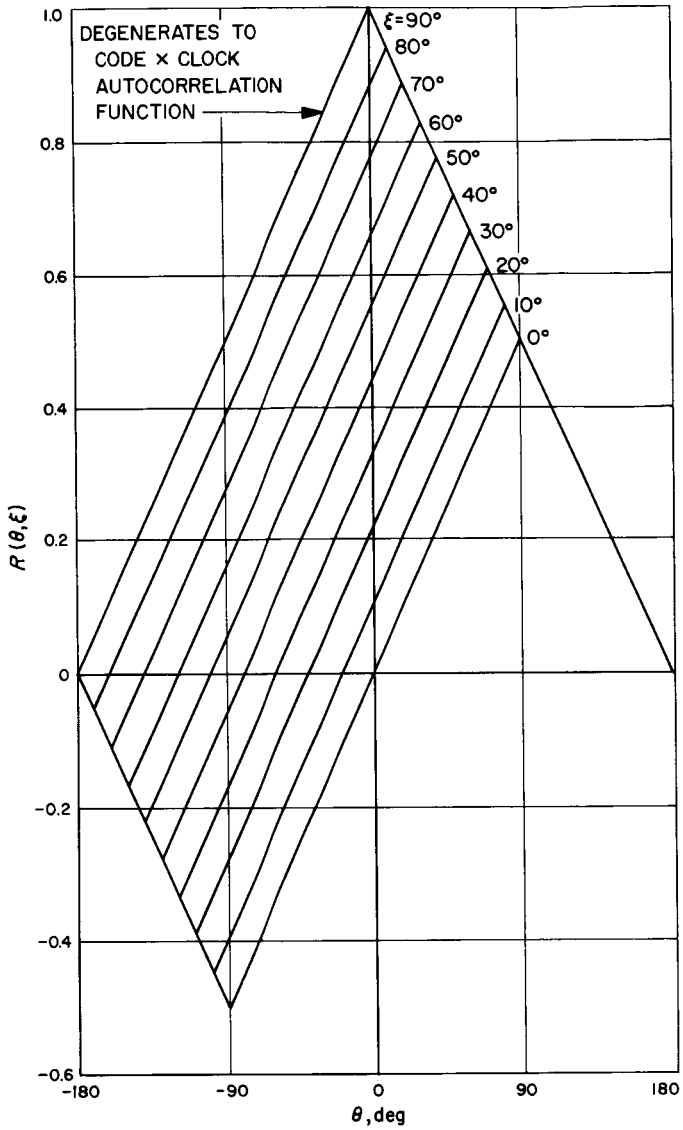

Figure 61. PN system correlation function $R(\theta, \xi)$ for square wave carrier and various phase errors ξ in 90-degree channel

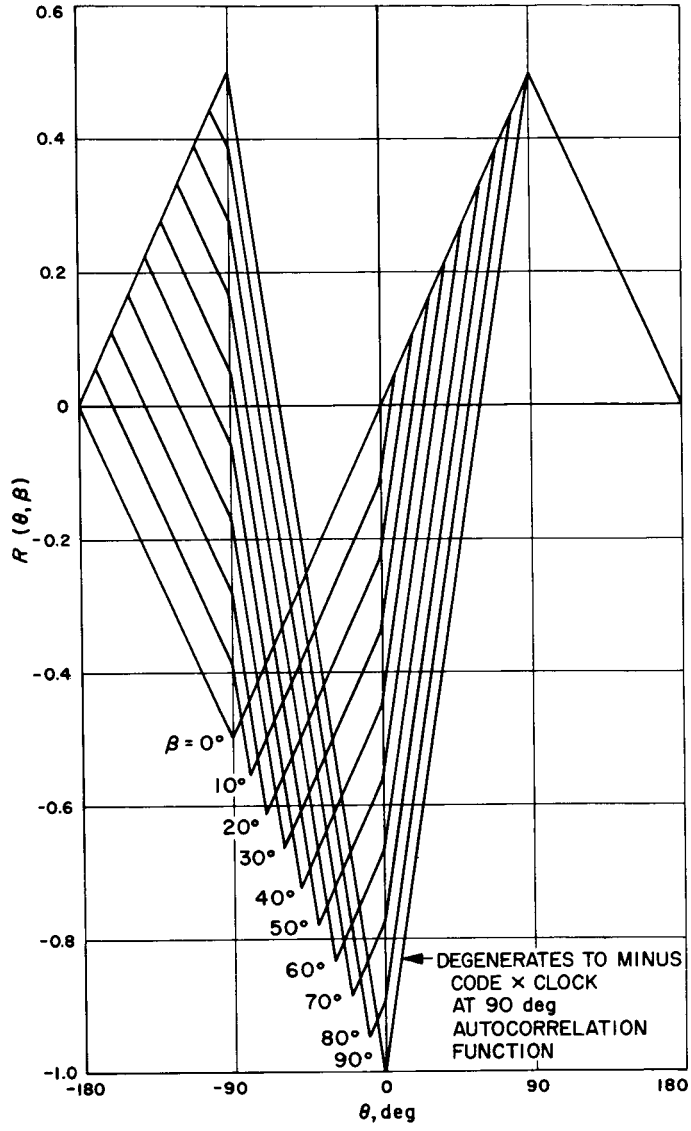

Figure 62. PN system correlation function $R(\theta, \beta)$ for square wave carrier and various phase errors β in 0-degree channel

Examination of the 15-bit PN code, 111100010011010, using the switched code mod-2 f_s criterion shows that no switching points exist where unambiguous error functions can be obtained. Solution to this dilemma is to consider a new code, PN*, which is the result of PN mod-2 f_s. This new code possesses the property of cyclic complementation, as shown in the example for the 15-length code:

111100010011010:111100010011010	PN
101010101010101:010101010101010	f_s
010110111001111:101001000110000	PN*

The autocorrelation function of PN* is shown in Figure 63b, and is found to be similar with the autocorrelation function of the cyclically complemented 7-bit PN code of Figure 63a. But note that the cyclically complemented 7-bit PN code may also be derived from PN mod-2 f_s. It is therefore stated, without formal proof, that all PN* obtained from PN mod-2 f_s possess the same general autocorrelation properties as shown in Figure 63a and b.

The cross correlation function (loop error function) between PN* × f_s and PN* × $f_s \angle 90°$ for the 30-bit PN* code is shown in Figure 64. The result is identical with

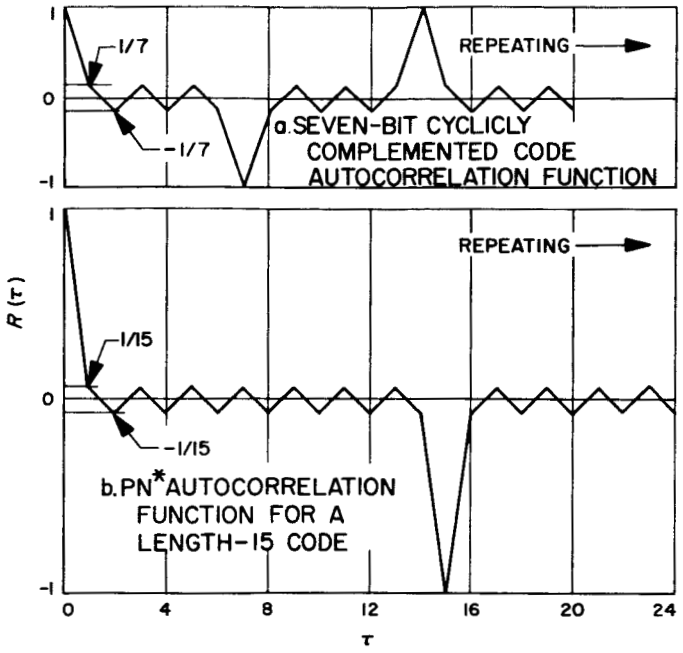

Figure 63. Autocorrelation functions

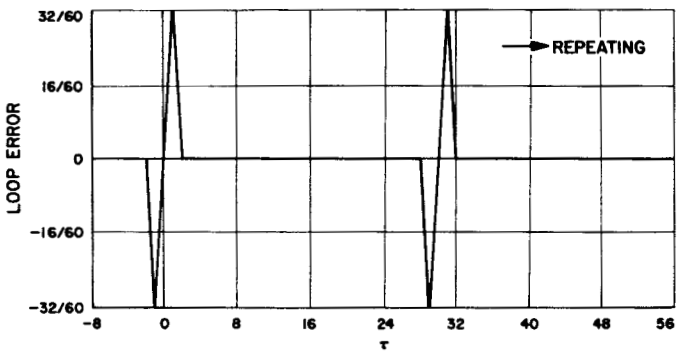

Figure 64. PN* loop error function

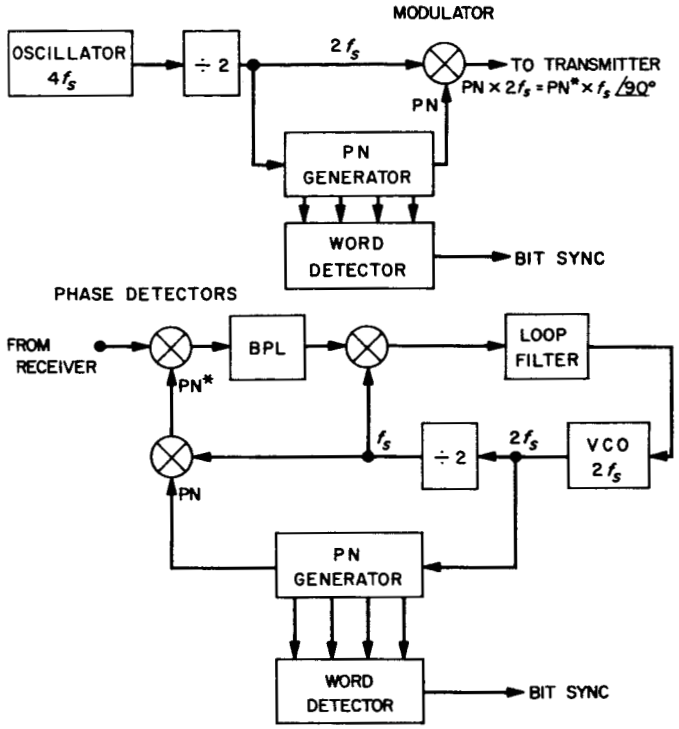

Figure 65. Modified synchronization system

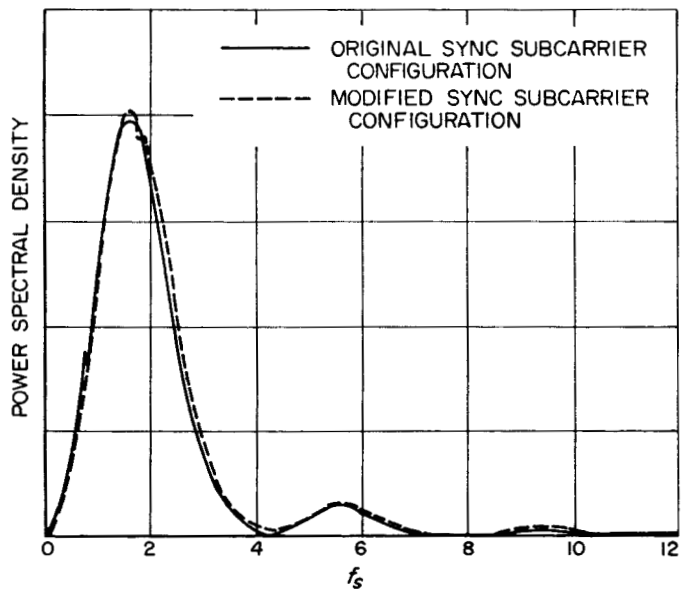

Figure 66. Spectrum analysis of PN-modulated sync subcarrier

that obtained for the cyclically complemented 7-bit PN code, and is free from ambiguous lock points. It can be seen from these results that the PN* code when substituted for the PN code of the sync system shown in *RS 36-6*, Figure 66, results in the desired unambiguous search and lock operation. A block diagram of the new mechanization using PN* codes is shown in Figure 65. (Note that $PN^* \times f_s \angle 90° = PN \times f_s \times f_s \angle 90° = PN \times 2f_s$.) This new mechanization results in a circuit and hardware simplification over the old code switching methods.

Laboratory tests have verified the error function obtained from the PN* code. It is also important to note that the general character of the modulator sync spectrum is not altered by the new mechanization since the waveforms obtained per switching period are the same in either case with only the ordering being changed. The measured spectrums obtained from the old and new code switching systems are shown in Figure 66.

PHYSICAL SCIENCES DIVISION

VII. Chemistry Research

A. Demonstration of Long-Range Proton-Proton Spin-Spin Coupling in the NMR Spectrum of Cyclohexene

D. D. Elleman and S. L. Manatt

For some time it was thought that proton-proton coupling constants were negligibly small across more than three bonds, but it has now been well demonstrated both theoretically (Ref 38) and experimentally (Refs 39 to 46) that long-range proton-proton coupling can exist over more than three bonds in many olefinic, allenic, and acetylenic molecules. Recently, several examples of transmission of long-range couplings through more than three consecutive single bonds have been reported by Roberts, et al (Ref 47), and Meinwald and Lewis (Ref 48). In this summary, we present another example of long-range proton-proton coupling obtained by means of NMR spectroscopy. During a study of the 60-mc high-resolution NMR spectrum of cyclohexene (see sketch), using the audio-sideband phase detection spin decoupling technique (Ref 49, also described in *RS 36-8*), a long-range coupling was found between the vinyl protons and the β-methylene protons (through two carbon-carbon single bonds).

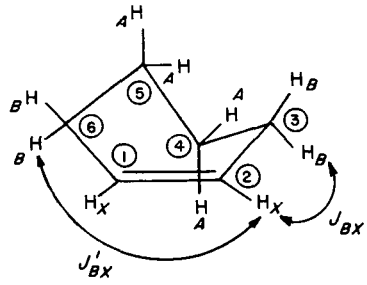

The high-resolution NMR spectrum of cyclohexene is shown in Figure 67a. The asymmetric triplet structure of the vinyl protons is a result of J_{BX} and J'_{BX} and could, if these were the only couplings, be considered as the X_2 region of a B_4X_2 system (Ref 50). At slower sweep rates, no significant additional fine structure of the triplet could be resolved. The methylene proton regions are very complex and make up the A_4B_4 part of an $A_4B_4X_2$ system. The up-field broad group was assigned to the β-methylene protons because there are fewer lines and several very

intense lines in this region. A-priori, the α-methylene proton region should be significantly more complicated because these protons are coupled with both the A_4 and X_2 protons. The down-field broad region is the broadest and shows signs of very complicated structure, as can be seen in Figure 67a.

When the vinyl and α-methylene protons were decoupled, as shown in Figure 67b, we observed that not only was the α-methylene proton region considerably simplified but also the β-methylene proton region was more completely resolved into sharp lines. Although the α-methylene region is still not as completely resolved as the β-methylene region, this difference is probably not due to incomplete decoupling but to a difference in the relaxation times of the two chemical types of protons. Evidence for this explanation is the fact that at slower sweep rates, or larger audio-modulation indices, considerable broadening was observed in the α-methylene signal.

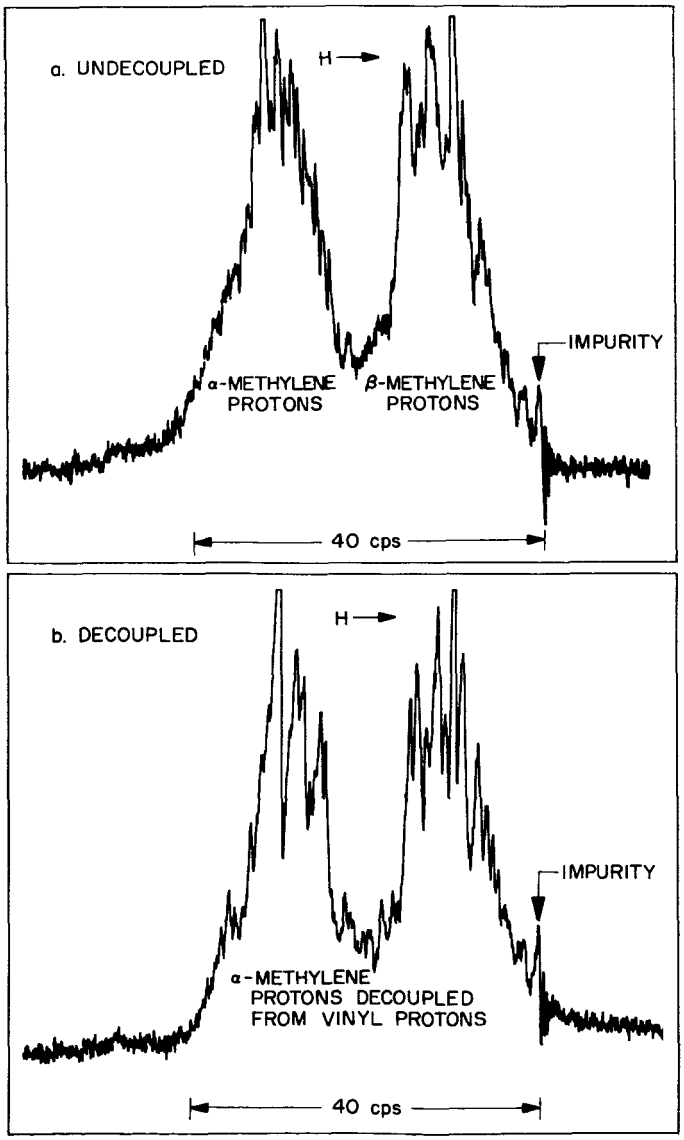

Figure 67. Nuclear magnetic resonance spectrum at 60 mc of methylene protons of cyclohexene, phase detected undecoupled and decoupled

The additional resolution of the β-methylene proton signals we interpret as evidence for a long-range coupling of these protons with the vinyl protons. From a careful scrutiny of the change in structure and line widths of this region from a number of spectra (both decoupled and undecoupled), it can be said that a doubling of the lines occurs in the undecoupled β-methylene signal. Thus, one additional proton is weakly coupling with each β-methylene group. This coupling is estimated to be 0.55 ± 0.05 cps (sign unknown).

There are several possible interpretations of the transmission of this coupling. It could result from coupling transmitted through four single bonds (for example, via C_2–C_3–C_4) or two pathways through five bonds (for example, via C_1–C_2–C_3–C_4 and C_1–C_6–C_5–C_4). The former explanation appears preferable as it is morein line with what is now known concerning the transmission of proton-proton couplings (Ref 38). There is yet a third mechanism for the transmission of this long-range coupling which has been suggested by Roberts, et al (Ref 47), and this is coupling across space. This mechanism is an attractive explanation for the very large long-range coupling (7 cps) observed in the bicyclo-[2,1,1]-hexane derivative recently studied by Meinwald and Lewis (Ref 48). As yet, there is no theoretical or clear-cut experimental evidence for this mechanism, but cyclic systems would seem a good place to look for this effect.

The 60-mc, high-resolution proton NMR spectrum of cyclopentene was also studied by the decoupling method, as shown in Figure 68. A-priori, we had expected to observe a similar long-range coupling but found none under very excellent spectrometer resolution. This result suggests that there is an angular dependence of this long-range coupling as has been found for other proton-proton couplings (Refs 38, 51).

From these results, it may be predicted that long-range proton-proton couplings should be present and perhaps observable in other olefinic systems such as in the methyl group of 1-butene, in cycloheptene, in cyclooctene and in 1,3-cyclooctadiene. Further study of such systems by the proton spin decoupling technique is in progress.

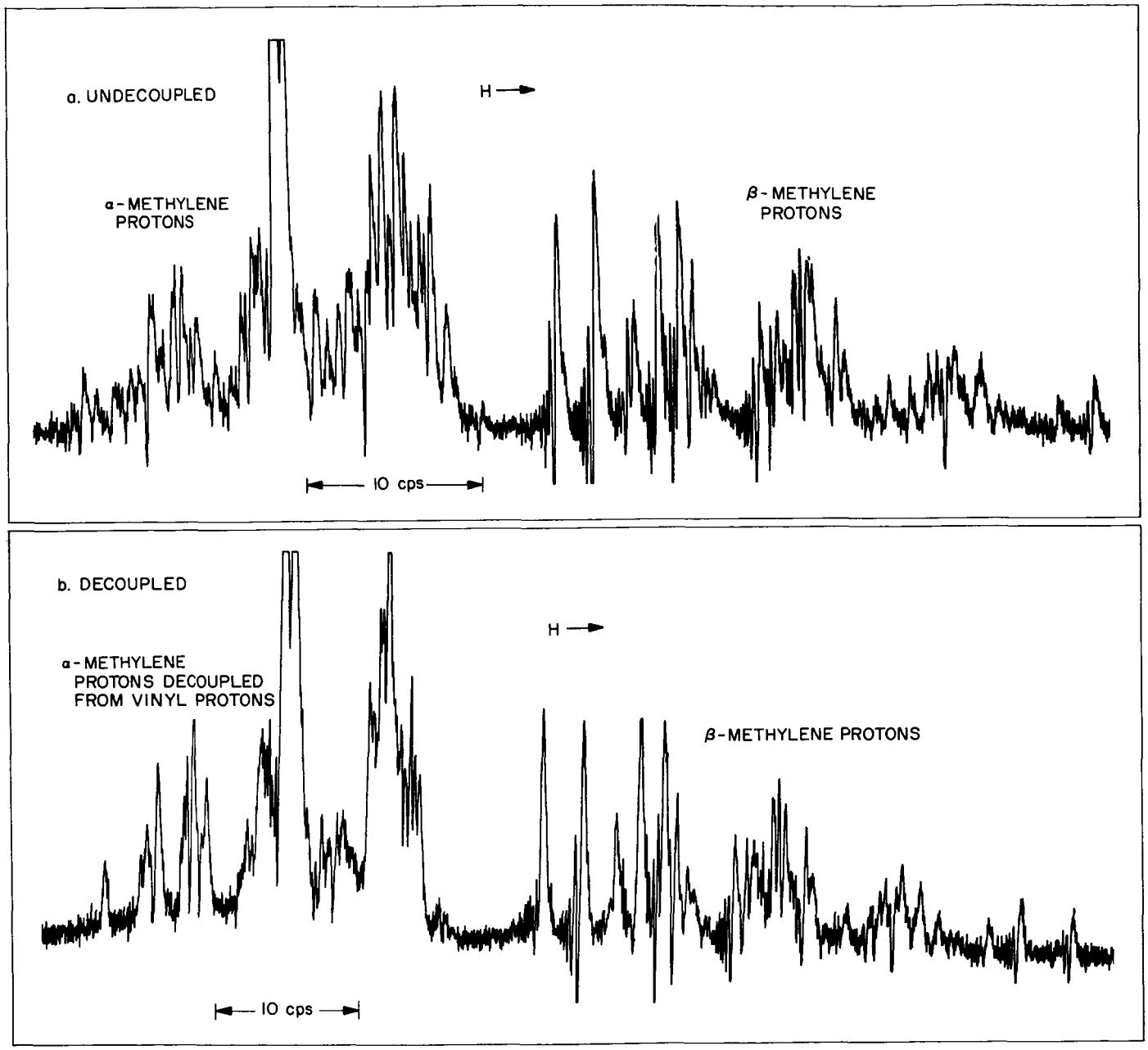

Figure 68. Nuclear magnetic resonance spectrum at 60 mc of methylene protons of cyclopentene, phase detected undecoupled and decoupled

B. Isothermal Diffusion with a Variable Density

O. T. Hanna

The diffusion equation for ordinary isothermal binary diffusion with composition-dependent density can be written for two dimensional flow (Ref 52) as follows:

$$\rho\left[\frac{\partial w}{\partial \theta} + u\frac{\partial w}{\partial x} + v\frac{\partial w}{\partial y}\right] = D\left[\frac{\partial}{\partial y}\left(\frac{\rho \partial w}{\partial y}\right) + \frac{\partial}{\partial x}\left(\frac{\rho \partial w}{\partial x}\right)\right] \quad (1)$$

This equation is valid for ideal solutions (i.e., perfect gas mixtures) for both laminar and turbulent flow, and the diffusivity D is essentially independent of composition.

Table 11. Nomenclature

$B = 1/M_1 - 1/M_2$
D = diffusion coefficient
$k_{var\,\rho}$ = variable density mass transfer coefficient
$k_{const\,\rho}$ = constant density mass transfer coefficient
M_i = $i = 1, 2$; pure component molecular weight
M = molecular weight of mixture, $1/M = Bw + 1/M_2$
p = pressure
$r = \ln M$
R = gas constant, $\rho = pM/Rt$
t = absolute temperature
u = vector velocity
u = longitudinal velocity component
v = transverse velocity component
w = mass fraction of diffusing component
w' = mass fraction of diffusing component for constant density
x = longitudinal coordinate, measured along surface
y = transverse coordinate, measured normal to surface
μ = dynamic viscosity
ρ = density, $\rho = pM/Rt$
θ = time

Subscripts

w = refers to conditions at the wall
∞ = refers to conditions in free stream or at centerline

Considering a perfect gas mixture, the density is given by

$$\rho = \frac{pM}{Rt} \tag{2}$$

and M, the molecular weight is related to the mass fraction w by

$$\frac{1}{M} = Bw + \frac{1}{M_2} \tag{3}$$

where $B = 1/M_1 - 1/M_2$. Thus, using Equations (2) and (3), we may write

$$\frac{\rho \partial w}{\partial i} = \frac{pM}{Rt}\left(-\frac{1}{BM^2}\right)\frac{\partial M}{\partial i} = \frac{-p}{BRt}\frac{\partial \ln M}{\partial i} \tag{4}$$

where i represents any independent variable. By using Equation (4) with t constant, Equation (1) can be rewritten as

$$p\left[\frac{\partial \ln M}{\partial \theta} + u\frac{\partial \ln M}{\partial x} + v\frac{\partial \ln M}{\partial y}\right] = D\left[p\frac{\partial^2 \ln M}{\partial y^2} + \frac{\partial}{\partial x}\left(p\frac{\partial \ln M}{\partial x}\right)\right] \tag{5}$$

since p is independent of y. Except when the pressure gradient $\partial p/\partial x$ is a significant part of the absolute pressure in systems where longitudinal diffusion is important, Equation (5) can be reduced to

$$\frac{\partial \ln M}{\partial \theta} + \mathbf{u} \cdot \nabla \ln M = D\nabla^2 \ln M \tag{6}$$

This equation is valid for laminar or turbulent flow with variable density, except for the unusual case of a strong pressure gradient coupled with longitudinal diffusion. Equation (6) was first derived, although somewhat differently, by Bedingfield and Drew (Ref 53). Putting $\ln M = r$, Equation (6) becomes

$$\frac{\partial r}{\partial \theta} + u\frac{\partial r}{\partial x} + v\frac{\partial r}{\partial y} = D\left[\frac{\partial^2 r}{\partial y^2} + \frac{\partial^2 r}{\partial x^2}\right] \tag{7}$$

To obtain exact solutions to isothermal, variable density mass transfer problems, Equation (7) must be solved simultaneously with the momentum equation, which is as follows:

$$\rho\left[\frac{\partial u}{\partial \theta} + u\frac{\partial u}{\partial x} + v\frac{\partial u}{\partial y}\right] = \frac{\partial}{\partial y}\left(\mu\frac{\partial u}{\partial y}\right) - \frac{\partial p}{\partial x} \tag{8}$$

Density variations cause a change in the velocity profile as is seen by referring to Equation (8). However, the wall mass flux is relatively insensitive to variations in the velocity profile, and thus the solution of Equation (7) using the constant density velocity profile would be expected to give an accurate value of the wall mass flux. Making this approximation, the variable density mass flux can be easily related to the constant density mass flux for any given geometry and wall boundary conditions, and for turbulent or laminar flow. This is done as follows.

For a given mass transfer situation (fixed geometry, boundary conditions, diffusivity, etc.) the constant density diffusion equation is written

$$\frac{\partial w'}{\partial \theta} + u\frac{\partial w'}{\partial x} + v\frac{\partial w'}{\partial y} = D\left[\frac{\partial^2 w'}{\partial y^2} + \frac{\partial^2 w'}{\partial x^2}\right] \tag{9}$$

The primes here serve as a reminder that these are the mass fractions in the case of a constant density. If, as discussed, the assumption is made that the effect of variable density on the velocity profile can be neglected in determining the wall mass flux, then u and v are the

same in Equations (7) and (9). Equations (7) and (9) are clearly analogous. By substitution it can be verified that

$$r = Aw' + E \tag{10}$$

where A and E are constants to be determined from the boundary conditions $r = r_w$ for $w' = w_w$, and $r = r_\infty$ for $w' = w_\infty$. The value of A is

$$A = \frac{r_\infty - r_w}{w_\infty - w_w} = \frac{\ln \frac{M_\infty}{M_w}}{w_\infty - w_w} \tag{11}$$

By differentiating Equation (10), the wall mass fluxes for the constant and variable density cases can be related.

$$\left.\frac{\partial r}{\partial y}\right|_w = \left.\frac{1}{M_w}\frac{\partial M}{\partial y}\right|_w = -M_w B \left.\frac{\partial w}{\partial y}\right|_w = \frac{\ln \frac{M_\infty}{M_w}}{w_\infty - w_w}\left.\frac{\partial w'}{\partial y}\right|_w \tag{12}$$

But $M_w B\,(w_\infty - w_w)$ is equal to $(M_w/M_\infty - 1)$ so that

$$\left.\frac{\partial w}{\partial y}\right|_w = \frac{\ln \frac{M_w}{M_\infty}}{\frac{M_w}{M_\infty} - 1}\left.\frac{\partial w'}{\partial y}\right|_w \tag{13}$$

Here the ratio $(\partial w/\partial y)_w/(\partial w'/\partial y)_w$ is the ratio of the mass fraction gradients at the wall in the variable density case to that in the constant density case. Since the mass transfer coefficients are usually defined in terms of these gradients, we have

$$\frac{k_{var\,\rho}}{k_{const\,\rho}} = \frac{\ln \frac{M_w}{M_\infty}}{\frac{M_w}{M_\infty} - 1} \tag{14}$$

This expression will be valid for both laminar and turbulent flow for any geometry, irrespective of the value of the Schmidt number. It will also be valid for any wall mass transfer boundary condition so long as both coefficients in Equation (14) refer to these conditions. Also, for low mass transfer rates, $k_{const\,\rho}$ can be determined by means of the constant property analogy between heat and mass transfer.

It must be noted that due to the neglect of density variations on the velocity profile, this expression will become less accurate at higher values of M_w/M_∞. By using the integral method with linear profiles to calculate laminar diffusion on a flat plate with zero normal velocity at the wall and a Schmidt number of unity, it can be demonstrated that Equation (14) is accurate within 15% for $1/5 < M_w/M_\infty < 5$, and within 30% for $1/10 < M_w/M_\infty < 10$, in this situation. Simultaneous heat and mass transfer results, to be presented in a later summary, bear this out. Equation (14) would be expected to apply with similar accuracy to other flow situations.

The variation of viscosity with composition has been neglected here, but this effect on the mass flux is small, of the same order as the previously neglected density effect. The effect of a composition-dependent viscosity on laminar constant-density diffusion from a flat plate can be obtained by applying the heat-mass transfer analogy to the results of Reference 54.

C. Chemical Equilibrium in Ionized Hydrogen System

J. King

An analysis of the chemical equilibrium in the ionized hydrogen system has been undertaken using the Debye-Huckel theory to determine the system's departure from ideal behavior caused by electrostatic interactions. The present analysis treats atomic hydrogen from 4000°K to 40,000°K at pressures of 1, 20, and 100 atmospheres.

The equilibrium in the system is expressed as

$$H \leftrightarrows H^+ + e^- \quad \text{or} \quad K = \frac{(H^+)\,(e^-)}{(H)} \tag{1}$$

Subsequent analyses will deal with such species as H_2, H_2^+ H_3^+ and H^-.

1. Method of Approach

The quantity in the Debye-Huckel formulation which measures a system's departure from ideality is the activity coefficient, γ. Its value is given by

$$\gamma_i = \exp\left(-\frac{z_i^2 e^2 b}{2DkT}\right) \tag{2}$$

where

$$b^2 = \frac{4\pi e^2}{DkT}\sum_i n_i z_i^2 \tag{3}$$

The average number of ions of kind i with charge $z_i e$ in the medium of dielectric constant D is given by n_i.

The equilibrium constant for Reaction (1) can also be expressed as (Ref 55)

$$K = \frac{\left(\frac{Q_{H^+}}{\gamma_+^{3/2}}\right)\left(\frac{Q_{e^-}}{\gamma_-^{3/2}}\right)}{Q_H} e^{-E_0^0/kT} \qquad (4)$$

Where the Q's are the molecular partition functions, and E_0^0 is the ionization potential at absolute zero.

2. Results

The equilibrium constants, activity coefficients, and percent ionization are shown in Figure 69 as a function of temperature at the different pressures.

Although the equilibrium constant as defined in Equation (1) is a function only of temperature, the small pressure dependence at high temperatures arises from the non-ideality of the system. In the region where RT becomes of the same order as the heat of the reaction, the equilibrium constants approach a constant value.

The minima in the activity coefficient curves are indicative of the maximum deviation from ideality. These occur at the temperatures corresponding to approximately 1/6 of the ionization potential of hydrogen. The minima may be explained by the fact that most of the thermal energy is used initially to ionize the atoms, whereas most of the energy after the minima is utilized in increasing the kinetic energy of the ionized particles. This increased kinetic energy causes the breakup of the structured ionic atmosphere in which a given ion is surrounded by a spherically symmetrical distribution of oppositely charged ions. The rupture of the ionic atmosphere minimizes the effects of the electrostatic interactions, and the system again approaches ideality.

This explanation accounts for both the pressure dependence of the minima and the fact that the percent ionization curves, shown in Figure 69c, have inflection points near the temperatures of the minima.

The percent ionization in an ideal hydrogen system is also shown in Figure 69c for comparison. The data was taken from Altman's (Ref 56) treatment of the idealized system. Although he concluded his analysis at 20,000°K, his calculations were extended to 40,000°K for comparison.

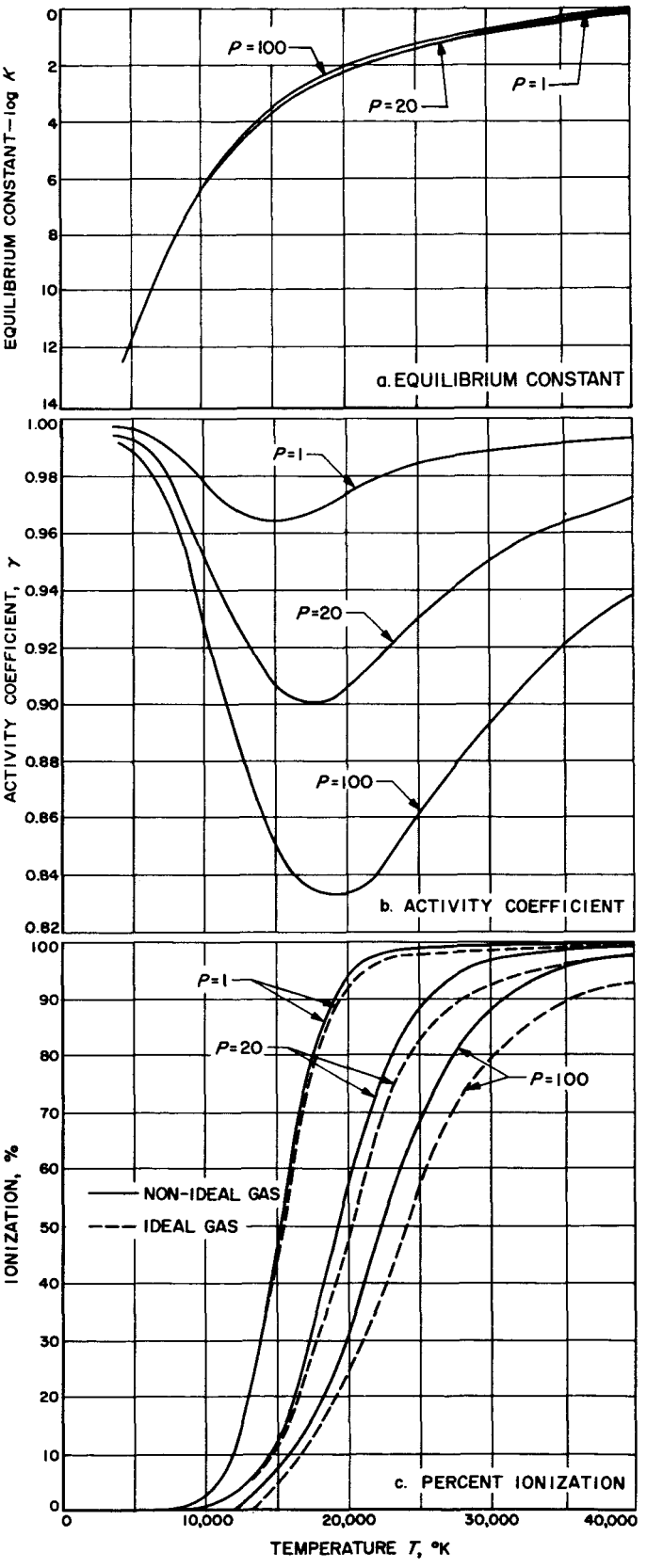

Figure 69. Effect of temperature on ionization

VIII. Physics Research

A. Fission Electric Cell Program: Capsule Calibration Experiment

W. F. Krieve

An experiment has been performed to obtain the background and leakage currents from the capsule designed for the fission electric cell capsule irradiations (*RS 36-8*). This experiment was performed in the in-core facility tube of the General Electric Nuclear Test Reactor (NTR).

The NTR can be operated at thermal power levels ranging from approximately 0.02 watt to a maximum of 30 kw. The unperturbed thermal neutron flux is 2.7×10^{11} at a power level of 10 kw. Maximum thermal flux in this reactor is therefore lower than the value to which the capsules will be subjected in the irradiation series; it is, however, possible to obtain with the NTR the capsule background and leakage currents as a function of power level.

The capsule used in this experiment was identical to those designed for use in the irradiation studies, except that the terminal and ion pump chamber were not hermetically sealed, and the cathode contained depleted uranium (0.22% U^{235}). This capsule was operated in air with no cooling facilities other than natural convection. Because of this lack of cooling, the magnetic suppressor field could not be run much larger than that necessary to suppress δ-electrons under zero voltage across the cell (2260 ev).

Equilibrium values of background and leakage current are reached rapidly because they result principally from gamma interactions, with some contribution from beta decay. The gamma interactions produce electrons instantaneously; the decay betas result from the neutron activation of aluminum, which has a half-life of 2.27 minutes. Thus, except for deterioration of the insulation due to extended exposure to ionizing radiation and neutrons, there are no long-term effects. Integrated doses anticipated in the capsule irradiations are 1 to 2 orders of magnitude lower than tolerance levels for the insulation.

Short-circuit output current from the capsule was measured with and without magnetic suppressor field at various reactor power levels. This short-circuit current is the algebraic sum of (1) background current due to the structural material of the cell, (2) the fission fragment current, and (3) any associated δ-electron current, when not suppressed.

Potentials, both positive and negative, between 100 and 2400 volts were applied to the capsule anode at various reactor power levels, and the currents were measured. This was done with and without magnetic field. The measured current would constitute the uncorrected leakage current.

The ion pump attached to the capsule was operated during the entire course of the experiment. Ion pump current readings were taken simultaneously with all of the other readings.

A preliminary analysis of the data has been completed, and the results can be summarized by the following set

of empirical equations, applicable when the reactor was above 10 watts power:

(1) Short-circuit current with no magnetic field

$$I = +5.28 \times 10^{-10} P^{1.09}$$

(2) Short-circuit current with magnetic field suppression

$$I = +6.72 \times 10^{-10} P^{1.07}$$

(3) Leakage current with positive potential applied to the anode and a reactor power level of 10 kw

$$I = -5.68 \times 10^{-9} E^{0.84}$$

(4) Leakage current with a positive potential of 1000 volts applied to the anode

$$I = -4.28 \times 10^{-7} P^{0.59}$$

(5) Same as (3) except negative potential

$$I = +6.14 \times 10^{-9} E^{0.81}$$

(6) Same as (4) except negative potential

$$I = +4.50 \times 10^{-7} P^{0.58}$$

where I is the current in amperes, P the reactor power level in kw, and E the applied potential in volts.

The polarity of the short-circuit current indicated that the capsule anode was at a positive potential above ground. This means that within the capsule there is a net flow of electrons from the anode to the cathode, and these constitute a current in the same direction as that which results from fission fragments going from the cathode to anode. Although the uranium used on the present cathode was depleted, the fragment current is calculated to be 3.22×10^{-10} amperes at a reactor power level of 10 kw, or about 4% of the short-circuit current with field. The measured short-circuit current with magnetic field would be the sum of this fragment current and the Compton and beta decay electron background current. Without magnetic field, the measured short-circuit current would be this same quantity minus the δ-electron current, and also minus the additional number of background electrons stopped in the anode because their trajectories were altered by the magnetic field. The existence of this last group of electrons was verified during reactor operation at very low power levels, and also when subcritical. Under these conditions, current with magnetic field was smaller than current without magnetic field. At subcritical and very low power levels, the gamma energy per thermal neutron is large as compared to the value at high power levels; consequently, the number of fissions becomes negligible, and the current difference would be due to the additional electrons stopped in the anode.

A major portion of the current loss with applied potentials was in the coaxial cable from the capsule to the instrumentation. Approximately 6.5 feet of cable was in the region of high radiation within the reactor. The remainder of the cable (25 feet) was in a region of from 5 to 500 mr/hr. Losses in the feed-through insulator and from the anode to ground through the vacuum interspace constituted the remainder of the leakage current. Leakage current was lower with a positive applied potential than with a negative potential. An analysis of the data to determine this and the mechanism of the current loss has not yet been done. It is noteworthy that the magnetic field had no effect on the leakage current; thus, there was no glow discharge within the capsule.

The ion pump functioned satisfactorily throughout the entire experiment. Ion pump current increased with increase in reactor power level. This increase in current can be attributed to additional gas pressure in the capsule due to radiation-induced outgassing, ionization in the pumping chamber, and current leakage in the insulation with increase in radiation density.

The results of this calibration experiment indicate that the capsule, as designed, should perform within the limits required for the irradiation program.

B. Electron Distribution Function of a Weakly Ionized Gas in a Magnetic Field and Time Dependent Electric Field

C. S. Wu and J. Zmuidzinas

1. Introduction

In this summary, the behavior of a slightly ionized gas is investigated when in the presence of a uniform magnetic field and a time-dependent electrical field. It is postulated that the plasma is homogeneous and that, before the external fields are imposed, it possesses a Maxwellian velocity distribution corresponding to the gas temperature T. The problem under study is the determination of the subsequent electron velocity distribution function of such a plasma, as well as the evolution of the corresponding average electron energy and drift velocity.

The Boltzmann equation for the present problem may be simplified by dropping the collision integrals describing the electron-electron and electron-ion encounters. Only the electron-atom collisions, for which the conventional close-binary collision model may be assumed valid, are considered. Again, we assume that most of the collisions are elastic. This implies that the average electron energy is low and the external field is not very strong.

In this analysis, the fields generated by the internal distributions and motions of the charged particles are postulated to be negligible compared to the applied fields. Hence, in the Boltzmann equation, both $\mathbf{E}$ and $\mathbf{B}$ are considered to be known quantities, and hereafter we will write the electric field $\mathbf{E}$ in the following form:

$$\mathbf{E} = \mathbf{E}_0 \phi(t)$$

where $\phi(t)$ is any given function of time which is bounded and continuous at all times.

With the initial Maxwellian distribution, we obtain a solution for the subsequent time ($t > 0$) based on the assumption that the anisotropic part of the distribution function is a small perturbation of the isotropic distribution.

2. Deduction of the Governing Integro-Differential Equation

Under the assumptions stated previously, the electron distribution function $f(\mathbf{v}, t)$ is considered to satisfy the Boltzmann equation of the following form (Ref 57):

$$\left[\frac{\partial}{\partial t} - \frac{e}{m}(\mathbf{E} + \mathbf{v} \times \mathbf{B}) \cdot \frac{\partial}{\partial \mathbf{v}}\right] f(\mathbf{v}, t) = \int_{v_m} \int_{\Omega} [f'_m f' - f_m f] \, g \sigma_m \, d\Omega \, d\mathbf{v}_m \quad (1)$$

In order to solve Equation (1) for $f(\mathbf{v}, t)$, we shall postulate that the electron distribution function may be written:

$$f(\mathbf{v}, t) = f^{(0)}(v, t) + \mathbf{E}_0 \cdot \mathbf{v} f^{(1)}(\mathbf{v}, t) + (\mathbf{B} \times \mathbf{E}_0) \cdot \mathbf{v} f^{(2)}(v, t) + \mathbf{B}(\mathbf{B} \cdot \mathbf{E}_0) \cdot \mathbf{v} f^{(3)}(v, t) \quad (2)$$

The initial conditions of the unknown functions $f^{(0)}$, $f^{(1)}$, $f^{(2)}$, and $f^{(3)}$ may be given as follows at $t = 0$:

$$\begin{aligned} f^{(0)}(v, 0) &= N\left(\frac{m}{2\pi KT}\right)^{3/2} \exp\left(-\frac{mv^2}{2KT}\right) \\ f^{(1)}(v, 0) &= 0 \\ f^{(2)}(v, 0) &= 0 \\ f^{(3)}(v, 0) &= 0 \end{aligned} \quad (3)$$

Following a similar discussion (Ref 58), we obtain

$$\frac{\partial f^{(0)}}{\partial t} = \frac{1}{v^2}\frac{\partial}{\partial v}\left\{\left[\frac{e}{m}\frac{v^3}{3}(f^{(1)} + B^2 \cos^2\gamma \, f^{(3)}) E_0^2 \phi(t)\right] + \left[\frac{m}{M}\frac{v^4}{l} f^{(0)} + \frac{KT}{M}\frac{v^3}{l}\frac{\partial f^{(0)}}{\partial v}\right]\right\} \quad (4)$$

$$\frac{\partial f^{(1)}}{\partial t} = -\frac{v}{l} f^{(1)} + \frac{e}{m}\left[\frac{1}{v}\frac{\partial f^{(0)}}{\partial t}\phi(t) - B^2 f^{(2)}\right] \quad (5)$$

$$\frac{\partial f^{(2)}}{\partial t} = -\frac{v}{l} f^{(2)} + \frac{e}{m} f^{(1)} \quad (6)$$

$$\frac{\partial f^{(3)}}{\partial t} = -\frac{v}{l} f^{(3)} + \frac{e}{m} f^{(2)} \quad (7)$$

where m and M are the electronic and atomic masses, respectively, l the mean free path of electrons, and γ the angle between the field vectors $\mathbf{B}$ and $\mathbf{E}$.

Combining the above equations, we obtain an integro-differential equation for $f^{(0)}$ for $t > 0$.

$$\frac{\partial f^{(0)}}{\partial t} = \frac{1}{v^2}\frac{\partial}{\partial v}\left\{\frac{e^2 E_0^2 \phi(t) v}{3m^2} \times \int_0^t e^{-\nu(t-t')} [\cos^2\gamma + \sin^2\gamma \cos\omega(t-t')] \times \frac{\partial f^{(0)}(v, t')}{\partial v}\phi(t') \, dt' + \frac{mv}{M}\left[v^3 f^{(0)} + \frac{mv^2}{4KT}\frac{\partial f^{(0)}}{\partial v}\right]\right\} \quad (8)$$

where ν is the collision frequency, and ω the cyclotron frequency. For simplicity, hereafter we denote

$$u = \frac{v}{a}$$

$$a = \left(\frac{2KT}{m}\right)^{1/2}$$

$$\varepsilon = \frac{m}{M}$$

$$g(u, t) = f^{(0)}(v, t)$$

Then Equation (8) becomes finally

$$u^2 \frac{\partial g}{\partial t} = \frac{\partial}{\partial u}\left\{\frac{e^2 E_0^2 u^2}{6mKT}\phi(t) \times \int_0^t e^{-\nu(t-t')} [\cos^2\gamma + \sin^2\gamma \cos\omega(t-t')] \times \frac{\partial g(u, t')}{\partial u}\phi(t') \, dt' + \varepsilon\nu\left[u^3 g(u, t) + \frac{1}{2}u^2 \frac{\partial g}{\partial u}\right]\right\} \quad (9)$$

3. Method of Solution

a. Expansion of the function $g(u,t)$. In order to solve Equation (9), we have devised a method which contains two essential steps: (1) to expand the function $g(u,t)$ in terms of its moments, as defined in the following:

$$M_n = 2\int_0^\infty g(u,t)\,u^{n+2}\,du \tag{10}$$

and (2) to derive the "generating equation" for these moments.

To proceed, we first expand the function $g(u,t)$ in terms of Laguerre polynomials

$$g(u,t) = e^{-\lambda u^2}\sum_{k=0}^{\infty} a_k(\lambda,t)\,L_k^{1/2}(\lambda^2u^2) \tag{11}$$

where λ is a parameter which may be a function of t. The determination of $\lambda(t)$ is discussed later.

The Laguerre polynomial $L_k^{1/2}$ is defined in Reference 59 as follows:

$$L_k^{1/2}(\lambda^2u^2) = \sum_{n=0}^{k}\binom{k+\frac{1}{2}}{k-n}\frac{(-\lambda^2u^2)^n}{n!} \tag{12}$$

The reason for choosing the Laguerre polynomial of order ½ in particular is mainly based on its orthogonality property. The discussion of this choice may be found in the complete paper, in which it has also been shown that the coefficients a_k may be expressed in terms of the moments

$$a_k = \sum_{n=0}^{k}\binom{k}{n}\frac{(-1)^n\lambda^{2n+3}}{(n+\frac{1}{2})!}M_{2n}(t) \tag{13}$$

The choice of λ is then based on the criterion that the fastest convergence of Equation (11) be obtained.

b. Quasi-steady case. The quasi-steady case is defined when the following conditions hold true

$$\frac{\phi^{(k)}}{\nu^k} << \phi \qquad \frac{M_{2n}^{(k)}}{\nu^k} << M_{2n} \qquad k = 1, 2, \cdots$$

where $\phi^{(k)}$ and $M_{2n}^{(k)}$ denote the kth derivatives of ϕ and M_{2n}, respectively. The physical meaning of these conditions is that the changes of the functions ϕ and M_n for the time interval $\tau(-1/\nu)$ are small compared to the values of the functions. This situation enables us to have a "persistent" solution ($t >> \tau$) as follows:

$$g^\infty(u,t) = N[(\pi)^{1/2}a]^{-3}\lambda_\infty^3\,e^{-\lambda_\infty^2u^2}\sum_{k=0}^{\infty}\sum_{n=0}^{k}\binom{k}{n}(-1)^n\lambda_\infty^{2n}$$
$$\times[1+\Omega(t)]^{n+1}L_k^{1/2}(\lambda_\infty^2u^2) \tag{14}$$

where

$$\Omega(t) = \frac{e^2E_0^2\phi^2(t)}{3m\varepsilon KT}\left(\frac{\cos^2\gamma}{\nu^2}+\frac{\sin^2\gamma}{\nu^2+\omega^2}\right)$$

It is clear that now the optimum choice of λ_∞ is

$$\lambda_\infty(t) = [1+\Omega(t)]^{-1/2}$$

Then,

$$g^\infty(u,t) = N(\pi^{1/2}a)^{-3}[1+\Omega(t)]^{-3/2}\exp\left\{-\frac{u^2}{[1+\Omega(t)]}\right\} \tag{15}$$

because

$$\sum_{k=0}^{\infty}\sum_{n=0}^{k}\binom{k}{n}(-1)^nL_k^{1/2}(\lambda_\infty^2u^2) = 1$$

As a consequence,

$$\frac{\partial g^\infty}{\partial u} = -2N(\pi^{1/2}a)^{-3}u[1+\Omega(t)]^{-3/2}\exp\left\{-\frac{u^2}{1+\Omega(t)}\right\} \tag{16}$$

c. High-frequency oscillating field. The second special case is when the electric field **E** varies according to a time function $\phi(t) = e^{i\beta t}$. In this case, the approximation used previously is no longer valid if the frequency β is of the order of ν. However, simplification is still possible, since sometimes we only need the information contained in the first two moments, M_0 and M_2. To illustrate this point, fuller discussions will be given in Technical Report 32-102 (in print). A complete report of this work is also to be published in *Annals of Physics*.

IX. Gas Dynamics Research

Hypersonic Wake Studies

J. M. Kendall

The problem of identifying a body entering the atmosphere by observation of its trail has generated interest in the fluid mechanical and chemical processes in high-temperature turbulent wakes. Ionic recombination and diffusion rates of material vaporized from the body surface in the wake are of particular importance. The hypersonic wake problem has not been studied in detail. Currently, several investigators using firing ranges are studying the wake growth rate and measuring electron concentration. The wind tunnel offers certain advantages over firing ranges for the investigation of the fluid mechanical problem. Experiments with a two-dimensional wake in a tunnel are reported in Reference 60.

Sphere wake measurements have been initiated in the JPL 21-inch Hypersonic Wind Tunnel at a Mach number of 8, and Reynolds numbers between 30,000 and 250,000. Spheres, 0.5 inch in diameter and suspended on fine wires, permit measurements of pitot pressure, total temperature, and hot-wire anemometer signals up to 200 diameters downstream.

Figure 70 shows pitot pressure measurements of the wake development. The crosses in this figure indicate wake widths from firing range experiments which are collected in Reference 61. The dashed line is the calculated pressure profile for inviscid flow behind the observed bow shock wake, and is invariant in the stream direction. The results to date indicate that (1) the wake remains reasonably symmetric to $x/d = 200$; (2) the wake is turbulent, as indicated by its growth; (3) it is experimentally difficult to separate the bow shock wake from the viscous wake; (4) total temperature variation is less than 5% for $x/d > 4$; and (5) the hot-wire signal is generated partly by disturbances radiated from the turbulent tunnel wall boundary layers.

The next experiments will include tests at lower Mach numbers and will be concerned with detection of transition from laminar to turbulent wake flow.

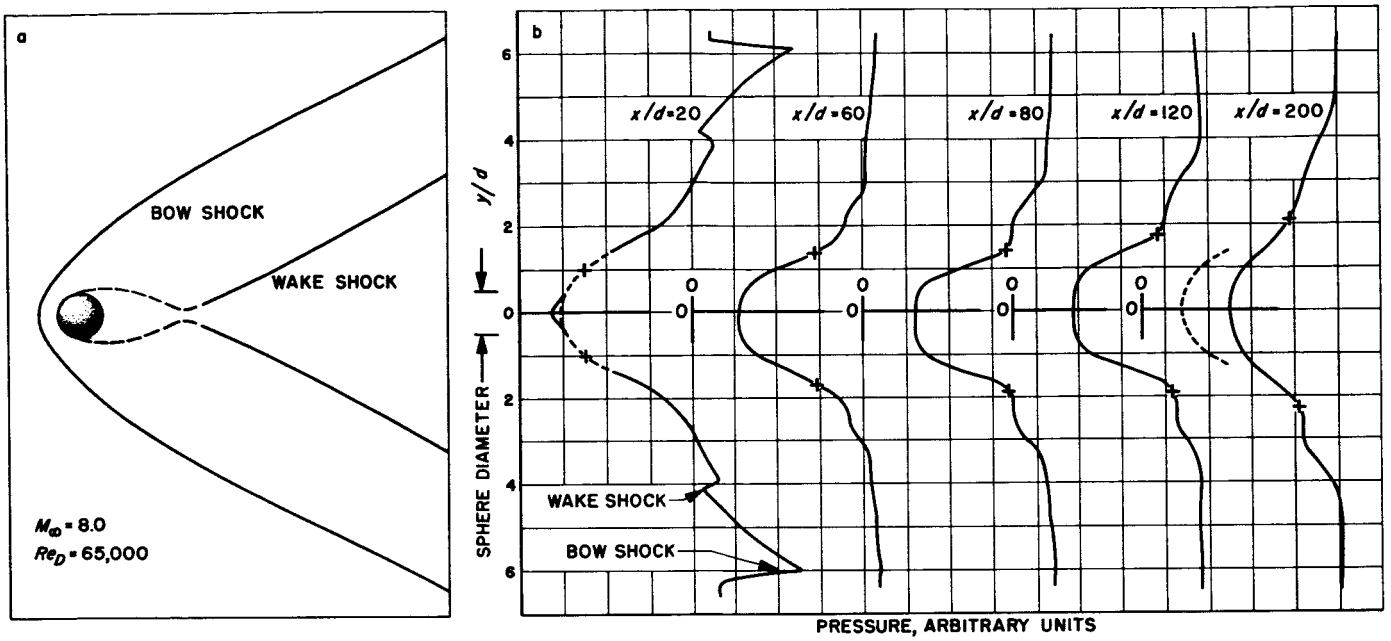

Figure 70. Pitot pressure in sphere wake

ENGINEERING MECHANICS DIVISION

X. Materials Research

A. Solid State Research

P. J. Shlichta

Growth and Perfection of Crystals

Orientation effects in sodium chloride crystals. As was reported previously (*RS 36-4*), sodium chloride crystals, when grown from melt as thin rods in the ⟨100⟩ direction, possess unusual ductility. Not only is this ductility greater than that observed in chemically polished cleavages of sodium chloride, but it is also far less subject to deterioration by aging or exposure to moisture or atmosphere.

Sodium chloride cleaves easily and perfectly along its {100} planes, and thus it is very difficult to cut the crystals in any other direction. Therefore, nearly all the data in the literature are concerned with ⟨100⟩ cleavages. It, therefore, seemed advisable to attempt to grow thin crystals in other orientations, especially along ⟨111⟩, which has a three-fold axis of symmetry, and ⟨110⟩ which has a two-fold axis of symmetry.

The crystals were grown in a manner similar to that described for thin ⟨100⟩ crystals. Despite the peculiarities described below, no difficulty was encountered in producing fairly uniform rods 2 to 5 mm thick. In fact, it proved feasible, by means of a special triple seed holder, to grow three crystals, one of each orientation, simultaneously, thus indicating that the steady-state growth rate is of the same order of magnitude for each orientation. The direction of crystal growth nearly always corresponds closely if not exactly with the ⟨100⟩, ⟨110⟩, or ⟨111⟩ axes; if a thin crystal is grown from an improperly aligned seed, it will grow at an angle from the vertical so as to maintain proper orientation. This is in contradistinction to thick crystals, which grow vertically regardless of orientation.

The ⟨100⟩ crystals are essentially square in cross section, due to the prominence of the {100} faces. The corners, however, are more or less rounded, indicating incipient development of {110} faces. After steady-state growth conditions are attained, which is usually about 5 to 9 mm after the beginning of growth, the thickness of the crystals (i.e., the distance between the {100} faces) either remains constant, except for major fluctuations in growth conditions, or changes monotonically. On the other hand, the roundness of the corners changes with minor fluctuations of pull rate or temperature, sometimes even giving the corners a rippled appearance (Fig 71a).

The ⟨110⟩ crystals grow as flat blades with two large planar {100} faces (Fig 71b). The thickness (i.e., distance between the {100} faces) is remarkably constant, always being about 3 mm if the seed is not too large. If a very thin (0.1 mm) seed is used, the growing crystal will rapidly thicken, in a series of abrupt steps (0.1 to 0.3 mm high) to a thickness of about 3 mm which will remain constant even though the width (in the ⟨110⟩ direction) varies from less than 4 mm to more than 30 mm. Changes in temperature or pull rate cause the width to fluctuate but leave the thickness unaffected. Occasionally, the thickness will increase slightly, by the development of new wedge-shaped steps, but not because of changes in growth conditions. In some cases the thickness has been observed to increase while the width is steadily decreasing due to rising temperature. We may, therefore, conclude that nucleation of new growth steps on {100} planes is difficult and insensitive to temperature and pull rate, but that lateral growth of {100} layers is rapid and easy. Growth in the ⟨110⟩ direction is at least equally rapid but there is no evidence of discrete {110} growth steps or faces. It is even possible that growth in the ⟨110⟩ direction can be explained entirely in terms of lateral growth of {100} steps. Instead of {110} faces, the edges of these ⟨110⟩ crystals have a ridged appearance which will be discussed below.

The ⟨111⟩ crystals are triangular in cross section, with ridged sides and smoother, rounded corners (Fig 71c). This immediately suggests that the growth form is not an equilibrium one but is a result of development of faces at the growth tip. (This implies that if the crystal were immersed for a long time in molten salt, at equilibrium conditions, it would assume an entirely different crystal habit.) Sodium chloride, in the ⟨111⟩ direction consists of alternate hexagonal close packed layers of sodium and chloride ions, so that if an equilibrium uniform-rod crystal form did exist, it would have six-fold symmetry. Note, for example, that both the sides and the vertices of the triangular cross section lie alike in ⟨110⟩ directions. Therefore, the distinction between sides and vertices must result from growth along directions at an acute angle from the ⟨111⟩ crystal axis. An examination of the tip of the crystals shows a rudimentary {111} face, normal to the growth direction and bounded by three flat {100} faces in positions corresponding to the sides of the triangle, between which are rounded projections in the ⟨110⟩ direction, extending out to form the vertices of the triangle. One may, therefore, predict that if a ⟨111⟩ crystal were removed from the melt, turned upside-down, and growth resumed in the opposite direction, the positions of the triangular sides and vertices would be reversed.

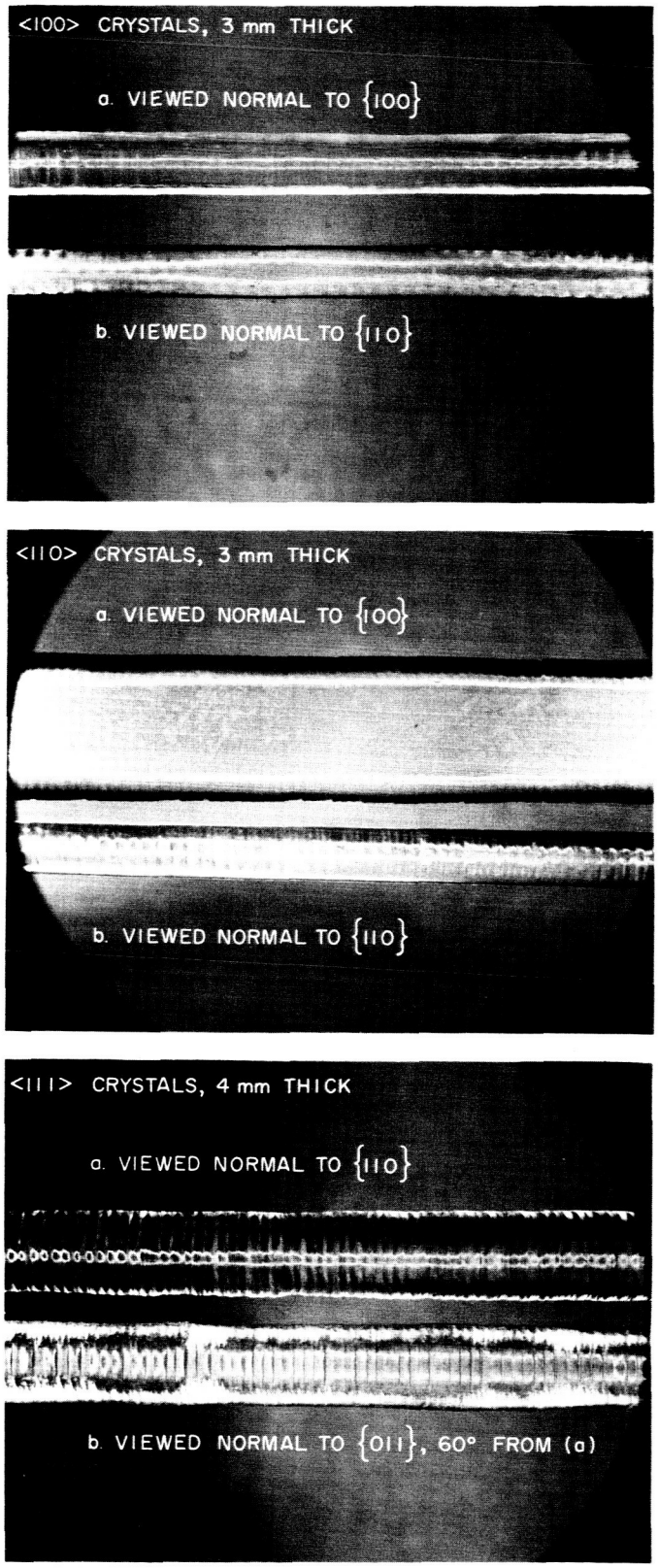

Figure 71. Sodium chloride crystals viewed from various angles

The ridges on the triangular sides are regularly spaced and apparently independent of thermal fluctuations (which do affect the overall diameter), pull rate, and seed rotation. An examination of a cleaved crystal in a goniometer indicates that the under surfaces of the ridges are {100} faces, whereas the upper surfaces are curved and of no especial orientation. This also applies to the ridged edges of the ⟨110⟩ crystals. This suggests that the ridges result from a slip-strike motion of the liquid–solid interface. This assumes that the crystal tip, at the surface of the melt tends to grow outward, perhaps because of rapid growth in the ⟨110⟩ directions. The under surfaces, however, are slow-growing {100} faces, so that a rim is formed which, as the crystal is pulled upward, carries the liquid meniscus up with it and continues to grow. Finally, when the surface tension is exceeded, the meniscus snaps back, and a new ridge begins to grow. This might result in an irregularity of growth rate which might adversely affect the perfection of the crystals.

The ductility of these crystals varies greatly with orientation. The ⟨100⟩ crystals can be bent in any direction. This plasticity is enhanced under water so that crystals can even be tied into knots (Fig 72). As has been previously reported (*RS 36-4*), the deformation is characterized by a complex network of {110} birefringence bands, probably resulting from dislocation pile-ups. The ⟨100⟩ crystals are also presumed to be ductile in tension; this has not been tried but qualitative tests show considerable ductility in compression. On the other hand the crystals show no obvious ductility in torsion, and exhibit brittle fracture without deformation if sufficient stress is applied. The ⟨110⟩ crystals show much greater resistance to bending in either the ⟨100⟩ or ⟨110⟩ direction. A crystal, water-polished to 4 mm diameter to eliminate possible complications from the ridges, was bent under water with considerable difficulty to an outer fiber strain of about 5%. Examination under polarized light showed no sharp {110} bands but rather a diffuse axial birefringence. On the other hand, the ⟨110⟩ crystals show some plasticity in torsion and can be bent in the {100} plane in the ⟨100⟩ direction, i.e., into a spiral. The ⟨111⟩ crystals so far appear to be brittle in both bending and torsion. Thus, all of the ductility so far observed can be accounted for in terms of slip of the {110} planes in the ⟨110⟩ direction, but this mechanism also predicts modes of ductility which have not been observed. For example, one would expect ⟨110⟩ crystals to bend very easily in the ⟨110⟩ direction by simple shear.

A quantitative investigation of the deformation characteristics of these crystals is now in progress.

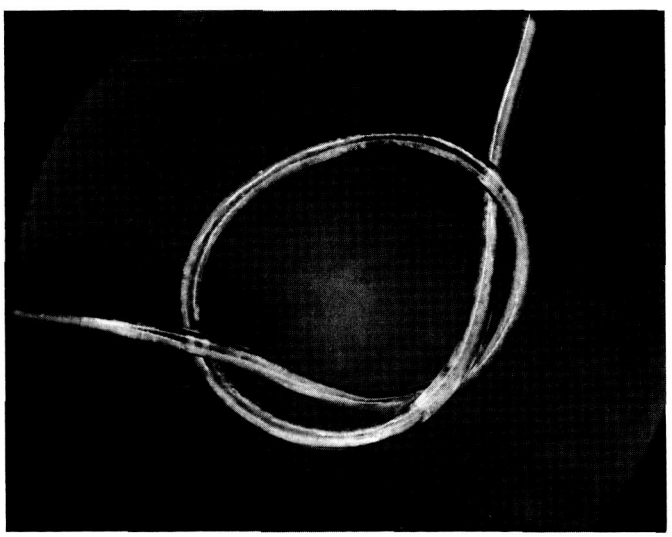

Figure 72. ⟨100⟩ sodium chloride crystal bent under water; diameter before immersion, 4 mm; diameter after bending, 2 mm

B. Graphite

W. V. Kotlensky

Graphite Tension Testing

In a recently completed series of tests on pyrolytic graphite, additional data have been obtained on the effect of strain rate on its tensile properties.

Tensile specimens used in these tests were machined from four blocks of pyrolytic graphite (24 × 6 × 0.25 in.) produced during the same run from CP methane by High Temperature Materials, Inc. The material was deposited at 2100°C and had a density of 2.20 gm/cm^3.

Definite growth cone size variations were apparent, and this led to the classification of specimens according to the growth cone diameter in the tensile specimen gage section as follows: small from 0.02 to 0.05 inch, and large from 0.05 to 0.10 inch. Generally, it was found that specimens with no large diameter growth cones in the gage section fractured at greater strengths and elongations than specimens with large diameter growth cones which usually fractured at a large growth cone.

The strain rate tests were made in duplicate at strain rates of approximately 2, 8, 30, and 160×10^{-4} sec^{-1} at room temperature, and at 2200, 2480, and 2760°C, respectively. The results of these tests are shown in Figure 73. As seen, there appears to be a definite strain rate effect on the ultimate tensile strength and elongation at 2480 and 2760°C, but no marked effect at room temperature and 2200°C. At a strain rate of 160×10^{-4} sec^{-1}, the ultimate tensile strength and the elongation at the four test temperatures are noted to be similar.

The decrease in tensile strength and elongation with increasing strain rate at 2480 and 2760°C may be dependent upon structural changes accompanying deformation which have been previously noted (Ref 62). At the lower strain rates, there is sufficient time for large increases in preferred orientation and crystallite perfection to occur. At the higher strain rates, the material fractures before such changes have time to occur. This effect is not noted at room temperature and 2200°C, because at these lower temperatures structural changes do not occur even at the lowest strain rates.

Although the relationship between the high-temperature tensile properties and the structure of pyrolytic graphite is not fully understood, the extent of stress-induced basal plane slip and plastic flow around stress concentrations would seem to be important. A complete study of the changes in structure which occur during this series of tests should provide information on this point.

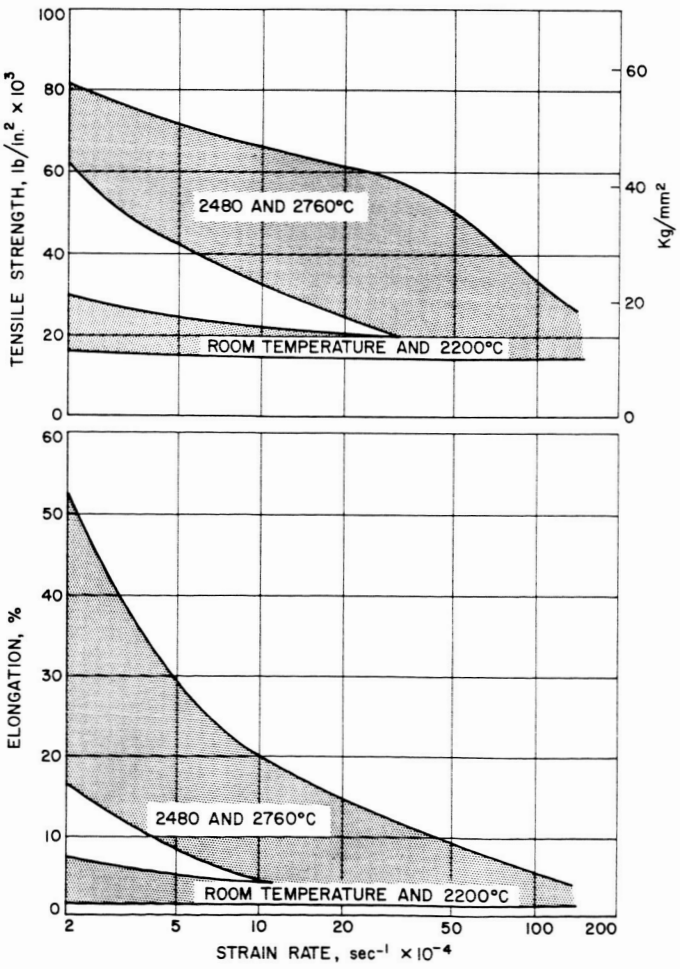

Figure 73. Ultimate tensile strength and elongation vs strain rate for pyrolytic graphite, Lot 170

C. Endothermal Materials

R. G. Nagler

A system for the collection and fractionation of degradation products from polymeric materials has been constructed and calibrated for use with the arc imaging furnace and radiant heater facilities. A schematic of the system is shown in Figure 74, and a photograph of the actual setup in conjunction with the arc imaging furnace described earlier (*RS 36-8* and *36-9*) is shown in Figure 75. The system is similar to that described by Friedman (Ref 63) with these modifications. Parallel collection systems are provided in order that, when possible, some differentiation may be made between the initial and the more steady-state products of degradation. Blowout

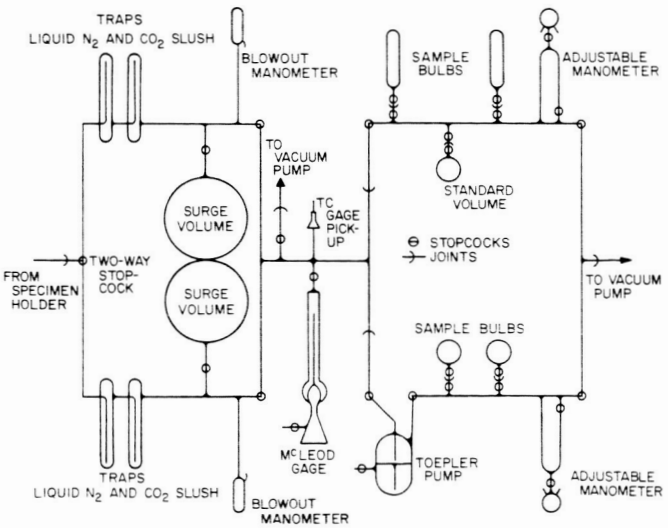

Figure 74. Collection and fractionation apparatus for degradation of polymeric materials

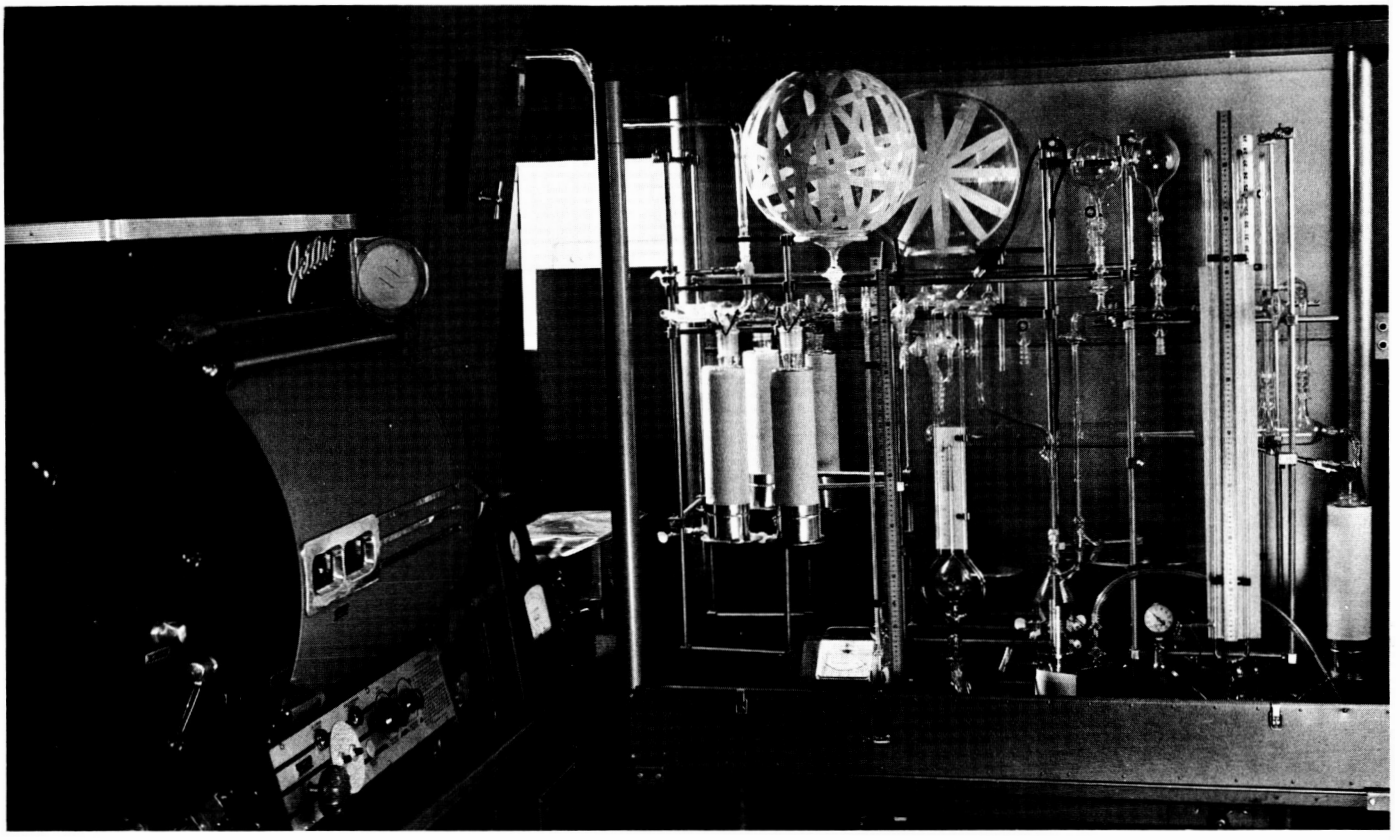

Figure 75. Degradation products collection apparatus in conjunction with arc imaging furnace facility

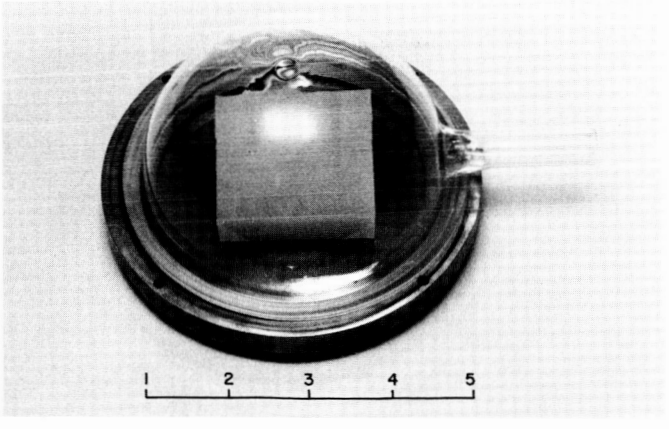

Figure 76. Specimen holder and dome for collection of degradation products from arc imaging furnace heating

manometers have been added to the collection system to act as a release for pressure surges. These manometers may also be used to monitor the amount of light fraction (i.e., the low molecular weight gases not trapped in liquid nitrogen) collected during a run.

A photograph of the specimen holder and dome used in this investigation is shown in Figure 76. As reported by Friedman (Ref 63), clouding of the dome caused by specimen splattering during vacuum operation is one of the major restrictions in the usefulness of this equipment. This problem has been reduced by using the pyrolytic graphite flux distributor described in *RS 36-8* when dealing with low heat fluxes or by providing inert atmospheres at pressures closer to atmospheric when dealing with high heat fluxes.

XI. Engineering Research

Solar Proton Shielding

D. F. Spencer

1. Correlation of February 23, 1956, Solar Flare Data

This analysis is a prelude to the determination of shielding weights for interplanetary manned spacecraft from a high-energy, high-intensity solar flare. The flare studied is the one which occurred on February 23, 1956. This flare should represent the maximum intensity of high-energy protons which need be shielded against.

An attempt to systematically correlate the experimental data of Van Allen and Winckler as reported by Bailey (Ref 64) and that of Meyer, Parker, and Simpson (Ref 65) has been made in order to determine the spread in integrated flux from this storm.

The method employed was to utilize the time- and energy-dependent data of Reference 65 to determine the diffusion coefficient of the protons vs energy. Where necessary, the particle integral intensity data of Reference 65 were extrapolated by means of an R^{-7} law as prescribed by the author, R being the magnetic rigidity of the primary particles. Although it is realized that this produces an overestimate of particle flux in the low-energy region, it does indicate a maximum flux; thus, it will produce a maximum shield thickness and weight.

Reference 65 provides a theoretical model that can be employed in determining the time-dependent characteristics of a solar storm. In particular, they obtain a solution to the time-dependent diffusion equation

$$\frac{\partial J(E)}{\partial t} = \kappa(E)\,\nabla^2 J(E) \tag{1}$$

where $J(E)$ is the particle density, t the time, κ the diffusion coefficient, and ∇^2 the Laplacian operator in spherical coordinates. This equation, when solved subject to their stipulated boundary conditions, yields the solution

$$J(E,r,t) = \frac{2}{3}a^4\frac{J_0(E)}{r}\sum_{n=0}^{\infty}\alpha_n^3\, e^{-\kappa\alpha_n^2 t}\,\frac{\sin[\alpha_n(b-r)]}{\sin[\alpha_n(b-a)]}$$

$$\left[\left(\alpha_n b + \frac{1}{3}a^2 b\alpha_n^3 + \frac{1}{9}a^4 b\alpha_n^5 - \frac{1}{9}a^5\alpha_n^5\right)\right] \tag{2}$$

where the roots α_n may be determined from

$$\left(\frac{1}{3}a^2\alpha_n^2 - 1\right)\sin[\alpha_n(b-a)] = a\alpha_n\cos[\alpha_n(b-a)] \tag{3}$$

In this equation, a is the inner shell radius, b the outer shell radius, $J_0(E)$ is the initial particle intensity, and r the radial coordinate. For $r < a$, the case of detection at the Earth's orbit,

$$J(E,r,t) = J(E,a,t) \tag{4}$$

Meyer, et al (Ref 65), only consider certain asymptotic solutions of the above equation. In order to utilize the preceding treatment on the data of Van Allen and Winckler, the author with the assistance of Mrs. C. Level, who performed the numerical computation, obtained exact solutions subject to the condition that $b = 5$ AU and $a = 1.4$ AU, as proposed in Reference 65.

This procedure then allowed the determination of $J(E,t)$ for the data of Reference 64 based on an extrapolation of $J\alpha R^{-5}$ as proposed by Van Allen and Winckler. This data was normalized to the experimental point at 17 hours, $R = 1.2$ Bev and $J = 1.3$ protons/cm^2 sec steradian. This extrapolation produces a maximum estimate of the particle fluxes in the high-energy region.

A linear rise in intensity from the initial detection of the flare to $t = 40$ minutes as shown from the data in

Reference 65, was assumed to determine the integrated dose. The diffusion coefficient vs energy is shown in Figure 77 as determined from the data of Meyer, et al.

Qualitatively, it may be argued that the trend is in the correct direction. For a collisionless plasma in an external magnetic field, it can be shown that

$$\kappa \propto \frac{1}{E^{1/2} n} \tag{5}$$

Since n increases much more rapidly than E decreases, κ should decrease. Actually, κ is a more complicated function than that given, since the solar storm particles must diffuse through the more dense low-energy solar wind. This tends to decrease the effect of n, the storm particle concentration on κ. This is seen to be consistent with the calculated values of κ (Table 12).

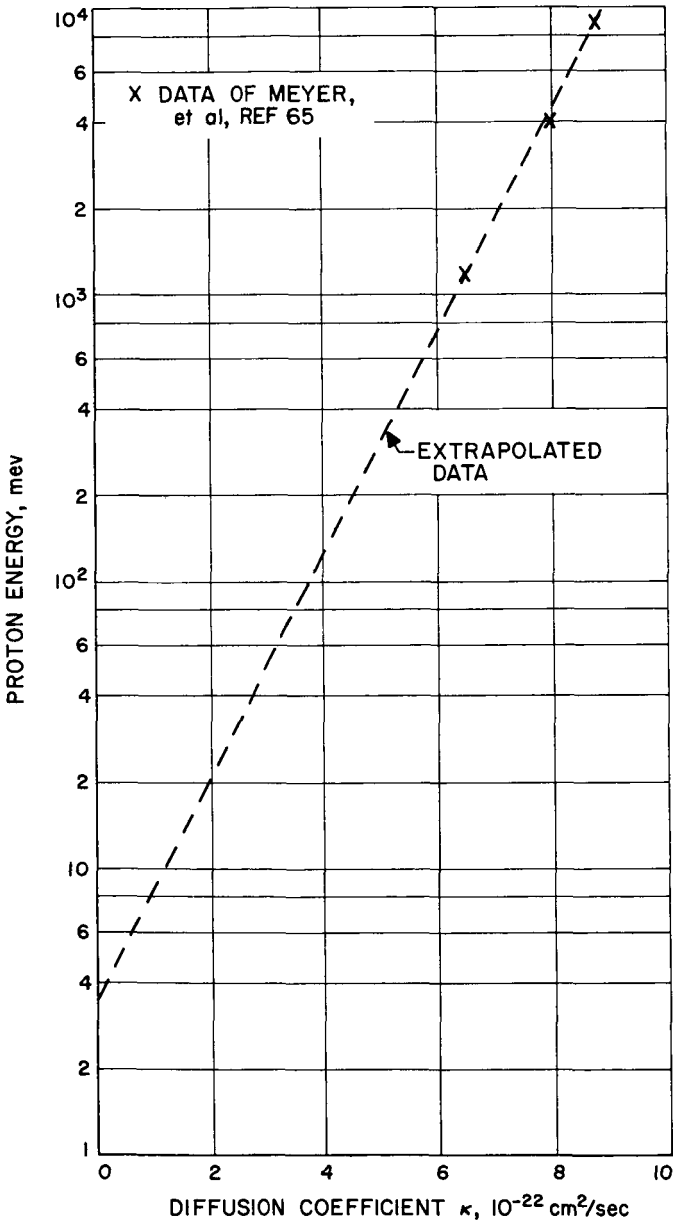

Figure 77. Solar flare proton diffusion coefficient vs proton energy derived from data of Meyer, et al

The time-integrated data of Meyer, et al and Bailey and the ratio of the intensities are tabulated in Table 12. It may be seen that in the energy range where the experimental data coincides ($E = 410$ mev), the agreement of results is quite good, using the theoretical model of Reference 65. Due to the difference in rigidity dependence determined by the two authors, there is quite a large divergence at the high- and low-energy ends of the spectrum. However, these data, coupled to a shield analysis which allows for first-order secondary neutron production, should predict an upper and possibly a lower shield weight limit for a high-energy, high-intensity solar storm. These results will be reported in subsequent *Research Summaries*.

Table 12. Integrated flux from February 23, 1956 solar flare

Energy, mev	Integrated flux, protons/cm²		Bailey flux
	Meyer data	Bailey data	Meyer flux
5	2.7×10^{15}	4.6×10^{11}	1.7×10^{-4}
110	3.5×10^{10}	1.3×10^{9}	3.7×10^{-2}
410	2.1×10^{8}	1.4×10^{8}	0.53
1200	2.1×10^{6}	7.7×10^{6}	3.6
4100	2.4×10^{4}	5.6×10^{5}	23
9100	2.6×10^{2}	3.7×10^{4}	140

2. Some Temporal Aspects of Solar Flares

A theoretical treatment of the trapping and loss of protons from a solar flare is difficult to formulate due to limited information on the mechanism of solar eruptions and interplanetary magnetic fields. Although this analysis does not provide the solution to this problem, it does indicate some interesting aspects.

If we assume that the protons are ejected radially from a point source and that only a z component of the magnetic field is present (which is approximately the case if the particles are emitted near the Sun's equator and the only component of the magnetic field is that of the interstellar field), to order of magnitude, the gyration radius of the particles is

$$r = \frac{mv}{\left(\frac{e}{c}\right) B_z} \tag{1}$$

where r is the gyration radius of the particle, m the particle mass, $e = 4.8 \times 10^{-10}$ stat coul, c the velocity of light, v the particle velocity, and B_z the external magnetic field strength. For 1.2 Bev incident particles (an upper limit for most flares) and with the intergalactic magnetic field strength of 6×10^{-6} gauss (Ref 66), the gyration radius is approximately 0.028 AU. This indicates that the thickness of the spherical shell assumed by Meyer (Ref 65) is too large (≈ 4 AU) and that the actual case is a thin region.

If we then consider the thin shell approximation given in Reference 65, the diffusion coefficient is 3.4×10^{20} cm²/sec for 1.2 Bev particles at the Earth's radius rather than 6.5×10^{22} cm²/sec as previously determined.

If the inner shell radius is retained at 1.4 AU, a fit to the experimental data using this diffusion coefficient can be obtained. The two models, thick and thin shell approximations, are compared in Figure 78.

Although the thick shell approximation appears to be the best fit to the data, the thin shell approach probably lies within the accuracy of the measurements (which is not mentioned by Meyer, et al).

Implicit in the above argument is the fact that the region from the Sun to 1.4 AU is, essentially, free of magnetic fields perpendicular to the direction of motion of the particle. If one assumes a normal density of low-energy particles (≈ 5 kev) of 100 protons/cm³, it is possible to determine the magnetic field at the Earth's orbit required to concur with the experimental diffusion coefficient considering the diffusion of the high-energy particles through the low-energy background.

Based on diffusion theory in the presence of an external magnetic field, the axial magnetic field strength at the Earth's distance, is of order 10^{-15} gauss. Thus, there appears to be a very low axial field strength at the Earth during a solar storm such as that of February 23, 1956. This suggests that the solar protons sweep out the interplanetary and interstellar magnetic field as they leave the Sun.

Finally, it is necessary to determine whether the interstellar magnetic field strength is sufficient to balance the kinetic pressure of the ejected particles. It is assumed that the normal low-energy background is distributed

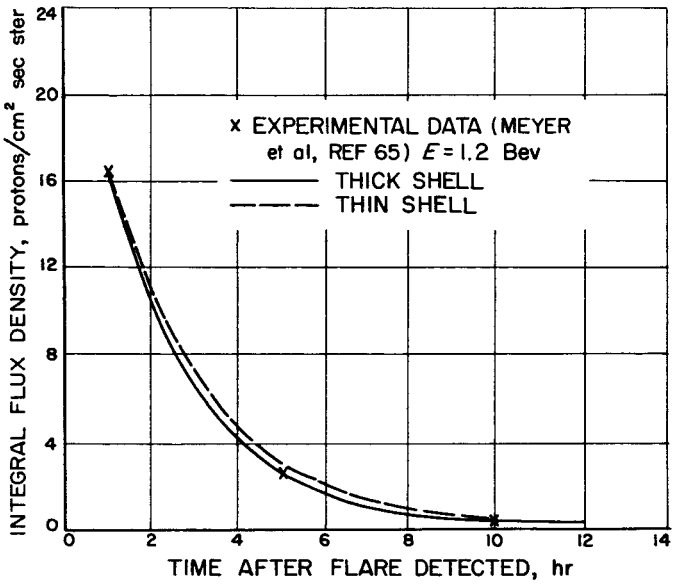

Figure 78. Comparison of thick-shell and thin-shell theory for solar flare of February 23, 1956

uniformly so that

$$\frac{B_z^2}{8\pi} = p \tag{2}$$

where B_z is the external magnetic field strength, and p is the total kinetic pressure of the protons from the solar storm, i.e.,

$$p = \sum_{i=1}^{N} \bar{J}_i (m_i \bar{E}_i)^{1/2} \tag{3}$$

where $\bar{J}_i$ is the ith average integral flux, $\bar{E}_i$ is the ith average energy, and m_i the proton mass.

Based on the extrapolated data of Meyer, et al, the external field required to confine all particles above 1.2 Bev energy is 6×10^{-6} gauss (the value of the interstellar magnetic field). In order to confine the higher density, lower energy protons, a magnetic field of approximately 10^{-3} gauss is required. This requires that the protons carry magnetic field lines with them. Since the axial field at the Earth's distance is quite small, as seen previously, it appears that a radial magnetic field frozen to the particles exists and that this field is converted to a z direction magnetic field at some distance past the Earth's orbit. This is consistent with the so-called "scrambled magnetic field" hypothesis which has been proposed.

PROPULSION DIVISION

XII. Liquid Propellant Propulsion

A. Combustion and Injection

G. I. Jaivin and A. J. Kelly

1. Atomization and Injection Hydraulics

Work has continued on the measurement of the local thickness and average velocity of a liquid sheet. The experimental method employed and a schematic drawing of the equipment can be found in *RS 36-5*, Volume II. Briefly, the technique involves the use of a thrust balance to measure the momentum of a sheet sector which, in conjunction with flow rate measurements, allows the sheet velocity and thickness to be computed.

Data obtained to date by this method are shown in Figure 79. The lowest velocity that could be measured corresponds to the condition of initial breakaway of the sheet from the edge of the probe. As the sheet velocity is increased, the radius at which sheet disintegration takes place decreases. The upper limit on velocity was established by the approach of the disintegration zone of the sheet to the probe location. As this zone approached the probe, a high-pitched whistling noise was audible and became progressively louder with closer approach. When the disintegration zone reached the probe the fluid leaving the probe became intermittent which resulted in erratic thrust readings. Data were taken up to the point where the noise generated by the breakup region became noticeable. The set of curves presented can therefore be considered to be bounded at the higher velocity end by

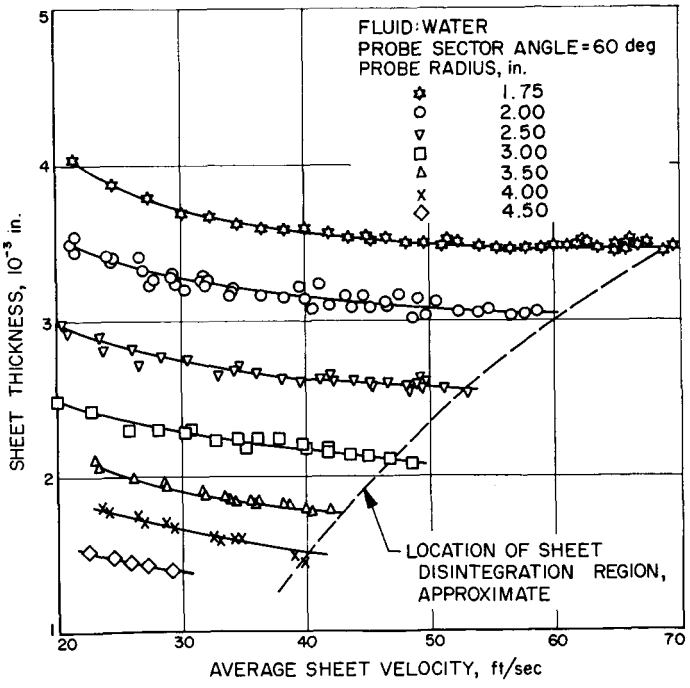

Figure 79. Sheet thickness vs sheet velocity at various radii

a line representing the approximate location of the sheet disintegration region.

Data representing the sheet thickness as a function of probe position for several different velocities are shown in Figure 80. It is of interest to note the shape of the curves presented. From continuity considerations, it is recognized that if the velocity throughout the sheet were constant the curves presented in Figure 80 should be hyperbolic in form. The departure from the hyperbolic shape is, in part, a measure of the velocity variations in the sheet. For the data shown, the maximum difference between a hyperbola passed through the midpoint of any curve and the curve itself does not exceed 4%.

The decrease in sheet thickness with increasing velocity represents the *vena contracta* effects induced by the sharp-edged orifice used to produce the sheet. No correction has been made to the data to account for the angle at which the sheet leaves the surface of the probe. The analysis assumes this angle to be 90 degrees. Measurements of this angle indicate that, in the worst case, the data may be in error by less than 1% because of this effect.

Work is in progress to evaluate photographically the visual characteristics of several reference sheet configurations. It is intended that this work will serve to demonstrate the gross differences which exist in the various types of sheets currently under investigation.

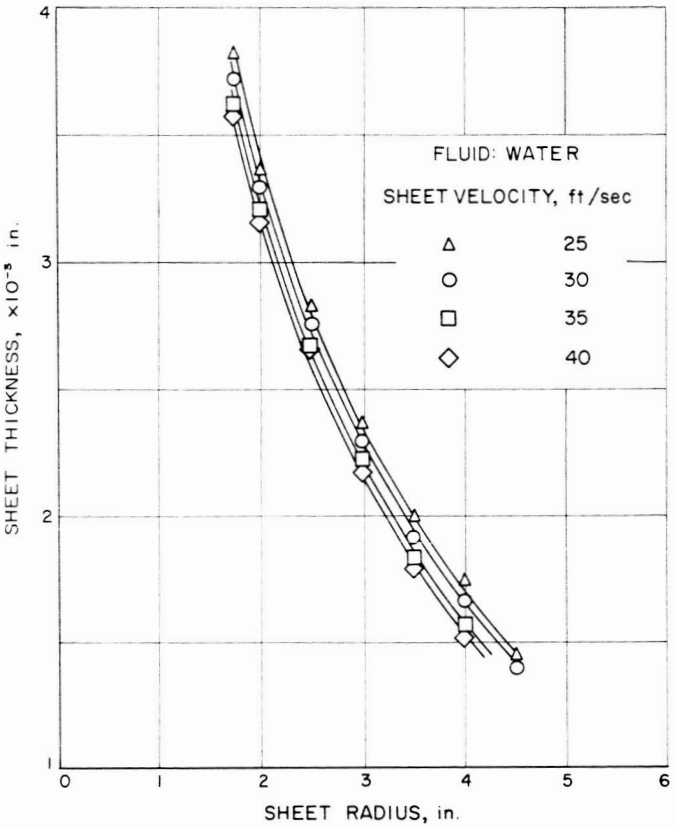

Figure 80. Sheet thickness vs sheet radius at various velocities

2. Resonating Chamber

The resonating chamber shown in Figure 81 was designed to provide a controllable source of sinusoidal gas pressure oscillations for use in the study of hydraulic feed systems and liquid jet dynamic characteristics. In order to simulate, as realistically as possible, the pressure field of a rocket chamber, the pressure fluctuations present in a cylindrical cavity driven at, or near, one of its various resonant frequencies were utilized.

The resonating chamber, previously described in *RS 36-6*, Volume II, Page 44, has been modified by the addition of a servocontrol system. The output of the tachometer, sensing siren speed and therefore the gas modulation frequency, is compared to a reference and the resulting error signal (tachometer output signal minus reference signal) is used to control a servovalve. The servovalve is in a shunt line between the inlet and outlet ports of the hydraulic motor which drives the siren. In the neutral position, it permits approximately 10% of the full-load flow to the hydraulic motor to be bypassed. The use of this bypass control permits the frequency of the siren to be controlled to within ±3 cps over its full frequency range (from 250 to 3000 cps), for extended periods of time.

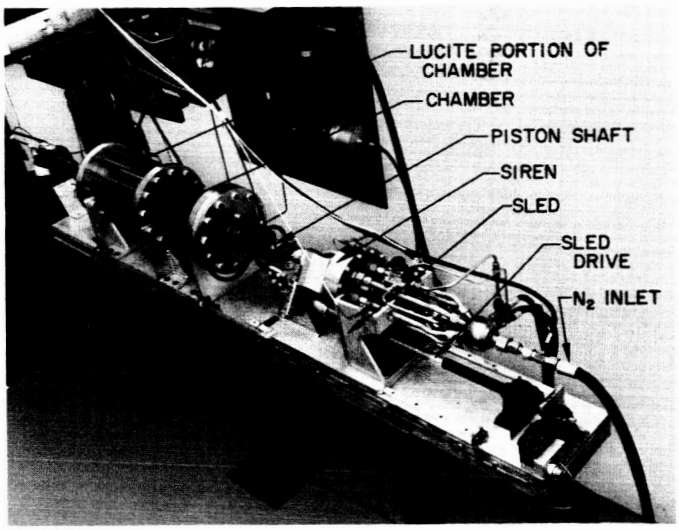

Figure 81. Resonating chamber

In order to check out the operation of the servocontrol system adequately, and accurately determine the various modes of operation of the resonating chamber, a series of tests has been conducted.

a. Instrumentation. Static chamber pressure was monitored with a standard laboratory test gage and the dynamic chamber pressure was measured with Kistler PZ-14 pressure transducers. The Kistler transducers were mounted on a common radial line 1.75 cm and 7.00 cm from the centerline of the chamber flush with the inside of the cylinder end closure, and the outputs were recorded on a Tektronix 551 dual-beam oscilloscope. A chromel–alumel thermocouple, mounted 1 cm from the centerline of the chamber in the same plane as the Kistler pressure transducers was used to measure chamber gas temperature. The output of the siren tachometer was monitored by a Beckman digital counter, which was set so as to display the siren frequency averaged over 1-second intervals.

b. Theory and experimental results. Using small perturbation theory, the resonant frequencies of a right circular cylinder filled with a gas of uniform properties can be written as:

$$w_{m,n} = c\left[\left(\frac{\alpha_m}{R}\right)^2 + \left(\frac{n\pi}{1}\right)^2\right]^{1/2}$$

where $w_{m,n}$ is the resonant frequency, c the acoustic velocity, α_m the mth zero of the Bessel function J_1, R the radius of the chamber, l the length of the chamber, and n an integer.

Initial measurements have indicated that a reasonable correlation exists between this equation and experiment. Figure 82a is a photographic analog of the pressure variation due to the first longitudinal mode ($m = 0$, $n = 1$, i.e., 0, 1 mode). The bottom trace represents the output of the transducer mounted 1.75 cm from the centerline of the chamber, and the upper trace from the one mounted 7.00 cm from this centerline. The vertical scale is 2.5 psi per major division and the horizontal scale 2 ms per major division. The counter indicated a frequency of gas modulation of 482 ±3 cps. Using the acoustic velocity of nitrogen, at the temperature indicated by the thermocouple, the mean chamber pressure (91 psig) and the known length of the chamber, the frequency for the first longitudinal (0, 1) mode calculated from the analytical relationship was 475 cps.

It was found that, when the chamber was driven at the exact calculated resonant frequency, distorted pressure wave shapes of the form shown in Figure 82b (same scales as Figure 82a, frequency 478 ±3 cps) were produced. In actual operation, the chamber was excited at a frequency slightly higher than that corresponding to the resonance peak so as to get a nearly pure sinusoidal waveform.

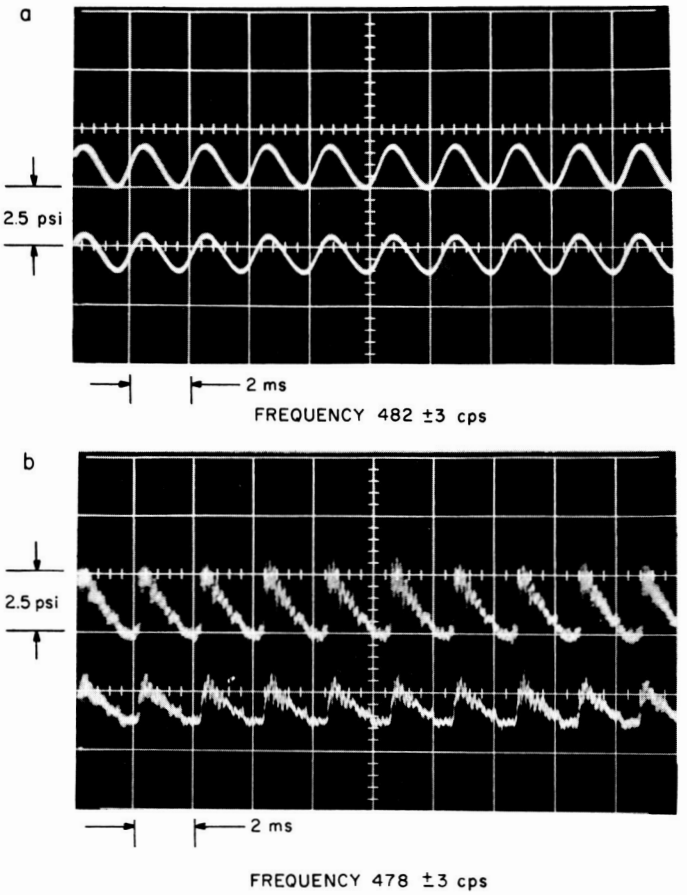

Figure 82. First longitudinal mode resonance

Figure 83 represents pressure variations attributable to a typical radial mode ($m = 1$, $n = 0$, i.e., 1, 0 mode). The transducers are in the same position and the vertical scale is the same as in Figures 82a and b. The time scale is 0.2 ms per major division. The high-frequency hash (at about 40 kc), which appears on this trace, can be

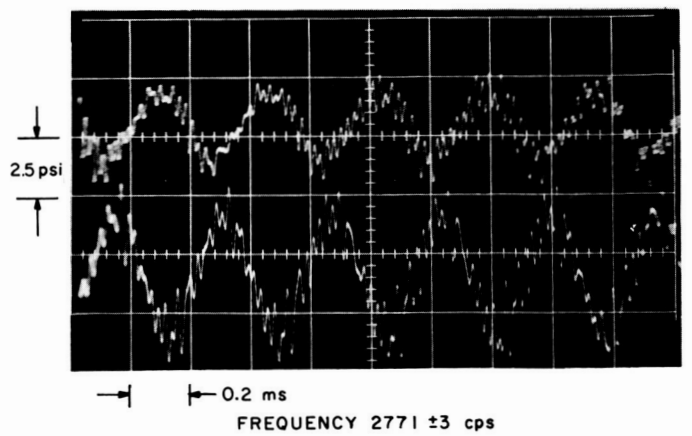

Figure 83. Radial mode resonance

attributed to the Kistler gages ringing at their natural frequency, induced by high-frequency oscillation of the chamber end closure. The calculated resonant frequency, using the chamber conditions indicated at the time the data for Figure 83 were taken, is 2740 cps, and the predicted peak amplitude ratio (the peak pressure amplitude 7.00 cm from the centerline of the chamber, top trace, over the peak pressure amplitude 1.75 cm from the centerline, bottom trace) is -0.459. The minus sign indicates that the two pressures are 180 degrees out of phase. The measured frequency was 2771 ± 3 cps, and the amplitude ratio -0.49 ± 0.05, so that it can be seen that the experimental correlation is quite good.

Work is continuing on the reduction of data from tests wherein a constant-area liquid line and jet were subjected to oscillating chamber pressures. These series of experiments will be described in the near future.

B. Heat Transfer and Fluid Mechanics

A. B. Witte and E. Y. Harper

Heat Transfer in Rocket Motors

An experimental investigation of heat transfer in rocket motors is being continued to determine the effect of thrust-chamber geometry, injector type, and operating conditions on the axial heat flux distribution in thrust chambers. These tests are being made at chamber pressures between 100 and 300 psia with nitrogen tetroxide (N_2O_4) and hydrazine (N_2H_4) as bipropellants at a nominal mixture ratio of 1.0. Semilocal, steady-state heat fluxes have been measured calorimetrically in 8-to-1, 4-to-1, and 1.64-to-1 contraction-area-ratio nozzles and were compared in References 67 and 68, and in *RS 36-7*, Volume II, and *RS 36-8*, Volume I, to the analytical prediction given in Reference 69.

Recently, a 1.64-to-1 contraction-area-ratio uncooled nozzle, which has the same inner contour as the 1.64-to-1 calorimetrically cooled nozzle described in References 67 and 68 was fabricated, and instrumented with numerous wall thermocouples to deduce local values of heat flux by a transient wall temperature measurement technique. A more detailed description of this nozzle is found in *RS 36-9*, Volume I. An eight-orifice pair, splash plate (Enzian) type injector and a 17.0-inch L^* were used for all tests. The combustion chamber was 5 inches in diameter and 8 inches long. For the tests discussed here, the chamber pressure was approximately 97 psia and the thrust was 1200 pounds.

Figure 84 shows a typical variation of experimental heat flux with wall temperature for a transient thermocouple plug in the uncooled nozzle. To interpret the results of Figure 84, it is necessary to recall from *RS 36-9*, Volume I, the procedure of calculating heat fluxes in the uncooled nozzle. The distribution of temperature with respect to radial distance and time between two recorded temperature boundary conditions is deduced by solving the heat conduction equation in finite difference form on an IBM 7090 computer. The inner thermocouple is embedded nominally 0.020 inch from the gas-side surface. A fifth-order polynomial is fitted to the generated temperature distribution and extrapolated to the surface where the heat flux is then calculated by evaluating the Fourier equation. The severe oscillations (Fig 84), which appear for the first 0.8 second (eight lowest wall temperature points), are the combined effect of the combustion starting transient and the initial poor fit and, consequently, inaccurate extrapolation of the polynomial to the surface. When a computer check case was run using smooth input data (obtained from an analytical solution) for the inner thermocouple temperature boundary condition, approximately five time intervals (0.50 sec) were required before the oscillation ceased. Therefore, it is believed that the severe initial oscillations shown in Figure 84 do not represent real changes in heat flux. Chamber pressure records indicate that it requires approximately 0.125 second to obtain the total chamber pressure from ignition. The highest heat flux is then actually attained after approximately 0.125 second, which occurs after two ther-

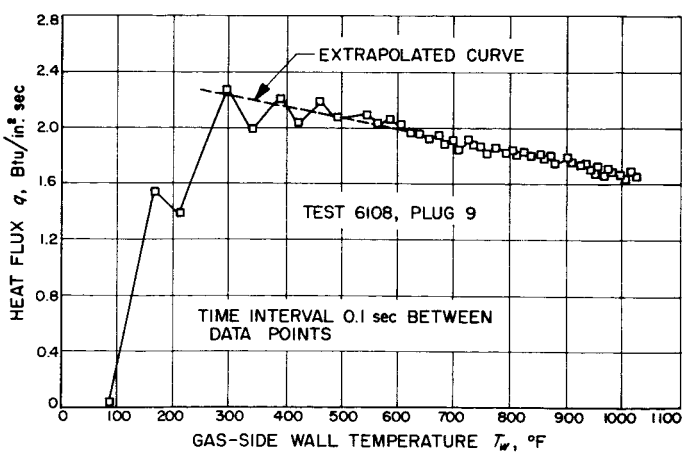

Figure 84. Typical heat flux vs gas–side wall temperature for uncooled nozzle

mocouple samples. The combined effect of the relatively slow sampling rate (every 0.050 sec, although input temperatures to the computer were in 0.100-sec time increments) and recording response time causes the heat flux curve to rise gradually instead of peaking immediately at approximately 0.125 second. Any data taken from the oscillation region were obtained by extrapolation back from the nearly linear region following the oscillations. Curves of this type were drawn for all 17 transient thermocouple plug locations in the nozzle so that the heat flux variation with wall temperature could be interpreted. The orientation of these plugs is shown in Figure 85.

Figure 86 shows the variation of the experimental enthalpy heat transfer coefficient h_{ie}, with gas-side wall temperature for one of two tests described here at a chamber pressure of 97 psia. The enthalpy heat transfer coefficient is obtained from Equation (1) as:

$$h_{ie} = \frac{q_e}{(i'_0 - i'_w)} \tag{1}$$

where $(i'_0 - i'_w)$ is the difference between the stagnation and wall enthalpy as defined in References 67 and 68, and q_e is the experimental value of heat flux taken from curves similar to the one shown in Figure 84. The temperature heat transfer coefficient h_T (commonly denoted as h) is related to h_i by Equation (2)

$$h_i = \frac{h_T}{\bar{c}_p} \tag{2}$$

where $\bar{c}_p$ is the average specific heat (including effects of chemical reaction) across the boundary layer. The dashed portion of each solid curve shown in Figure 86 represents results which were read from the extrapolated region of curves similar to Figure 84. A cursory observation of the dependence of h_{ie} on T_w at the various plug locations indicates several trends. All but one of the curves (that for Plug 15) at constant area ratio exhibited a negative slope which is predicted by Reference 69, being a consequence of the variable properties correction. Plug 15 exhibited a positive slope which is contrary to prediction and will be discussed in a later comparison. For purposes of comparison, the predicted slope (slope only, not magnitude of h_i predicted) is shown in Figure 86 for Plugs 7, 11, and 15. Except for the results of Plugs 12, 13, and 14, in the contraction region, h_{ie} increases with decreasing area ratio and increasing mass flux as expected. Contraction region heat fluxes which equal or exceed the throat values similar to the values of Plugs 12 and 13 have been observed and reported in References 67 and 68. There, it

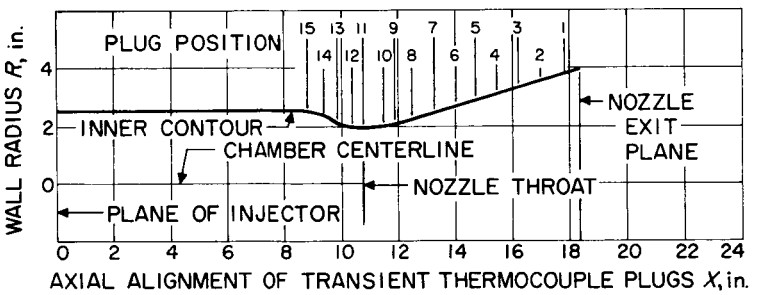

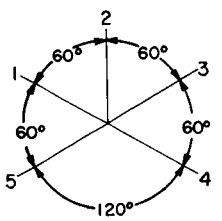

CIRCUMFERENTIAL ALIGNMENT ORIENTED LOOKING UPSTREAM (NUMBERS INDICATE CIRCUMFERENTIAL POSITION)

PLUG No.	AXIAL DIST[a] in.	AREA RATIO	CIRCUMFERENTIAL POSITION	NOZZLE REGION
1	17.70	3.47	1	EXPANSION
2	17.04	3.14	3	
3	16.29	2.79	1	
4	15.54	2.45	3	
5	14.79	2.14	1	
6	14.04	1.85	3	
7	13.29	1.58	1	
8	12.54	1.33	3	
9	11.92	1.10	1	
10	11.57	1.03	3	EXPANSION
11_1	10.88	1.00	2	THROAT
11_2	10.88	1.00	4	
11_3	10.88	1.00	5	THROAT
12	10.42	1.02	1	CONTRACTION
13	9.92	1.09	3	
14	9.42	1.29	1	
15	8.92	1.50	3	CONTRACTION

[a] AXIAL DISTANCE FROM NOZZLE ENTRANCE PLANE

Figure 85. Transient thermocouple plug locations in uncooled nozzle

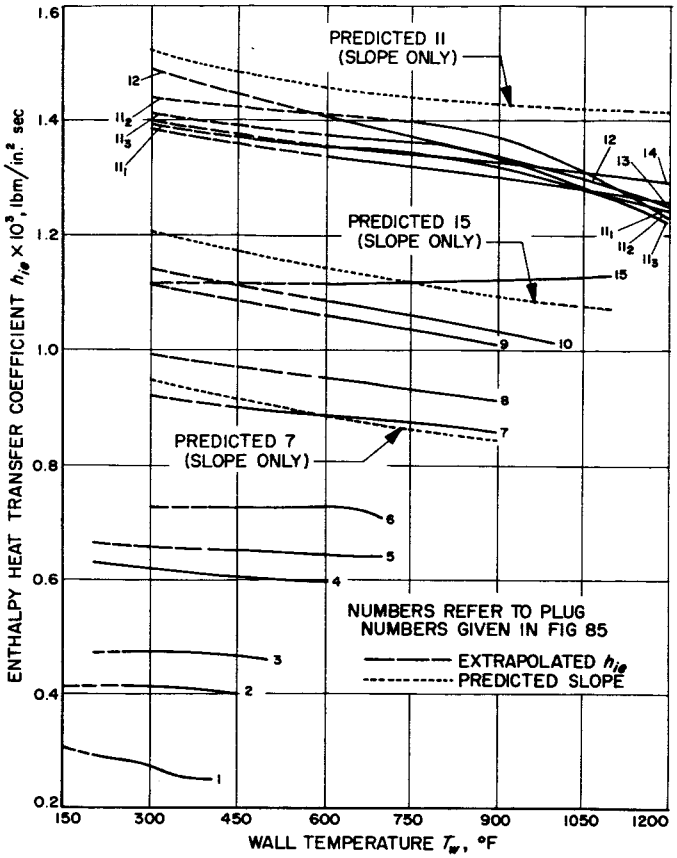

Figure 86. Enthalpy heat transfer coefficient vs wall temperature for Test 6107

was concluded that this shift of heat flux maxima was due only in part to the sonic line shift discussed in Reference 70. The high value of h_{ie} at Plug 14 is believed due to local combustion effects causing locally high velocities.

The axial heat flux distributions for the uncooled nozzle at wall temperatures of 400, 600, and 900°F, respectively, are compared with the prediction of Reference 69 in Figures 87 and 88. In addition, Figure 87 includes the results of a test (Test 60-8) using an identically inner contoured calorimetrically cooled nozzle at nominally the same wall temperature. The predicted heat flux curve is based on that c^* determined for the uncooled tests. The prediction will suffice, within 1%, for the calorimetric test as well. The uncooled nozzle operating conditions are shown in Table 13.

The scatter in the heat flux data from the two uncooled tests appears to be about the same, yet Test 6108 generally indicates higher heat flux values in the contraction and throat regions than does Test 6107. Inspection of the circumferential throat measurements of heat flux during either test indicates an apparent 5% repeatability

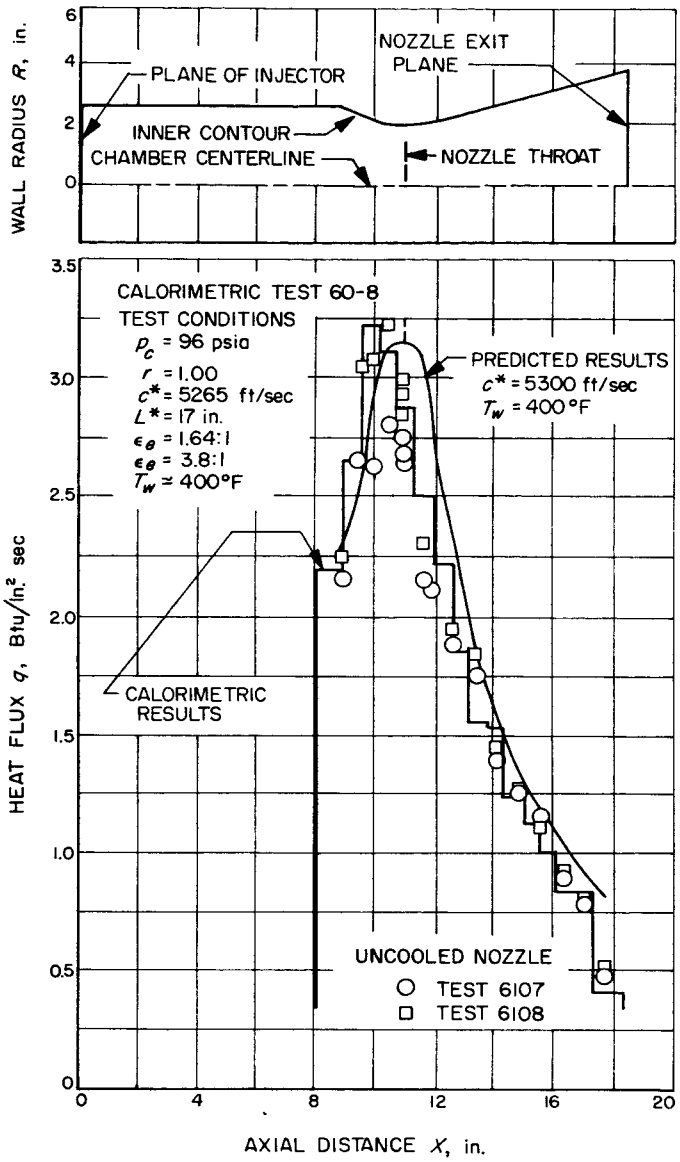

Figure 87. Comparison of calorimetric and uncooled heat flux for 1.64-to-1 nozzle

which includes both experimental error and circumferential variation in heat flux between the three measurement locations. In Figure 87, there is generally good repeatability between uncooled nozzle tests, and good agreement between the uncooled and calorimetrically cooled nozzle results in the expansion region. The agreement seen in this region indicates that axial temperature gradients in the uncooled nozzle are not severe enough to significantly alter heat fluxes obtained by the transient thermocouple method (based on the assumption of only radial heat flow) compared with those obtained by the steady-state calorimetric measurements. These preliminary results suggest that the transient thermocouple

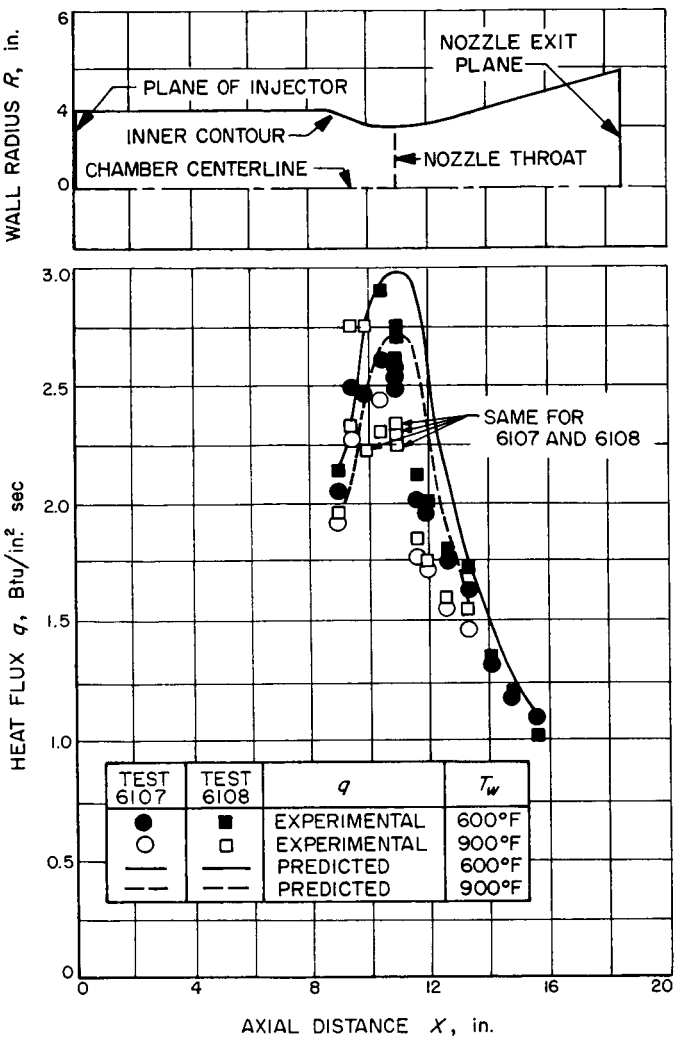

Figure 88. Heat flux distribution of uncooled nozzle at 600 and 900°F gas–side wall temperature

method of determining nozzle heat flux distributions is valid for the conditions of these tests. Further data must be obtained to demonstrate its general validity.

The results of both the uncooled and the calorimetrically cooled nozzles in the expansion region indicate, as has past experience, that the prediction overestimates the heat flux. Calculations indicate that at 97-psia chamber pressure flow separation occurs approximately 17.0 inches downstream of the injector at an area ratio of 3.17. This is indicated by the low value of heat flux at the last plug (Plug 1) and last calorimetric cooling passage at the nozzle exit.

It is speculated here, as in References 67 and 68 for the calorimetric results, that differences in heat flux for the contraction and throat region among Tests 6107, 6108, and 60-8 are due in part to the nonuniformities of the combustion process which significantly perturb the uniform flow model in these regions. Differences may also arise between the uncooled and calorimetric results because the plugs indicate point values of heat flux, whereas the calorimetric results represent an average value for the axially short circumferential cooling passage. The results of Plug 15 indicated an unusually broad oscillating heat flux maximum with temperature and a positive rather than a negative slope of h_{ie} vs T_w (Fig 86). The slope of the extrapolated curve of heat flux vs wall temperature was only slightly negative compared to trends seen with all other plugs. Since no irregularities in input data and computing procedure were observed for this thermocouple plug, no explanation can be made at this time concerning the atypical slope correlation of Plug 15 in Figure 86.

Table 13. Uncooled nozzle operating conditions

Test No.	Chamber pressure, p_c, psia	Mixture ratio, r	Characteristic velocity, c^*, ft/sec	Characteristic length, L^*, in.	Contraction area ratio, ε_c	Expansion area ratio, ε_e
6107	96.96	0.983	5300	17.0	1.64 to 1	3.78 to 1
6108	97.62	0.991	5299	17.0	1.64 to 1	3.78 to 1

The heat flux distributions taken at 600 and 900°F wall temperature shown in Figure 88 generally follow the same trends that were established at 400°F wall temperature in Figure 87. There is, however, much closer agreement of nozzle heat fluxes between Tests 6107 and 6108 at 900°F wall temperature than at 400 and 600°F wall temperature. The values of heat flux at 900°F wall temperature occur several seconds after the lower wall temperature points and are in a region of very low heat flux oscillation of the type described previously (Fig 84). It is believed that the lesser agreement at lower wall temperatures is partly due to the inability to properly extrapolate the data into the region of oscillating heat fluxes. Since plug positions in the expansion region have lower heat fluxes and hence attain relatively lower wall temperatures, points at the higher expansion area ratios are not available for comparison at 600 and 900°F with data at 400°F wall temperature. The decrease in the magnitude of heat flux for increasing wall temperatures of 400, 600, and 900°F is in agreement with the decreased driving potential for heat transfer at these higher wall temperatures.

A non-dimensional comparison of experimental and predicted enthalpy heat transfer coefficients h_{ie}/h_{ia}, for the

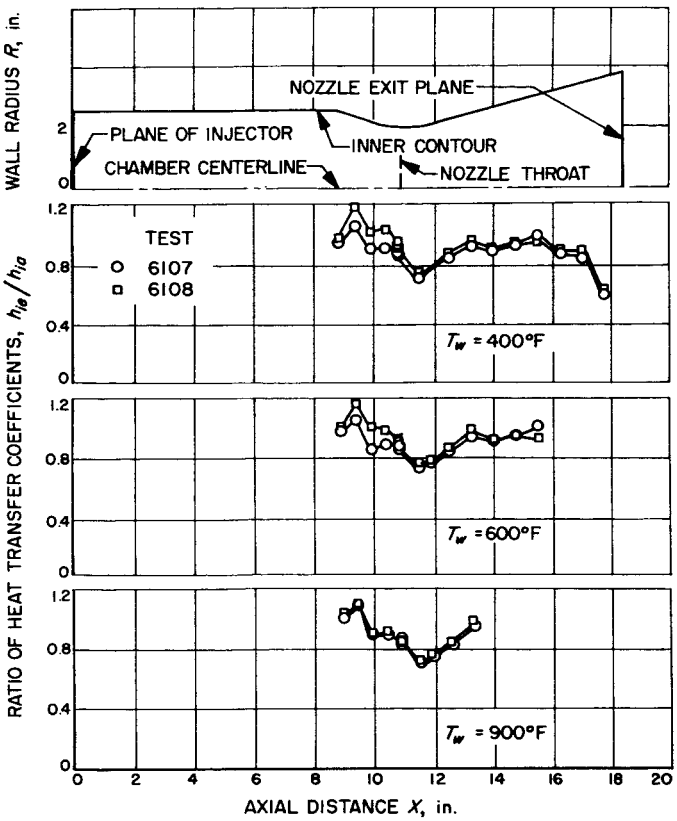

Figure 89. Comparison of uncooled nozzle enthalpy heat transfer coefficient to prediction at 400, 600, and 900°F wall temperatures

uncooled nozzle is shown in Figure 89. Except at the 400 and 600°F wall temperature comparisons for Plugs 12, 13, and 14, located in the contraction region, results between tests are generally in good agreement. In Test 6107, these same plugs indicate nearly constant values of h_{ie}/h_{ia} for all wall temperatures, whereas in Test 6108 these plugs give results which are nearly constant at 400 and 600°F but decrease approximately 10% and agree with the results of Test 6107 at 900°F wall temperature.

Except for the higher values of h_{ie}/h_{ia} for Plug 14, a nearly linearly decreasing, then increasing trend of h_{ie}/h_{ia}, with axial distance is observed between Plug 15, $h_{ie}/h_{ia} = 1.0$ (contraction region) and Plug 7, $h_{ie}/h_{ia} = 0.85$ (expansion region), with the minimum value appearing at Plug 10, $h_{ie}/h_{ia} = 0.75$ (expansion region). Except for Plug 1 located in the separated flow region, h_{ie}/h_{ia}, from Plug 7 to the exit, remains nearly constant at a value of 0.85.

A comparison of the uncooled and calorimetrically cooled nozzle results in the expansion region, where circumferential variations are believed to be very small, has indicated that the method of deducing heat fluxes with the uncooled nozzle is apparently valid. This technique has the advantage of measuring point values of heat flux, which calorimetric measurements may obscure, and will therefore be useful in making measurements in the regions strongly influenced by local combustion dominated flows.

XIII. Solid Propellant Propulsion

A. Polymer Synthesis and Characterization

A. J. Havlik and J. Moacanin

1. Bulk and Solution Properties of Polyoxypropylene Glycols

Some of the problems of the chemical structure of polyoxypropylene glycols (PPG) which have been considered in prior work at JPL are: (1) the molecular weight distribution; (2) the type and distribution of hydroxyl end group, primary or secondary, and (3) the quantity and distribution of foreign functional groups, e.g., carbonyls, olefine peroxides and acetals.

Previously, the molecular weight distributions in commercially available PPG's 400, 750, and 1200 were estimated by molecular distillation. Gas–liquid chromatography techniques (GLC) have now been successfully applied to fractionate PPG's 150, 250 and 425 (Ref 71, *RS 36-3*, Vol I, Part II) as well as the first nine homologs of a polyoxyethylene glycol resin. Also, di- and tripropylene glycols could be resolved into their respective structural isomers. Proton magnetic resonance experiments showed that commercially available DPG contains 60% primary and 40% secondary hydroxyls. The PMR method was also used to establish the structures of the three structural isomers of DPG (Ref 72). Work is still in progress on the problem of foreign functional groups.

Previously, the PPG fractions obtained by distillation (M_n 200 to 1500, determined by end group analysis) were used to correlate the molecular weight to the bulk kinematic viscosity ν. Now, the intrinsic viscosity $[\eta]$-molecular weight relationship has been defined, and the ν-molecular weight relationship extended to higher molecular weights. Polyoxypropylene glycols of molecular weights up to 20,000 were obtained by solution fractionation of a sample of PPG obtained from the polymerization of propylene oxide in the presence of about 10% by weight of powdered potassium hydroxide at room temperature and atmospheric pressure.

A number of PPG fractions were characterized by steady flow viscosities determined in bulk and in solution in five different solvents, as well as by their number-average molecular weights. The plot of $[\eta]$ vs M_n given in Figure 90 shows that $[\eta]$ is proportional to M_n. The

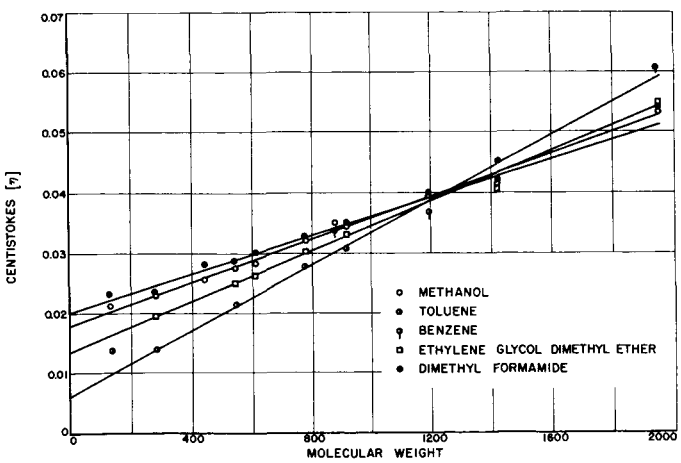

Figure 90. Molecular weight–intrinsic viscosity relationship for polyoxypropylene glycols in five solvents at 25.0°C

straight lines representing this relationship have a common point of intersection at a molecular weight of about 1200. For molecular weights above the intersection point, the linear relationship is rapidly replaced by the exponential Mark-Houwink relationship, $[\eta] = KM^a$, as shown in Figure 91. Here $[\eta]$ for PPG fractions are given together with those previously obtained for 2,4-toluene-diisocyanate-extended PPG's (Ref 73). For the latter samples, M is the weight average molecular weight M_w; for the fraction $M=M_n \approx M_w$.

Kinematic viscosities in bulk, ν, were determined on PPG's with molecular weights up to 16,000. A plot of $\log \nu$ vs $\log M$ is shown in Figure 92. A straight line of unit slope fits the data well for molecular weights greater than 700 and less than 8000. The direct proportionality between ν and M is predicted by Bueche's theoretical treatment of ν (Ref 74) for polymers whose molecular weights are less than that necessary for formation of molecular entanglements. The non-linearity of the lower portion of the plot may reflect the increased importance of hydrogen bonding of the hydroxyl end groups at the low molecular weights. The increase in slope above 8000 suggests this to be the critical molecular weight M_c, above which molecular entanglements become effective. The line through the points above M_c was drawn with a slope of 3.4, a value observed for other polymer systems (Ref 75). Although this slope is not well defined by the available data, the existence of a break in the line is clearly indicated.

The M_c for PPG corresponds to a value of 400 for the critical chain length, Z_c. A comparison of the Z_c for PPG

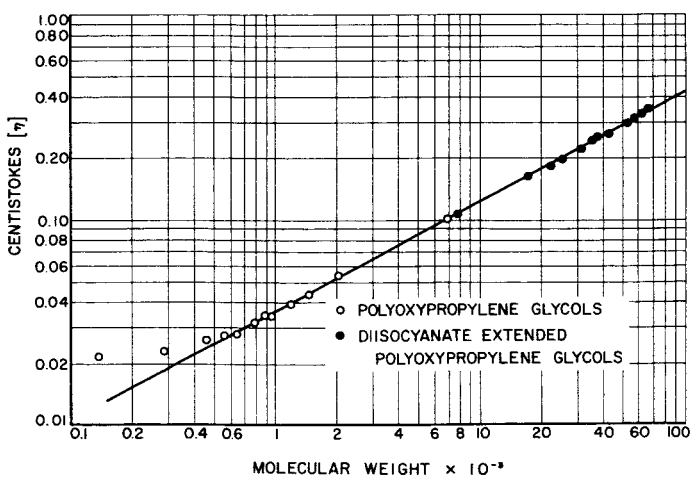

Figure 91. Molecular weight–intrinsic viscosity relationship in methanol at 25.0°C

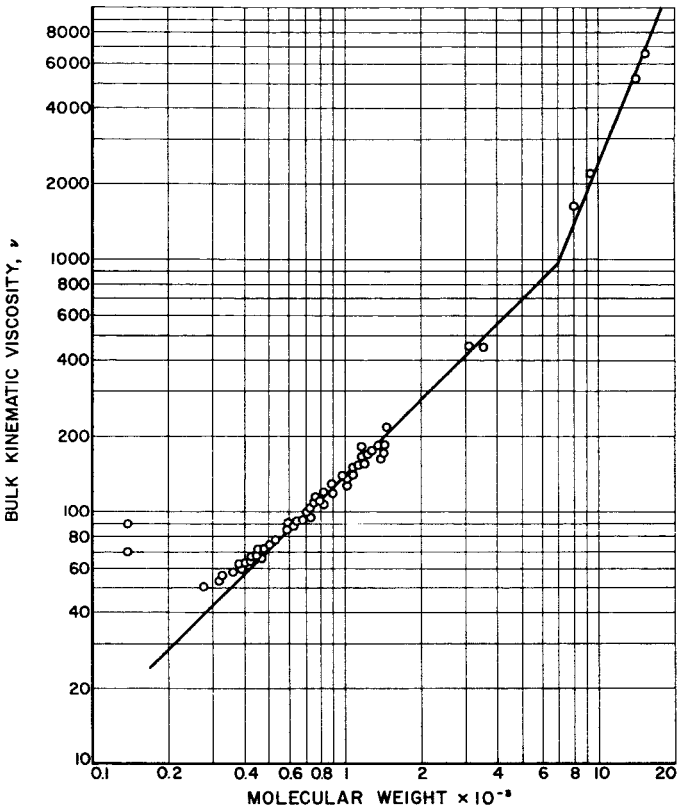

Figure 92. Molecular weight–bulk viscosity relationship for polyoxypropylene glycols at 25.0°C

and the various polymers is given in Table 14. These data show that the PPG is intermediate between polar and non-polar polymers in the establishment of molecular entanglements. If a high value of Z_c is an indication of greater chain flexibility for a polymer, then it would appear that PPG is a more flexible polymer than a polyester but less flexible than polyisobutylene. Further work will be required, however, to evaluate the effect of the ether linkages on Z_c in PPG and the relative importance of the polarity and the reduction in the barriers to free rotation.

Table 14. Critical chain length, Z_c, for various polymers

Polymer	Z_c at break
Poly (dimethylsiloxane)	950
Polystyrene	730
Polyisobutylene	610
Polyoxypropylene glycol	400
Decamethylene sebacate	290
Poly (methylmethacrylate)	208

Studies are underway to determine the temperature dependencies of the bulk and solution properties of PPG's. Additional work is in progress to extend the molecular weight range investigated to above 200,000.

B. Polymer Degradation Mechanisms

J. D. Ingham and N. S. Rapp

Thermal Degradation of a Polyurethane Polymer

The thermal degradation of polymers is being studied to determine the mechanisms of chemical interactions and to investigate the feasibility of developing non-destructive chemical methods for monitoring the extent of degradation and determining the storage life of solid propellants on the basis of structural chemical changes. For the present work, an uncrosslinked polyurethane analog of propellant binders has been prepared from polyoxypropylene glycol (PPG) and toluene-2,4-diisocyanate (TDI). Ultimately the relative susceptibilities of the ether and urethane linkages to bond scission and branching will be studied in vacuum, under inert and oxidative atmospheres, and in the presence and absence of additives.

a. Preparation of polymer and preliminary experiments. The catalyst (ferric acetylacetonate, 0.02 wt % of polymer) was dissolved in the TDI, which was then added to the polypropylene glycol (NCO/OH mole ratio of 1.05) and cured for 70 hours at 60°C. The polymer was prepared in a dry box under nitrogen (relative humidity 2.5%). After curing, it was dissolved in benzene and stored in the dry box. The intrinsic viscosity in benzene was 0.71 dl/gm, which is higher than that reported previously for a similar polymer (Ref 73). However, the PPG used in the present work may have contained less monofunctional hydroxyl impurity.

Viscosities were measured in benzene with Zhukov viscometers at 25 ± 0.02°C and $[\eta]$ calculated from a single measurement using an assumed k' of 0.39 and the equation

$$\frac{\eta_{sp}}{C} = [\eta] + k'[\eta]^2 C$$

Changes in infrared spectra of polymer films on heating at 80°C for 2 weeks in air and in a nitrogen atmosphere indicated small increases in hydroxyl or amine and decreases in urethane hydrogen. The spectrum of a bulk sample heated under nitrogen at 245°C for 24 hours was similar but indicated greater scission of urethane bonds.

To determine qualitatively the effects of oxygen and water on degradation of the bulk polymer, samples under dry nitrogen, dry air, and water-saturated nitrogen are being heated at 80°C. At intervals, samples are withdrawn for intrinsic viscosity measurements utilizing an appropriate gas purge during sample withdrawal. Results are shown in Figure 93. Although these data suffer from the limitations of uncontrolled sample thickness, and variable oxygen and water vapor pressures, they show that bond scission is much more rapid in the presence of oxygen. Furthermore, these changes occur at moderate temperatures. It appears that the initial degradation rate is higher in the absence of oxygen if water is present. Degradation of a benzene solution at 60°C in air was in

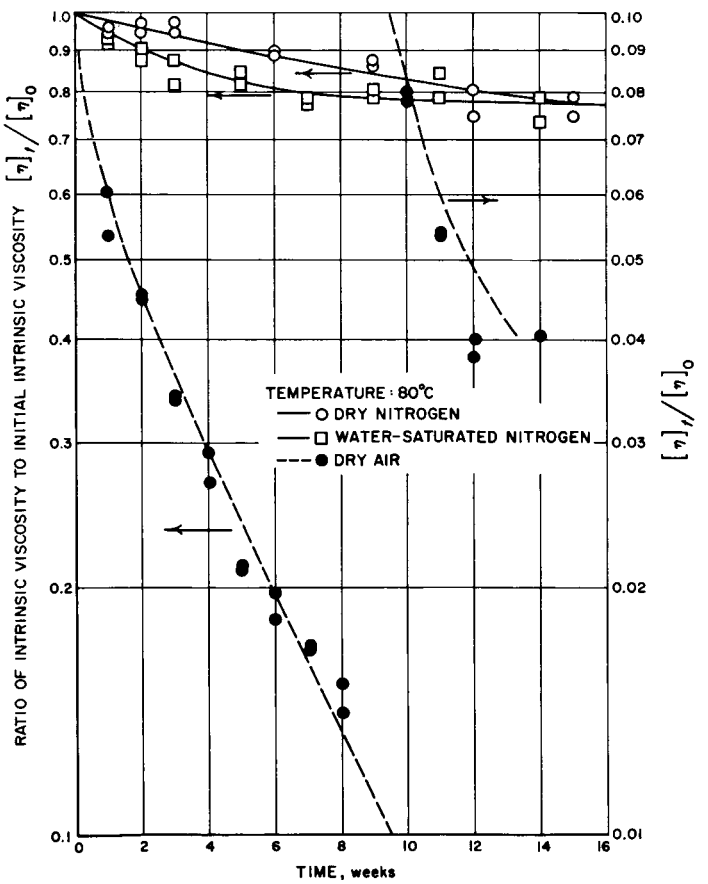

Figure 93. Degradation of polyoxypropylene-polyurethane in nitrogen, water-saturated nitrogen, and dry-air atmospheres

qualitative agreement with the data on bulk polymer of Figure 93. The degradation rate in carbon tetrachloride was greater by almost an order of magnitude. Extensive data on degradation in solutions of a similar polymer are given in *CBS 67* and *68*.

b. Degradation of polymers in vacuum and investigation of products. Since preliminary tests indicated that no degradation occurred when a sample was heated at 60°C for 24 hours, 80°C for 24 hours, and 100°C for 17 hours in vacuum, studies at 200°C were initiated with the ultimate objective of determining the degradation products and some features of the mechanism of degradation without the complications of oxidative reactions or catalysts.

After evacuating and degassing for 1 hour at 80°C, polymer samples (1 gm) were sealed in tubes fitted with breakseals and then degraded at 203 ±3°C for 24 hours. The intrinsic viscosity (determined from multiple concentration data) of seven samples fell to 0.32 ±0.02 dl/gm. Mass spectrographic analysis of the vapor over the samples showed the presence of CO_2 and trace amounts of other components with the major mass peak at 43 or 58. Since the parent peaks for acetone, propylene oxide, and acetaldehyde appear at 43 or 58, it is probable that one or a combination of these is present. Components other than carbon dioxide could not be detected by vapor-phase chromatography.

Quantitative analysis for CO_2 was carried out on a 6-foot silica gel column at 90°C. Calibrations were carried out by injection of known amounts of CO_2 before and after sample analysis. It appears that insufficient CO_2 (0.016 meq/gm or 1.6 mole % of CO_2 initially present as urethane) was evolved to account for the number of linkages broken as indicated by the decrease from 0.71 to 0.34 in intrinsic viscosity which could correspond to 6% urethanes ruptured. It is possible that the molecular weight distribution of the degraded polymer changed in such a way as to make any estimate of cuts from viscosity measurements unreliable, or that some of the CO_2 may have recombined with the polymer on cooling prior to analysis. From the limited data obtained, it appears that the only volatile product found in readily detectable amounts is carbon dioxide and that the degradation possesses random scission features, as opposed to chain unzipping to give large amounts of low molecular weight fragments.

Previous studies (Refs 76, 77) suggest that a minimum of one equivalent of CO_2 per equivalent of urethane scission would be expected, but that the amount of CO_2 found per cut could be much more; also, numerous reactions leading to branching can occur. In addition, scission at bonds other than the urethane, such as labile peroxide or others, has not been excluded. If reactions other than urethane scission have occurred to any extent, a correlation between CO_2 evolution and bond scission would not be expected, although CO_2 could still be produced. Thus, in order to establish the mechanism of PPG–TDI polymer degradation, it will be necessary to determine number average molecular weights, weight average molecular weights, molecular weight distributions, carbon dioxide evolution, and other chemical changes as a function of time and temperature. Because of the small concentration of functional groups formed (which may be less than 0.01 meq/gm), much further work on the development of analytical methods will be required. In addition, a reasonably rapid means of fractionating the polymer is needed. Development of a method utilizing elution column chromatography from an inert substrate is in progress.

References

1. Goles, G. G., Fish, R. A., and Anders, E., "The Record in the Meteorites—I. The Former Environment of Stone Meteorites as Deduced from K^{40}-Ar^{40} Ages," *Geochimica et Cosmochimica Acta,* 19:177–195, 1960.
2. Geiss, J., and Hess, D. C., "Argon-Potassium Ages and the Isotopic Composition of Argon from Meteorites," *Astrophysical Journal,* 127:224–236, 1958.
3. Foote, W. M., "Preliminary Note on the Shower of Meteoric Stones Near Holbrook, Navajo County, Arizona, July 19th, 1912," *American Journal of Science,* 4th ser., 34:437–456, 1912.
4. Quirke, T. T., "The Richardton Meteorite," *Journal of Geology,* 27:431–448, 1919.
5. DuFresne, E. R., and Anders, E., "The Record in the Meteorites—V. A Thermometer Mineral in the Mighei Carbonaceous Chondrite," *Geochimica et Cosmochimica Acta,* 23:200–208, 1961.
6. Gentner, W., and Zahringer, J., "Kalium-Argon-Alter einiger Tektite," *Zeitshrift für Naturforschung,* 14a:686–687, 1959.
7. Clarke, V. C., Bollman, W. E., and Scholey, W. J., *Design Parameters for Ballistic Interplanetary Trajectories—Part I, One-Way Transfers to Mars and Venus,* Technical Report 32-77, Jet Propulsion Laboratory, Pasadena, November 1, 1961.
8. Dyson, J., "Precise Measurement by Image-Splitting," *Journal of the Optical Society of America,* 50:754–757, 1960.
9. Muller, P., "Un nouveau micrometre a double image," *L'Astronomie,* 61:265–266, 1947.
10. Muller, P., "L'aplatissement de Mars," *L'Astronomie,* 62:201–203, 1948.
11. Dollfus, A., "Optique Astronomique," *Comptes Rendus,* 235: 1477, 1952.
12. Muller, P., *Communications et Memoires,* p. 92, Comite National Francais d'Astronomie. Reunions scientifiques tennes a Paris Centenaire de la decouverte de Neptune, Paris, 1948.
13. Muller, P., "A propos du diamètre de Mercure," *L'Astronomie,* 69:82–83, 1955.
14. Kuiper, G. P., *Atmospheres of the Earth and Planets,* University of Chicago Press, Chicago, 1952.
15. De Vaucouleurs, G., *Journal of Geophysical Research,* 64:1739, 1959.
16. De Vaucouleurs, G., *Diameters of Terrestrial Planets.* Geophysics Corporation of America, Boston (to be published), 1961.
17. Baumert, L. D., and Stiffler, J. J., "Inequivalent Hadamard Matrices," *Research Summary 36-9,* Vol I, p 28, June 1961.
18. Husain, Q. M., "On the Totality of the Solutions for the Symmetrical Incomplete Balanced Block Designs: $\lambda = 2$, $k = 5$ or 6," *Sankhya,* 7:204–208, 1943.
19. Golomb, S. W., Welch, L. R., and Goldstein, R. M., *Cycles from Nonlinear Shift Registers,* Progress Report 20-389, Jet Propulsion Laboratory, Pasadena, August 31, 1959.
20. Hales, A. W., "Generation of Periodic Pulse Patterns," *Research Summary 4,* Jet Propulsion Laboratory, Pasadena, August 15, 1959.
21. Victor, W. K., and Choate, R. L., *Design Techniques for Low Power Telemetry,* Technical Report 32-153, Jet Propulsion Laboratory, Pasadena.
22. Carson, J. R., "Frequency Modulation: Theory of the Feedback Receiver Circuit," *Bell System Technical Journal,* 18(No. 3): 395–403, July 1939.
23. Chaffee, J. G., "The Application of Negative Feedback to Frequency Modulation Systems," *Bell System Technical Journal,* 18(No. 3):404–437, July 1939.
24. Sydnor, R. L., "Investigation of an FM Demodulator with Negative Feedback," *Research Summary 36-9,* Vol I, p 32, Jet Propulsion Laboratory, Pasadena, July 1, 1961.
25. Ruthroff, C. L., and Emloe, L. H., "Threshold Effects of the FM Demodulator with Feedback," *URSI-IRE* Joint Meeting, May 4, 1961.
26. Gagliardi, R. M., and Miller, T., "Minimum Power Wideband Communication System for Space Vehicles," *Proceedings of National Telemetering Conference,* May 22–24, 1961.
27. Choate, R. L., "Analysis of Phase Modulation Communications Systems," *IRE Transactions on Communications Systems,* CS-8(No. 4):224–227, December 1960.
28. Viterbi, A. J., "On Coded Phase Coherent Communications," *IRE Transactions on Space Electronics and Telemetry.* SET-7 (No. 1): March 1961.
29. Titsworth, R. C., and Welch, L. R., *Modulation by Random and Pseudo-Random Sequences,* Progress Report 20-387, Jet Propulsion Laboratory, Pasadena, June 12, 1959.
30. Davenport, W. B., and Root, W. L., *Random Signals and Noise,* McGraw-Hill Book Co., Inc., New York, 1958.
31. Gilden, M., and Mathasi, G. L., "A Nearly Optimum Wide-Band Degenerate Parametric Amplifier," *Proceedings of the IRE,* 49(No. 4): 833, April 1961.
32. Silver, S., *Microwave Antenna Theory and Design,* pp 144–149, McGraw-Hill Book Co., New York, 1949.
33. Maserjian, J., *A Semiconductor Approach to Microelectronics,* Technical Report 34-206, Jet Propulsion Laboratory, Pasadena, December 2, 1960.
34. Campbell, I. E., *High-Temperature Technology,* John Wiley, Inc., New York, 1956.
35. Darnell, J. R., and Yntema, L. F., article in *The Technology of Columbium,* B. W. Gonser, Ed., John Wiley, Inc., New York, 1958.

36. Viterbi, A. J., *Acquisition and Tracking Behavior of Phase-Locked Loops,* External Publication 673, Jet Propulsion Laboratory, Pasadena, July 14, 1959.

37. Titsworth, R. C., and Welch, L. R., *Modulation by Random and Pseudorandom Sequences,* Progress Report 20-387, Jet Propulsion Laboratory, Pasadena, June 12, 1959.

38. Karplus, M., "Theory of Proton Coupling Constants in Unsaturated Molecules," *Journal of the American Chemical Society,* 82:4431–4432, 1960; "Proton Spin Coupling by Pi Electrons," *Journal of Chemical Physics,* 33:1842–1849, 1960.

39. Alexander, S., "Relative Signs of Spin-Spin Interactions in Nuclear Magnetic Resonance," *Journal of Chemical Physics,* 28:358–359, 1958.

40. Waugh, J. S., and Fessenden, R. W., "Strong Coupling in Nuclear Resonance Spectra," *Journal of Chemical Physics,* 30:944–949, 1958.

41. Banwell, C. N., Cohen, A. D., Sheppard, N., and Turner, J. J., *Proceedings of the Chemical Society,* 266–267, 1959.

42. Whipple, E. B., Goldstein, J. H., Mandell, L., Reddy, G. S., and McClure, G. R., *Journal of the American Chemical Society,* 81:1321–1326, 1959.

43. Whipple, E. B., Goldstein, J. H., and Mandell, L., *Journal of Chemical Physics,* 30:1109, 1959.

44. Whipple, E. B., Goldstein, J. H., and Stewart, W. E., *Journal of the American Chemical Society,* 81:4761–4764, 1959.

45. Muller, N., and Pritchard, D. E., *Journal of Chemical Physics,* 31:768–771, 1959.

46. Bothner-By, A. A., and Naar-Colin, C., *Journal of the American Chemical Society,* 83:231–236, 1961.

47. Davis, D. R., Lutz, R. P., and Roberts, J. D., "Nuclear Magnetic Resonance Spectroscopy; Long Range Spin-Spin Couplings in Saturated Molecules," *Journal of the American Society,* 83:246–247, 1961.

48. Meinwald, J., and Lewis, A., "Long-Range Spin-Spin Couplings in the NMR Spectra of Bicyclohexanes," *Journal of the American Chemical Society,* 83:2769–2770, 1961.

49. Kaiser, R., *Review of Scientific Instruments,* 31:963–965, 1960; Freeman, R., *Molecular Physics,* 3:435–439, 1960.

50. Pople, J. A., Schneider, W. G., and Berstein, H. J., *High-resolution Nuclear Magnetic Resonance,* McGraw-Hill Book Co., New York, 1959.

51. Karplus, M., "Contact Electron-Spin Coupling of Nuclear Magnetic Moments," *Journal of Chemical Physics,* 30:11–15, 1959.

52. Eckert, E. R. G., and Drake, R. M., *Heat and Mass Transfer,* 2nd Ed., McGraw-Hill Book Co., New York, 1959.

53. Bedingfield, C. H., and Drew, T. B., "Analogy between Heat Transfer and Mass Transfer," *Industrial and Engineering Chemistry,* 42:1164–1173, 1950.

54. Hanna, O. T., and Myers, J. E., "Laminar Boundary Layer Flow and Heat Transfer from a Flat Plate for Variable Viscosity," *American Institute of Chemical Engineers Journal* (in press), 1961.

55. Harned, H. S., and Owen, B. B., *The Physical Chemistry of Electrolytic Solutions,* Chapter 1, Reinhold Publishing Co., New York, 1957.

56. Altman, D., *Thermodynamic Properties and Calculated Rocket Performance of Hydrogen to 20,000°K,* Report No. 20-106, Jet Propulsion Laboratory, Pasadena, September 3, 1956.

57. Chapman, S., and Cowling, T. G., *The Mathematical Theory of Non-uniform Gases,* Cambridge University Press, England, 1952.

58. Wu, C. S., *Proceedings of the Royal Society A,* 259:518, 1961.

59. Magnus, W., and Oberhettinger, F., *Functions of Mathematical Physics,* Chelsea Publishing Company, New York, 1954.

60. Demetriades, A., Some Hot-Wire Anemometer Measurements in a Hypersonic Wake. *Proceedings of the Heat Transfer and Fluid Mechanics Institute,* Stanford University Press, 1961.

61. Hromas, L., and Lees, L., *Turbulent Diffusion in the Wake of a Blunt-Nosed Body at Hypersonic Speed,* to be published, Space Technology Laboratories, Inglewood, 1961.

62. Kotlensky, W. V., and Martens, H. E., *Tensile Properties of Pyrolytic Graphite to 5000°F,* Technical Report 32-71, Jet Propulsion Laboratory, Pasadena, March 10, 1961.

63. Friedman, H. L., *The Pyrolysis of Plastics in a High-Vacuum Arc Imaging Furnace,* TIS-R60SD380, General Electric MSVD, Space Sciences Laboratory, May 1960.

64. Chandrasekhar, S., and Fermi, E., "Magnetic Fields in Spiral Arms," *Astrophysical Journal,* 118:113–116, 1953.

65. Meyer, P., Parker, E. N., and Simpson, J. A., "Solar Cosmic Rays of February 23, 1956, and Their Propagation Through Interplanetary Space," *Physical Review,* 104(No. 3):768 November 1, 1956.

66. Bailey, D. K., "Abnormal Ionization in the Lower Ionosphere Associated with Cosmic-Ray Flux Enhancements," *Proceedings of the IRE,* 47:255, February 1959.

67. Welsh, W. E., and Witte, A. B., *A Comparison of Analytical and Experimental Local Heat Fluxes in Liquid-Propellant Rocket Thrust Chambers,* Technical Report 32-43, Jet Propulsion Laboratory, Pasadena, February 1, 1961.

68. Welsh, W. E., and Witte, A. B., *A Comparison of Analytical and Experimental Local Heat Fluxes in Liquid-Propellant Rocket Thrust Chambers,* ASME Publication, Paper No. GI-AV-59, presented at ASME Aviation Conference, March 13, 1961.

69. Bartz, D. R., "A Simple Equation for Rapid Estimation of Rocket Nozzle Convective Heat Transfer Coefficients," *Jet Propulsion,* 27(No. 1):49–51, January 1957.

70. Shapiro, A. H., *The Dynamics and Thermodynamics of Compressible Fluid Flow,* Vol II, pp 830–833, Ronald Press, New York, 1954.

71. Havlik, A. J., Landel, R .F., and Moacanin, J., "The Influence of Urea Groups on the Properties of Diisocyanate-Linked Polyethers," *Tenth Canadian High-Polymer Forum,* Ste Marguerite, Canada, September 1960.

72. Havlik, A. J., and Hildebrandt, A. F., "Structures of Dipropylene Glycols from Nuclear Magnetic Resonance Spectroscopy," *Journal of Polymer Science,* XLI:533–535, 1959.

73. Moacanin, J., "Diisocyanate-Linked Polymers," *Journal of Applied Polymer Science,* I:272–282, 1959.

74. Bueche, F., "Viscosity, Self-Diffusion, and Allied Effects in Solid Polymers," *Journal of Chemical Physics,* 20:1959–1964, 1952.

75. Fox, T. G., Gratch, S., and Loshaek, S., *Rheology,* Vol I, Chapter 12, F. Eirich, Ed., Academic Press, New York, 1956.

76. Dyer, E., and Osborne, D. W., "The Thermal Degradation of a Polythiolcarbonate," *Journal of Polymer Science,* XLVII: 349–359, 1960.

77. Fletcher, M. A., Lalsin, M. W., and Plant, S. G. P., "The Pyrolysis of Some Complex Urethanes," *Journal of the Chemical Society,* London, Part IV:3898–3902, 1953.